

Copyright  
by  
Huai Huang  
2012

**The Dissertation Committee for Huai Huang Certifies that this is the approved  
version of the following dissertation:**

**Plasma Damaging Process of Porous Ultra-Low-k Dielectrics and  
Dielectric Repair**

**Committee:**

---

Paul S Ho, Supervisor

---

Maxim Tsoi

---

Chih-Kang Shih

---

Rui Huang

---

Zhen Yao

**Plasma Damaging Process of Porous Ultra-Low-k Dielectrics and  
Dielectric Repair**

**by**

**Huai Huang, B.S.**

**Dissertation**

Presented to the Faculty of the Graduate School of

The University of Texas at Austin

in Partial Fulfillment

of the Requirements

for the Degree of

**Doctor of Philosophy**

**The University of Texas at Austin**

**August 2012**

## **Dedication**

To my parents

## **Acknowledgements**

I would like to thank my research advisor Prof. Paul S. Ho for his guidance and support. Without him, this dissertation would not have been completed. I will always look up to him for his professionalism and wisdom. I would also like to thank other members of my committee, Prof. Rui Huang, Prof. Chih-Kang Shih, Prof. Zhen Yao, Prof. Maxim Tsoi, for their support and advice.

The plasma and low-k interaction project was first supported by Intel Corp. and then by Applied Materials, Inc. I would like to thank them for the financial support. Many thanks go to Yifeng Zhou, Andrew Li, Kevin Zhou, Jeremiah T. Pender, Michael D. Armacost and David Kyser of Applied Materials, Inc. as well as Michael D. Goodner, Michael L. McSwiney, Mansour Moinpour and Grant M. Kloster of Intel Corp. for providing low-k samples and discussions.

I am deeply indebted to my colleagues in this project. Junjun Liu graduated right before I joined the group, but I was able to have many valuable discussions with him. I was so lucky to work with Hualiang Shi and Junjing Bao. They guided me into the project, taught me how to use the equipment and collaborated on many projects. I am grateful to other members (or former members) of the interconnect and packaging group, including (but not limit to) Bin Li, Zhiquan Luo, Min Ding, Gary Lu, Brook Zhao, Lijuan Zhang, Scott Smith, Soo Young Choi, Xuefeng Zhang, Qiu Zhao, Zhuojie Wu, Linjun Cao, Yiwei Wang, Tengfei Jiang. I sincerely thank them for their help and support. Special thanks go to Dr. Jay Im for his help and advices on my writing and research projects. And many thanks go to Ms. Jo Ann Smith for her administrative support and kindness.

I would like to thank Dr. Mikhail R. Baklanov of IMEC for the fruitful discussions about plasma induced damage to porous low-k dielectrics.

I would like to express my appreciation to the staff members of Microelectronic Research Center, Center for Nano and Molecular science, Texas Materials Institute and the student mechanic shop.

Finally, I want to thank all my friends and family for their support and companion through my long PhD years. Special thanks go to my host father Mr. Roger Labodda. His hospitality made my life in the foreign country much easier. And I am grateful to have him proof read this dissertation for grammar mistakes even though he knows nothing about microelectronics. I thank my parents for their love and support. This dissertation is dedicated to them.

# **Plasma Damaging Process of Porous Ultra-Low-k Dielectrics and Dielectric Repair**

Huai Huang, Ph.D.

The University of Texas at Austin, 2012

Supervisor: Paul S. Ho

The Ultra-low-k material is required to reduce the RC time delay in the integrated circuits. However, the integration of the porous low-k material into the on-chip interconnects was impeded by the plasma induced damage during etching and photoresist stripping processes. This dissertation aims to study the mechanism of plasma damage to porous ultra-low-k dielectrics with the objective to minimize the damage and to develop methods and processes to restore the low-k dielectric after the plasma damage.

First, the plasma etching induced surface roughening was studied on blanket porous SiCOH films in the fluorocarbon based plasma. Substantial surface roughening was found in the low polymerization region, where the surface roughening process was initiated by the unevenly distribution of surface fluorocarbon polymers in the pore structure and enhanced by ion induced surface densification. With oxygen addition, the surface densification layer increased the radial diffusion rate difference between the top and the bottom of the pits, resulting in further increase of the surface roughness. The best process optimization was found at a “threshold point” where the surface polymerization level is just high enough to suppress the roughness initiation.

The second part of this dissertation investigates the mechanism of the oxygen plasma damaging process. The roles of plasma constituents (i.e. ions, radicals and

photons with different wavelengths) were differentiated by an on-wafer filter system. Oxygen radical was identified as the most critical and its damage effect was enhanced by photons with wavelength smaller than 185nm. The oxygen radical kinetics in the porous structure of low-k, including diffusion, reaction and recombination, was described analytically with a plasma altered layer model and then simulated with a Monte Carlo computational method, which give guidelines to minimize the damage. The analytical model of oxygen radical kinetic process is also used to investigate the oxygen plasma damage to patterned low-k structure, which is confirmed by experiments.

Finally, the dielectric recovery was studied using silylation and UV broadband thermal treatment, both individually and in combination. After both vapor and supercritical CO<sub>2</sub> silylation, surface carbon and hydrophobicity were partially recovered. However, the recovery effect was limited to the surface. In comparison, UV treatment can effectively remove water from the bulk of the damaged film and consolidate the silanol bonds with the help of thermal activation. The combination of UV and silylation treatments is more effectively for dielectric recovery than UV or silylation alone. The “UV first” treatment provided a better recovery in sequential processes. Under the same conditions, simultaneous treatments by silylation and UV irradiation achieved better bulk and surface recovery than the sequential process.

## Table of Contents

List of Tables.....	xiii
List of Figures .....	xiv
Chapter 1: Introduction .....	1
1.1. Development of Cu/low-k interconnect .....	1
1.2. Low dielectric constant materials.....	5
1.3 Cu/low-k integration challenges.....	11
1.4. Descriptions of dissertation research.....	16
Chapter 2: Experimental techniques .....	18
2.1. Plasma processing systems .....	18
Capacitively coupled plasma.....	18
Inductively coupled plasma.....	20
Downstream plasma .....	20
2.2. Characterization techniques .....	21
2.2.1. FTIR .....	23
2.2.2. X-ray photoelectron spectroscopy (XPS).....	28
2.2.2.1. Overview .....	28
2.2.2.2. XPS peak deconvolution .....	29
2.2.2.3. XPS depth profiling.....	31
2.2.2.4. Angle resolved XPS .....	31
2.2.2.5. XPS measurement of patterned structure .....	32
2.2.3. Other experimental techniques.....	33
Chapter 3: Etching induced roughening of Porous SiCOH .....	34
3.1. Introduction and overview .....	34
3.2. Mechanism of fluorocarbon plasma etching.....	35
3.3. Experimental setup.....	39
3.4. Experimental results.....	40
3.4.1. CHF <sub>3</sub> /Ar Plasma chemistry .....	40

3.4.2. O <sub>2</sub> addition.....	47
3.4.3. H <sub>2</sub> addition.....	52
3.5. Discussions.....	55
3.5.1. Etch rate.....	55
3.5.2. Surface roughening mechanism .....	56
Polymerization .....	57
Surface densification.....	60
Ion and neutron transport .....	61
Radical diffusion .....	61
3.5.3. Effect of DHF dipping.....	62
3.6. Summary .....	63
Chapter 4: Oxidative plasma induced damage to porous low-k dielectrics .....	65
4.1. Roles of Ions, Radicals and Photons in oxidative plasma Damage Formation .....	66
4.1.1. On wafer-filter Experiments.....	66
4.1.1.1. Description of the on-wafer filter method.....	66
4.1.1.2. Experimental details.....	68
4.1.1.3. Experimental results.....	73
4.1.2. Roles of the Ions.....	76
4.1.3. Roles of the Photons.....	79
VUV radiation and radicals acting synergistically to enhance the plasma damage .....	79
Mechanisms of VUV photon enhancement .....	79
Damage by VUV radiations only.....	82
4.1.4. Roles of the Radicals.....	83
4.2. The kinetics of radical-lowk interaction.....	84
4.2.1. Kinetics of radical diffusion process.....	84
Diffusion.....	85
Reaction.....	86
Recombination .....	86
4.2.2. The analytical method .....	86

4.2.2.1. The Thiele Model.....	86
4.2.2.2. The further development of the Thiele Model with Carbon evolution.....	89
4.2.2.3. Predictions and Applications.....	90
4.2.3. Monte Carlo simulations of radical kinetics .....	91
4.2.4. Radical diffusion in patterned structure .....	99
4.2.4.1. Analytical results for patterned structures.....	99
4.2.4.2. Experiments.....	105
4.3. Summary .....	110
Chapter 5: Dielectric Recovery .....	111
5.1. Experimental setups .....	113
5.2. Silylation process on O <sub>2</sub> plasma damaged low-k dielectrics.....	115
5.2.1. Overview and literature survey .....	115
5.2.2. Vapor phase silylation.....	121
The experimental setup .....	121
The results and discussion.....	122
The steric hindrance effect and silylation efficiency .....	129
5.2.3. Supercritical CO <sub>2</sub> silylation process.....	131
Overview and the use of supercritical CO <sub>2</sub> silylation.....	131
Experimental setup and result .....	134
Discussion .....	141
5.3. UV and thermal treatment.....	141
5.3.1. Overview .....	141
5.3.2. The wave length selection for dielectric recovery. ....	143
5.3.3. Experimental setup and mechanism of thermal assisted UV curing .....	145
5.3.4. Thermal activation and UV interaction.....	147
5.3.5. Other process optimizations.....	153
Recovery Time .....	153
Ambient effect.....	156
5.4. UV and silylation combined.....	161

5.4.1. Overview: .....	161
5.4.2. Experimental results and analysis .....	162
5.4.2.1. Sequential process .....	162
5.4.2.2. Simultaneous process .....	164
5.5. Summary .....	168
Chapter 6: Summary and future work .....	169
6.1 Summary .....	169
6.2. Recommendations for the ULK plasma process integration.....	172
6.3. Future work .....	173
References .....	175

## List of Tables

Table 2-1: Characterization techniques for low-k materials .....	22
Table 2-2: FTIR peak assignments of SiCOH low-k dielectrics[20].....	26
Table 2-3: Molecular structure, connectivity and FTIR peak[23][24].....	27
Table 2-4: Molecular structure unit of Si-O-Si and their FTIR peaks and bond angles. .....	27
Table 4-1: The plasma constituents and their angular distributions in a plasma system. .....	67
Table 4-2: The filter mask combinations used in the on-wafer filter experiments. The filters are placed 0.7 mm above the low-k surface unless specified otherwise. ....	73
Table 4-3: Bond dissociation energy and associated wavelengths in diatomic molecules[63].....	80
Table 5-1: Summary of silylation studies. ....	118
Table 5-2: Summary of silylation studies (continued).....	119
Table 5-3: Areas of major FTIR peaks and results from measurement of water contact angles. (Courtesy of Junjing Bao).....	136
Table 5-4: Parameters for water desorption mechanisms[103][104].....	151
Table 5-5: Comparison of silylation and UV process.....	161

## List of Figures

Figure 1-1: Typical cross-sections of the interconnect structure indicating the hierarchical scaling.[2] .....	2
Figure 1-2: Schematic diagram of BEOL interconnect RC circuit model.[3] .....	3
Figure 1-3: Gate and interconnect delay versus feature size.[2] .....	4
Figure 1-4: ITRS 2009 effective dielectric constant roadmap. ....	7
Figure 1-5: A brief history of low-k materials development. ....	8
Figure 1-6: Structure of the SiCOH material[7].....	10
Figure 1-7: Schematic drawing of via-first dual damascene process (illustrated by Hualiang Shi).....	13
Figure 1-8: Schematic drawing of O <sub>2</sub> plasma ashing induced bonding configuration changes to porous SiCOH low-k dielectric (illustrated by Hualiang Shi). .....	14
Figure 1-9: Leakage current increase induced by O <sub>2</sub> plasma treatment[10]. ....	15
Figure 2-1: Schematic representation of plasma chambers in damascene processing. (a) RIE, (b) Oxford ICP etcher, (c) Remote plasma with a neutralize grid. ....	19
Figure 2-2: A typical FTIR spectrum of the SiCOH material.....	24
Figure 2-3: Schematic illustration of X-ray photoelectron spectroscopy. ....	29
Figure 2-4: XPS Carbon peak deconvolution (a) pristine SiCOH film, (b) Ar plasma damaged low-k film, (c) fluorocarbon polymerization (80% CHF <sub>3</sub> , 20% Ar) .....	30
Figure 2-5: XPS detections on patterned structure: (a) trench bottom detections, (b) sidewall detection.....	32

Figure 3-1: Schematic of surface reaction mechanism during fluorocarbon etching of SiO <sub>2</sub> [38].....	36
Figure 3-2: Experimental procedures of porous SiCOH material surface roughening study.....	40
Figure 3-3: Thickness reduction and surface roughness after etching. (Total flow rate: 50sccm, Pressure: 40mtorr, Power: 300W, Time: 4min).....	41
Figure 3-4: (a) Thickness reduction and (b) surface roughness after etching and after 90s DHF dipping. (Total flow rate: 50sccm, Pressure: 40mtorr, Power: 300W, Time: 4min).....	42
Figure 3-5: Fluorocarbon polymerization by XPS analysis: (a) Carbon peak evolution and (b) Individual peak area over whole carbon peak ratio.....	44
Figure 3-6: (a) Thickness reduction and (b) roughness at 40/80 mtor.....	45
Figure 3-7: Effect of (a) etch time and (b) DC bias at CHF <sub>3</sub> 10%.....	46
Figure 3-8: Sum of all CF peak areas over total C peak area measured by XPS with or without O <sub>2</sub> addition. (Total flow rate: 50sccm, Pressure: 40 mTor, Power: 300W, Time: 4min.).....	48
Figure 3-9: The effect of O <sub>2</sub> addition on (a) Thickness reduction and (b) roughness. (Total flow rate: 50sccm, Pressure: 40 mtor, Power 300W, Time: 4min.).....	49
Figure 3-10: Effect of O <sub>2</sub> addition on (a) Thickness reduction and (b) roughness after DHF dipping. (Total flow rate: 50sccm, Pressure: 40 mtor, Power 300W, Time: 4min.).....	50
Figure 3-11: Effect of (a) etch time and (b) plasma power with O <sub>2</sub> addition at CHF <sub>3</sub> 30%.....	51

Figure 3-12: Thickness reduction of SiCOH film etching with H <sub>2</sub> addition. (Total flow rate: 50sccm, Pressure: 40 mtor, Power 300W, Time: 4min.).	53
Figure 3-13: Surface roughness of SiCOH film after etching with H <sub>2</sub> addition. (Total flow rate: 50sccm, Pressure: 40 mtor, Power 300W, Time: 4min.).	53
Figure 3-14: Fluorocarbon polymerization by XPS analysis:(a) carbon peak ratios of CHF <sub>3</sub> /Ar with 2% O <sub>2</sub> and 2% H <sub>2</sub> addition; (b) Comparison with pure CHF <sub>3</sub> /Ar and CHF <sub>3</sub> /Ar with 2%O <sub>2</sub> addition only.	54
Figure 3-15: Summary of etch rate dependency on surface polymerization.....	55
Figure 3-16: Summary of the dependency of surface roughness on surface polymerization.....	58
Figure 3-17: Schematics of the micromask formation and the occurrence of the roughening process.....	59
Figure 3-18: Relation of surface roughness threshold with CF peak areas over total C peak area ratio by XPS analysis.	60
Figure 3-19: Thickness reduction after etching and then after DHF dipping of plasma chemistry with or without a 2% O <sub>2</sub> addition. (Total flow rate: 50sccm, Pressure: 40 mtor, Power 300W, Time: 4min.).....	63
Figure 4-1: The schematic of the on-wafer filter structures and the interaction of the plasma constituents.	68
Figure 4-2: (a) ICP and (b) RIE system for on-wafer filter studies of the porous SiCOH.....	69
Figure 4-3: the transmission spectra of (a) MgF <sub>2</sub> , (b) CaF <sub>2</sub> , (c) quartz and (d) UV grade fused silica.....	71
Figure 4-4: The transmission ranges of the optical filters.....	72
Figure 4-5: The reduction of Si-CH <sub>3</sub> /Si-O .....	75

Figure 4-6: The thickness reduction after oxygen plasma treatment .....	75
Figure 4-7: The FTIR –OH and physisorbed water peak area .....	76
Figure 4-8: (a) Thickness reduction and (b) methyl reduction of He plasma, CO2 plasma, and CO2 plasma with the He plasma pretreatment.(courtesy of Hualiang Shi).....	78
Figure 4-9: Quantum-chemical calculation of the threshold wavelengths for Si-CH3 dissociation of octamethylcyclotetrasiloxane[64].....	81
Figure 4-10: The pore structure inside ULK dielectric (a) real case; (b) simplified model.....	84
Figure 4-11: Kinetics of radical diffusion, reaction, and recombination inside pore structure.....	87
Figure 4-12: Thickness reduction and methyl depletion on plasma damaged SiCOH films with different k value. (courtesy of Hualiang Shi).....	91
Figure 4-13: Diffusion mode in a pipe structure.....	92
Figure 4-14: the flowchart of the Monte Carlo simulation of the radical kinetics.	93
Figure 4-15: Effect of carbon concentration on the carbon depletion profiles.(a) schematic diagram of the cross-section view of plasma damaged pSiCOH film; (b) carbon element profile by TOF-SIMS; (c) carbon profile by Monte Carlo simulation.....	94
Figure 4-16: Monte-Carlo simulations of the depth profile of carbon concentration as a function of (a) diffusion probability and (b) recombination probability. .....	96
Figure 4-17: Time evolution of the carbon concentration. (a) Monte Carlo simulation; Experimental (b)methyl peak and (c) thickness vs plasma treatment time.....	97

Figure 4-18: The influence of the carbon depth profile by the relative reaction probability and the recombination probability. ....	98
Figure 4-19. (a) Sidewall damage of patterned low-k structure and (b) kinetics of radical diffusion, reaction, and recombination inside trench. ....	100
Figure 4-20: Oxygen radical density distribution in low-k region inside the trench of patterned low-k structure.....	103
Figure 4-21: The contour plots of oxygen radical density distributions in low-k region inside trench of patterned low-k structure (a) $x=0\text{nm}$ , $d=60\text{nm}$ , (b) $x=100\text{nm}$ , $d=60\text{nm}$ , (c) $x=0\text{nm}$ , $d=150\text{nm}$ , and (d) $x=100\text{nm}$ , $d=150\text{nm}$ . ....	104
Figure 4-22: The experimental set up of gap structure with a Si mask to simulate the radical kinetics in a patterned structure with a hardmask. ....	105
Figure 4-23: Damage formation by O radicals to the ULK with different hardmask materials (a) thickness reduction, (b) methyl depletion.....	107
Figure 4-24: The experiment set up of gap structure with Si mask and optical filters to simulate the radical kinetics in a patterned structure with hardmask.	108
Figure 4-25: Plasma damage produced by O radicals to the ULK with a photo excited $\text{SiO}_2$ hardmask.....	109
Figure 5-1: The simulated effective dielectric constant with a damaged layer versus half-pitch low-k thickness.[77] .....	111
Figure 5-2: SEM images of ULK film undercut below the edge of the cap layer after DHF dipping. Damage-driven undercut with ULK films has made subsequent metal fill very difficult.[78].....	112
Figure 5-3: The schematic diagram of the silylation and UV treatment chamber.	114

Figure 5-4: The schematic diagram and photograph of the silylation and UV treatment system.....	115
Figure 5-5: The schematic diagram of silylation process on a damaged low-k surface. ....	116
Figure 5-6: The schematic diagram of the experimental setup used in silylation study. (a) Carrier gas bottle, (b)MFC, (c) Bubbler, (d) Heating stage, (e) Turbo pump, (f) Mechanical pump, (g) Temperature controller....	121
Figure 5-7: The schematic diagram of silylation process. (a) TMCS, (b) DMDCS, (c) legend.....	122
Figure 5-8: The XPS spectra analysis of the silylation recovery process. (a) Carbon over silicon ratio, (b) C1 over total C 1s peak area,(c) Carbon decomposition diagram of the C 1s peak. ....	124
Figure 5-9: Contact angle measurement of after DMDCS and TMCS silylation.	125
Figure 5-10: FTIR spectra analysis of silylation recovery process. (a) The whole spectrum, range 522-4000cm <sup>-1</sup> , (b) Enlargement of -OH/ physisorbed water, (c) -OH/H <sub>2</sub> O peak area over Si-O-Si peak area ratio and (d) Si-(CH <sub>3</sub> ) <sub>x</sub> bonds.....	127
Figure 5-11: MIS measurements of low-k film. Dielectric constant after damage was compared with that after DMDCS and TMCS silylation. The black line indicates the pristine dielectric constant 2.2.....	128
Figure 5-12: Schematic diagram of the silylation process to show the formation of the silanol bond on the damaged low k surface.(a) The steric hindrance effect prevents the simultaneous capture of more than one silanols with a monofunctional silylation agent. (b) Di-functional silylation agents react with two neighboring silanols simultaneously. ....	131

Figure 5-13: The phase diagram of a single substance.[96].....	132
Figure 5-14: scCO <sub>2</sub> Silylation System. (Courtesy of Prof. Kwon Taek Lim and Prof. Keith P. Johnston) .....	134
Figure 5-15: FTIR spectra of the sample after plasma O <sub>2</sub> ashing, scCO <sub>2</sub> TMCS silylation and subsequent annealing. (Courtesy of Junjing Bao) ...	135
Figure 5-16: FTIR of TMCS scCO <sub>2</sub> process with increasing pressure (a) Methyl peak; (b) –OH peak. ....	138
Figure 5-17: FTIR spectra of TMCS scCO <sub>2</sub> process with increasing process time(a) Methyl peak; (b) –OH peak.....	139
Figure 5-18: FTIR spectra comparison of scCO <sub>2</sub> TMCS, HMDS and DMDCS silylation processes (a) Methyl peak; (b) –OH peak.....	140
Figure 5-19: Possible structural modifications induced by UV radiation.....	142
Figure 5-20: Schematic spectral response of four important properties (k-value, Modulus, Porogen Removal and Porogen crosslinking) of a hypothetical low-k material, overlaid on some commercially available UV bulbs (Xe arc, Hg arc, and electrodeless Fe, H, bulbs) UV spectra selection. [102] .....	144
Figure 5-21: UV spectrum of the H <sup>+</sup> bulb installed in the fusion F600S UV curing system. <a href="http://www.miltec.com/Catalog/Miltec%20Catalog%2014.pdf">http://www.miltec.com/Catalog/Miltec%20Catalog%2014.pdf</a> .....	144
Figure 5-22: FTIR spectrum of pristine, O <sub>2</sub> damaged and UV cured low-k films. (a) the whole spectrum, (b) the –OH bond and physisorbed water, (c)Si-CH <sub>3</sub> Bond, and (d) Si-O-Si bond.....	146
Figure 5-23: FTIR spectrums of low-k film after oxygen plasma damage and then after thermal curing at 400°C for 1 hour. ....	147

Figure 5-24: FTIR methyl peak and silanol peak of thermal cured and thermal assisted UV cured film .....	148
Figure 5-25: Contact angle of thermal cured and thermal assisted UV cured film	149
Figure 5-26: FTIR methyl peak and silanol peak of thermal assisted UV cured film at different curing temperatures. ....	149
Figure 5-27: Contact angle measurement of thermal assisted UV cured film at different curing temperatures. ....	150
Figure 5-28: Schematic drawing of the various OH species in silica based dielectrics. ....	150
Figure 5-29: FTIR methyl peak and silanol peak of thermal assisted UV cured film at different curing temperature.....	155
Figure 5-30: Contact angle measurement of thermal assisted UV cured film at different curing time.....	156
Figure 5-31: XPS surface carbon of UV treated pristine low-k material under different chamber ambient.....	157
Figure 5-32: FTIR silanol bonds and methyl bonds peak areas of UV treated pristine low-k material under different chamber ambient.(a) FTIR silanol spectrum, (b) FTIR silanol bonding peak ratio, (c) methyl bonds.	158
Figure 5-33: Contact angles of UV treated pristine low-k material under different chamber ambient .....	159
Figure 5-34: FTIR of ambient effect of damaged film, vacuum cure is the best on water removal.....	160
Figure 5-35: Contact angle of the film to show the ambient effect on curing. ...	160
Figure 5-36: XPS and Contact angle measurement results of sequential treatments	163

Figure 5-37: FTIR silanol and methyl bond peak area ratio of sequential treatments. .....	163
Figure 5-38: XPS and Contact angle measurement results of simultaneous silylation and UV treatments.....	165
Figure 5-39: FTIR silanol and methyl bond peak area ratios of simultaneous silylation and UV treatments.....	165
Figure 5-40: Comparison of XPS and Contact angle measurement results of sequential and simultaneous treatments. ....	167
Figure 5-41: Comparison of FTIR silanol and methyl bond peak area ratios of sequential and simultaneous treatments. ....	167

## **Chapter 1: Introduction**

### **1.1.DEVELOPMENT OF CU/LOW-K INTERCONNECT**

Integrated Circuit (IC) is one of the greatest inventions of mankind and can be found in virtually all electronic devices such as computers, mobile phones, and automobiles. The fabrication of integrated circuits is normally composed of two parts: building the complementary metal-oxide-semiconductor (CMOS) devices on the substrate of semiconductor material (e.g. silicon wafer) and forming interconnections between these semiconductor devices. The former process is normally referred to as “the front end of line” (FEOL) process and the latter is called “the back end of line” (BEOL) process.

In the integrated circuit, the interconnect wiring structure serves as an essential system in providing clock signals, electrical signals, power distribution and ground distributions. It includes the metal wires that connect the individual devices (e.g. transistors, capacitors, and resistors) and the interlayer dielectrics (ILD) that isolate and mechanically support the wires. Due to the complexity of the very-large-scale integration (VLSI), the modern interconnect structure contains a hierarchical system with more than 8 levels of metallization layers. The cross section of a typical interconnect structure is shown in Figure 1-1.

To achieve better chip performance, semiconductor manufacturers have been shrinking the transistor size, resulting in increased speed and device density. The scaling of the transistor was well described by Moore’s law for almost 50 years, whereby the number of transistors placed on an integrated circuit increased exponentially, doubling approximately every two years[1].

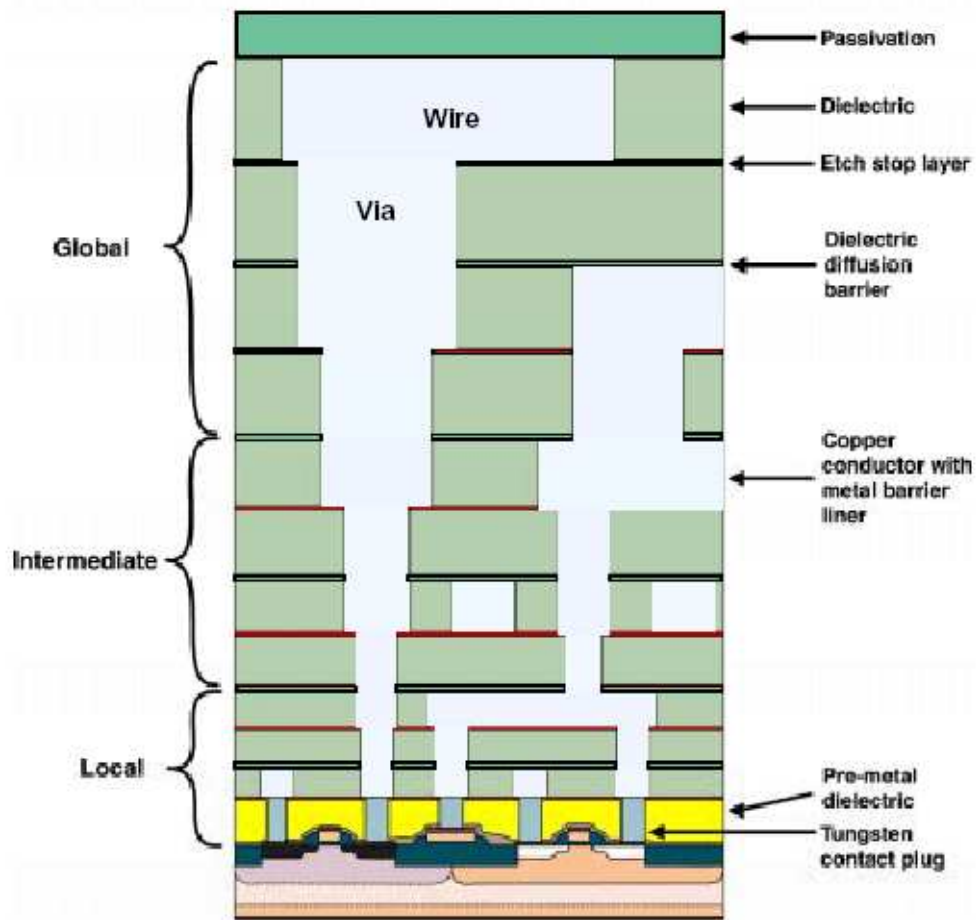


Figure 1-1: Typical cross-sections of the interconnect structure indicating the hierarchical scaling.[2]

The speed of an electrical signal in an IC is governed by two components: the switching time of an individual transistor, known as the transistor gate delay, and the signal propagation time between transistors, known as interconnect or RC delay, where R is metal wire resistance and C is ILD capacitance.

The RC delay of interconnect structure can be evaluated by a simple first-order model proposed by Bohr[3]. The simplified structure used in this model is shown in Figure 1-2 where the metal line has resistivity ( $\rho$ ), width ( $W$ ), thickness ( $T$ ), and length ( $L$ ). The metal line resistance ( $R$ ) can be expressed as:

$$R = \frac{\rho L}{WT} \quad (1.1)$$

Four parallel capacitors are used to indicate the interline capacitance ( $C_L$ ) and inter-plane capacitance ( $C_p$ ),

$$C_L = \frac{k\epsilon_0 TL}{S} \quad (1.2)$$

$$C_p = \frac{k\epsilon_0 WL}{T_1} \quad (1.3)$$

So the total capacitance ( $C$ ) can be approximated as:

$$C = 2(C_L + C_p) = 2k\epsilon_0 L \left( \frac{T}{S} + \frac{W}{T_1} \right) \quad (1.4)$$

where  $k$  is the dielectric constant of dielectrics,  $\epsilon_0$  the permittivity in vacuum,  $S$  and  $T_1$  the metal spacing.

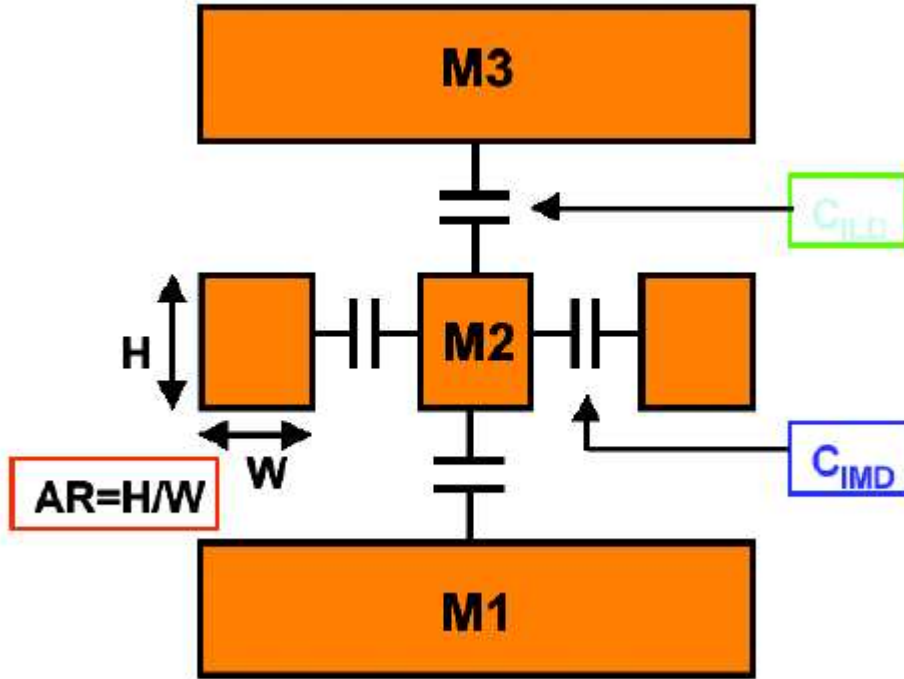


Figure 1-2: Schematic diagram of BEOL interconnect RC circuit model.[3]

The product of R and C then becomes:

$$RC = 2k\rho\varepsilon_0 \left( \frac{L^2}{SW} + \frac{L^2}{TT_1} \right) \quad (1.5)$$

By assuming  $T = T_1$  and  $S = W = \frac{P}{2}$ , where  $P$  is the pitch length, equation 1.5 is reduced to:

$$RC = 2k\rho\varepsilon_0 \left( \frac{4L^2}{P^2} + \frac{L^2}{T^2} \right) \quad (1.6)$$

When feature size is large, the RC delay was negligible in comparison with the signal propagation delay (Figure 1-3). For sub-micron technology, however, the RC delay becomes the dominant factor limiting the device performance.

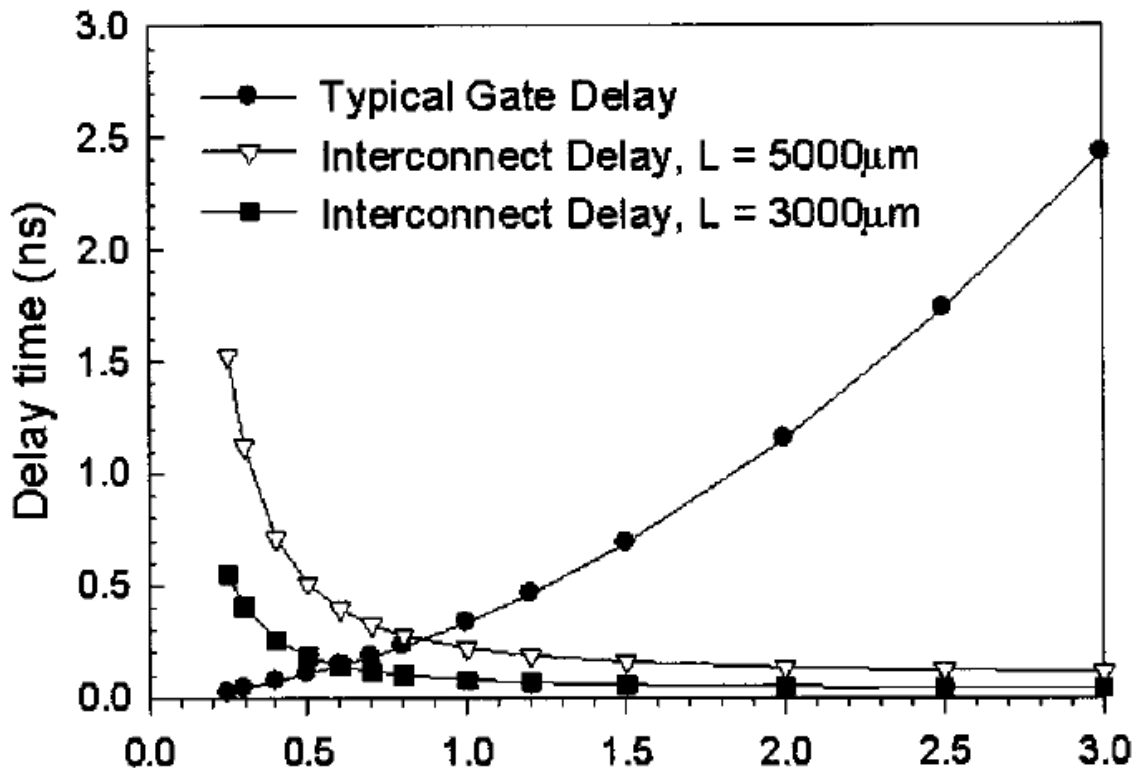


Figure 1-3: Gate and interconnect delay versus feature size.[2]

To reduce the RC delay, two approaches are used. One is to optimize the wiring configuration, particularly the upper level of interconnects (the semi-global and the

global levels), which limited by the circuit design. The second is to improve the material properties (i.e. resistivity and dielectric constant). The traditionally Al/SiO<sub>2</sub> for interconnects have to be changed to new materials. To reduce the resistivity of the metal wire, Al (2.65μΩ·cm) was replaced by Cu (1.70μΩ·cm), which reduced the resistivity by ~30%. The reduction of the dielectric constant can be achieved by replacing SiO<sub>2</sub> (k=4.2) with low-k materials.

The change to low-k materials also has the benefits of reducing “cross-talk” between lines and of reducing the dynamic power consumption. This reduces the noise of the device during operation and making the device more power efficient, both are important for CMOS devices with continuing scaling of device dimensions. The device power is given by[4]:

$$P = \alpha CV^2 f \quad (1.7)$$

where  $\alpha$  is the activity factor,  $C$  the capacitance,  $V$  the power supply voltage and  $f$  the clock frequency.

## **1.2.LOW DIELECTRIC CONSTANT MATERIALS**

A low dielectric constant (low-k) material is any dielectric with a  $k$  value lower than that of SiO<sub>2</sub> (4.2). The lowest possible k value is that of a gas or vacuum with value of 1. The technology to incorporate a gas or vacuum into the interconnect structure is called “air gap”. While Cu is the most probable choice of metal for interconnects to improve resistance since no other metal can offer notable gains, the choices of low-k dielectrics are many. Therefore, the further reduction of RC delay relies on the continuous development of low-k material with a dielectric constant lower than SiO<sub>2</sub>, the standard dielectric material used for interconnect, which has a dielectric constant of 4. As shown in the graph from the international technology roadmap for semiconductors

(ITRS) (Figure 1-4), the effective dielectric constant is decreasing and is expected to reduce to below 2 in the future.

The dielectric constant can be described by Clausius-Mossotti-Debye equation[5]:

$$\frac{k-1}{k+2} = \frac{N}{3\epsilon_0} \left( \alpha_e + \alpha_i + \frac{\mu^2}{3kT} \right) \quad (1.8)$$

where  $N$  is the density of the material (number of molecules per  $\text{cm}^3$ ).  $\alpha_e$  is the electronic polarization, which describes the displacement of the cloud of bond electrons with reference to the nucleus under an applied electric field.  $\alpha_i$  is the ionic polarization, which is induced by the displacement of the nuclei by the applied electric field, thereby stretching or compressing the bond length.

The third term in equation (1.8),  $\left(\frac{\mu^2}{3kT}\right)$ , describes the dipolar polarization, where  $\mu$  is the orientation polarizability,  $k$  is the Boltzmann constant and  $T$  is the temperature. The term  $\frac{\mu^2}{3kT}$  is the thermal averaging of the permanent electric dipole moments in the presence of an applied field.

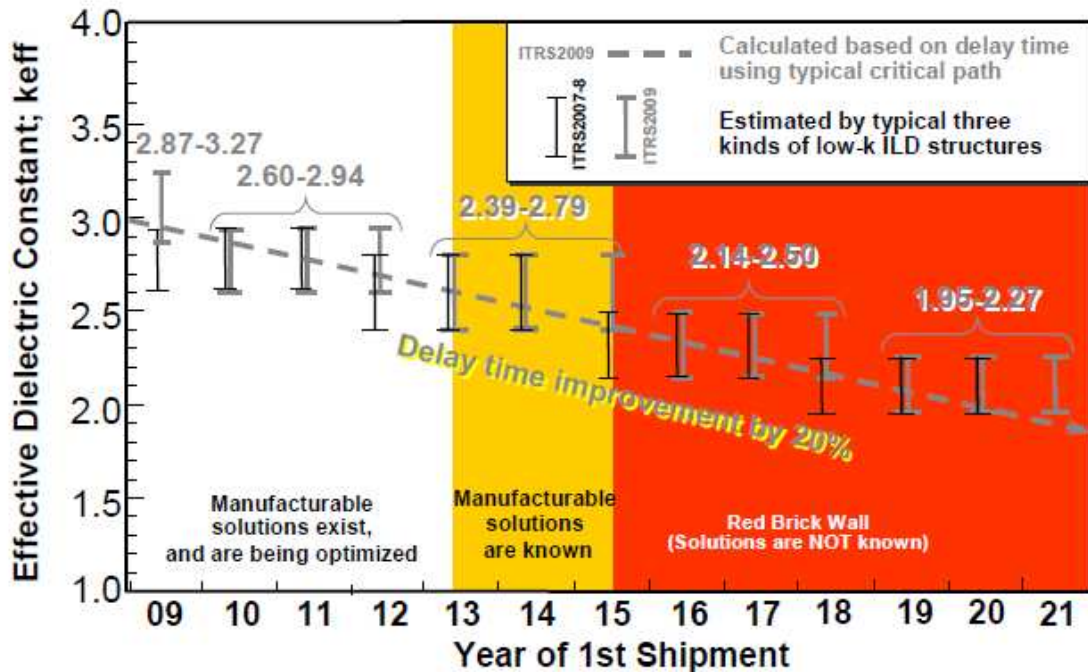


Figure 1-4: ITRS 2009 effective dielectric constant roadmap.

Equation 1.8 points out the two directions in order to reduce the dielectric constant, one by reducing the polarizability of a material and the other is to decrease the density of the material. The history of the low-k material is well described in several reviews[6][7][8]. The organic polymers were considered at first because they can be formed with no-polar C-C bonds. However, this class of material had issues, including thermal instability at high temperature, weak mechanical properties and high coefficient of thermal expansions (CTE). These factors present significant difficulties for integration in the existing IC processing technology. This has led to the development of the main approach adopted by the industry which is to use SiO<sub>2</sub>-liked low-k materials. This class of materials can be easily integrated into the existing technology since the SiO<sub>2</sub> integration is highly developed. The polarizability of SiO<sub>2</sub> can be reduced by introducing less polarized bonds, such as Si-F, Si-H, or Si-CH<sub>3</sub>, into the silicon network. The history

of this approach is summarized in Figure 1-5. Fluorosilicate glass (FSG), which contains low-polar Si-F bonds, was first used to lower the dielectric constant from 4.1 to 3.8. Then the path was separated by deposition methods, whether the material is deposited by a spin on or chemical vapor deposition (CVD) method. A common spin-on material used is methylsilsesquioxane (MSQ) with Si-CH<sub>3</sub> bonds and hydrogen silsesquioxane (HSQ) with Si-H bonds. CVD was chosen for the predominant path for its integration benefits.

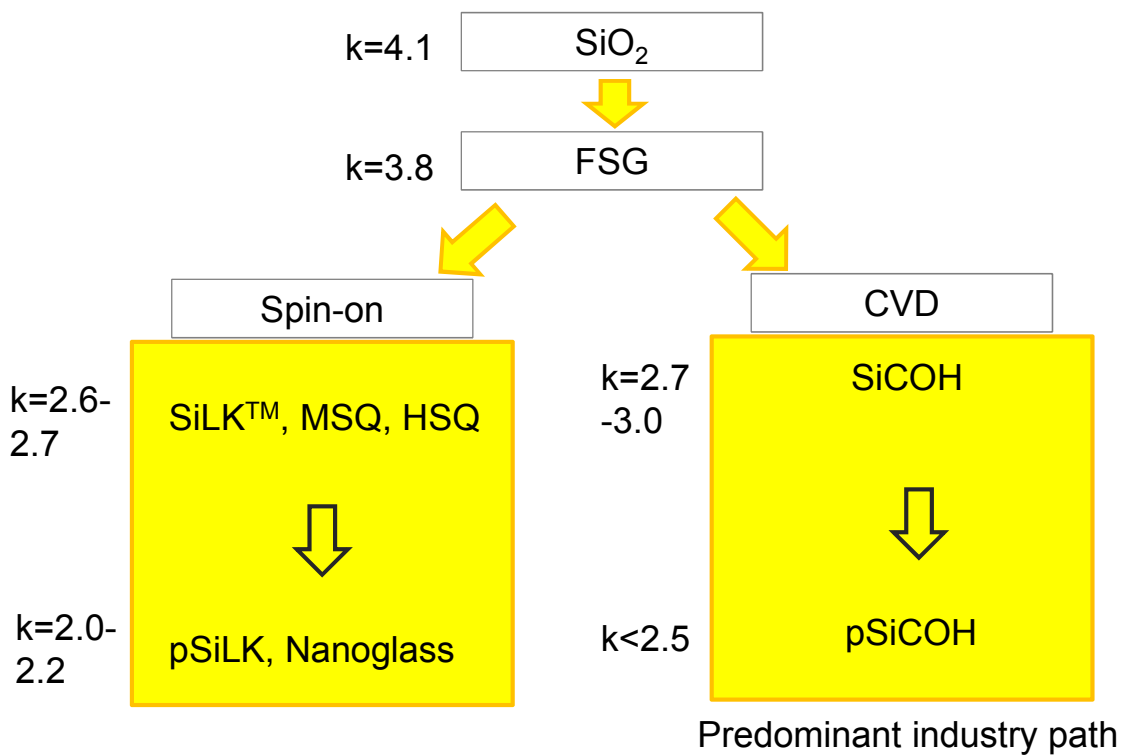


Figure 1-5: A brief history of low-k materials development.

The material of choice from 90nm technology node has been SiCOH materials[8]. The name “SiCOH” describes the elemental composition of the material but does not represent the stoichiometry. The SiCOH material is formed by introducing carbon molecular bonds (mainly through CH<sub>3</sub> groups) into a silica matrix, which reduces both

the total polarizability as well as the density of the material. The SiCOH materials (or SiOCH in different references), therefore, is also called carbon-doped oxide (CDO) or organosilicate glass (OSG) which could be used interchangeably throughout this dissertation.

The implementation of SiCOH materials can reduce the effective k value to 2.7. To achieve lower k value, the density of the material needs to be further reduced by introducing porosity in the low-k material. The k value of a porous material with porosity  $P$  is expressed by the following equation:

$$\frac{k-1}{k+2} = (1-P) \cdot \frac{k_m-1}{k_m+2}$$

where  $k_m$  is the dielectric of the matrix material without porosity and all pores are assumed to empty or filled with a substance that has  $k=1$ . With the introduction of porosity, the ultra-low-k (ULK) material, which is defined as material that has a k value lower than 2.5, was produced.

The ULK material studied in this dissertation (without specifying otherwise) is a porous SiCOH (p-SiCOH) material provided by Applied Materials. It is branded as Black Diamond (BD) III and has a dielectric constant of 2.2 and a porosity of ~ 33%.

The technique for deposition of this porous SiCOH material is by plasma-enhanced chemical vapor deposition (PECVD) using porogen incorporation. This is the most used approach in the industry and first introduced by Grill et al.[9]. In this process, the film is deposited using at least two precursors in the plasma, where one of them is a pure organic molecule referred to as a “porogen”. The other precursor consists of silicon atoms and organic radicals and is called the “matrix” precursor. The plasma interaction of these precursors forms a “hybrid” film composed of an organosilicate-based matrix enclosing the porogens. Then, the porogens are removed by a post-deposition treatment

such as thermal annealing or UV treatment, resulting in a porous SiCOH film with ultra-low-k properties.

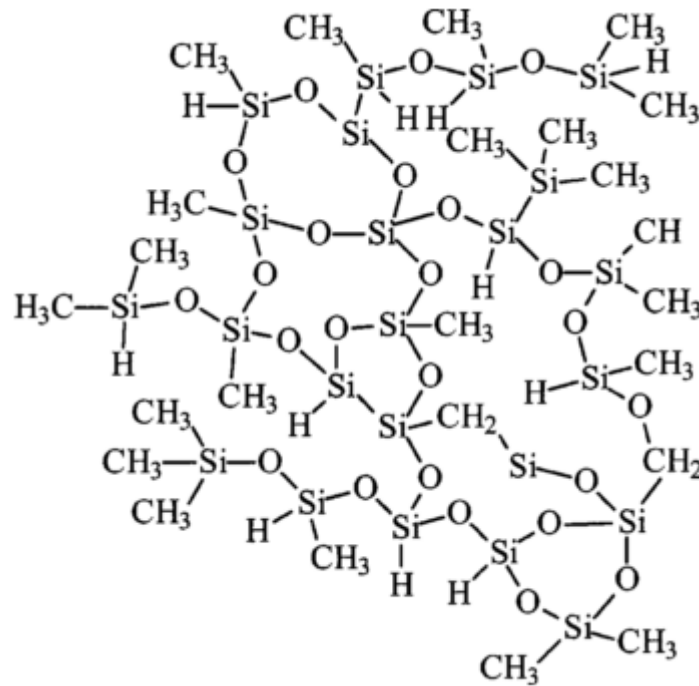


Figure 1-6: Structure of the SiCOH material[7].

Figure 1-6 shows the typical structure of the SiCOH material. The backbone structure of the SiCOH material is the Si-O-Si silica matrix which primarily provides the mechanical strength of the material. Depending on the Si-O-Si bonding angles, the backbone structures are further categorized into the cage structure ( $\sim 150^\circ$ ), the network structure ( $\sim 144^\circ$ ) and the sub-oxide ( $< 140^\circ$ ) structure. The bonding characteristics have been analyzed by Fourier Transform Infra-Red Spectroscopy (FTIR) and the details of the analysis are described in Chapter 2. In general, the network structure is the base silicon dioxide structure where a cage structure is incorporated, creating nano-size voids in the material. The dimension of the pore is nominally of 0.5 nm in diameter,

corresponding to a volume of  $0.065 \text{ nm}^3$ . In the SiCOH dielectric, hydrogen bonds and methyl bonds are connected to the Si-O-Si backbone structure, providing the low polarity bonds and hydrophobicity.

### 1.3 CU/LOW-K INTEGRATION CHALLENGES

The introduction of carbon and the addition of the porosity successfully lowered the dielectric constant. However, it also introduced new integration issues. First, as compared to silica, the decrease in network connectivity and the reduction of density strongly impact the dielectric mechanical properties. Second, methyl bonds are chemically weak and thus can be easily damaged by plasma or wet processes. The porosity increases the accessible surface area and worsens the damage process.

For the Al/SiO<sub>2</sub> technology, the metal is deposited thermally or by sputtering and followed by lithographic patterning prior to the deposition of the dielectric insulator. In this process, the post-deposition damage to the dielectric material is minimized. Unfortunately, for the Cu/Low-k integration, copper cannot be patterned by dry etch as it does not form volatile compounds. As a result, a completely different approach called “damascene” has been developed for fabricating the copper metallization structure. The word “damascene” comes from an ancient art of inlaying different metals into a substrate layer to produce intricate patterns. A simplified damascene process includes the following steps:

- 1, the dielectric layer is deposited on top of the substrate (by PECVD and curing);
- 2, the photoresist (PR) is deposited on the dielectric and then patterned by lithography;
- 3, trench is formed by dry (plasma) etch using the PR mask;
- 4, the residual photoresist is removed by plasma stripping or ashing;

- 5, deposition of the diffusion barrier (by CVD);
- 6, deposition of copper seed layer (by CVD) and copper electroplating;
- 7, chemical mechanical polish (CMP) of copper to remove excessive copper on the top surface;
- 8, a cap layer is deposited to protect copper surface.

In this process flow, the dielectric layer is most likely to be damaged by at least 3 steps: the plasma etching process (step 3), the plasma photoresist stripping or ashing process (step 4) and the CMP wet process (step 7).

The dual damascene process, most commonly used in the industry to form Cu/low k interconnect structures, simplifies the process by using only one metal deposition step to fill the lines and the vias. However the number of plasma etching and stripping steps is not reduced. As shown in the typical “via first” dual damascene process in Figure 1-7, the via wall has to undertake the etching and stripping process for two times, worsening the low-k damage.

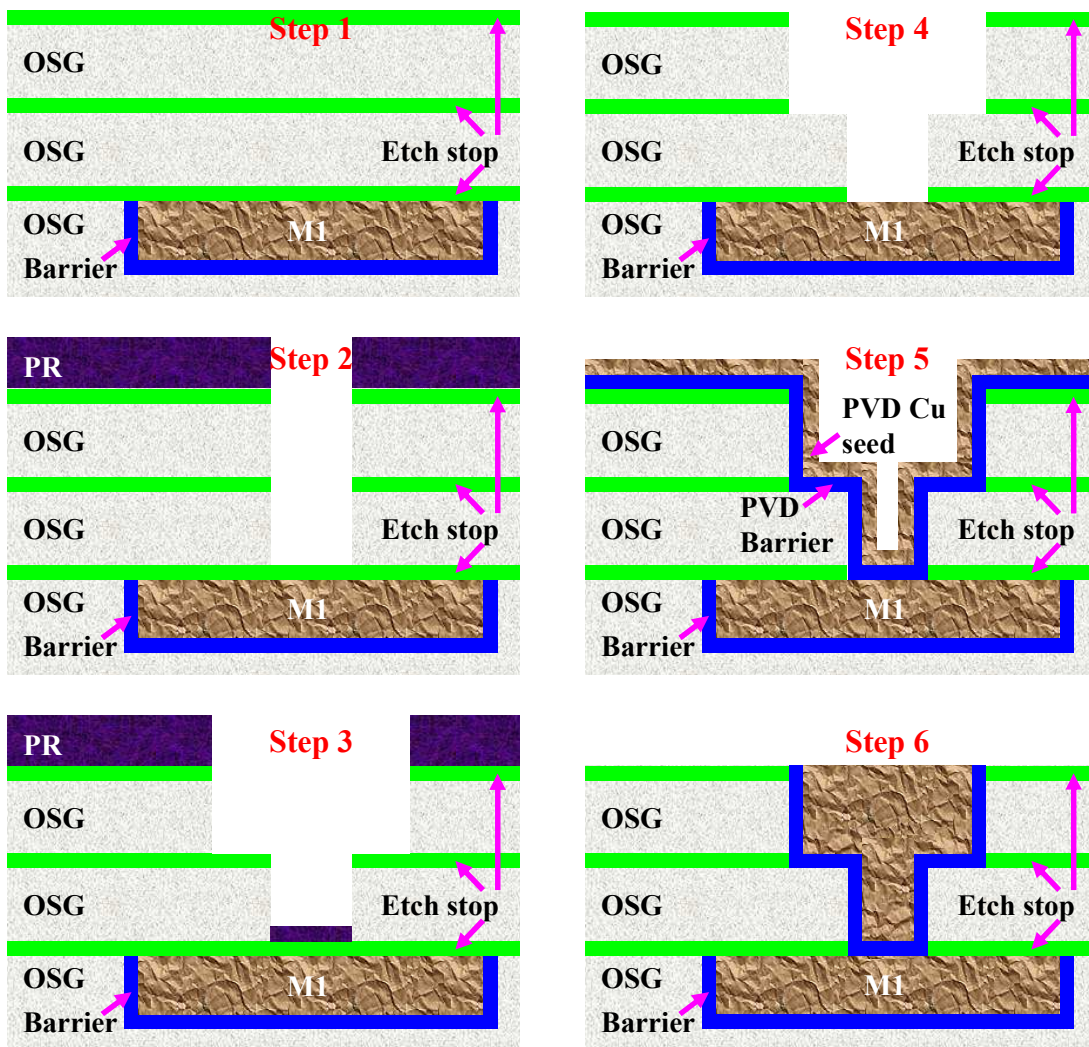


Figure 1-7: Schematic drawing of via-first dual damascene process (illustrated by Hualiang Shi).

The plasma stripping or ashing process is the most detrimental process. This is simply because the same plasma chemistry that removes the organic photoresist also removes the organic methyl bonds in the SiCOH material. As indicated in the schematic graph in Figure 1-8, the oxidative plasma removes the low-polar methyl bonds and replaces them with high-polar silanol and Si-CH=O bonds. Further reactions completely remove the carbon groups and create a carbon depleted region. More importantly,

compared to the hydrophobic methyl bonds, the silanol bonds are hydrophilic and can easily absorb the moisture in the ambient. The physisorbed water is highly polarized ( $k \sim 80$ ), which greatly increases the effective dielectric constant of the low-k material. In addition, the removal of the carbon group can induce pore collapse, resulting in a higher density. This, together with densification caused by the ions, can also increase the dielectric constant.

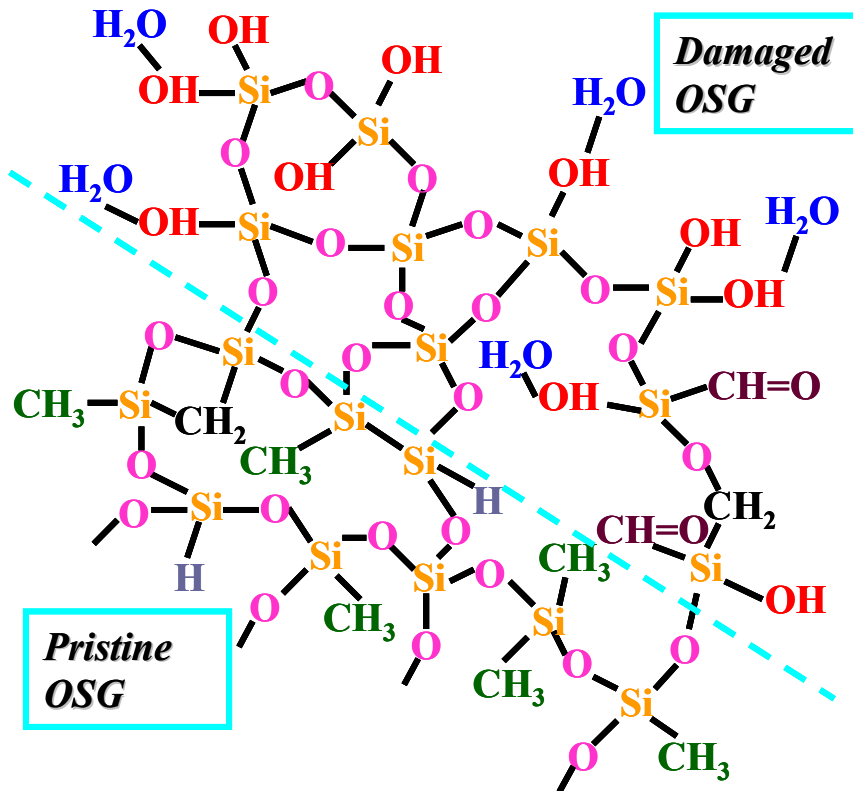


Figure 1-8: Schematic drawing of  $O_2$  plasma ashing induced bonding configuration changes to porous SiCOH low-k dielectric (illustrated by Hualiang Shi).

The high-polar components introduced by the plasma damage also lead to an increase of the leakage current (Figure 1-9) and a lowered breakdown voltage, creating serious concerns for the reliability of these advanced structures.

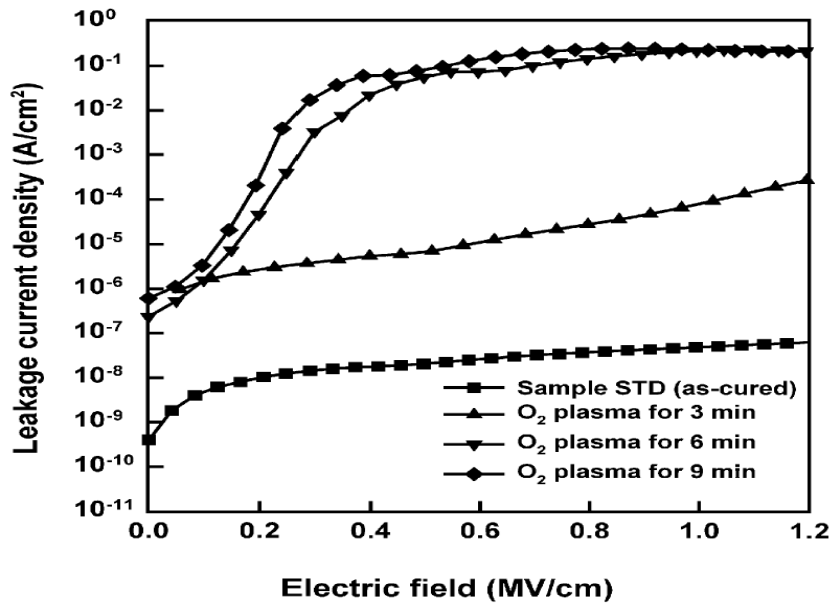


Figure 1-9: Leakage current increase induced by O<sub>2</sub> plasma treatment[10].

In the plasma etching process, the fluorocarbon based plasma chemistry is commonly used. Fluorine in the plasma removes the Si atoms in the low-k material by forming volatile SiF<sub>x</sub>. It also reacts with carbon by forming COF<sub>2</sub>, resulting in carbon depletion. The damage can be increased by gas additions such as oxygen. The effect of carbon depletion is similar to what is described in the plasma stripping damage. Compared to plasma stripping damage, the etching damage is relatively small. This is because the fluorocarbon polymer formed on the surface of the low-k material can block the diffusion of the detrimental plasma species. However, certain level of surface polymerization can significantly roughen the low-k surface, causing issues in barrier deposition and other areas. The details of the etching damage and the study carried out in this thesis are discussed in Chapter 3.

CMP process can damage the low-k material by contamination and to induce moisture uptake[11]. Although the low-k damage by CMP process is not the focus of this

work, the damage caused by CMP can be recovered by same methods that recover the plasma induced low-k damage, such as silylation and UV treatment[12].

#### **1.4. DESCRIPTIONS OF DISSERTATION RESEARCH**

The purpose of this dissertation is to understand the low-k plasma interaction and damage mechanism in an effort to minimize the plasma induced damage as well as to find a solution to remedy the low-k degradation.

Chapter 2 discusses the experimental techniques that are extensively used throughout this dissertation. The plasma systems used to process low-k sample are reviewed. These systems include capacitively coupled plasma (CCP), inductively coupled plasma (ICP) and downstream plasma (DSP). Then, the low-k characterization techniques, such as Fourier transform infrared spectroscopy (FTIR), X-ray photoelectron spectroscopy (XPS), will be discussed.

As the first plasma damaging step in the damascene process sequences, the low-k damage generated from the etching process is discussed in Chapter 3. The etching mechanism is reviewed in the beginning of this chapter. Then, the experimental study of etching damage and surface roughening are presented. The experiments were carried out with CHF<sub>3</sub>/Ar based plasma. The etching rate and the surface roughness were measured and correlated with surface polymerization. The etching damage and the surface roughening damage mechanism were measured and the results are characterized in terms of surface polymerization, surface densification, radical diffusion and ion transportation.

Chapter 4 is dedicated to understand the plasma stripping and ashing process. It is organized as two parts. The first part of this chapter presents the experiment that separated the plasma constituents with a “gap” structure set up on the wafer surface. This gap structure enabled us to separate the plasma constituents including ions, radicals and

photons and to study their respective roles in the formation of the plasma damage on the low k surface.. The second part focuses on one of the plasma constituents, the oxygen radicals. The radical diffusion process is described by an analytical model based on radical diffusion, reaction and recombination. The damage process was then simulated using the Monte Carlo method. This led to the formulation of a kinetic model of radical diffusion which provides guidelines for damage minimization. This kinetic model is also applied to the radial transportation in the trench microstructures, which is investigated by experimental studies with gap structures.

Chapter 5 investigates the dielectric recovery method including silylation and UV thermal treatment applied separately and in combination. The silylation processes recover the surface carbon and hydrophobicity but the recovery is limited to the surface. The UV thermal treatment reduces the effective k value by removing the bulk water and silanols. The results obtained in our study showed that a combined silylation and UV treatment provide a more effective method for dielectric recovery of plasma damage.

## Chapter 2: Experimental techniques

To study the plasma damage to low-k material, the low-k film needs to undergo plasma processing and then characterized. This chapter describes the general plasma processing tools and the characterization techniques used in this study. Special designed instruments, such as on-wafer filter structure and UV curing system will be discussed in the subsequent chapters.

### 2.1. PLASMA PROCESSING SYSTEMS

Plasma is a collection of free atoms or molecules in which a certain portion of the particles are ionized. Low temperature plasmas are used extensively in the fabrication process of microelectronic devices. Highly reactive radicals contained in the plasma allow chemical reactions to occur that are not possible under ordinary conditions. Ions can be extracted from the plasma surface at high energies to impinge onto the surface to be studied in a normal direction, thereby enabling the anisotropic etching of the surface.

According to the type of external energy input, plasma sources used in the IC fabrication can be classified into capacitively coupled, inductively coupled and wave sources[13]. The capacitively coupled plasma (CCP) and the inductively coupled plasma (ICP) are the most commonly used types.

#### *Capacitively coupled plasma*

Reactive ion etch (RIE), which uses a CCP source, has been the most widely used plasma source for thin film processing. Figure 2-1(a) shows the typical configuration of the RIE system. It is composed of two parallel plate electrodes, with the bottom connected to a radio frequency (RF) power and the top electrode grounded. The RF energy is coupled to the electron and ions by the electric field between the two electrodes. As electrons are much lighter than the ions, they exit the plasma faster and build up a

negative bias at the bottom electrode. This self-bias accelerates ions toward the surface in an angle normal to the surface, thus making anisotropic etching possible. Therefore, RIE is very suitable for the dielectric etching process.

The etching study in Chapter 3 used the Plasmatherm 790 RIE system, which has an 8 inch chuck and is powered with 13.56 MHz RF power. In Chapter 5, the plasma damaged samples for dielectric repair studies were processed using an Oxford Instruments Plasmalab 80 RIE system and a TRION Oracle RIE system with similar configurations.

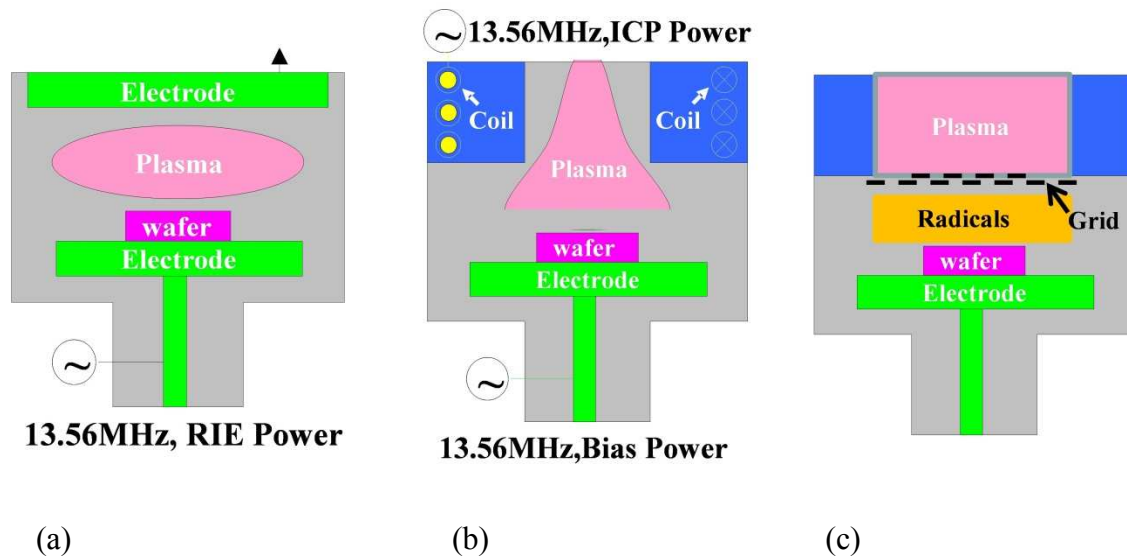


Figure 2-1: Schematic representation of plasma chambers in damascene processing. (a) RIE, (b) Oxford ICP etcher, (c) Remote plasma with a neutralize grid.

RIE systems work well for many applications but have several drawbacks. In particular, RIE cannot sustain a high plasma density as the efficiency of plasma generation reduces dramatically as the RF power increases. On the other hand, the self-bias increases as more power is added, which increases the ion energy. As a result,

plasma density and ion energy in the RIE system are coupled and cannot be changed separately.

### ***Inductively coupled plasma***

ICP sources can sustain a higher plasma density ( $10^{11}$ - $10^{12}$  electrons/cm<sup>3</sup>, sometimes they are referred to as high-density plasma HDP reactors) than the CCP source ( $10^9$ - $10^{10}$  electrons/cm<sup>3</sup>). In ICP reactors, plasma density and ion energy are controlled separately. The energy is transferred to electrons through inductive coupling by a coil isolated from the plasma using a dielectric layer. The oscillating magnetic field induces an oscillating current in the plasma and, contrary to the CCP case, penetrates the bulk plasma directly with little power coupling through the sheaths. This allows a very efficient energy transfer and creates highly dissociated and dense plasmas. This also results in a low self-bias (between 10-15 and few tens of eV) which does not depend on plasma source power. As a result, plasma density can be easily increased without increasing ion energy.

Figure 2-1(b) shows the schematic of ICP-RIE dual system (Oxford Instruments Plasmalab 80 Plus ICP-RIE ) used in the oxidative plasma study in Chapter 4. The ICP source on the top is connected to a 13.56 MHz RF power. In order to control ion energy, a second generator (13.56 MHz RF) is capacitively coupled to the substrate. In this way, plasma density and ion energy can be optimized separately.

### ***Downstream plasma***

Another way to classify plasma sources is by the proximity of the plasma to the substrate. In Figure 2-1 (a) and (b), the plasma are close to the substrate to be processed. In downstream plasma (DSP) reactors, the substrate is placed well away from the power absorption region or even completely removed from the plasma. As a result, the plasma

density is low and short-lived radicals could not reach the substrate. Downstream plasma is also referred to as remote plasma.

As shown in Figure 2-1 (c), in order to minimize the plasma induced damage by ions and VUV photons, special grids can be used to remove charged species and block photon radiations. As a result, only neutral radicals could reach the surface of a wafer in a remote plasma system and the damage from high-energetic species can be minimized or avoided. In particular, a neutral beam plasma can be generated and used to reduce the plasma damage to the low-k materials [14][15].

## **2.2. CHARACTERIZATION TECHNIQUES**

Many analytical techniques have been used in this study to characterize the plasma damage of low-k films. Table 2-1 lists the commonly used low-k material characterization techniques that have been found in the literature. Due to availability and efficacy of the tools, not all of the tools or techniques are used in this dissertation. Fourier transform infrared spectroscopy (FTIR) and X-ray photoelectron spectroscopy (XPS) are most important characterization tools used in this study. The principles of the FTIR and XPS techniques and data analysis are described in Section 2.2.1 and Section 2.2.2.

Most of the characterization techniques can be used to characterize blanket films. The characterization techniques for patterned structures, particularly the side wall damage, are limited to only a few options such as scanning electron microscopy (SEM) and energy-filtered transmission electron microscopy (EFTEM)[16]. However, SEM cannot quantify the chemical concentration and the use of EFTEM cannot monitor the bonding change. In Chapter 4, a gap structure was used to simulate the plasma damage to sidewall on blanket film.

<b>Technique</b>	<b>Acronym</b>	<b>Applications</b>
<b>Fourier transmission infra-red spectroscopy</b>	FTIR	Bonding configuration
<b>X-ray photoelectron spectroscopy</b>	XPS	chemical composition, bonding configuration
<b>Spectroscopic ellipsometer</b>	SE	Thickness, index of refraction
<b>HF decoration</b>		Carbon depletion
<b>Atomic force microscopy</b>	AFM	Surface roughness, Morphology
<b>Metal-insulator-semiconductor</b>	MIS	Sample prepare for electronic measurement
<b>X-ray reflectivity</b>	XRR	Thickness, density
<b>scanning electron microscopy</b>	SEM	Morphological characteristics
<b>Transmission electron microscopy</b>	TEM	Morphological characteristics
<b>Scatterometry</b>		Morphology
<b>Ellipsometric porosimetry</b>	EP	Porosity, pore size distribution
<b>(Tim of fly) secondary ion mass-spectrometry</b>	(TOF)-SIMS	the depth profile of the elements
<b>Thermal desorption spectroscopy</b>	TDS	Water evaporation[17]
<b>Energy-filtered transmission electron microscopy</b>	EFTEM	Precise location element analysis
<b>Electron spin resonance</b>	ESR	UV induced defects[18]
<b>Nuclear magnetic resonance</b>	NMR	UV induced defects[19]

Table 2-1: Characterization techniques for low-k materials

### **2.2.1. FTIR**

Fourier transform infrared spectroscopy (FTIR) is a powerful tool for characterization of the bonding configuration or molecular structure of dielectric materials. In the infrared (IR) range, atoms in solid materials have various types of vibration modes, including asymmetrical stretching, symmetrical stretching, in-plane bending (scissoring or rocking) and out-of-plane bending (wagging or twisting). Once the IR photon energy matches the characteristic energy difference between two energy levels of specific vibration modes, IR absorption occurs, creating an absorption spectrum. This spectrum, therefore, can be used to map the chemical bonding configurations and with proper intensity calibration, the measured spectral intensity can be used to determine the amount of the chemical bonds in the dielectric surface.

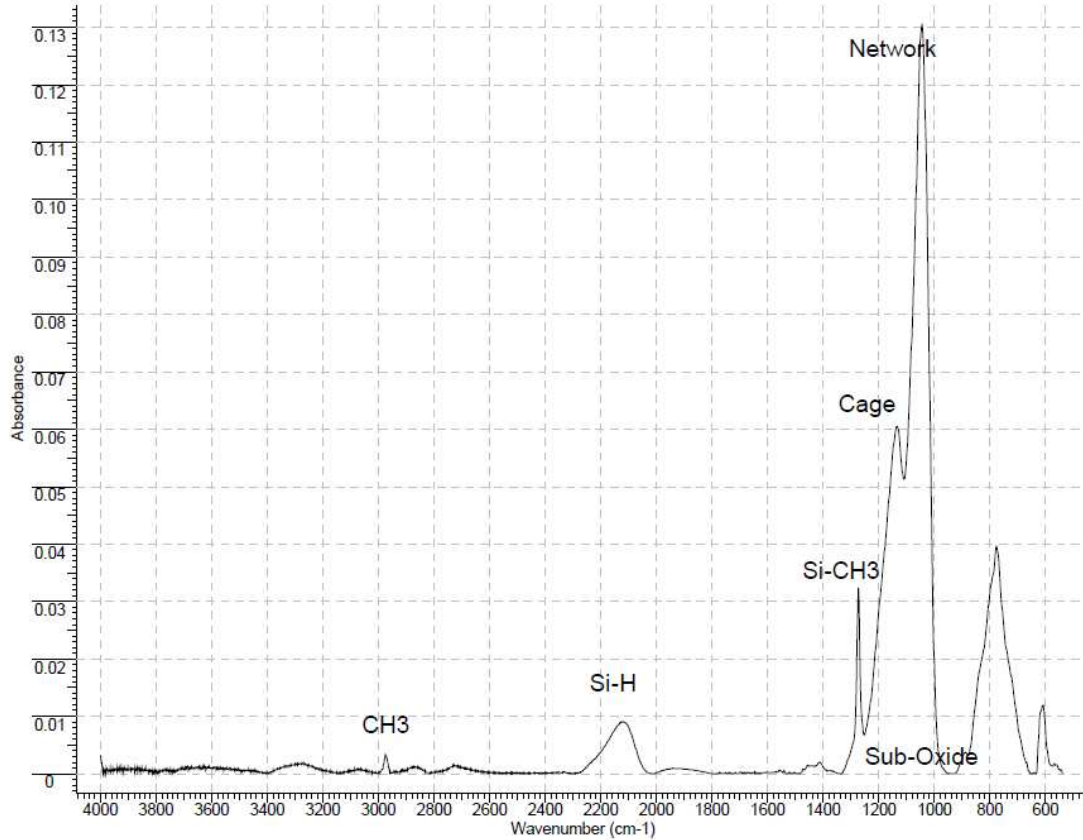


Figure 2-2: A typical FTIR spectrum of the SiCOH material

In this study, a Nicolet Magna 560 Spectrometer was applied in the transmission mode for FTIR measurement. The operating conditions of the instrument are: wavenumber resolution  $\sim 4 \text{ cm}^{-1}$ , the number of scan  $\sim 256$ , and the wavenumber range  $\sim 4000 \text{ cm}^{-1} - 520 \text{ cm}^{-1}$ .

Figure 2-2 shows a typical FTIR spectrum for SiCOH material. The spectral structure of low dielectric constant SiCOH film has been studied extensively by the FTIR technique[20][21]. One example is by Grill et al. [20] who summarized the FTIR peak assignments of SiCOH low-k dielectrics. The results are tabulated in Table 2-2, which were used as a reference for the peak identification in this dissertation.

By directly comparing of the measured and the reference FTIR spectra, the changes in bonding configurations can be monitored. When the change is small, the differential FTIR technique can be applied. The differential FTIR spectrum is created by subtracting two FTIR spectra after adjusting for the thickness difference. This way the detail of subtle bonding changes can be observed [22]. In a differential FTIR, the negative peak indicates a reduction of the concentration of a specific bond while a positive peak indicates the increase of bond concentration.

In the study of porous low k dielectrics, the interpretation of the bonding changes can be difficult due to the porogen releasing and the peak superposition. As a result, not all the peaks in Table 2-2 are used. The absorption bonding peaks frequently used in this dissertation are peaks associated with Si-CH<sub>3</sub> (1260-1290 cm<sup>-1</sup>), -OH and physisorbed water (3000-3600 cm<sup>-1</sup>) and Si-O-Si (1000-1200 cm<sup>-1</sup>). According to the connectivity of the molecular unit, the Si-CH<sub>3</sub> bond can be divided into three peaks[23]. Their peak assignments are summarized in Table 2-3. As discussed in Chapter 1, the Si-O-Si backbone structures can also be deconvoluted and categorized into the cage structure (~150°), the network structure (~144°) and the sub-oxide (<140°) structure depending on the Si-O-Si bonding angles. Their FTIR peak assignments are listed in Table 2-4.

TMCTS	$k=2.8$	$k=2.05$	Mode	Comment
2968	2969	2968	$\nu^s$ C-H <sub>3</sub>	$sp^3$ CH <sub>3</sub>
2906			$\nu^s$ C-H <sub>3</sub>	$sp^3$ CH <sub>3</sub>
	2916	2932	$\nu^s$ C-H <sub>2</sub>	$sp^3$ CH <sub>2</sub>
	2880	2875	$\nu^s$ C-H <sub>2</sub>	$sp^3$ CH <sub>2</sub>
	2232		$\nu^s$ Si-H	H-SiO <sub>3</sub>
	2178		$\nu^s$ Si-H	H-SiO <sub>2</sub> Si
2165			$\nu^s$ Si-H	H-SiOSi
		1740,	$\nu$ C=O	As deposited only
		1714		
		1461	$\delta$ C-H <sub>2</sub>	CH <sub>2</sub> isolated from Si
1405	1412	1412	$\delta^s$ C-H <sub>3</sub>	SiMe <sub>x</sub>
	1358	1379	$\delta$ C-H <sub>2</sub>	Si-CH <sub>2</sub> -Si
1259	1273	1274	$\delta^s$ C-H <sub>3</sub>	SiMe <sub>x</sub>
	1135	1140	$\nu^s$ Si-O-Si	Cage
				Si-O-Si angle $\sim 150^\circ$
			$\nu$ C-O	Si-O-C
1063	1063	1065	$\nu^s$ Si-O-Si	Network (network)
				Si-O-Si angle $\sim 144^\circ$
	1023	1035	$\nu^s$ Si-O-Si	Silicon suboxide,
				Si-O-Si angle $< 144^\circ$
				D <sub>3h</sub> ring structure
	890		$\delta$ H-Si-O	H-SiO <sub>3</sub>
			$\nu$ Si-C, $\rho^s$ CH <sub>3</sub>	SiMe <sub>2</sub>
865			$\delta$ H-Si-O	H-SiO <sub>2</sub> Si
	848	843	$\delta$ H-Si-O	Network smaller angle
			$\nu$ Si-C, $\rho^s$ CH <sub>3</sub>	SiMe <sub>3</sub>
	802	800	$\nu$ Si-C, $\rho^s$ CH <sub>3</sub>	SiMe <sub>2</sub>
754			$\nu$ Si-C, $\rho$ Si-CH <sub>3</sub>	SiMe <sub>1</sub>
	773	779	$\nu$ Si-C, $\rho$ CH <sub>3</sub>	SiMe <sub>1</sub>
			$\nu$ Si-C, $\rho^s$ CH <sub>3</sub>	SiMe <sub>3</sub>
710	730	720	$\nu^s$ Si-O-Si	
	440	440	$\delta$ of O-Si-O	Network and ring opening vibrations

Table 2-2: FTIR peak assignments of SiCOH low-k dielectrics[20].

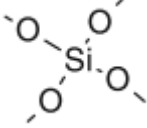
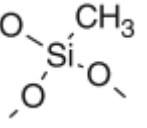
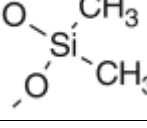
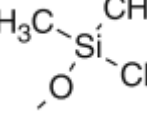
Structure		Connectivity	Wavenumber(cm <sup>-1</sup> )
	Si-O <sub>4</sub>	Q	1060
	O-Si-CH <sub>3</sub>	T	1270
	O <sub>2</sub> -Si(CH <sub>3</sub> ) <sub>2</sub>	D	1260
	O <sub>3</sub> -Si(CH <sub>3</sub> ) <sub>3</sub>	M	1250

Table 2-3: Molecular structure, connectivity and FTIR peak[23][24].

Structure	Peak Position(cm <sup>-1</sup> )	Bond Angle (degree)
Cage	1135	~150
Network	1060	~144
Sub-Oxide	1028	<140

Table 2-4: Molecular structure unit of Si-O-Si and their FTIR peaks and bond angles.

The integrated peak area of the FIR spectrum is proportional to the film thickness as well as the concentration and molar absorptivity of bond. For a stable bond, the total Si-O-Si peak areas can be normalized and the total peak area is proportional to the low-k film thickness. In this way, the ratios of the Si-O-Si spectral peaks can be used to measure the bonding concentration. In this study, the FTIR peak area ratios such as Si-

CH<sub>3</sub>/Si-O and -OH/Si-O were applied to study the methyl depletion and moisture uptake, respectively. For ashing or curing process, the change of the total Si-O-Si peak area is negligible. In this case, the Si-OH<sub>3</sub> or -OH peaks can be compared directly.

## 2.2.2. X-ray photoelectron spectroscopy (XPS)

### 2.2.2.1. Overview

Due to the penetration of the IR source, the intensity of the FTIR detects the bulk change of the bonding characteristics in low-k films. Thus surface bonding changes in less than 30nm are difficult to differentiate by FTIR due since it is not a particularly surface sensitive technique. X-ray photoelectron spectroscopy (XPS), on the other hand, are sensitive to the surface chemical composition and bonding configuration.

The schematic setup for XPS measured is shown in Figure 2-3. On the surface, the electrons of the material absorb the X-ray photon energy and escape from the atom to vacuum and detected by a spectrometer. The kinetic energy of this photoelectron is measured by an electron energy analyzer. Because the energy of the X-ray is known, the binding energy of each emitted electron can be determined by the following equation:

$$E_B = h\nu - E_K - e\phi \quad (2.1)$$

where  $E_B$  is the binding energy of core level electron,  $h\nu$  is the characteristic energy of X-ray photon,  $E_K$  is the kinetic energy of ejected photoelectrons and  $e\phi$  is the work function of the detector[25]. Since the electrons are easy to be block by the material, the detection depth is generally limited to less than 10nm depending on the escaping path.

The binding energy, which is the energy required to release an electron from its atomic or molecular orbital, is a characteristic value of atoms or molecules. Therefore, it can be used to identify elements inside a material. Typical binding energy values used in

this dissertation include C1s (-285 eV), Si2p (-103 eV), O1s (-532 eV) and F1s (-686 eV). The C 1s peak measured from a pristine SiCOH film is shown in Figure 2-4(a).

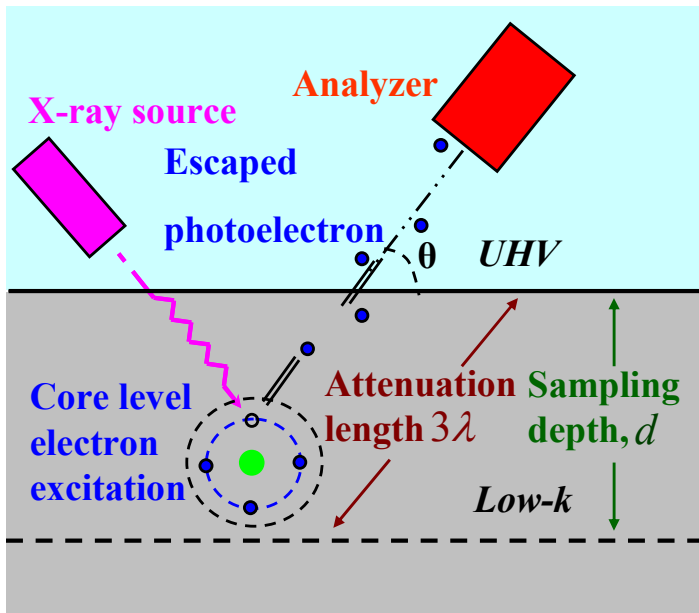


Figure 2-3: Schematic illustration of X-ray photoelectron spectroscopy.

XPS results in this study were obtained by an Axis Ultra DLD XPS spectrometer from Kratos Analytical Company. The X-ray source was a monochromatic 1486.7eV  $K\alpha$  Al source with 0.16eV energy width. Due to the pass-energy setting of electron energy analyzer and the peak-width of X-ray source, the ultimate energy resolution of the spectrum is usually 0.4-0.6 eV.

#### 2.2.2.2. XPS peak deconvolution

Based on the charge potential model[26], the core level chemical shift can be interpreted as:

$$E_i = E_i^0 + kq_i + \sum_{i \neq j} \frac{q_i}{r_{ij}} \quad (2.1)$$

Where  $E_i$  is the binding energy of core level electron in the  $i^{\text{th}}$  atom,  $E_i^0$  is the energy reference,  $q_i$  is the charge on the  $i^{\text{th}}$  atom, and  $\sum_{i \neq j} \frac{q_i}{r_{ij}}$  is the potential on the  $i^{\text{th}}$  atom due to the surrounding atoms.

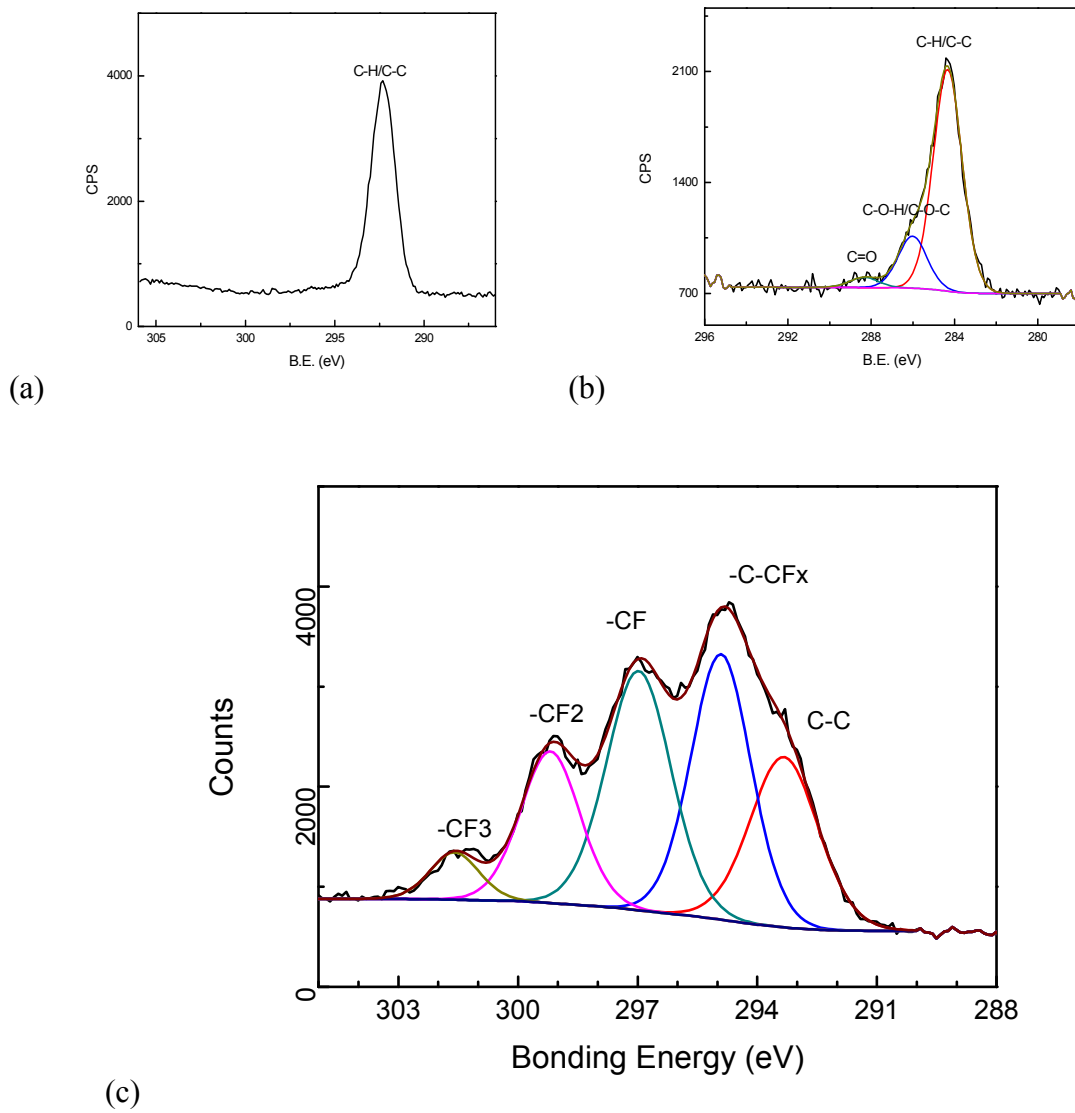


Figure 2-4: XPS Carbon peak deconvolution (a) pristine SiCOH film, (b) Ar plasma damaged low-k film, (c) fluorocarbon polymerization (80% CHF<sub>3</sub>, 20% Ar)

As indicated by Eq. (2.1), the binding energy shifting of one element peak due to the presence of a specific chemical bond can be identified. For example, the C peak of a SiCOH film after Ar plasma damage can be decomposed into C-H/C-C peak, C-O peak and C=O peak as shown in Figure 2-4(b). In Figure 2-4(c), the fluorocarbon surface polymerization was further analyzed by deconvoluting the XPS surface carbon peak into -C-C, -C-CFx, -CF, -CF<sub>2</sub> and -CF<sub>3</sub> groups[27].

#### **2.2.2.3. XPS depth profiling**

The depth profiles of element concentration and bonding configuration can be obtained by XPS scan with the help of ion sputtering. In XPS depth profiling, the film is thinning down to the desired depth by 2 keV Ar ion sputtering at an incident angle of 45° and then followed by a XPS scan. The XPS depth profile is believed to be more accurate than the secondary ion mass spectrometry (SIMS). However, the main concern of both techniques is that the material re-deposition of the ion sputtering can affect the film properties and alter the real surface concentration, especially for the porous low-k materials. For material with a gradual change surface concentration gradient, such as a damaged low-k film, the accuracy of the depth profile can also be affected by the density dependency of the sputtering rate.

#### **2.2.2.4. Angle resolved XPS**

Angle resolved XPS (ARXPS) can detect the depth dependence of the element concentration within 10 nm of the film. As indicated in Figure 2-4, the electron take-off angle  $\theta$  is defined as the angle between the detection direction and the film surface. As discussed in Section 2.2.2.1., the XPS detection depth is limited by the electron escaping distance. When the take-off angle changed from normal to  $\theta$ , the electron escaping distance from the same depth increase by a factor of  $1/\sin\theta$ . Hence, compared with XPS

scan at a take-off-angle  $90^\circ$ , the one at  $30^\circ$  provides information for the near-surface bonding characteristics.

#### 2.2.2.5. XPS measurement of patterned structure

ARXPS can be potentially used to analysis the plasma damage on patterned structures. As indicated in Figure 2-5, at normal detection angle, the electron emission on the sidewall is blocked by the TiN hardmask and the carbon concentration of the trench bottom is detected. At a tilted angle, the electron emission of the trench bottom is shaded by the trench wall, resulting in pure signals from the sidewall. In this way, the plasma damage to the sidewall and trench bottom can be differentiated.

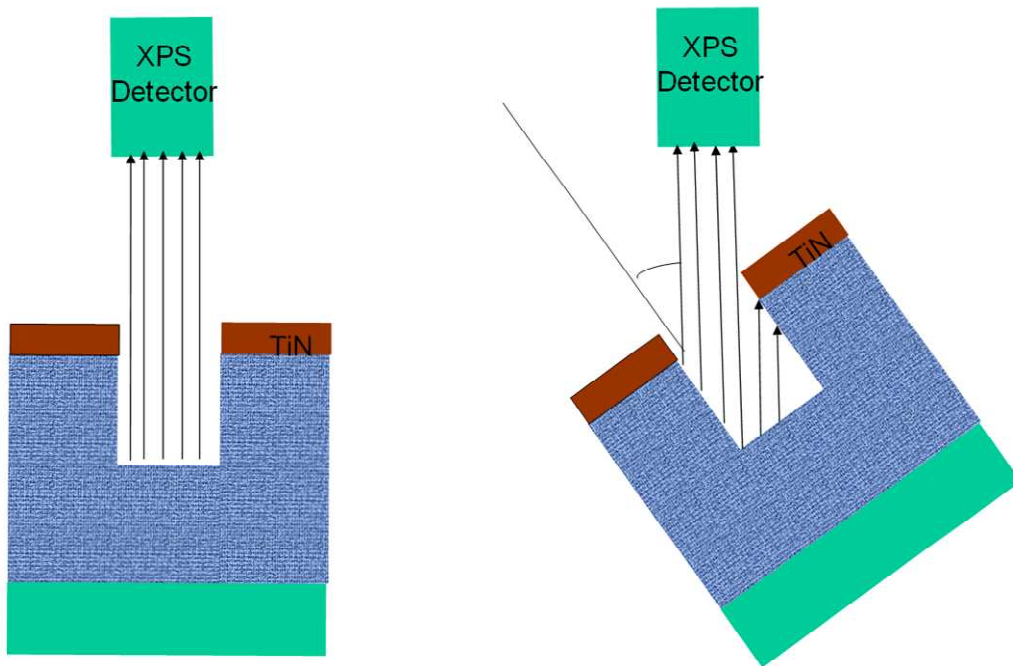


Figure 2-5: XPS detections on patterned structure: (a) trench bottom detections, (b) sidewall detection.

Worsley et al. used this technique to investigate the plasma damage in patterned ULK structures [28]. However, this technique requires very specific pattern design. The

top surface should not contain Si or carbon and the area of the grid has to be sufficiently large to allow XPS detection and target locating. The aspect ratio of the trench is also critical for the signal detection.

### **2.2.3. Other experimental techniques**

The film surface roughness was measured by Digital Instruments atomic force microscopy (AFM) 3000 under the tapping mode. The scanning area was  $1\ \mu\text{m} * 1\ \mu\text{m}$ . The surface roughness was expressed as the root mean square (RMS) of the surface morphology.

The water contact angle provides a measure of the surface energy and the surface hydrophobicity. In this dissertation, water contact angle of low-k dielectrics was measured by a CA100 Ramé-Hart Goniometer.

A J. A. Woollam M-2000 Spectrometer was used to measure low-k film thickness based on a Cauchy mode fitting procedure. Spectroscopic ellipsometer (SE) also measure the index of refraction of the low-k material. However, the index of refraction of the SiCOH material under study is not connected to the dielectric constant.

A metal-insulator-semiconductor (MIS) structure was fabricated to measure the dielectric properties. An HP 4194A Impedance/Gain Phase Analyzer was applied to measure the changes in the dielectric constant, C-V hysteresis, and leakage current of low-k dielectrics after plasma processing.

## **Chapter 3: Etching induced roughening of Porous SiCOH**

### **3.1. INTRODUCTION AND OVERVIEW**

As discussed in Chapter one, in order to meet the demands of RC delay reduction, Cu/low-k interconnect was introduced to the integrated circuits, replacing Al/SiO<sub>2</sub>. Unlike aluminum, copper cannot form volatile compounds and therefore is very difficult to be etched with plasma and to form patterns with vertical sidewalls. As a result, the trenches and vias have to be patterned on low-k material with anisotropic plasma etching. However, the plasma etching process could also damage the low-k material. The chemical composition of low-k dielectrics is tailored to reduce the dielectric constant, for example, the adding of methyl bonds. These modifications also make it prone to plasma damage. When porosity is introduced to further reduce the k value, the material is even weaker.

The detrimental effects of plasma etching process on low-k dielectric are exhibited in two aspects: the low-k degradation and the surface roughness formation. The low-k degradation in the etching process is similar to that in many other plasma processes (e. g. stripping and ashing), which is normally caused by carbon depletion and is shown as an increase in the effective dielectric constant. In particular, not only oxygen atoms remove carbon, but fluorine in the etching process also removes it by forming volatile fluorocarbons like COF<sub>2</sub>. Compared to low-k degradation in plasma stripping, the damage in etching is less of a problem. With a proper choice of etching chemistry, either the damage layer can be etched away (in the bottom case) or the low-k material can be protected by a carbon-fluorine polymer layer (normally on the side wall). On the other hand, the problem of surface roughness is unique to etching of porous low-k materials and can cause severe impact on at least three aspects of the back end of line integration. First, the roughness on the sidewall or bottom can significantly degrade the continuity of

the diffusion barrier, which leads to copper diffusion. A thicker barrier layer may solve the continuity issue but it increases the copper resistivity.[29] Second, the roughness on the low-k surface can pass down to the barrier and copper interface which can change the copper microstructure and increase copper resistivity and electromigration concerns [30][31][32]. Last but not the least, the roughness on the sidewall can affect the critical dimension along the line which can induce a change in interline capacity[33][34].

In this Chapter, the surface roughening of porous SiCOH low-k under  $\text{CHF}_3/\text{Ar}$  plasma reactive etching (RIE) is investigated focusing on the roughening mechanism on blanket wafers which is similar to the roughness at the bottom of the trenches. First, the mechanism of low-k plasma etching is reviewed in Section 3.2. Experimental methods are explained in Section 3.3 and experimental results are displayed in Section 3.4. The mechanism of etch front roughness is then discussed in Section 3.5.

### **3.2. MECHANISM OF FLUOROCARBON PLASMA ETCHING**

In order to study the etch damage and roughness formation, it is necessary to first understand the etch mechanisms.

Si-based low-k materials (SiCOH) are etched by fluoro(hydro)carbons  $\text{C}_x\text{H}_y\text{F}_z$ , where hydrogen is not required. Fluorine must be included in the plasma etching chemistry because Si can only be removed by forming volatile  $\text{SiF}_x$  compounds. Other halides are not used due to their low etch rates and contaminations to the etch equipment. Fluorine is also able to remove carbon by forming volatile fluorocarbons like  $\text{COF}_2$ , which could degrade the dielectric property due to possible carbon depletion when diffused into the bulk low-k.

The etch of  $\text{SiO}_2$  uses the same plasma chemistry and was well documented in the literature[35][36][37][38][39]. It is known that the etch of  $\text{SiO}_2$  in fluorocarbon plasma is

governed by a thin fluorocarbon layer that grows on the surface[40][41]. As shown in Figure 3-1, the polymer layer is formed by deposition of  $C_xF_y$  radicals in the plasma. It is the main inhibitor for the transport of species and the delivery of activation energy to the  $SiO_2$ . At the polymer interface, the oxygen in  $SiO_2$  reacts with the fluorocarbon species in the polymer to release etching products like  $COF_x$ . Si in the  $SiO_2$  reacts with F in the polymer to produce  $SiF_x$  products. While at the plasma polymer interface, the polymer layer is consumed by energetic ion sputtering.

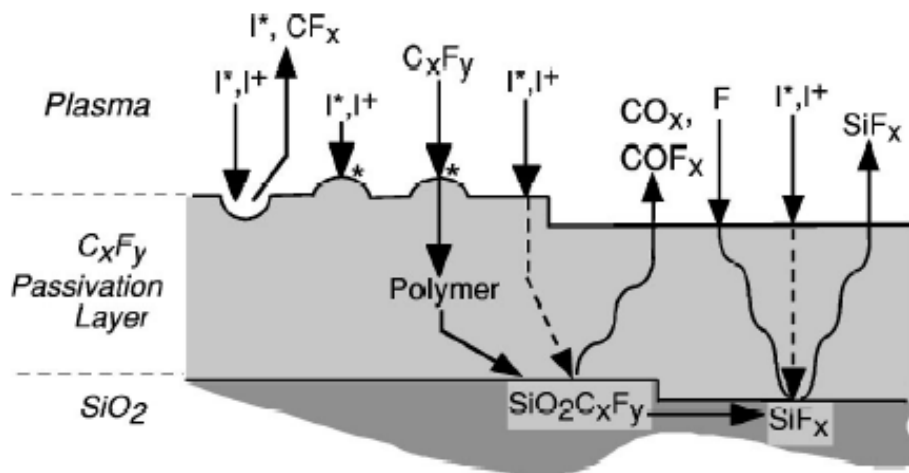


Figure 3-1: Schematic of surface reaction mechanism during fluorocarbon etching of  $SiO_2$ . [38]

The thickness and chemical composition of the polymer layer plays an important role in controlling the etching process. For example, a thick polymer layer limits the ion energy delivery and reactive species transportation, resulting in a low etching rate. An inverse relationship between the etch rate and the polymer thickness is observed[40]. A very thin polymer layer also produces low etch rate due to the lack of reactants.

The thickness and chemical composition of the polymer layer are governed by the plasma condition and by the composition of the material itself. Among the plasma

parameters, ion bombardment is critical to the efficiency of the etch process since it provides the necessary activation energy to break the strong Si-O bonds and controls the thickness of the polymer layer by sputtering. Without the presence of ion bombardment, the etching process could stop and become pure polymer deposition. Generally speaking, the higher ion energy leads to the thinner polymer layer. Another important parameter that affects the thickness of the polymer layer is the polymerization rate, which is commonly described by the C/F ratio. Plasma chemistry with higher C/F ratio is considered more polymerizing, therefore generating a thicker polymer layer, which was also confirmed in the etching study of SiCOH materials[42].

The important role of the surface polymerization also applies to SiCOH low-k materials. Besides the etching rate control and more importantly, the surface polymerization prevents the diffusion of F atoms and protects the sidewalls of the etch pattern. However, if too strong, the polymerization will slow down the etch rate or even stop etching and cause heavy residues and post-etch cleaning issues. When the polymerization and the etch rate are well balanced, the polymer film passivates the sidewalls without affecting the vertical etch rate, resulting in a vertical etch profile. It can also seal the porous surface and prevent the penetration of unwanted chemicals into the bulk of the porous low-k material.

The polymerization rate can be controlled in different ways. One approach is to tune the C/F rate by mixing low-polymerizing gases (e.g. CF<sub>4</sub>) with high-polymerizing gases (e.g. CHF<sub>3</sub> and CHF<sub>2</sub>). The advantage of this approach is that it simplifies the low-k plasma interaction by allowing only fluorocarbon species in the plasma chemistry. The other approach is to add non-fluorocarbon additives (e.g. Ar, O<sub>2</sub>, N<sub>2</sub>, H<sub>2</sub>), which gives more freedom in the process optimization. Argon gas can be added to the plasma to dilute the polymerizing process while supplying the ion sputtering process to reduce the

polymer layer thickness. Oxygen easily breaks polymers reaction with carbon and hydrogen. Even a small fraction of oxygen significantly reduces polymer deposition and increases the SiCOH etching rate [43]. However, oxygen addition also greatly damages SiCOH. Excessive O radicals react with the methyl bonds in the bulk low-k and cause its degradation. The reduction of the polymerization enhances the diffusion of detrimental species (i.e. O and F) into to the low-k sidewalls, resulting in bowed profile. Hydrogen reacts with F radicals to form HF, thereby increasing the C/F ratio and polymerization.

When SiO<sub>2</sub> is replaced by SiCOH, the formation of the polymer layer will be affected by the material composition. For example, the less oxygen present in a dielectric, the thicker the fluorocarbon film formed on the top of the dielectric[42].

The major cause of difference in dielectric etching between SiCOH and SiO<sub>2</sub> is the presence of porosity. The porosity of the low-k material greatly complicates the etching process by allowing diffusion of fluorine and other plasma species. Studies (Posseme et al. [44]) found that, because of the diffusion process, the reactive layer formed during a porous low-k etch is a mixed layer composed of C, Si, O and F atoms. In comparison, the fluorocarbon film is localized at the top surface for dense SiCOH material. Iba et al. [45] used a two layer model to describe the reactive surface region formed by the C<sub>4</sub>F<sub>6</sub>/O<sub>2</sub>/Ar plasma chemistry. In their model, a damaged layer is formed beneath the traditional fluorocarbon layer. At low polymerizing chemistry, both O radical and fluorine diffuse through the thin C<sub>x</sub>F<sub>y</sub> top layer resulting in a hydrophilic methyl-less damage layer. At high polymerizing chemistry, the thick C<sub>x</sub>F<sub>y</sub> layer blocks the oxygen diffusion. The damaged layer is formed mainly by fluorine diffusion and thus remains hydrophobic. At vertical etching direction, the damaged layer can be removed by the chemical sputtering effect. Therefore, low-k etching damage is the result of a competition between the etch rate and the diffusion rate of active species (O, F). A careful balance of

plasma conditions is required to minimize the damage, to form the desired profile and to maintain the etch rate.

The porosity of the low-k materials also causes severe roughness on the etch front, which is not observed in the dense low-k dielectrics[44][46]. The surface roughening of porous SiCOH material in fluorocarbon plasma chemistry is the focus of this chapter.

### **3.3. EXPERIMENTAL SETUP**

The experimental study of surface roughening process was conducted on porous SiCOH low-k film under  $\text{CHF}_3/\text{Ar}$  plasma reactive etching (RIE). The low-k film under study is Black Diamond (BD) III deposited on 300mm silicon wafer using PECVD method by Applied Materials. It is a 500nm thick porous SiCOH film with dielectric constant of 2.2 and a porosity around 32% [47].

The experimental procedures are schematically shown in Figure 3-2. The low-k wafer was cut into one inch square coupons and etched in 8" 790<sup>TM</sup> Plasma-Therm RIE etcher. The etcher generates capacitively coupled plasma between parallel-plate electrodes with the substrate electrode bias at 13.56MHz. The low-k coupons were treated in the RIE chamber as a function of  $\text{CHF}_3$  concentration, gas pressure, RF power and time. The surface roughness after etching and after 90s Diluted HF (DHF) dipping was measured by Veeco atomic force microscopy. It was then correlated with the thickness reduction by ellipsometry and with surface fluorocarbon concentration by X-ray Photoelectron Spectroscopy (XPS).

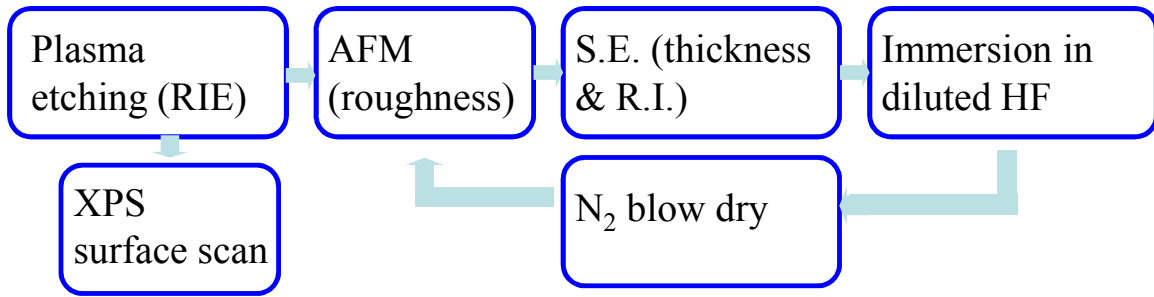


Figure 3-2: Experimental procedures of porous SiCOH material surface roughening study.

### 3.4. EXPERIMENTAL RESULTS

#### 3.4.1. CHF<sub>3</sub>/Ar Plasma chemistry

Figure 3-3 shows the surface roughness in root mean square (RMS) and thickness reduction as a function of CHF<sub>3</sub> concentration in a CHF<sub>3</sub> /Ar mixed gas feed. The thickness reduction after etching peaked at 10% CHF<sub>3</sub> and then decreased continuously with the increasing ratio of CHF<sub>3</sub>. At 100% CHF<sub>3</sub>, the thickness reduction was negative, indicating a pure polymer deposition instead of etching. Concurrently, the roughness after etching peaked at 2% CHF<sub>3</sub>, then decreased quickly and finally reached a constant level beyond 15% CHF<sub>3</sub>.

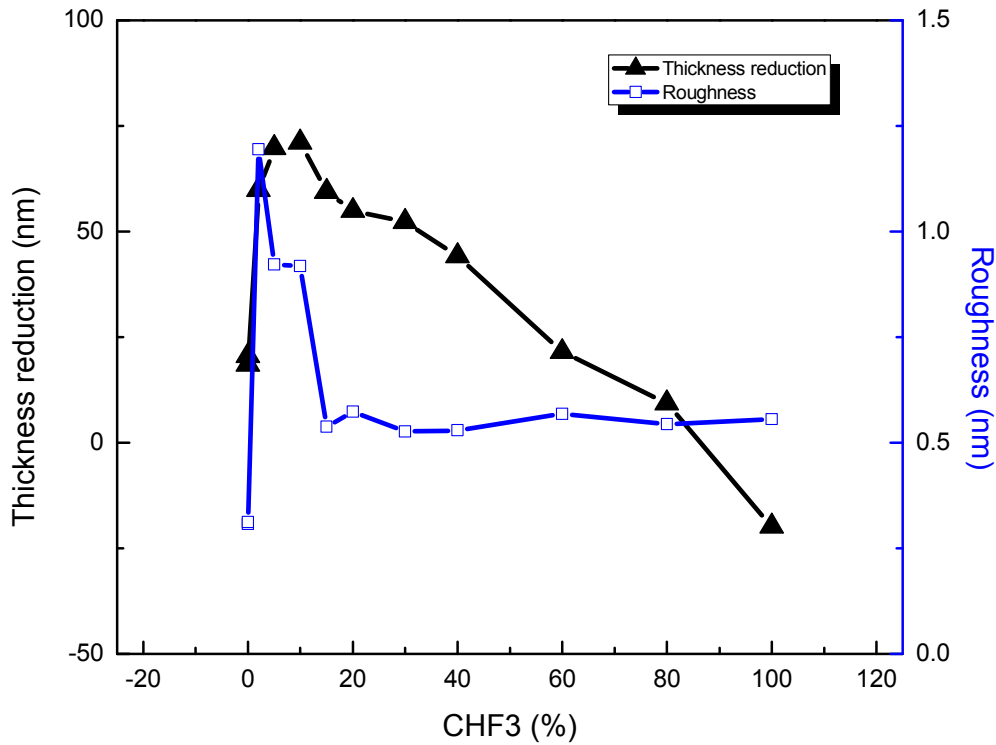
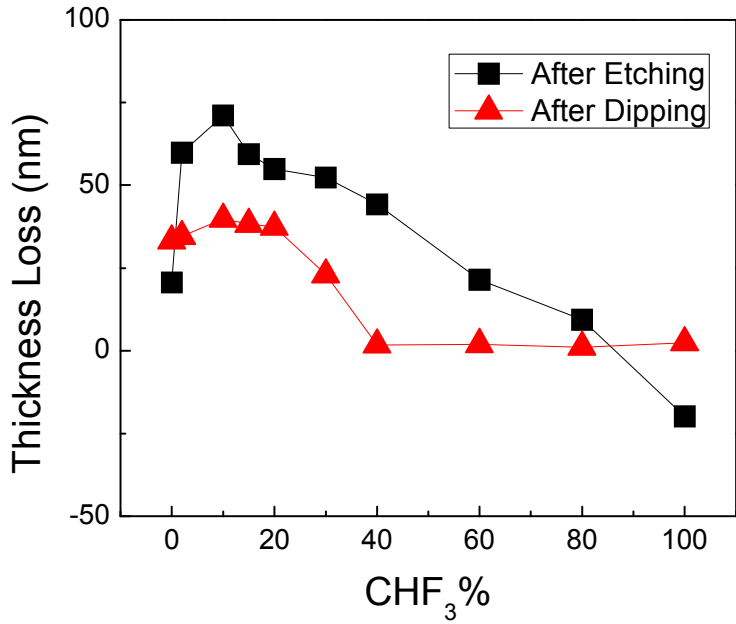
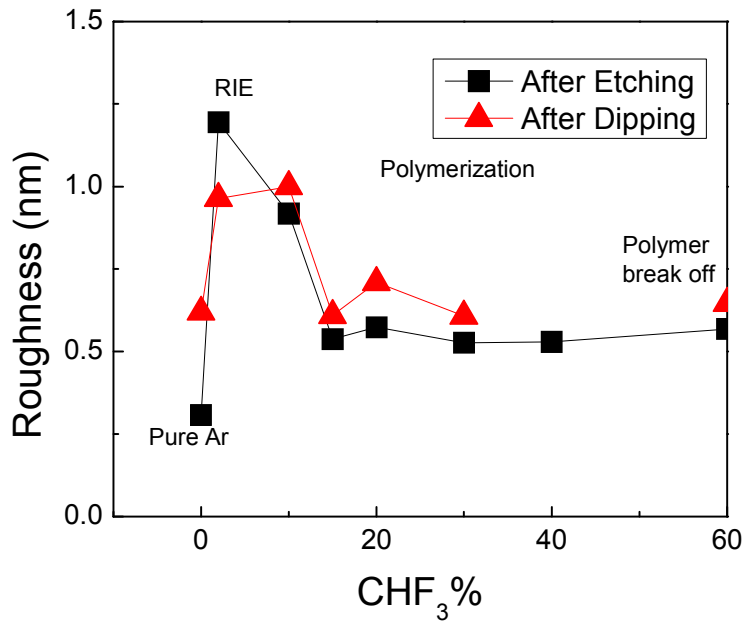


Figure 3-3: Thickness reduction and surface roughness after etching. (Total flow rate: 50sccm, Pressure: 40mtorr, Power: 300W, Time: 4min).

In wafer processing, diluted HF (DHF) dipping is usually used to remove the surface damaged layer of low-k material after the plasma process. This is because the carbon depleted damaged SiCOH becomes more SiO<sub>2</sub> like and therefore can be easily removed by DHF. As shown in Figure 3-4(a), after 90 seconds DHF dipping, the film thickness continued to shrink at low percentage of CHF<sub>3</sub>, indicating low-k damage. However, the thickness of the low-k film remained about the same at high percentage of CHF<sub>3</sub>, which was probably due to the high HF resistivity of thick fluorocarbon polymerization layer. On the other hand, DHF dipping only slightly changed the surface roughness (Figure 3-4(b)).



(a)



(b)

Figure 3-4: (a) Thickness reduction and (b) surface roughness after etching and after 90s DHF dipping. (Total flow rate: 50sccm, Pressure: 40mtorr, Power: 300W, Time: 4min).

Surface polymerization was analyzed using the XPS surface carbon peak. The XPS C1s spectra of low-k films at different etching chemistry are shown in Figure 3-5(a). The figure clearly shows the growth of multiple  $-CF_x$  as the  $CHF_3$ % increase in the total feeding gas flow rate. The XPS surface carbon peaks were then decomposed into  $-C-C$ ,  $-C-CF_x$ ,  $-CF$ ,  $-CF_2$  and  $-CF_3$  groups[27][48]. The decrease of  $-C-C$  ratio over the total C area and the increase of  $-CF$ ,  $-CF_2$ , and  $-CF_3$  in Figure 3-5(b) indicate a continuously growing surface fluorocarbon polymerization layer. As surface charging continues to occur due to the presence of the polymer layer induced during XPS measurement, the energy of the XPS peak can change. The increasing shift of the main peak position in Figure 3-5(a) also confirms the polymer layer thickening. Due to the diffusion of the  $C_xF_y$  into the porous structure of the ULK material, the surface polymer layer is rather a mix layer with no clear boundary depth. Therefore, the word “surface polymerization” is often used as it indicates both the fluorocarbon polymer concentration of the surface layer and the penetration depth of the fluorocarbon species.

The pressure effect was studied by measuring the thickness reduction and roughness at 40 and 80mTorr. However, no significant change in trend was observed (Figure 3-6). With longer etching time and higher plasma power, the thickness reduction increased while the surface roughness remained about the same as at 10%  $CHF_3$  (Figure 3-7).

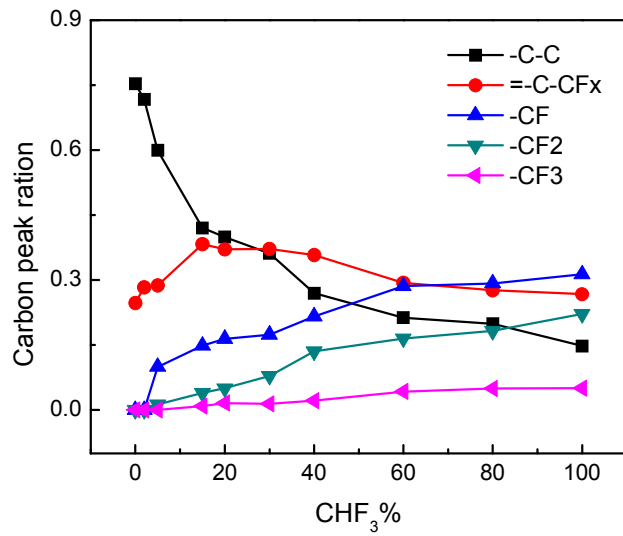
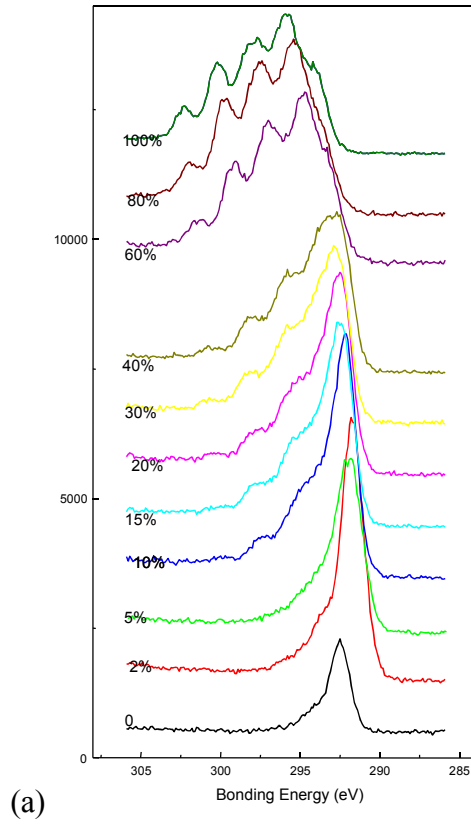
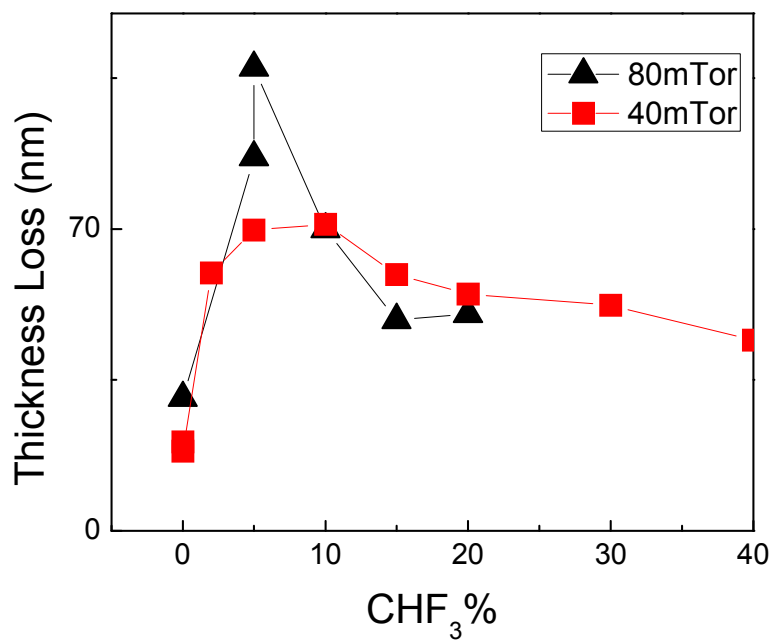
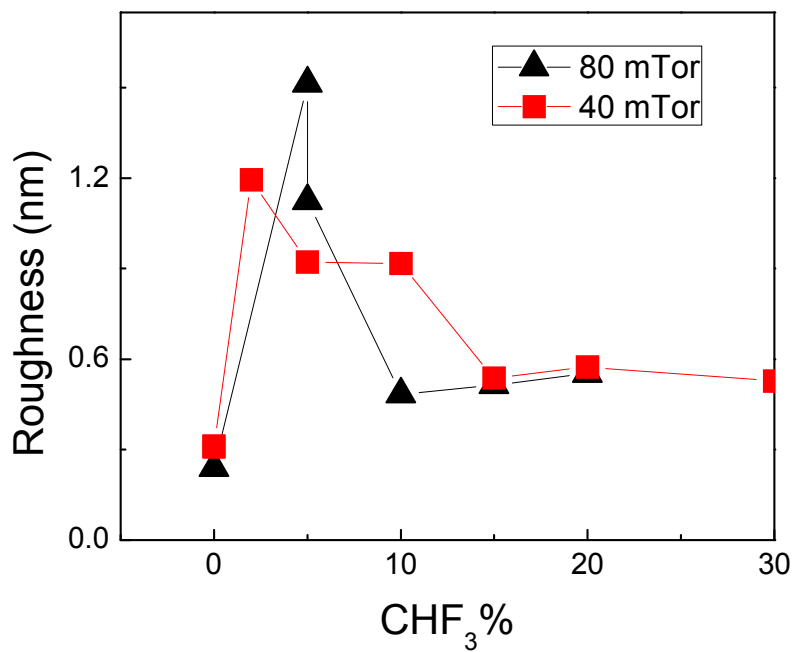


Figure 3-5: Fluorocarbon polymerization by XPS analysis: (a) Carbon peak evolution and (b) Individual peak area over whole carbon peak ratio.

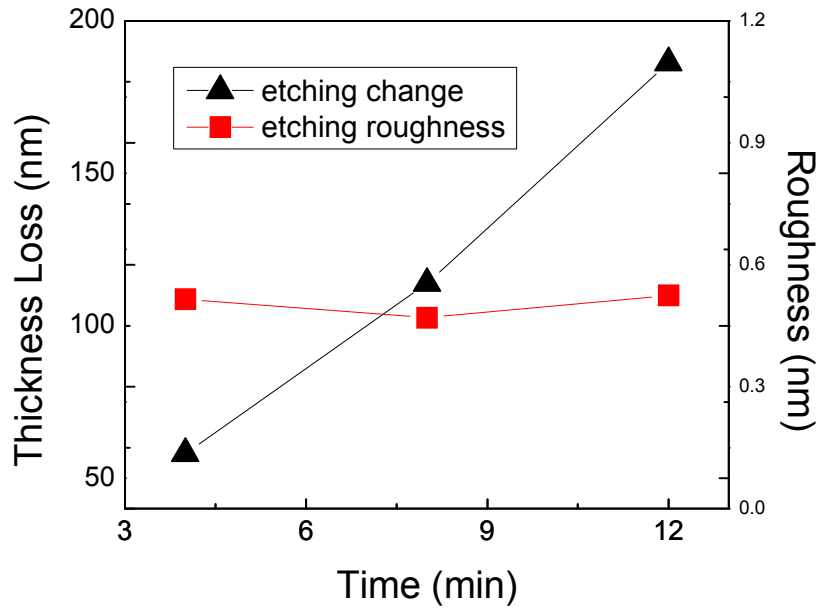


(a)

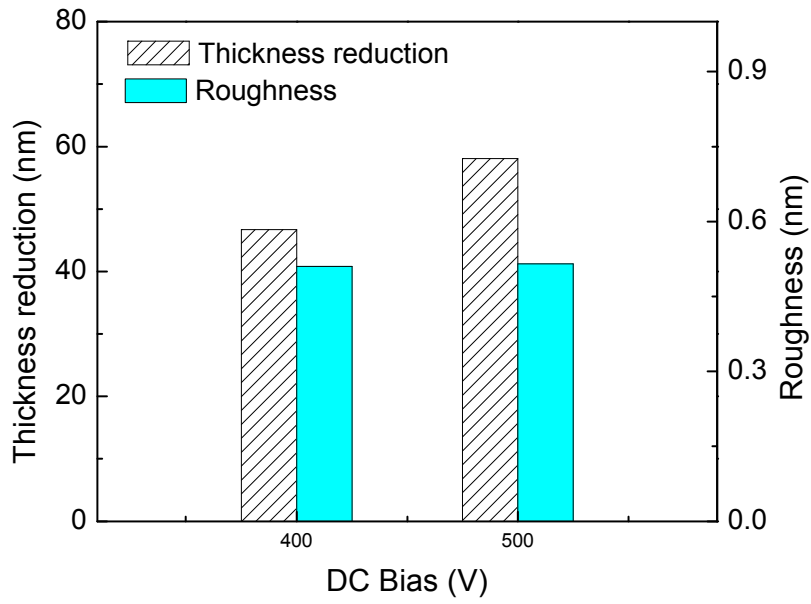


(b)

Figure 3-6: (a) Thickness reduction and (b) roughness at 40/80 mtor.



(a)



(b)

Figure 3-7: Effect of (a) etch time and (b) DC bias at CHF<sub>3</sub>10%.

### 3.4.2. O<sub>2</sub> addition

The effects of O<sub>2</sub> addition on CHF<sub>3</sub>/Ar plasma experiments were investigated by introducing a 2% O<sub>2</sub> into the plasma. With O<sub>2</sub> addition, the ratio of fluorocarbon to total carbon bonds was found to increase with the concentration of the CHF<sub>3</sub> gas (Figure 3-8). The ratio at same CHF<sub>3</sub>% was lower than with the one without O<sub>2</sub> addition, indicating a lower fluorocarbon polymerization level. With O<sub>2</sub> addition, the etching yield increased more than double of that with pure CHF<sub>3</sub>/Ar chemistry (Figure 3-9). At low concentration of CHF<sub>3</sub>, the surface roughness was greatly increased due to the O<sub>2</sub> addition, exceeding 10nm at the peak (Figure 3-9). The thickness reduction after DHF dipping was close to that of pure CHF<sub>3</sub>/Ar chemistry without O<sub>2</sub> (Figure 3-10(a) and the roughness was reduced after DHF dipping (Figure 3-10(b)). The surface roughness and etching loss increased with etching time and RF power (Figure 3-11). As shown in Figure 3-9, when CHF<sub>3</sub> concentration was above 40%, the roughness was greatly reduced while a reasonable etching rate was maintained. The implications will be explained in the discussion section.

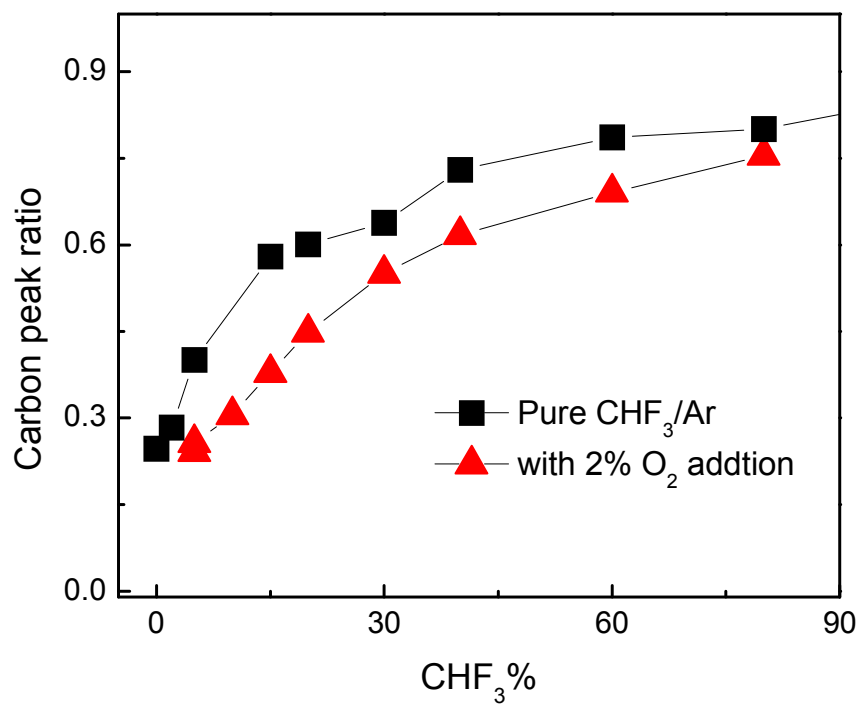
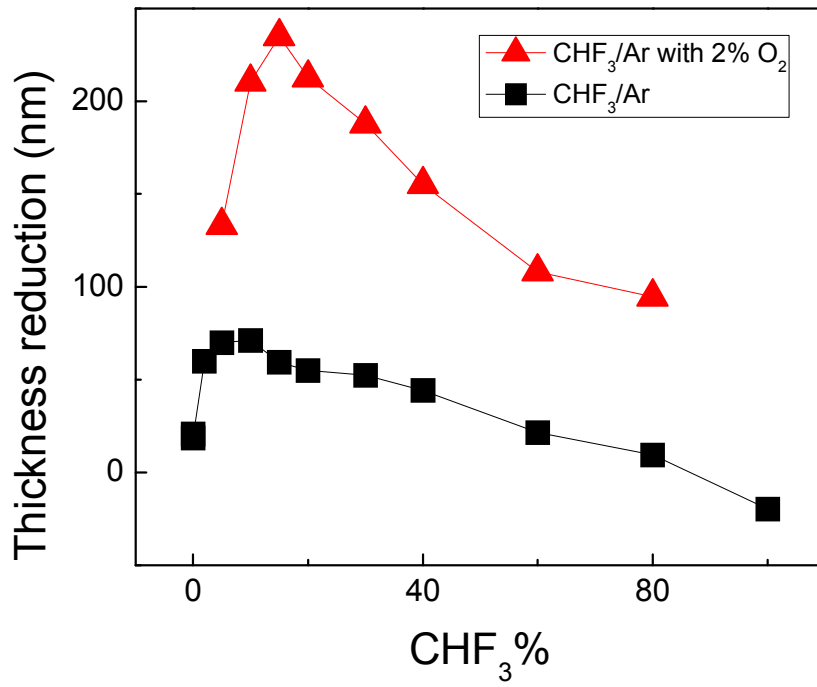
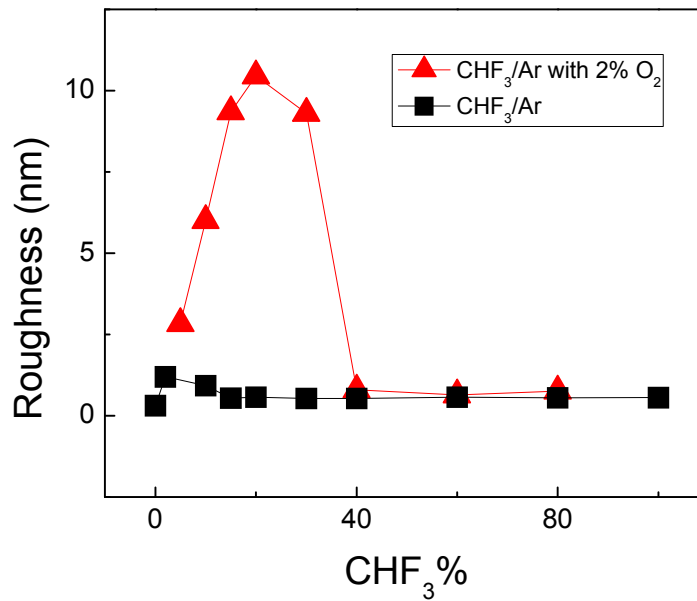


Figure 3-8: Sum of all CF peak areas over total C peak area measured by XPS with or without O<sub>2</sub> addition. (Total flow rate: 50sccm, Pressure: 40 mTor, Power: 300W, Time: 4min.)

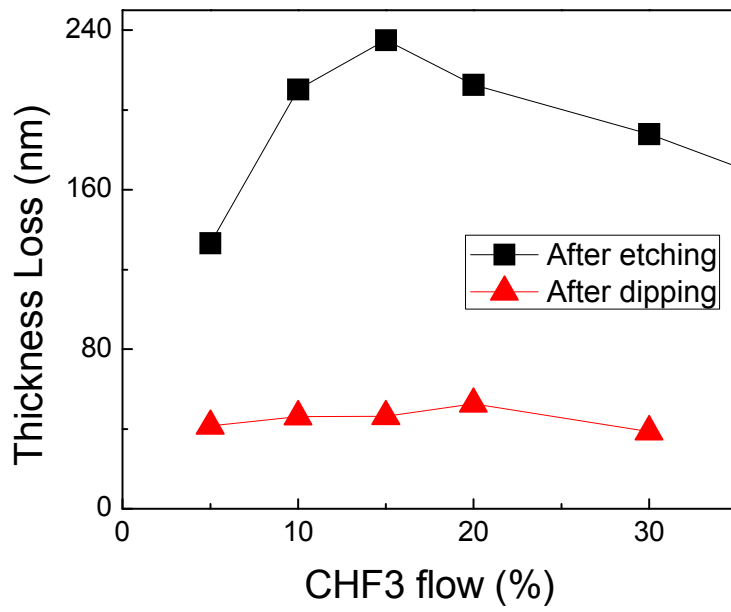


(a)

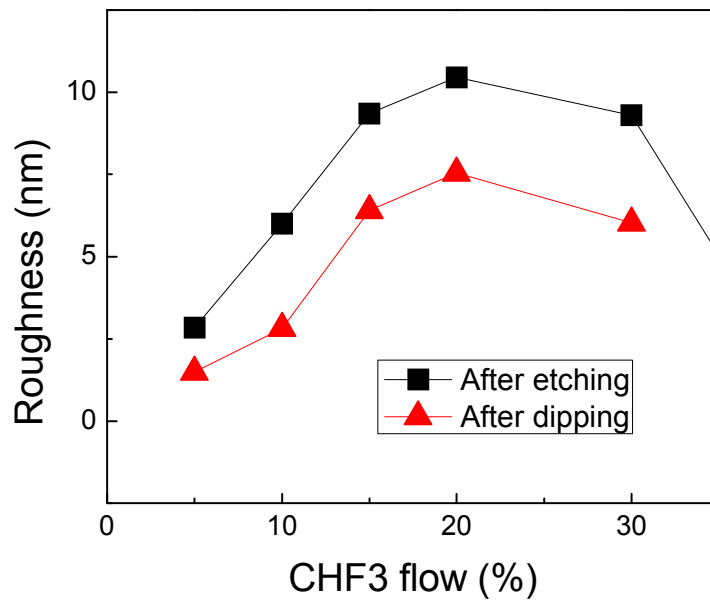


(b)

Figure 3-9: The effect of O<sub>2</sub> addition on (a) Thickness reduction and (b) roughness. (Total flow rate: 50sccm, Pressure: 40 mtor, Power 300W, Time: 4min.)

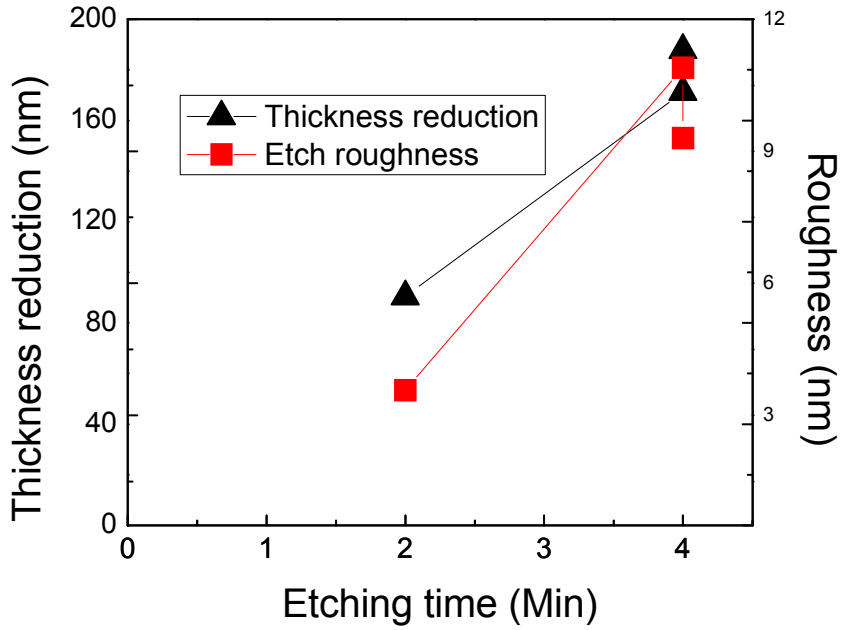


(a)

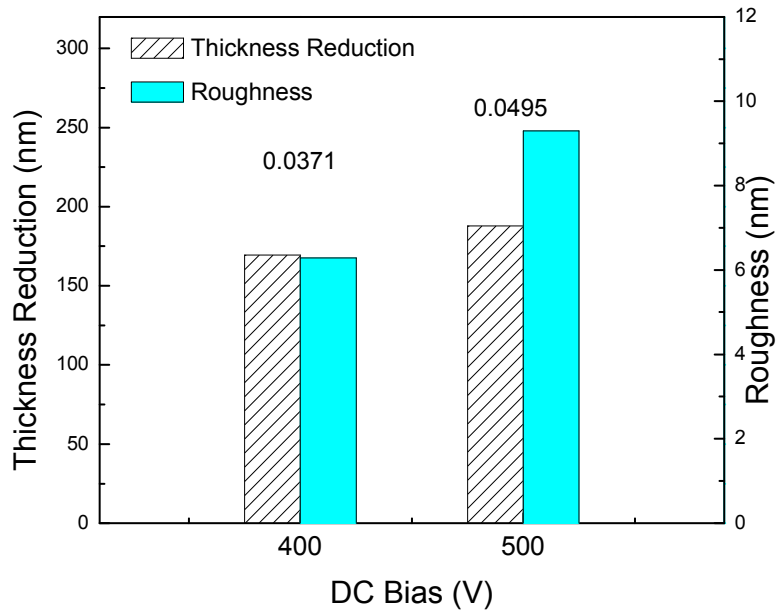


(b)

Figure 3-10: Effect of O<sub>2</sub> addition on (a) Thickness reduction and (b) roughness after DHF dipping. (Total flow rate: 50sccm, Pressure: 40 mtor, Power 300W, Time: 4min.)



(a)



(b)

Figure 3-11: Effect of (a) etch time and (b) plasma power with O<sub>2</sub> addition at CHF<sub>3</sub> 30%.

### 3.4.3. H<sub>2</sub> addition

Hydrogen reacts with Fluorine to form hydrogen fluoride, thereby increasing the C/F ratio in the fluorocarbon plasma chemistry. As a result, it is expected that the thickness of surface fluorocarbon layer will increase and the etch rate will reduce. The effect of H<sub>2</sub> addition was investigated. As shown in Figure 3-12, both etch rates for CHF<sub>3</sub>/Ar and CHF<sub>3</sub>/Ar/O<sub>2</sub> plasma chemistries generally decreased with a 2% H<sub>2</sub> addition although there are a few exception points at the low CHF<sub>3</sub> flow rate. For the CHF<sub>3</sub>/Ar/H<sub>2</sub> plasma chemistry, the etching rate in general is too small to discuss its practical use. The etching process quickly turned into a pure polymer deposition process, particularly with increasing CHF<sub>3</sub> flow rate. The surface roughness was measured for the CHF<sub>3</sub>/Ar/O<sub>2</sub>/H<sub>2</sub> plasma chemistry as shown in Figure 3-13. The roughness followed the same trend as the other two curves (i.e. CHF<sub>3</sub>/Ar and CHF<sub>3</sub>/Ar/O<sub>2</sub>). The XPS surface carbon peaks are illustrated in Figure 3-14(a) and are compared with CHF<sub>3</sub>/Ar and CHF<sub>3</sub>/Ar/O<sub>2</sub> chemistry at Figure 3-14(b). The ratio of fluorocarbon to total carbon bonds maintained the same trend with increasing CHF<sub>3</sub> concentration, but the experimental results were more scattered, probably due to the difficulty of controlling the mixing of four gas species.

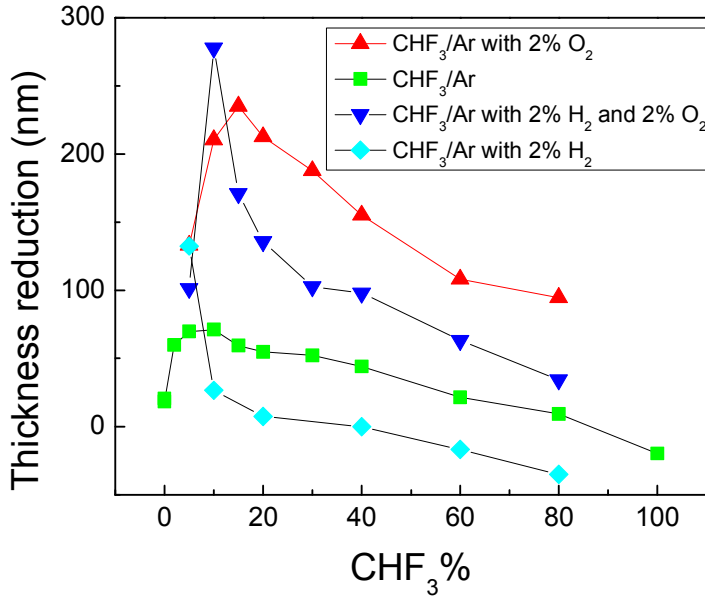


Figure 3-12: Thickness reduction of SiCOH film etching with H<sub>2</sub> addition. (Total flow rate: 50sccm, Pressure: 40 mtor, Power 300W, Time: 4min.)

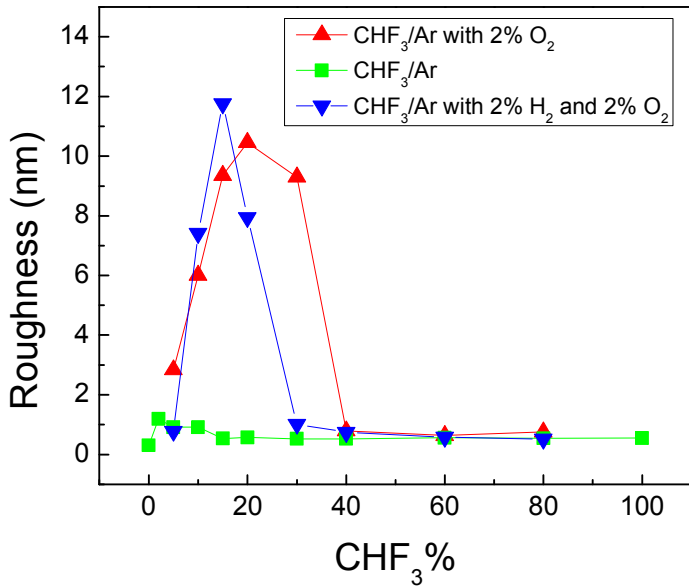
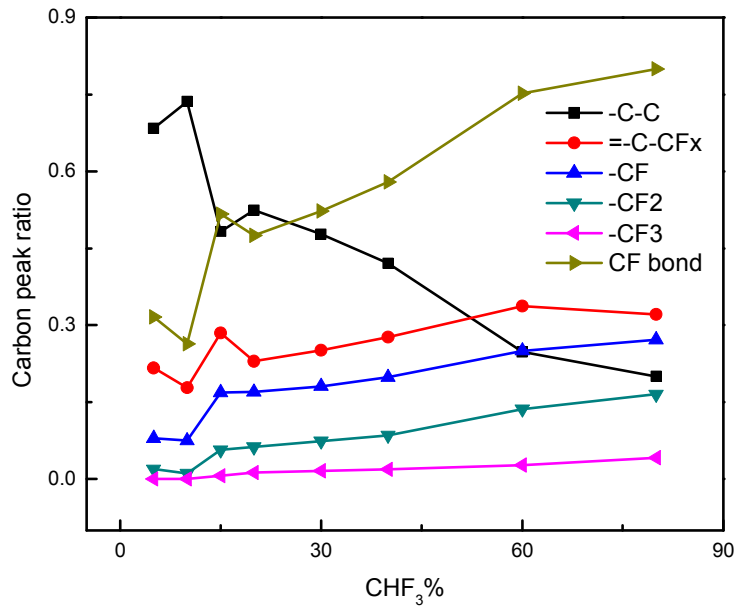
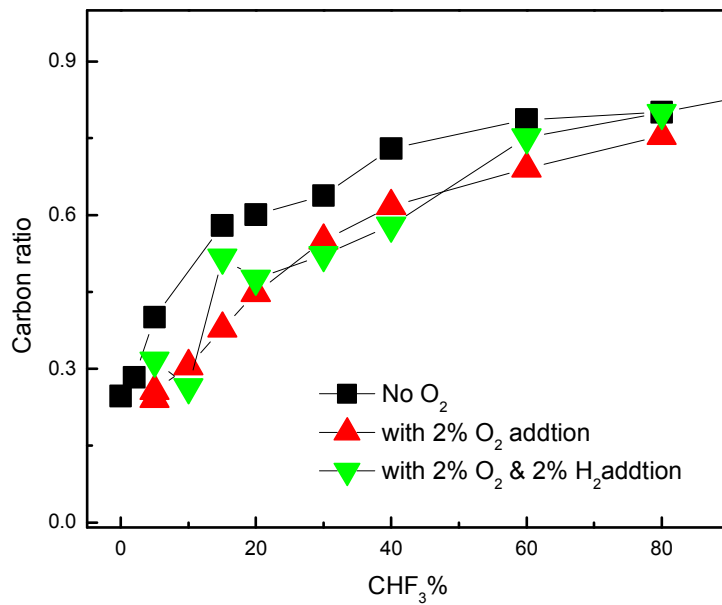


Figure 3-13: Surface roughness of SiCOH film after etching with H<sub>2</sub> addition. (Total flow rate: 50sccm, Pressure: 40 mtor, Power 300W, Time: 4min.)



(a)



(b)

Figure 3-14: Fluorocarbon polymerization by XPS analysis:(a) carbon peak ratios of CHF<sub>3</sub>/Ar with 2% O<sub>2</sub> and 2% H<sub>2</sub> addition; (b) Comparison with pure CHF<sub>3</sub>/Ar and CHF<sub>3</sub>/Ar with 2%O<sub>2</sub> addition only.

### 3.5. DISCUSSIONS

#### 3.5.1. Etch rate

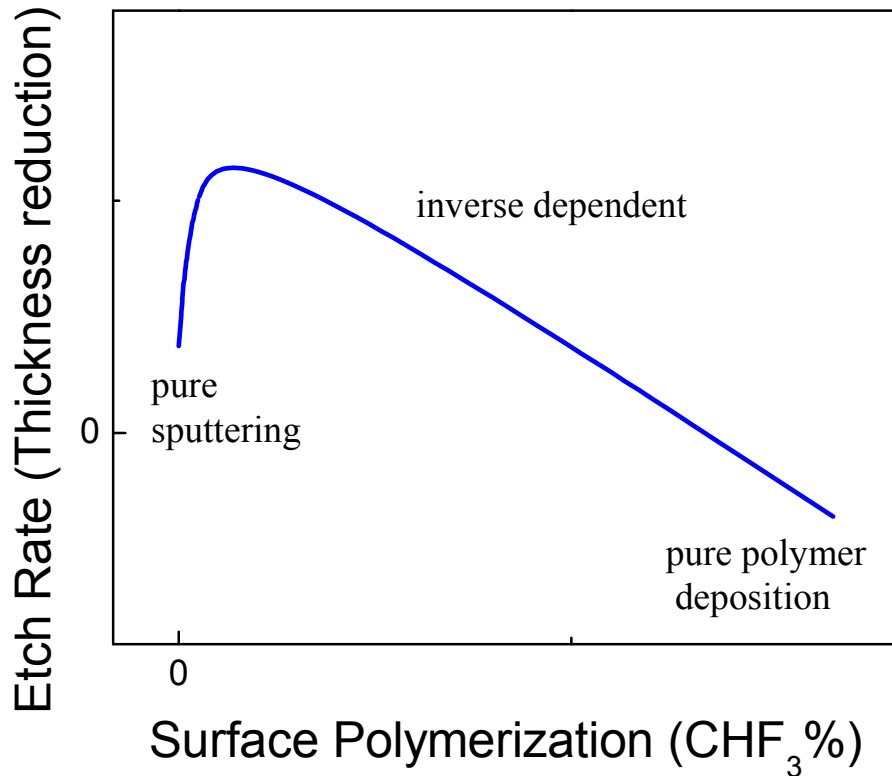


Figure 3-15: Summary of etch rate dependency on surface polymerization.

Since the surface polymerization monotonically increased with  $\text{CHF}_3$  concentration in the feeding gas as shown in Figure 3-5 and Figure 3-8, the trends of etch rate and surface roughness vs  $\text{CHF}_3$  concentration can be correlated with surface polymerization. Figure 3-15 summarize the general trend found in the results of the thickness reduction experiments for all four plasma chemistries. At 0%  $\text{CHF}_3$  (i.e. pure Ar), the SiCOH material was etched due to physical sputtering by the argon ions and the etch rate was low. As discussed in Section 3.3., when  $\text{CHF}_3$  was added to the feeding gas,

the fluorine started to break the strong Si-O bonds with the help of the hot ion and formed volatile  $\text{SiF}_x$ , turning the etch process into a reactive ion etch. The etch rate peaks after the formation of a very thin surface polymerization. Then, as the polymerized layer grows thicker, it blocks the transport of ion energy and reaction resultant, thereby reducing the etch rate. At a high polymerization rate, it becomes a pure polymer deposition.

As observed in Figure 3-9, the etch rate increased drastically with only a 2% oxygen addition. This is not only because oxygen consumes carbon to reduce the C/F ratio in the polymerization chemistry but also due to diffusion of the oxygen into the low-k material. Oxygen radicals react with the methyl bonds in the SiCOH material even without the help of the ion energy (refers to Chapter 4 for details). This compensates the function of fluorine and significantly accelerates the etching process.

Due to diffusion of O and F atom into the porous low-k, the fluorocarbon layer is not limited to the surface of the film as in the cases of  $\text{SiO}_2$  and the dense SiCOH material, but rather to an extended mix layer as we discussed in Section 3.3. The surface polymerization level (measured by XPS fluorocarbon peak ratio) can, therefore, be interpreted as the concentration of fluorocarbon bonds in the surface mixed layer rather than due to the thickness of the surface fluorocarbon polymer layer. Although the definition is changed, the consistent explanation of etch rate dependence on the surface polymerization level implies that the surface polymerization still plays an important role in the etching process and therefore is critical to roughness formation.

### **3.5.2. Surface roughening mechanism**

The surface roughening of porous SiCOH is a complex phenomenon and involves many aspects of plasma low-k interaction, including surface polymerization, surface

densification, ion transport and radical diffusion. The study of the surface roughening mechanism is discussed in this section.

### ***Polymerization***

A similar trend of surface roughness development is found in experimental results of all three plasma chemistry as illustrated in Figure 3-3, Figure 3-9 and Figure 3-13. This is schematically illustrated in Figure 3-16. At a very low polymerization region, the plasma etching is dominated by ion sputtering. Ion sputtering densifies the porous low-k surface and smoothes out the surface morphology. As a result, the root mean square (RMS) of argon etched p-SiCOH (0.3nm) is even lower than that of the pristine film (~0.4nm). Nevertheless, the surface roughness of the porous SiCOH film increases quickly with the addition of the polymerization species and peaks at a low polymerization level.

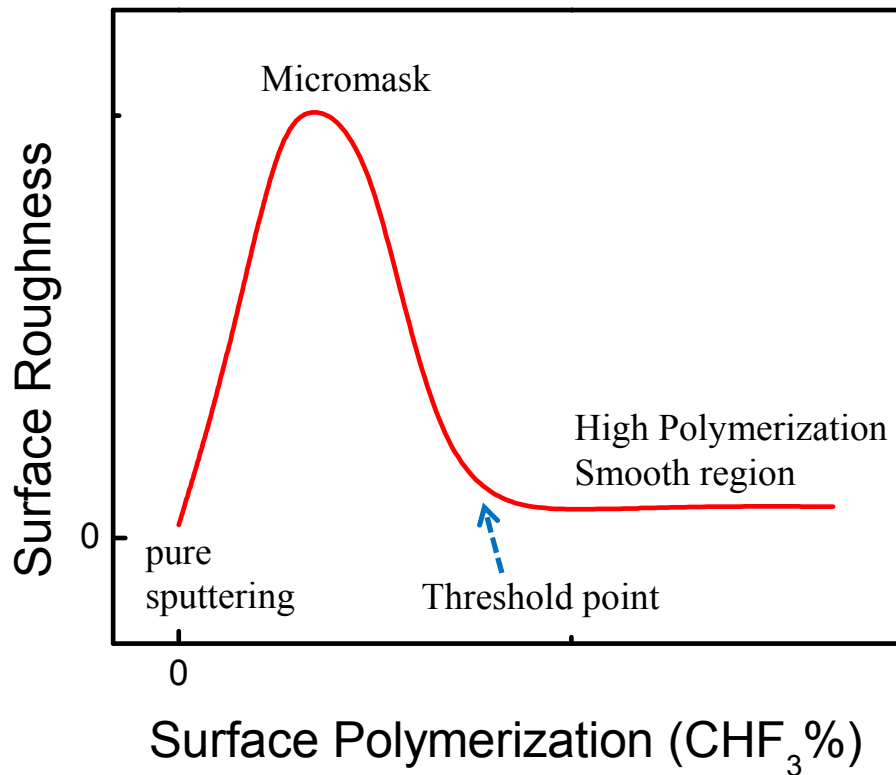


Figure 3-16: Summary of the dependency of surface roughness on surface polymerization.

The prominent roughness peak at low CHF<sub>3</sub> concentration can be approximately explained by a micro-masking theory [46]. Due to the porous microstructure in the SiCOH material used in this study, the polymerizing species diffused into the pore structures have different ion reception angles. As shown in Figure 3-17, ion bombardment is shadowed at the green circled areas, creating a small polymer-rich area. In comparison, the bottom area of the pore and the top area receive more ion bombardment, resulting in a thinner polymerized region. The different levels of the polymerization lead to different etch rates. Therefore, small pits responsible for the surface roughness are created.

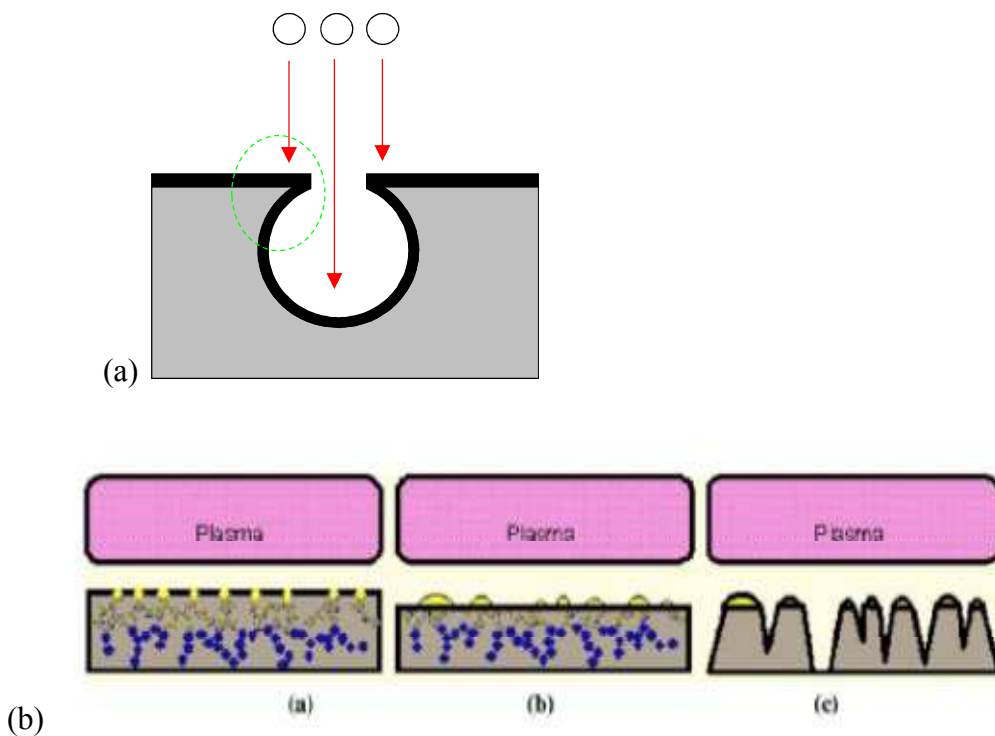


Figure 3-17: Schematics of the micromask formation and the occurrence of the roughening process.

This roughening process is greatly suppressed at higher polymerization chemistry. As abundant  $C_xF_y$  species fill multiple layers of the pore structures all at once, ion shadowing effect are stopped and evens out the etch rate differences are even out. This prevents the initiation of the roughness formation and creates a smooth region. As shown in Figure 3-16, the beginning of this smooth region is defined as the “threshold point”. Due to the reverse dependency of the etch rate on polymerization, the “threshold point” is the most likely point to find the best etch efficacy without surface roughening, and therefore, is important for process optimization. In this study, the “threshold points” for  $CHF_3/Ar$  chemistry,  $O_2$  addition and  $O_2/H_2$  addition were found at 15%, 40% and 30%  $CHF_3$  flow rate ratios respectively. Interestingly, the “threshold points” for  $CHF_3/Ar$  chemistry and  $CHF_3/Ar/O_2$  chemistry were found to correspond to the same XPS carbon-

fluoride peak ratio (0.6) as illustrated in Figure 3-18. With the H<sub>2</sub> addition, the “threshold point” of CHF<sub>3</sub> decreases from 40% to 30% as the hydrogen reduces the polymerizing rate. This observation confirms the critical roles of surface polymerization for the porous SiCOH roughening.

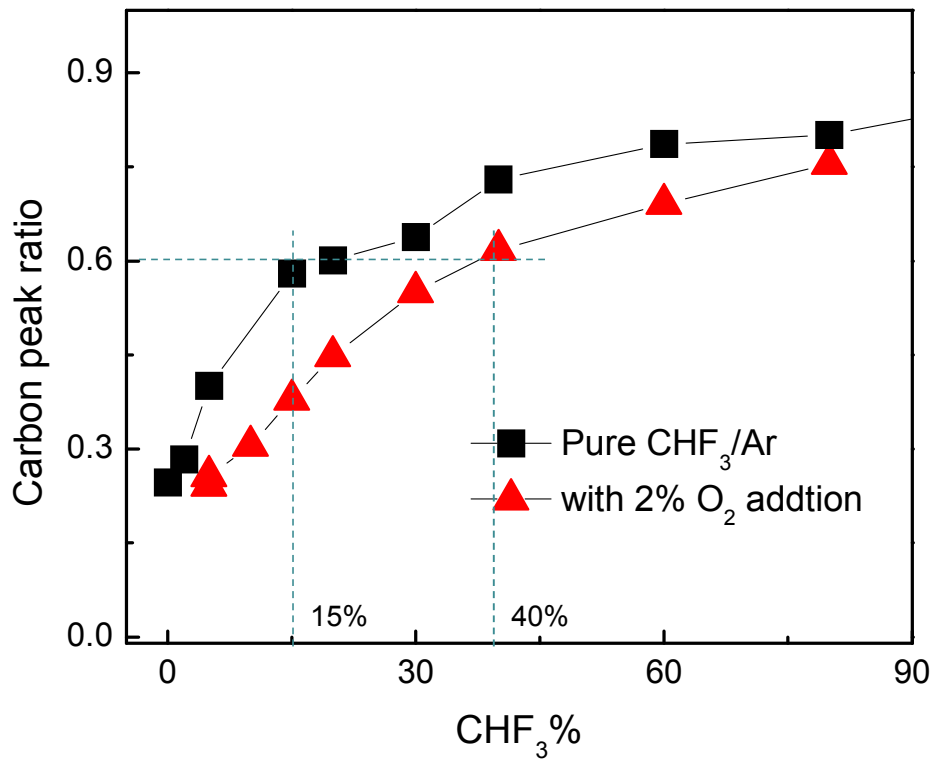


Figure 3-18: Relation of surface roughness threshold with CF peak areas over total C peak area ratio by XPS analysis.

### ***Surface densification***

The ion induced surface densification is well known in the plasma processes of porous low-k material (Chapter 4). The densified layer on the surface blocks the diffusion of reaction radicals, thereby reducing the etch rate. In the roughening process, the pits are

initiated by the polymer micromask effect. Due to the ion shadowing, the low-k material is denser on the top of the pits than in the bottom, enhancing the roughness growth.

The cracking of the surface densified layer was used to explain the roughness initiation by Bailly et al. [49]. However, it alone cannot explain the strong polymerization dependency of roughening process described in this chapter.

### ***Ion and neutron transport***

Surface roughness growth is assisted by the localized polymerization and surface densification. In Figure 3-7, the roughness stays constant as the etch depth increases, indicating a mechanism that limits the roughness growth. The slowdown of the oxide etch rate with structure aspect ratios is known as reactive ion etching (RIE) lag and has been explained by ion shadowing and differential charging of the sidewalls, among other factors [50][51]. This effect limits the roughness growth and eventually locks the roughness value.

### ***Radical diffusion***

The surface roughness is greatly increased when 2% oxygen was added into the plasma chemistry as show in Figure 3-9(b). As discussed in Section 3.5.1, the diffusion of oxygen radicals significantly increased the low-k etch rate. Due to the surface densification, oxygen radical diffusion is blocked on the top of the etch pits. Therefore, the etching rate at the pit bottom is much higher than the pit top, resulting in a high surface roughness. In general, oxygen reacts with the low-k material without the help of ion energy, thereby reducing the RIE lag effect by ion shadowing. This explains the continued growth of roughness as observed in Figure 3-11(a).

### 3.5.3. Effect of DHF dipping

DHF dipping experiment was performed to investigate the mechanism of plasma damage in the plasma etching process. Plasma species, such as oxygen and fluorine atoms, diffuse into the porous low-k material and remove the methyl bonds, thereby creating a highly damaged dielectric layer. This carbon depleted layer is expected to be removed by the DHF dipping process because its chemical property is similar to  $\text{SiO}_2$ . However, the diffusion of  $\text{C}_x\text{F}_y$  in the etching chemistry complicates the damage formation process due to the high resistivity of fluorocarbon to HF wet etching. At high  $\text{CHF}_3$  concentration, the fluorocarbon enriched layer on the top surface will completely stop the DHF etching as shown in Figure 3-4. At low  $\text{CHF}_3$  concentration, the localized fluorocarbon distribution not only induces the surface roughening but also makes it possible for using DHF dipping to etch off the damaged layer. Therefore, the thickness reduction by DHF indicates the thickness of the plasma damaged layer at low surface polymerization region.

As discussed in Section 3.3., damage is the result of a competition between the etch rate and the diffusion rate of active species ( $\text{O}^*$ , F) causing the damage. In other words, the thickness of the damaged layer is equal to the diffusion distance minus the etching distance. Interestingly, although the  $\text{CHF}_3/\text{Ar}/\text{O}_2$  chemistry had a much higher etching rate, the thickness reduction by DHF dipping is almost the same as etching without the 2% oxygen addition in the plasma chemistry as compared in Figure 3-19. This suggests that the thickness of the damage layer is primarily determined by the amount of fluorine diffusion instead of the concentration of the oxygen radicals.

The surface roughness, after the DHF dipping of the etched film, was reduced as shown in Figure 3-9(b). The interpretation of the roughening after DHF dipping is complicated because it is related not only to the radical diffusion during the plasma

etching process but also to the variation of surface etching in the DHF wet etching process due to uneven distribution of the fluorocarbon polymer.

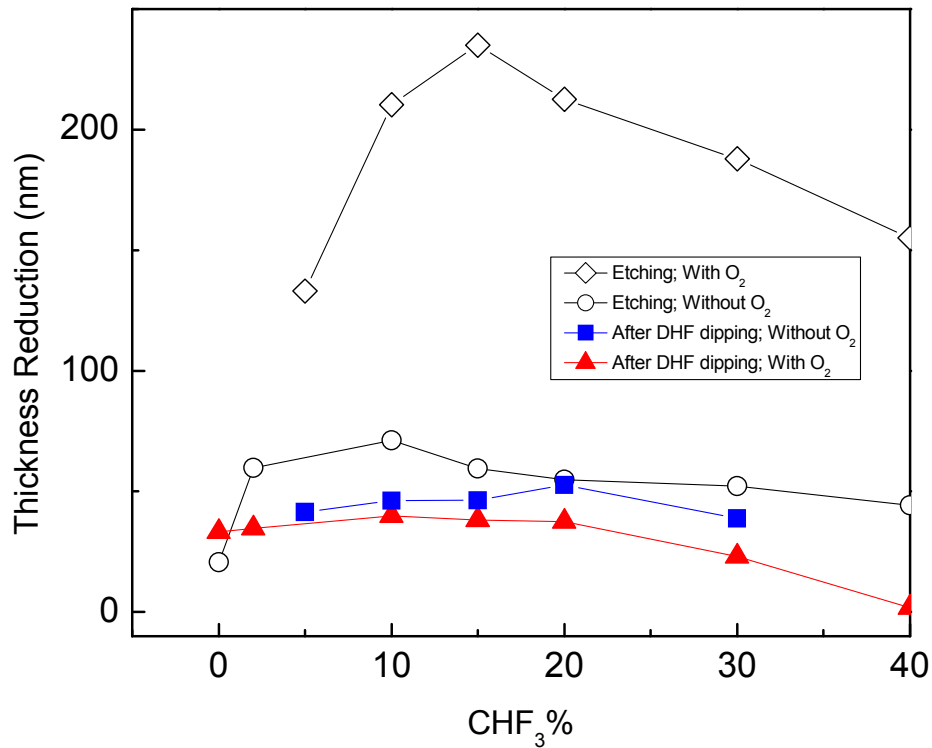


Figure 3-19: Thickness reduction after etching and then after DHF dipping of plasma chemistry with or without a 2% O<sub>2</sub> addition. (Total flow rate: 50sccm, Pressure: 40 mtor, Power 300W, Time: 4min.)

### 3.6. SUMMARY

Etch front roughness of porous low-k dielectrics is a complex problem relating to etching chemistry, etching kinetics and film properties. The porosity of the low-k material was found to be the root cause of the surface roughening. The porosity microstructures induced the uneven distribution of surface polymerization, initiating the

surface roughness morphology. The porous nature of the low-k material also led to the surface densification by ion bombardment. This created a denser but uneven layer on the top of the pits that blocked the radical diffusion and thus enhanced the roughening process. With O<sub>2</sub> addition, both the etch rate and surface roughness increased dramatically and continued to increase with etching time and higher bias voltage.

With higher surface polymerization, the surface roughening was suppressed resulting in a smooth region. The starting point of this smooth region was identified as the “threshold point” where the lowest surface roughness vs etch depth ratio can be found. The surface polymerization level for the “threshold point” was found to occur around 0.6 in XPS fluorocarbon peak ratio.

## **Chapter 4: Oxidative plasma induced damage to porous low-k dielectrics**

As we discussed in Chapter 1, the plasma photoresist stripping or ashing process is the most detrimental to the porous SiCOH low-k material. The main reason is because the oxidative plasma used to remove the organic photoresist can also be harmful to the organic component of SiCOH material. The oxidative plasma induced damage is enhanced by the porous structures in the ULK, creating serious integration challenges. There have been many studies conducted in this area[52][53][54]. The plasma damage of low-k dielectrics was found as a complex phenomenon involving both physical and chemical effects; the former arises from ion bombardment, depending on the energy distribution and flux for each ionic species, while the latter involves chemical reactions between the plasma and low-k constituents and/or induced by plasma radiation (photochemistry). The increase of the dielectric constant directly correlates with the changes in bonding configuration, the formation of carbon-depleted layer, film shrinkage and surface densification.

Although the plasma damage to low-k material has been extensively studied, the basic mechanism of plasma damage process still needs further understanding. The understanding of oxidative plasma interaction with the low-k material can provide guidelines and solutions to minimize the plasma induced damage and thus ensure the integration of the next generation IC interconnects.

This chapter is organized into two parts. In the first part, experiments were carried out by using an on-wafer filter system of a gap structure that allows distinguishing the individual roles of radicals, ions and photon. The effect of photon radiation in the vacuum ultraviolet (VUV) range was further separated into 3 energy range using four glass filters (i.e. fused silica, quartz, CaF<sub>2</sub> and MgF<sub>2</sub>).

In the second part, the mechanism of damage formation by oxidative plasma is analyzed by considering the kinetics of plasma interaction with porous low-k dielectrics, i.e. the kinetics of radical diffusion, reaction, and surface recombination in the pore structure of low-k dielectrics. In addition, the kinetic process of radical low-k interaction is simulated by a Monte Carlo computation method.

The analysis of radical kinetics can be applied to studying oxidative plasma damage to the low-k patterned structures with a hard mask on the dielectric surface. An analytical solution for damage distribution along the vertical direction of the sidewall was derived and confirmed with a gap structure experiment that simulates the patterned trench structure.

#### **4.1. ROLES OF IONS, RADICALS AND PHOTONS IN OXIDATIVE PLASMA DAMAGE FORMATION**

##### **4.1.1. On wafer-filter Experiments**

###### ***4.1.1.1. Description of the on-wafer filter method***

In a typical oxidative plasma generator, the active plasma constituents include ions, radicals and photons. The ions, accelerated by the electrical field applied by a RF bias, are highly collimated so that it can create an anisotropic etching profile. Radicals, the oxygen atoms in this case, are electrically neutral and driven by random gas phase collision, thereby having an isotropic momentum distribution. The photons, generated from the electron energy transitions in the plasma, are coming from the whole plasma body. Therefore, the photon radiations are near isotropic and depend on the plasma geometry. When a remote plasma system (e.g. remote ICP plasma) is used, the photon directions near the surface are close to vertical. The angular distribution of ions, radicals and photons on the low-k surface are summarized in Table 4-1.

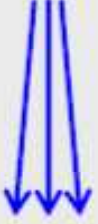
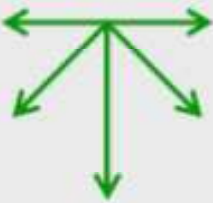
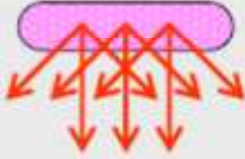
	Ions	Neutrals	Radiation
Angular distribution at surface	Highly collimated	Isotropic (random gas phase collisions)	Near isotropic, depends on plasma geometry
			

Table 4-1: The plasma constituents and their angular distributions in a plasma system.

As indicated in the schematic diagram Figure 4-1, an on-wafer filter system can be built to differentiate the roles of ions, radicals and photons. Compared to full plasma exposure at position (1), a silicon mask blocks both the ions and the visible/UV photons at position (2). However, radicals can diffuse into the space under the mask, becoming the only plasma constituent that interacts with the low-k film. When the silicon mask is replaced by an optical glass filter, photons can pass through the glass window and react with the low-k film. The damage of the low-k film at position (3) is, therefore, a synergetic effect of radical and photons. At position (4), the glass filter is placed directly on the low-k film to evaluate only the influence of photons. By carefully selecting the cut-off wavelength of the optical filters, the effects of the photons in different energy ranges can be differentiated. In comparison, the silicon mask can also be considered as a

photon filter that permits the transmission of the photon with wavelength of 1.5  $\mu\text{m}$  and above. However, photon interactions at this energy level are negligible.

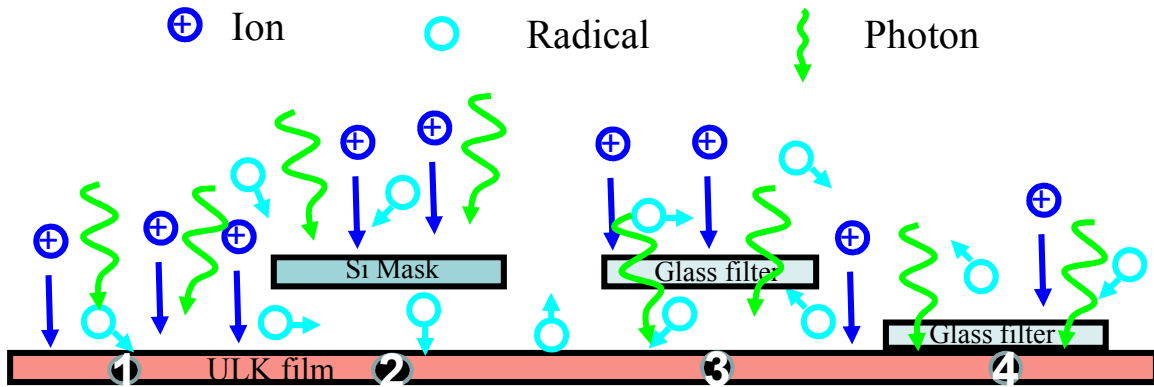


Figure 4-1: The schematic of the on-wafer filter structures and the interaction of the plasma constituents.

#### 4.1.1.2. Experimental details

The on-water filter system described above was used to investigate the plasma induced damage to porous SiCOH film. The porous SiCOH low-k film was supplied from Applied Materials with a dielectric constant of 2.2 and a porosity of around 33%. The 100 nm thick SiCOH film deposited on a 12 inch (100) silicon wafer was cut into 1 inch by 10 mm coupons and put into an Oxford Instruments Plasmalab 80 Plus ICP Etch Chamber.

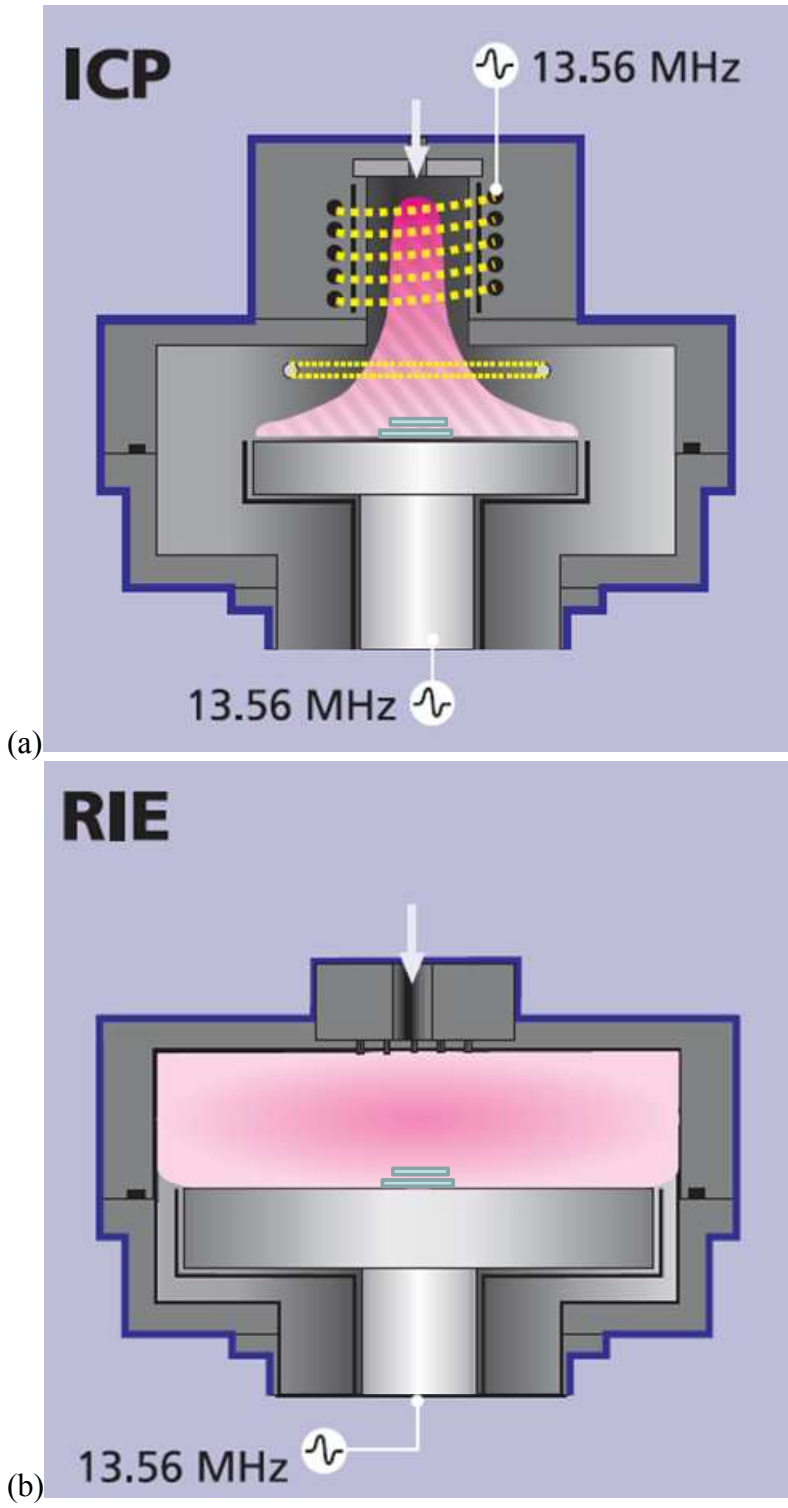


Figure 4-2: (a) ICP and (b) RIE system for on-wafer filter studies of the porous SiCOH.

The geometry of the plasma chamber is shown in Figure 4-2(a). The inductive coupled plasma was generated from about 2 inches above the ULK film with an excitation frequency of 13.56 MHz, providing a high plasma density of  $\sim 5 \times 10^{11}/\text{cm}^3$ . Ion energy is controlled by a RF bias of 13.56 MHz at the substrate electrode. In this plasma setup, the ions and the photons are both highly collimated with directions perpendicular to the film surface, which ensure the filtering of photon energy. In comparison, the on-wafer filter experiment was conducted in a RIE chamber described in Figure 4-2(b)., The photon filters failed to function because of the plasma geometry, mainly due to the photon leak on the side of the filter structure.

Silicon mask is 10mm $\times$ 10mm square and 0.3mm thick, cut from a 4 inch double-side-polished (100) silicon wafer. Glass filters (MTI Inc.) are 10mm $\times$ 10mm in square and 1 mm thick. In position (2) and (3) of Figure 4-1, they are supported by silicon spacers at two sides with a 0.7mm spacing from the low-k surface. The small size of the structure minimized its influence on the plasma density and ion energy distribution. The influences of filter absorption were tested with 2 mm thick filters and no significant differences were observed[55].

In order to evaluate the effect of the photon energy, four glass filters are used in this study including MgF<sub>2</sub>, CaF<sub>2</sub>, quartz and UV grade fused silica. As shown in their transmission spectra in Figure 4-3, the MgF<sub>2</sub> filter has the lowest cut-off wavelength of around 125 nm which are transparent to almost all vacuum UV (VUV) and UV photons. CaF<sub>2</sub> filter has a higher cut-off  $\sim$ 135 nm which blocks the photons with energy higher than 135 nm. Next, the quartz filter has a cut-off wavelength of 160 nm. The UV grade fused silica has the highest cut-off wavelength of 185 nm, which blocks all VUV photons. The permitted ranges of these filters are summarized in Figure 4-4.

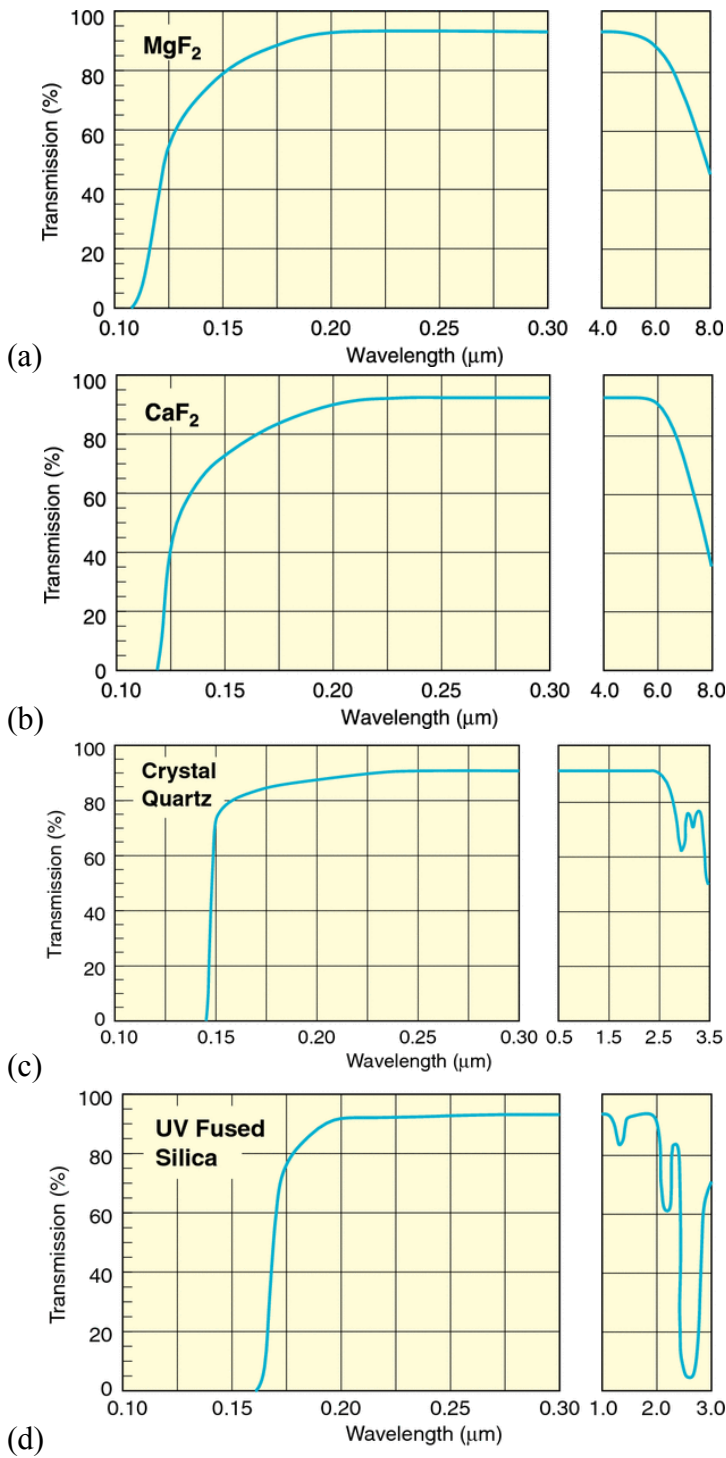


Figure 4-3: the transmission spectra of (a) MgF<sub>2</sub>, (b) CaF<sub>2</sub>, (c) quartz and (d) UV grade fused silica.

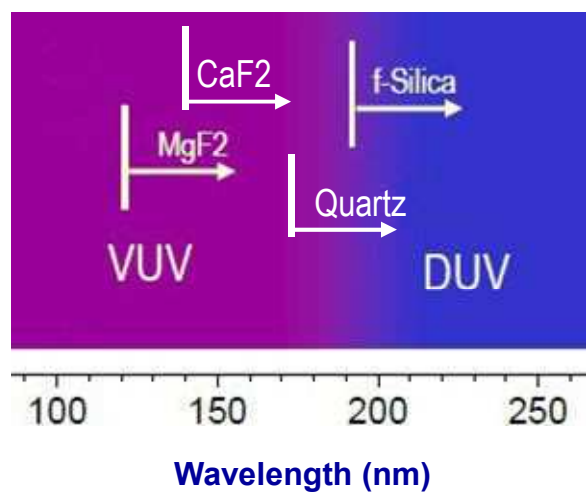


Figure 4-4: The transmission ranges of the optical filters.

With the variation of filter configurations, seven samples are used in this study to distinguish the influences of ions, radicals and photon radiations from the process plasma. These filter configurations are summarized in Table 4-2. In configuration (a), no filter was used and the low-k sample was exposed to all plasma constituents. The plasma damage is the synergetic effects of ions, radicals and photon radiations of all wavelengths. In configuration (b), the silicon mask was positioned 0.7 mm above the low-k films to investigate the effect of radicals. In configuration (c), (d), (e) and (f), UV grade fused silica (f-Silica), quartz, CaF<sub>2</sub> and MgF<sub>2</sub> filters were used respectively. The filters were positioned 0.7 mm above the film to evaluate the effects of VUV and UV radiation interactions with radicals. The effect of photon energy in four regions was differentiated by these four filters. In configuration (g), the MgF<sub>2</sub> filter was placed directly on the film surface to separate the influence of VUV and UV photon radiation from the plasma.

<b>Treatment Type</b>	<b>Filter used</b>	<b>Permitted Constituents</b>
<b>(a)</b>	No filter	Radicals, Photons (All), Ions
<b>(b)</b>	Silicon	Radicals
<b>(c)</b>	Fused silica	Radicals, Photons (Wavelength >185 nm)
<b>(d)</b>	Quartz	Radicals, Photons (Wavelength >160 nm)
<b>(e)</b>	CaF <sub>2</sub>	Radicals, Photons (Wavelength >135 nm)
<b>(f)</b>	MgF <sub>2</sub>	Radicals, Photons (Wavelength >125 nm)
<b>(g)</b>	MgF <sub>2</sub> (no spacing)	Photons (Wavelength >120nm)

Table 4-2: The filter mask combinations used in the on-wafer filter experiments. The filters are placed 0.7 mm above the low-k surface unless specified otherwise.

All the samples with different filter configurations were treated with the same plasma conditions (ICP power: 200W, RF bias: 100W, pressure 5 mtorr, flow rate: 20 sccm, treatment time: 150 seconds). After plasma damage, the thickness reduction and chemical bonding composition of the films were measured by spectroscopic ellipsometry and FTIR spectroscopy.

#### ***4.1.1.3. Experimental results***

The concentration of methyl bonds (Si-CH<sub>3</sub>) in the SiCOH material directly correlates to its dielectric constant. The methyl bonds after plasma damages are quantified by Si-CH<sub>3</sub> absorption peak in the transmission FTIR spectroscopy at about 1275 cm<sup>-1</sup>. It is then normalized with FTIR Si-O-Si peak (around 1105 cm<sup>-1</sup>). Figure 4-5 shows the reduction of methyl bonds compared to the pristine film. The largest methyl reduction was found at configuration (d), (e) and (f), which is the synergetic effect of radicals and VUV photons. Compared to the methyl reduction with only the radicals

(conf. (b)), VUV photons enhanced the radical damage. Photon with wavelength over 185nm did not change the damage effect with radicals. The methyl depletion of the fully exposed film (conf. (a)) was smaller than the films damaged by the radicals alone or the radicals plus photons, indicating ion bombardment reduced the plasma damage. This is probably because the ion-induced surface densified layer hindered the radical diffusion. The configuration (g) has the least methyl depletion and close to zero, suggesting that VUV and UV photons do not cause methyl damage or that the reduction cannot be observed by FTIR measurement.

The bulk methyl reduction also causes pore collapses and thickness reduction. The thickness reduction results in Figure 4-6 shows the same trend with the exception of the sample (a). The relatively large thickness reduction at configuration (a) may be due to the sputtering effect of ions in addition to chemical induced shrinkage.

The FTIR –OH bonds and physisorbed water peak areas was illustrated in Figure 4-7. The general trend is similar to the methyl reductions but more exception points were observed. This was probably due to the instability in plasma conditions and moisture absorption. Similar instability was observed by Hualiang Shi in the same plasma system[55].

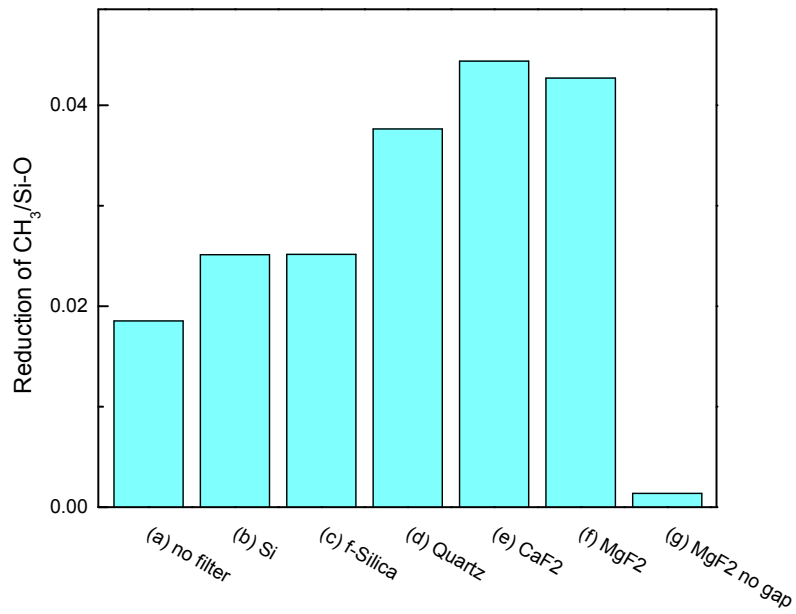


Figure 4-5: The reduction of Si-CH<sub>3</sub>/Si-O

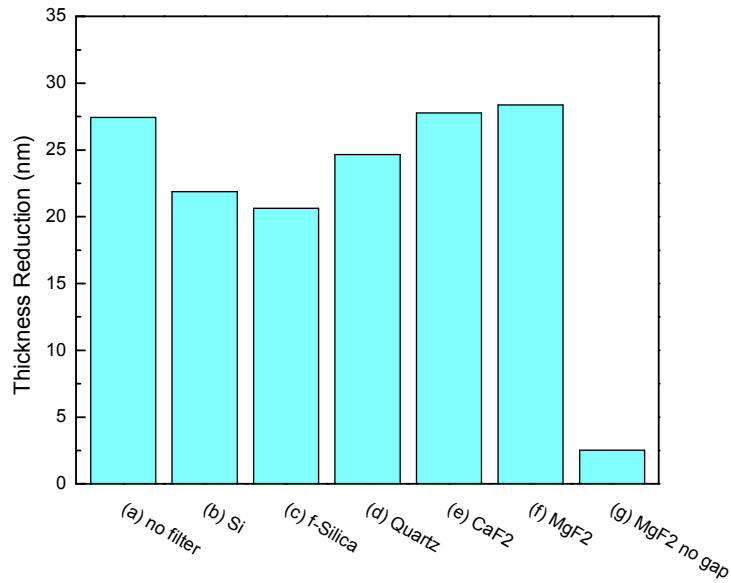


Figure 4-6: The thickness reduction after oxygen plasma treatment

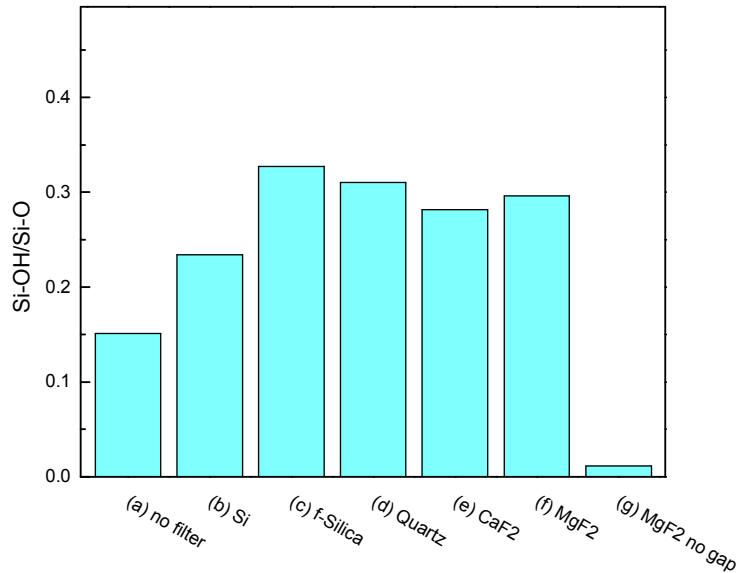


Figure 4-7: The FTIR –OH and physisorbed water peak area

#### 4.1.2. Roles of the Ions

As discussed in Chapter 3, ion bombardment plays an important role in the SiCOH etching process in the fluorocarbon based plasma. Ion bombardment not only provides the activation energy for fluorine silicon reaction but also reduces the surface polymerization by ion-sputter effect, thereby controlling the etching rate. In an inert gas plasma (e.g. Ar, He plasma), ion bombardment directly removes the target material by momentum and energy transfer between the ions and the target nuclei or the bound and free electrons inside the target. By considering the collision cascade process of target atoms induced by the energetic ions and the different atom-atom interaction potentials, the energy dependence of the etch yield via a physical or an ion-enhanced chemical process is described in a sputter yield model[56][57]:

$$Y(E) \approx A(\sqrt{E} - \sqrt{E_{th}}) \quad (4.1)$$

where  $A$  is inversely proportional to the surface binding energy and  $E_{th}$  is the threshold energy or the minimum energy required to remove an atom from its position in the lattice.

However, as shown in Section 4.1.1.3, more modifications were observed on the films under the filters than the fully exposed film, indicating that ion bombardment reduces the plasma-induced damage. This phenomenon, although seemingly counterintuitive, is consistent with many other studies[58][59][60] and is rooted from the porosity of the p-SiCOH material. Oxygen radicals react with Si-CH<sub>3</sub> without the help of ion energy. The oxygen radicals diffuse into the porous structure in a speed that is much faster than ion sputtering or ion induced chemical reaction, thereby causing more damage. On the other hand, ion bombardment densifies the surface of the porous low-k, creating a barrier layer to block the oxygen radical diffusion. This ion-induced surface densification can be limited to a very thin layer by careful process control so that the increase of the effective k value by itself can be acceptable.

This mechanism can be used to reduce the plasma induced damage. In order to minimize the damage, a two steps process was applied to the porous SiCOH film. Step one used RIE Helium plasma (RIE power 150W, 5 mtor, 20 sccm, 150 seconds) to induce a “surface densified skin layer” to seal the pores and block the radical diffusing. In this step, the plasma conditions such as ion energy were carefully controlled to limit the densification depth. In step two, the low-k film was treated ICP CO<sub>2</sub> plasma (ICP 150 W, 5 mtor, 20 sccm, 150 seconds). ICP plasma was used in this step to generate a high radical density for efficient PR stripping. As shown in Figure 4-8, the one with “Helium plasma pretreatment” has less damage in thickness reduction and methyl depletion than the one with ICP CO<sub>2</sub> plasma alone.

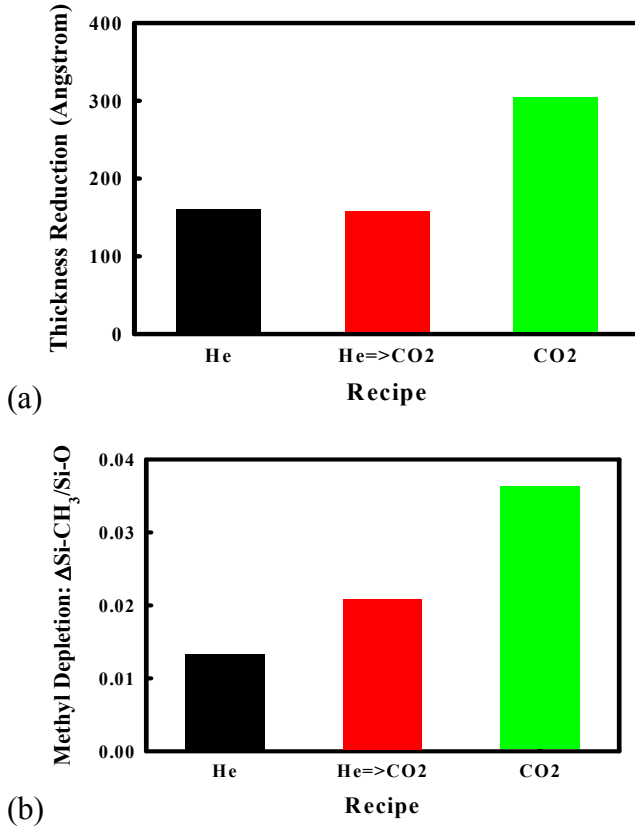


Figure 4-8: (a) Thickness reduction and (b) methyl reduction of He plasma, CO2 plasma, and CO2 plasma with the He plasma pretreatment.(courtesy of Hualiang Shi)

However, the technological application of the ion induced densification during integration might be limited due to obvious geometrical aspects. The ion bombardment is highly collimated and is usually parallel to the sidewalls. Therefore, damage induced by radical diffusion through the vertical sidewalls, which is the main issue of the low-k integration, cannot be easily reduced by sputtering-driven surface densification.

### 4.1.3. Roles of the Photons

#### *VUV radiation and radicals acting synergistically to enhance the plasma damage*

As discussed in Section 4.1.1.3., VUV photons enhance the plasma damage caused by the radicals. This result is in good agreement with other studies[61][62]. The four glass filters and the Si mask were used to investigate the synergistic effect of photon radiation and radiation in four energy zones. The damage under the fused silica filter was found to be almost the same as that under the Si mask. Starting from the quartz filter (permits wavelength above 165 nm), the damage increased as the photon started to act synergistically with the radicals, as indicated by more film shrinkage and methyl depletion. The enhancement of the plasma damage became even more prominent when photons with higher energy were involved with the implementation of the CaF<sub>2</sub> and MgF<sub>2</sub> filters. The results indicate that photons with wavelength below 185nm (or above 6.7eV) were responsible for the damage enhancement.

#### *Mechanisms of VUV photon enhancement*

Two mechanisms can be considered to explain the damage enhancement caused by the VUV photon. The first explanation is the possibility of direct scission of Si-CH<sub>3</sub> bonds by VUV photons. When the photon energy is greater than the bond dissociation energy of Si-CH<sub>3</sub>, the S-C bonds have a high probability to break and create Si dangling bonds and CH<sub>3</sub> radicals. The generated active sites can operate as initial centers for further reaction with damaging radicals and molecules.

Bond	Si-O	Si-C	Si-H	Si-Si	C-H	C-O	C-C	O-H
<b>Bond energy(eV)</b>	8.3	4.7	<3.1	3.4	3.5	11.2	6.3	4.4
<b>Wavelength (nm)</b>	149.6	265.0	399.9	366.1	353.6	111.1	197.1	279.8

Table 4-3: Bond dissociation energy and associated wavelengths in diatomic molecules[63].

The dissociation energies of the pertinent chemical bonds in low k dielectrics are listed in Table 4-3. For Si-C bonds, the energy is 4.7 eV (265 nm), which is lower than the energy threshold defined by the fused silica filter of 6.7eV (185 nm). The higher energy required for the session of Si-CH<sub>3</sub> can be explained by the quantum-chemical calculation from Prager et al.[64][64] As shown in the diagram in Figure 4-9, the quantum-chemical calculation on octamethyl-clotetrasiloxane reveals that a threshold wavelength of 190 nm is needed for the molecule to be excited to the lowest singlet state. The molecule then undergoes an intersystem crossing into an excited triplet state, where the Si-CH<sub>3</sub> dissociation occurs. Therefore, the energy of about 6.5 eV (190 nm) for the lowest singlet state is necessary for the session Si-CH<sub>3</sub>, despite the low bond dissociation energy of about 4.7eV. This is also in good agreement with their experiment of Si-CH<sub>3</sub> degradation after irradiation with 172 nm or 222 nm UV lamps.

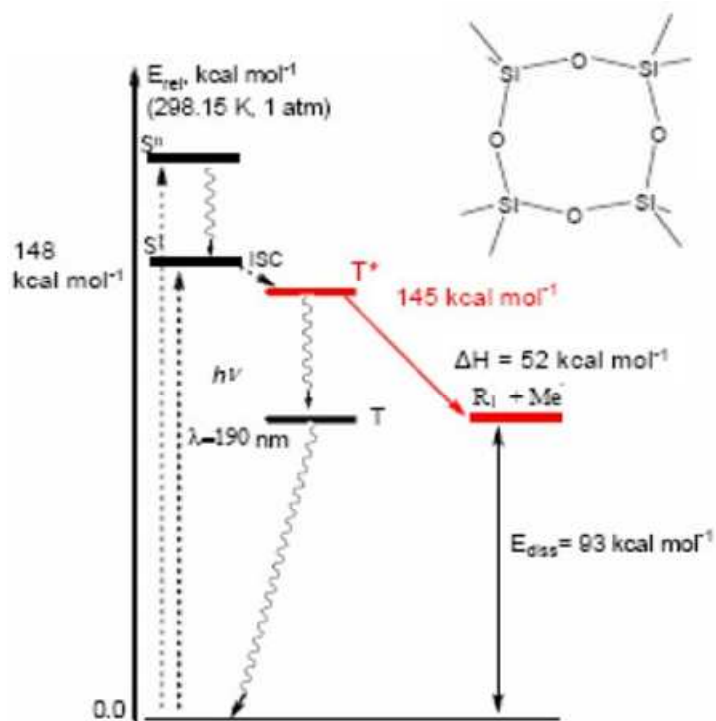
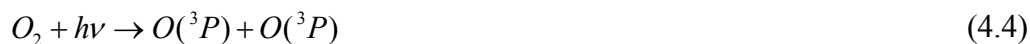


Figure 4-9: Quantum-chemical calculation of the threshold wavelengths for Si-CH<sub>3</sub> dissociation of octamethylcyclotetrasiloxane[64].

The VUV-induced photodissociation of O<sub>2</sub> molecules is another possible mechanism. In atmospheric physics, it is believed that UV with wavelength below 230 nm can dissociate O<sub>2</sub> molecules into two oxygen atoms.



This is supported by many experimental observations. For example, with the excitation of a 157nm laser beam, Lin et al.[65] observed the following reactions:



The O atom created by VUV-induced photodissociation could increase the radical density under the filter, thereby creating more methyl depletion. Moreover, VUV

radiation can penetrate into the bulk of the ULK material and suppress the recombination reactions of oxygen radicals, enhancing the radical diffusion process.

However, there were a few observations that are contradictory to this proposed mechanism. For example, the experiment with a fused silica filter showed negligible effect by photo-dissociation of VUV with wavelength from 185 nm to 230 nm. In another experiment, Lee et al. used a VUV excimer lamp to investigate the synergic effect of VUV photons (147 nm) and O<sub>2</sub> molecules, but only negligible damage was observed on the ULK film[66]. One possible explanation is that the distance between the photodissociation region and the sample are too large and the radicals may recombine before they reach the film. More precise experiments are needed to evaluate the contribution of the VUV-induced photo-dissociation effect.

#### ***Damage by VUV radiations only***

We have demonstrated that VUV photons could break the Si-CH<sub>3</sub> bonds in the porous low k dielectrics. The direct damage by VUV radiation alone was found in Lee et al.'s experiment with a 147 nm UV excimer lamp[66] and other UV curing studies[67][68][69]. However, the results of configuration (g) from Section 4.1.1.3. (i.e. Mgf2 mask direct contact with the SiCOH surface) showed that VUV/UV photon alone only caused negligible film shrinkage and methyl depletion. This was in good agreement with results of Takeda et al.[62] and De Marneffe et al.[70] One possible explanation is that the filter placed on top of the low-k film kept the reaction product from leaving the reaction zone. For this reason, the probability of an inverse reaction of methyl radical with Si dangling bonds can be significant. In the case of experiments with VUV lamps, the reaction product can fly in to the vacuum or ambient gas, resulting in a permanent damage.

#### **4.1.4. Roles of the Radicals**

In the on-wafer filter experiments, the plasma induce damage was significant once radicals were present, indicating the importance of the radicals in the damage process. However, this set of experiments did not reveal new information about the radical damage process. In the next section, the kinetics of radical-SiCOH interaction will be discussed in detail.

## 4.2. THE KINETICS OF RADICAL-LOWK INTERACTION

As already mentioned, radicals are the essential agents to remove the organic photoresist. For the plasma photoresist stripping process, ions and photons can be avoided by using remote plasma and special grids in order to minimize the ULK damage. However, radicals must be present to remove the photoresist residuals.

In previous studies [55], the plasma damage was found proportional to the radical density at the low-k surface. Radicals react with the organic component of SiCOH material, particularly the methyl bonds, leading to their removal and subsequent hydrophilization of the low-k material. This damage process is enhanced by the porous structures of the ULK. A quantitative description of the radical diffusion into the pores is important to understand the plasma damage formation.

### 4.2.1. Kinetics of radical diffusion process.

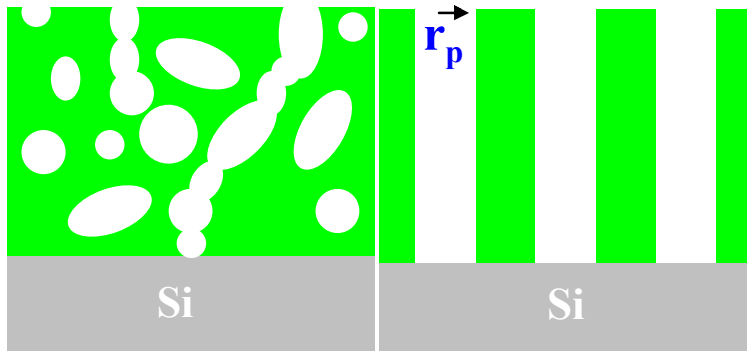


Figure 4-10: The pore structure inside ULK dielectric (a) real case; (b) simplified model.

The porous structure of the p-SiCOH material is a mixed structure of many connected or isolated pores as illustrated in Figure 4-10 (a), which describes the porosity, the pore radius and the pore connection length in the low k dielectric. Radicals diffuse through the path formed by the connected pores, react with the ULK and recombine on

the side wall. For simplicity, the pore structure can be described as a bundle of many parallel and vertical cylindrical holes.

This kinetic process of radical low-k interaction is a combined process of radical diffusion, reaction and recombination and is analyzed in this section.

### ***Diffusion***

Diffusion process is driven by the density gradient of the diffusing species where the free particles diffuse from a high density area to a low density area. In a phenomenological approach, the diffusion flux is proportional to the minus gradient of concentration and expressed by the Fick's law as:

$$F|_x = -D \bullet \frac{d\phi}{dx}|_x \quad (4.5)$$

The diffusion constant  $D$  is well studied under different conditions. For example, when the mean free path is relatively long compared to the pore size, the particles hit the pore wall before they hit each other. This condition is defined as Knudsen diffusion, which describes the radical diffusion in porous SiCOH. In the simplified pore model (Figure 4-10(b)),  $D$  is expressed as

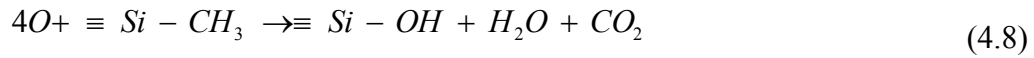
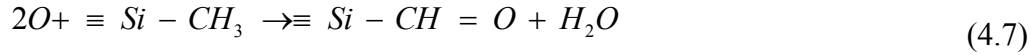
$$D = 97.0r_p \sqrt{\frac{T}{M}} \quad (4.6)$$

where  $r_p$  is the pore radius,  $M$  is the molecular weight of plasma radicals and  $T$  is the temperature.

From the atomistic point of view, diffusion is considered as a result of the random walk of the diffusing particles. This diffusion process, therefore, can be simulated by the Monte Carlo method.

### **Reaction**

As discussed in Chapter 1, oxygen radicals react with carbon groups in the p-SiCOH material. The dominant reaction paths are listed as[71]:



### **Recombination**

The surface recombination of oxygen radicals can be written as



Baklanov *et al.* reported two possible surface recombination mechanisms for the OSG surface: Eley-Rideal and Langmuir-Hinshelwood mechanisms, with their recombination rates depending on the substrate temperature and surface active sites[72].

## **4.2.2. The analytical method**

### **4.2.2.1. The Thiele Model**

The problem of diffusion of active species in pores has been extensively studied in heterogeneous catalysis starting from the work by Thiele[73] who first described the effect of in-pore diffusion on chemical reaction rates, using a simple geometric model with isotropic properties. Although this model is based on geometric shapes, it gave a good approximation of real porous materials[74]. Similar analyses have been used to describe the diffusion of radicals into the pores of low-k materials[75][72]

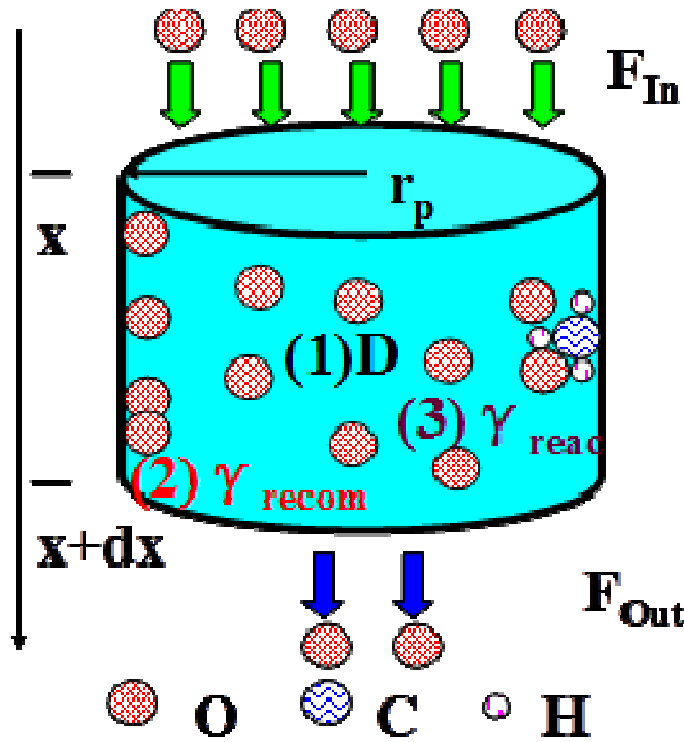


Figure 4-11: Kinetics of radical diffusion, reaction, and recombination inside pore structure.

A similar analytical approach is applied here to study the radical kinetic in the pore structures SiCOH low-k material. This approach uses the simplified pore structure as illustrated in Figure 4-10(b) and the pore radius is defined as  $r_p$ . One elemental pore volume from the long cylindrical pore is displayed in Figure 4-11. The mass balance of plasma radicals in this elemental pore volume  $dV = 2\pi r_p dx$  can be expressed as:

$$F_{In}|_x - F_{Out}|_{x+dx} = L_{react} + L_{recom} \quad (4.10)$$

where  $F_{In}|_x$  is the incoming flux at position  $x$ ,  $F_{Out}|_{x+dx}$  the outgoing flux at position  $x+dx$ , and  $L_{react}$  and  $L_{recom}$  are the loss of the radical species due to chemical reaction and recombination at the pore surface. As discussed in Section 4.2.1., for most plasma studies, the mean free path of the plasma species is about the order of 1 cm,

which is several orders of magnitude larger than the pore size (~several nm). As a result, the plasma species have much higher probability to collide with the pore wall than with each other. In this case, the mass transport is dominated by Knudsen diffusion with mass flux  $F = -\pi r_p^2 D \frac{d\phi}{dx}$  where the Knudsen diffusivity  $D = 97.0 r_p \sqrt{\frac{T}{M}}$ , with  $\phi$  being the plasma radical density,  $M$  the molecular weight of plasma radicals and  $T$  the temperature. The reaction loss can be expressed as  $L_{reac} = 2\pi r_p dx \phi C \gamma_{reac}$ , where  $C$  is the concentration of the reactive species in the low-k film and  $\gamma_{reac}$  represents the reactivity between plasma radicals and reactive species in the low-k film. Similarly, the loss of plasma radicals due to radical recombination on the pore surface can be expressed as  $L_{recom} = 2\pi r_p dx \phi \gamma_{recom}$  with  $\gamma_{recom}$  representing the recombination rate of plasma radicals on the pore wall. The mass balance equation can now be expressed as:

$$\frac{d^2\phi}{dx^2} - \frac{2[C\gamma_{reac} + \gamma_{recom}]}{Dr_p} \phi = 0 \quad (4.11)$$

For low substrate temperatures, the recombination rate  $\gamma_{recom}$  can be assumed to be constant. Under the condition of fast diffusion but slow reaction or fast recombination but slow reaction and a boundary condition of  $\phi(x \rightarrow \infty) = 0$ , an approximate solution can be deduced for Eq. (4.11) as:

$$\phi(x) = \phi_0 e^{-\frac{x}{\zeta}}, \quad (4.12)$$

where  $\phi_0$  is the oxygen radical density at the dielectric surface and the oxygen radical penetration depth  $\zeta$  is defined as

$$\zeta = \sqrt{\frac{Dr_p}{2[C\gamma_{reac} + \gamma_{recom}]}}. \quad (4.13)$$

The oxygen radical penetration depth represents the Thiele modulus in other references. From the expression of Eq.(4.13), the oxygen radical penetration depth is increasing with the pore radius and inversely dependent on the reaction rate and

recombination rate. The models devolved in most references stopped at this point. However, the model developed so far did not consider the carbon depletion factor. As the reaction goes on, the carbon concentration reduces, accompanied by the reduction of total reaction rate. The radical recombination becomes dominant at the carbon depleted area, thereby changing the process kinetics. In order to describe the full picture of the kinetic process, the carbon evolution needs to be considered.

#### 4.2.2.2. *The further development of the Thiele Model with Carbon evolution*

To deduce the rate of carbon concentration change in the porous low k dielectric, we apply the kinetic equation:

$$\frac{\partial C(x,t)}{\partial t} \sim -\phi C \gamma_{\text{reac}} \quad (4.14)$$

This leads to an approximate solution of  $C(x,t) = C_0 e^{-\phi(x)\gamma_{\text{reac}}t}$ , where  $C_0$  is the carbon concentration in the pristine OSG. The depth of carbon depletion layer  $L$  can now be derived by setting  $C(x = L, t = t_0) = \frac{C_0}{\sqrt{2}}$ , and we obtain:

$$L = \sqrt{\frac{Dr_p}{2\left(\frac{C_0}{\sqrt{2}}\gamma_{\text{reac}} + \gamma_{\text{recom}}\right)}} \ln\left(\frac{\phi_0\gamma_{\text{reac}}t_0}{\ln\sqrt{2}}\right) = r_p \sqrt{\frac{48.5\sqrt{\frac{T}{M_A}}}{\frac{C_0}{\sqrt{2}}\gamma_{\text{reac}} + \gamma_{\text{recom}}}} \ln\left(\frac{\phi_0\gamma_{\text{reac}}t_0}{\ln\sqrt{2}}\right) \quad (4.15)$$

In this form, the model predicts that the depth of the carbon depletion layer ( $L$ ) for an oxidative plasma is directly proportional to the pore radius ( $r_p$ ) and modulated by the kinetics of the Knudson diffusion and the surface reaction and recombination of the radicals. Therefore, the model predicts that the effect of plasma damage can be reduced by decreasing the pore radius ( $r_p$ ), the oxygen radical density in vacuum ( $\phi_0$ ), the plasma treatment time ( $t_0$ ) or conversely, by increasing the carbon concentration of the OSG film ( $C_0$ ) or the surface recombination rate of oxygen radical on the pore wall ( $\gamma_{\text{recom}}$ ). Temperature is one of the kinetic parameters in Eq. 4.15. However, the effect of

temperature is difficult to quantify simply from the equation because the reaction and recombination rate are both temperature dependent.

The above description of the kinetic process established “the plasma altered layer model”, and the analysis included the effect of carbon depletion.

#### ***4.2.2.3. Predictions and Applications***

The plasma altered layered model as described by Equation (4.15) provides certain guidelines to minimize plasma damage, including:

- (1) Decreasing the pore size ( $r_p$ )
- (2) Decreasing the oxygen radical density ( $\phi_0$ )
- (3) Decreasing the treatment time ( $t_0$ )
- (4) Increasing the carbon concentration ( $C_0$ )
- (5) Increasing the recombination rate ( $\gamma_{recom}$ )

The #2 and #3 approaches are difficult to apply because reducing the radical density and the treatment time also decrease the ability of PR removal. Approaches #1 and #4 involve the low-k material engineering while Approach #5 can be possibly achieved by UV excitation, where the UV wavelengths need to be above 200 nm to avoid radiation damage.

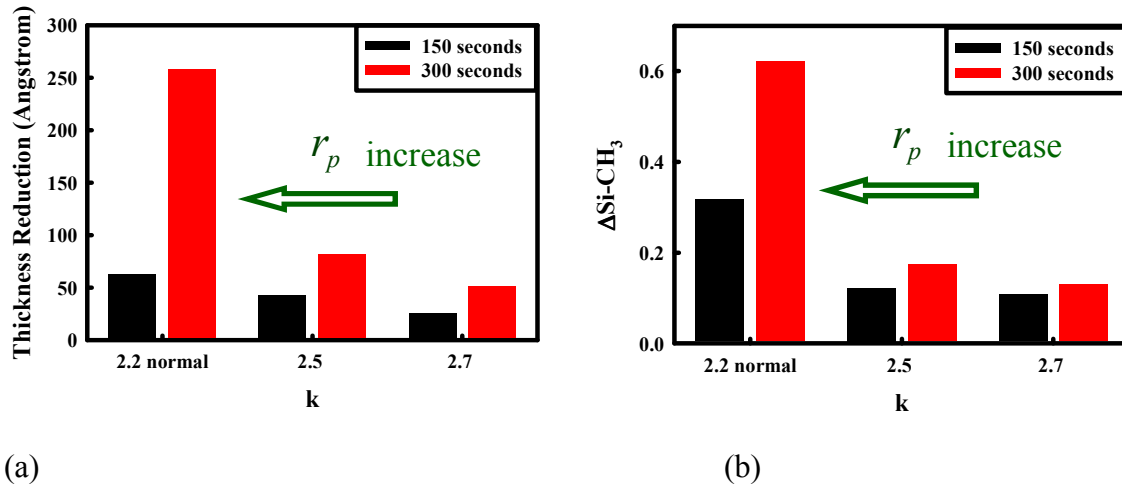


Figure 4-12: (a) Thickness reduction and (b) methyl depletion on plasma damaged SiCOH films with different k value. (courtesy of Hualiang Shi)

One example of using these approaches to reduce plasma damage is shown in Figure 4-12. The plasma induced damage increases with the decrease of the dielectric constant. One of the main reasons in damage reduction can be attributed to the increase pore radius ( $r_p|_{2.2} > r_p|_{2.5} > r_p|_{2.7}$ ).

#### 4.2.3. Monte Carlo simulations of radical kinetics

Considering the radical kinetics process described in Section 4.2.1., a Monte-Carlo program was developed using the Matlab software to simulate the profile of carbon concentration inside porous low-k dielectrics. The Monte Carlo method has several advantages over the analytical model described in Section 4.2.2. First, in the analytical model, many simplifications are made in the derivation in order to get the analytical solution. Second, the Monte Carlo code can easily visualize the carbon profile which would be difficult based on the analytical model. Third, the Knudsen diffusion condition used in the analytical mode is no longer applicable when the pore size shrinks down to about 1 nm, which is common for the nano-pore p-SiCOH developed most recently. As

indicated in Figure 4-13, a single file diffusion (SFD) condition is used instead for the low-k material with a pore size too small to allow more than one radical to pass. A complex modification for the analytical model is needed for SFD condition while this issue can be easily solved in the Monte Carlo code.

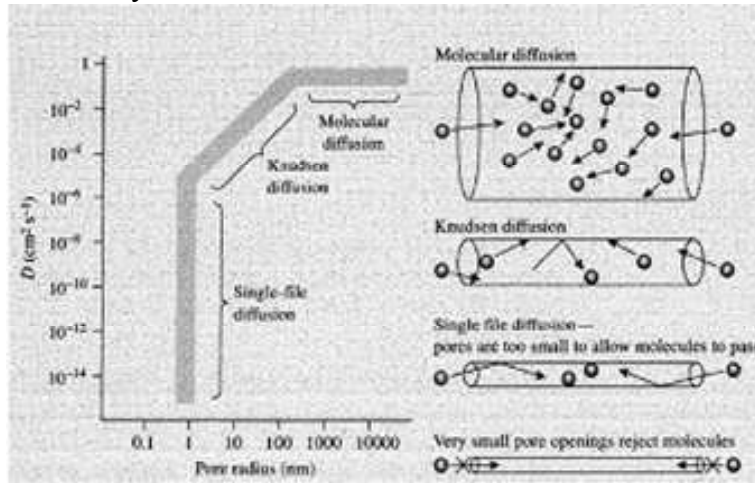


Figure 4-13: Diffusion mode in a pipe structure.

As indicated in Figure 4-10(b), the pore structures in porous low-k materials can be simplified as many long cylindrical tubes. In the Monte Carlo code, the pore walls of those tubes are unfolded into a 2 dimensional array, which is randomly filled with Si, C, O and H atoms in their stoichiometric proportions. This Monte Carlo model considers diffusion in an atomic view where the O radicals, or the probe O atoms, diffuse one-dimensionally from the top of the array towards the bottom. This describes the diffusion process as a random walk process instead of based on the phenomenological density gradient. The reaction process and the recombination process are described by reaction and recombination probabilities. As shown in the Monte-Carlo simulation flowchart in Figure 4-14, the incoming O atom recombines or reacts with C atom. Otherwise, it will have a chance to diffuse to the next level to start a new round of

interaction. The decisions are made according the probabilities of recombination, reaction and diffusion, which are the three main adjustable parameters. This model treat methyl bond simply as C atom. The number of probe O atoms (the incoming flux) are set to be consistent with the plasma density and treatment time in the plasma process. Though the real numbers of the recombination or reaction rate are unknown, we can qualitatively simulate the process by adjusting the parameters and compare the trend and the shape of the profile to experimental results in order to validate the model.

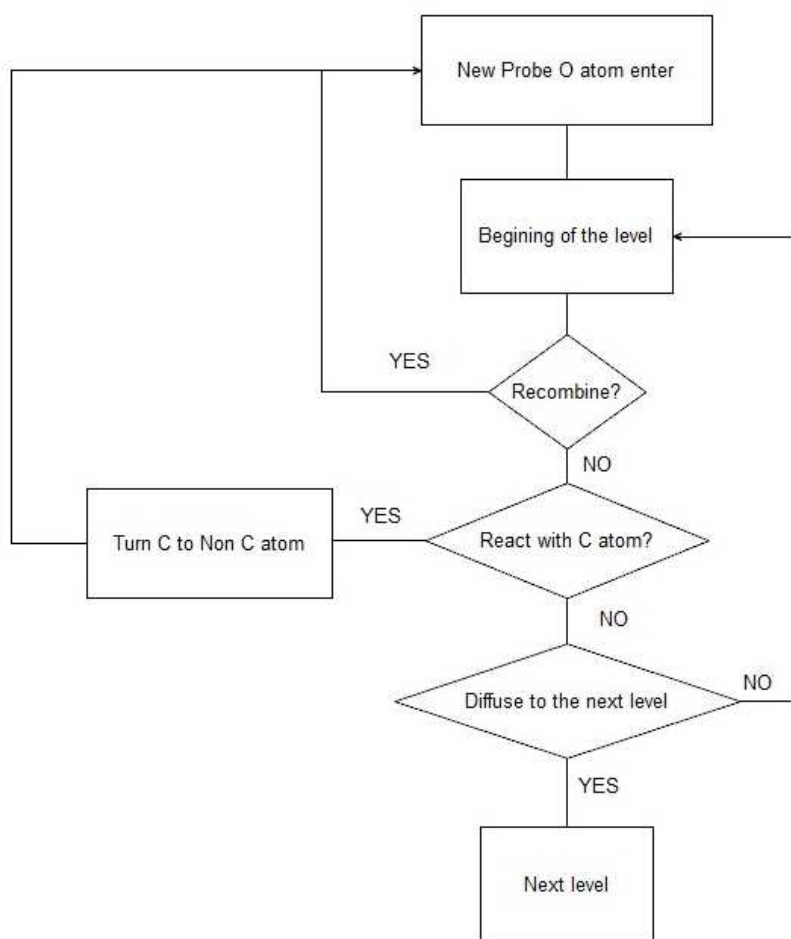


Figure 4-14: the flowchart of the Monte Carlo simulation of the radical kinetics.

The semi-2D simulations create the carbon profiles of the damaged low-k as shown in Figure 4-15(c) where the carbon profiles are created by the Monte Carlo simulation and the results are close to the experimental carbon profiles measured by TOF-SIMS. Overall, the low-k film with high carbon concentration has less damage than the low carbon film, which is consistent with the experimental results and the prediction made by the analytical model.

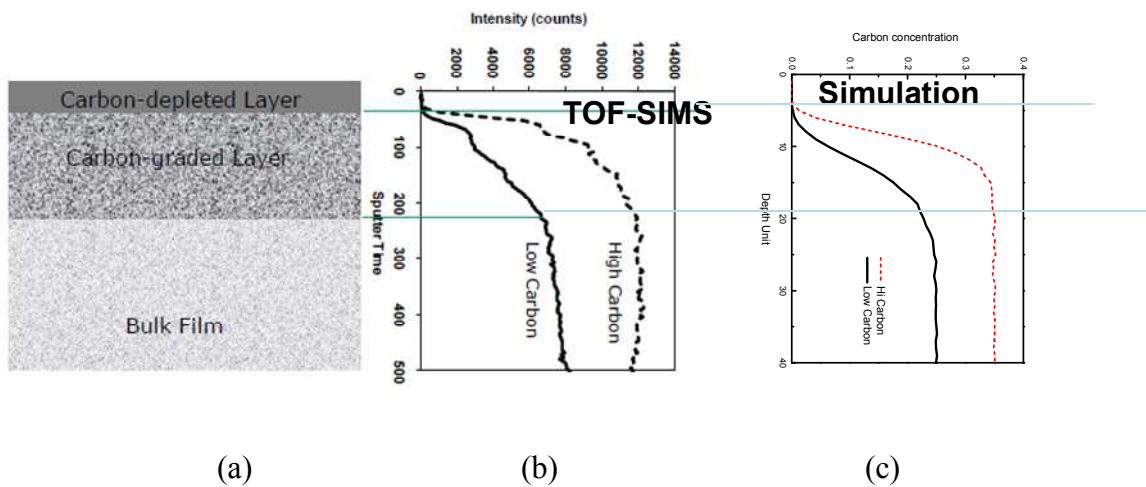
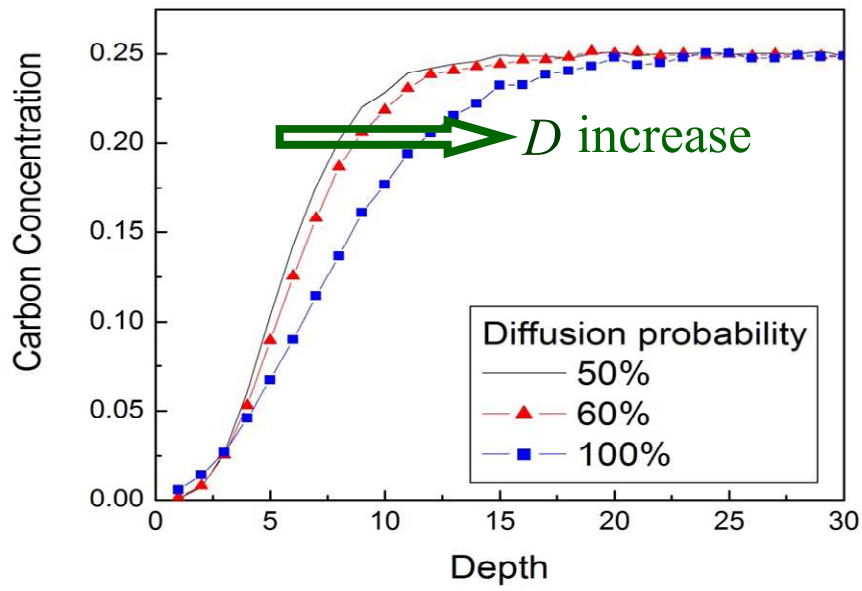


Figure 4-15: Effect of carbon concentration on the carbon depletion profiles.(a) schematic diagram of the crosssection view of plasma damaged pSiCOH film; (b) carbon element profile by TOF-SIMS; (c) carbon profile by Monte Carlo simulation.

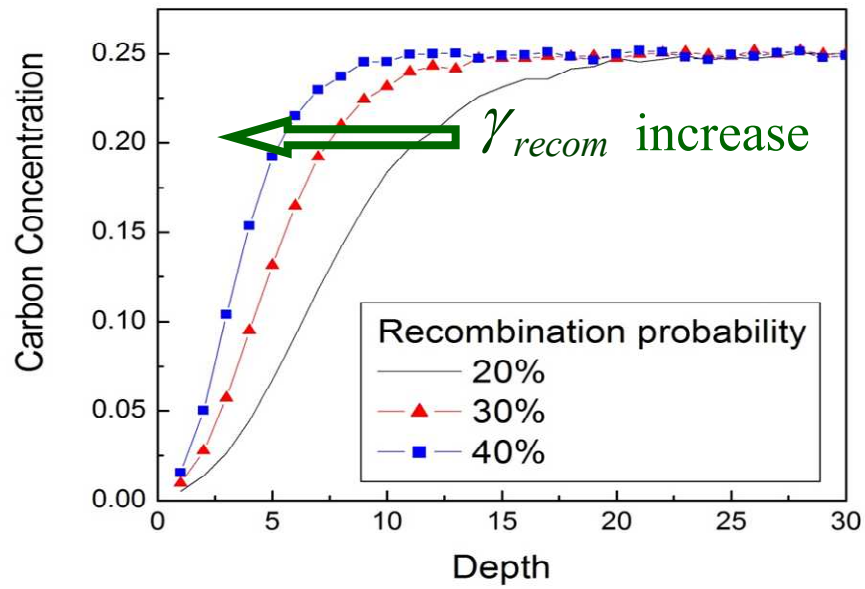
As shown in Figure 4-16, with the increase of radical diffusivity, the depth of carbon depletion layer is increased. In contrast, with an increase in the surface recombination rate, the depth of carbon depletion layer is reduced. Both of these numerical simulation results were consistent with the predictions of the analytical model.

Figure 4-17 (a) shows the simulation result of carbon concentration in the whole film vs treatment time. The speed of carbon depletion was slowed down by time. At the beginning of the plasma process, where there are sufficient carbon groups to react with

the oxygen radicals, the chemical reactions are dominant in the kinetic process. As the carbon concentration reduces, the recombination becomes dominant. The slowing down of carbon depletion rate is consistent with the experimental observations in Figs.14-17(a) and 14-17(b). In the actual plasma process, the diffusion rate will decrease as the chemical reaction induces pore collapse and densification of the low-k film.

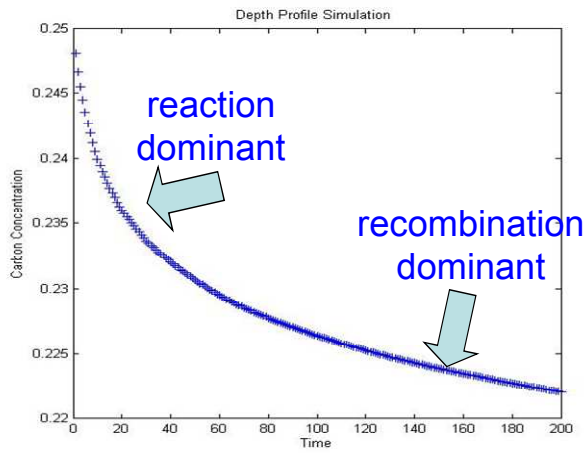


(a)

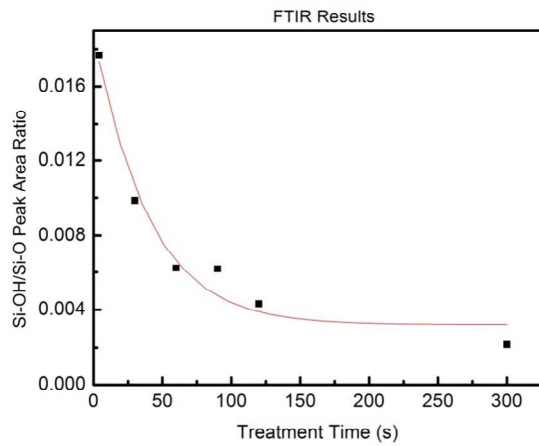


(b)

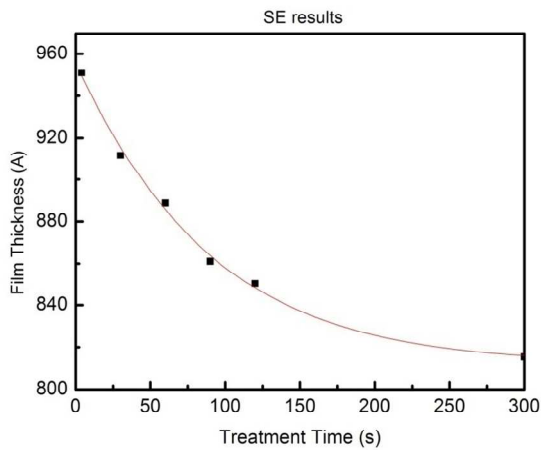
Figure 4-16: Monte-Carlo simulations of the depth profile of carbon concentration as a function of (a) diffusion probability and (b) recombination probability.



(a)



(b)



(c)

Figure 4-17: Time evolution of the carbon concentration. (a) Monte Carlo simulation; Experimental (b)methyl peak and (c) thickness vs plasma treatment time.

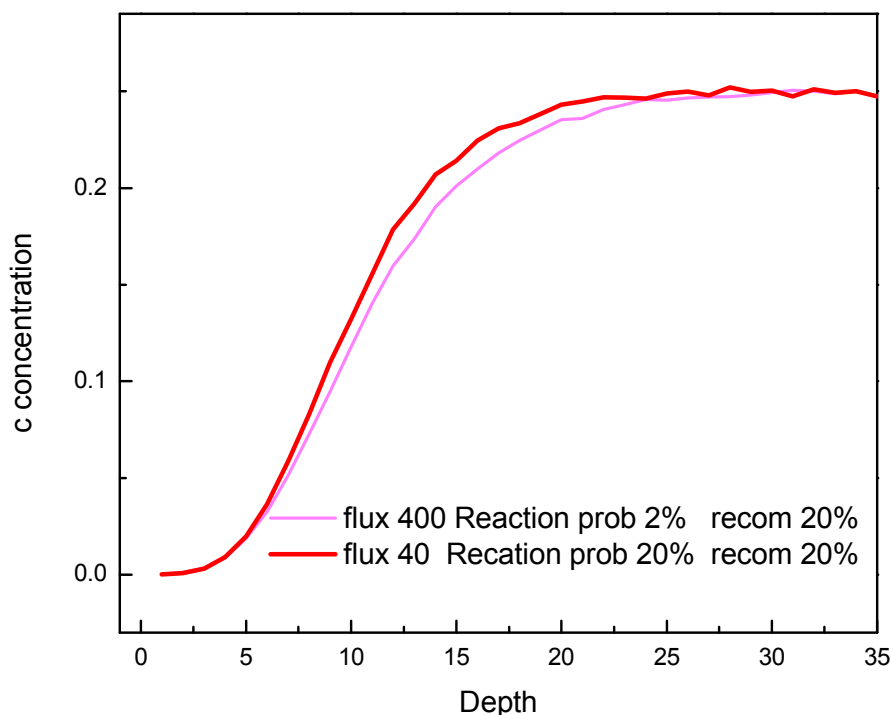


Figure 4-18: The influence of the carbon depth profile by the relative reaction probability and the recombination probability.

The reaction rate and the recombination rate in the radical low-k interaction are difficult to measure experimentally. However, the Monte Carlo model suggests that the ratio of reaction rate and recombination rate can be extracted to be consistent to the experimentally measured carbon depth profile. When the reaction probability is much larger than recombination probability, the profile will be steep as the carbon will be consumed layer by layer. When the reaction probability is much smaller than recombination probability, the carbon depth profile will be flatter since it is determined by the oxygen radical density depth profile.

#### 4.2.4. Radical diffusion in patterned structure

The analytical method used in Section 4.2.2. can also be applied to study the radical kinetics in the low-k structures with geometrical patterns and covered by a hard mask (HM) or a capping layer. Hard masks (e.g. TiN, TaN) are commonly used in low-k patterning to provide high selectivity etching. In many cases, a capping layer (e.g. SiO<sub>2</sub>) is placed between the ULK material and the hard mask to promote adhesion and reduce CTE mismatch. The radical kinetics can be used to investigate the influence of hard mask material properties and pattern geometries on low-k damage.

##### 4.2.4.1. Analytical results for patterned structures

As schematically shown in Figure 4-19, on the basis of radical diffusion ( $D$ ), reaction ( $\gamma_{\text{reac}}^*$ ), and surface recombination ( $\gamma_{\text{recom}}$ ) inside the trench of patterned low-k structure, the kinetics of mass transport of plasma radicals inside the trench can be formulated. Here  $\gamma_{\text{reac}}^*$  is the reaction rate of the oxygen radicals and is proportional to the carbon concentration inside the hardmask and ULK dielectrics. Because the mean free path of the plasma radicals is much larger than the trench width ( $W$ ) (~several hundred nm) and trench length ( $L$ ) (in the order of tens or hundreds of  $\mu\text{m}$ ), the Knudsen diffusivity dominates the mass transport with

$$r_p \approx \frac{W + L}{4} \quad (4.16)$$

The mass balance of oxygen radicals inside the elemental volume  $dV = WLdx$  was also represented by the following equations where the inward flux, outward flux, reaction loss, and recombination loss can be expressed as

$$F_{\text{In}}|_x = -WLD \frac{d\phi}{dx} \Big|_x \quad (4.17)$$

$$F_{\text{Out}}|_{x+dx} = -WLD \frac{d\phi}{dx} \Big|_{x+dx} \quad (4.18)$$

$$L_{\text{reac}} = 2(L + W)dx\phi\gamma_{\text{reac}}^* \quad (4.19)$$

$$L_{\text{recom}} = 2(L + W)dx\phi\gamma_{\text{recom}} \quad (4.20)$$

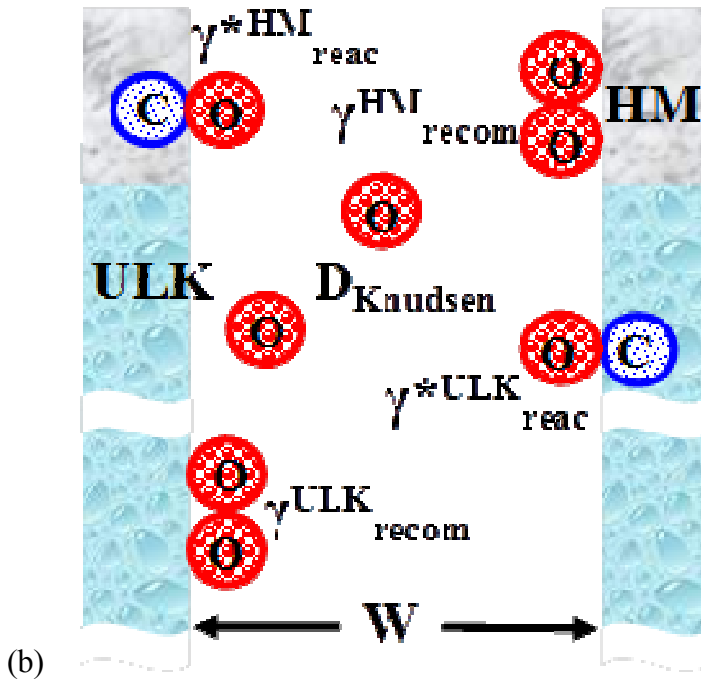
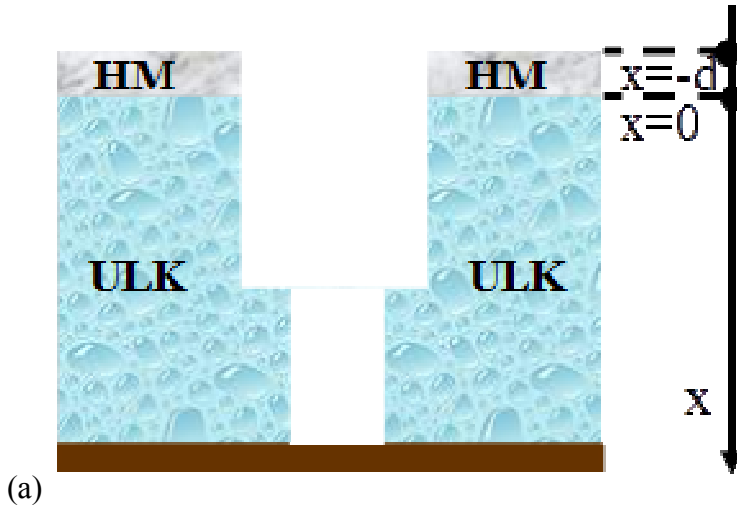


Figure 4-19. (a) Sidewall damage of patterned low-k structure and (b) kinetics of radical diffusion, reaction, and recombination inside trench.

The mass balance of oxygen radicals inside the elemental volume  $dV = WLdx$  is represented by Eq. (4.10). The inward flux, outward flux, reaction loss, and recombination loss can be expressed as

$$F_{In}|_x = -WLD \frac{d\phi}{dx} \Big|_x \quad (4.21)$$

$$F_{Out}|_{x+dx} = -WLD \frac{d\phi}{dx} \Big|_{x+dx} \quad (4.22)$$

$$L_{reac} = 2(L + W)dx\phi\gamma_{reac}^* \quad (4.23)$$

$$L_{recom} = 2(L + W)dx\phi\gamma_{recom} \quad (4.24)$$

For simplicity, consider only two regions  $\phi_i (i = 1, 2)$ . where the mass balance of the plasma radicals can be expressed as:

$$\frac{d^2\phi_i}{dx^2} = \frac{\phi_i}{\lambda_i^2} \quad (4.25)$$

$$\lambda_i = \sqrt{\frac{D}{2\left[\frac{1}{W} + \frac{1}{L}\right]\left[\gamma_{reac}^* + \gamma_{recom}^i\right]}} = \sqrt{\frac{97WL\sqrt{\frac{T}{M}}}{8\left[\gamma_{reac}^* + \gamma_{recom}^i\right]}} \quad (4.26)$$

where the region  $\phi_1$  is for  $-d < x < 0$ , and the hardmask region has a thickness  $d$  and the region  $\phi_2$  for the low-k region  $0 < x < \infty$  extending below the hardmask.  $\lambda_i$  is the diffusion distance of the radical, which increases with  $W$  and  $L$  and decreases with the increase of  $\gamma_{reac}^*$ ,  $\gamma_{recom}^i$ , and  $M$ . The mass balance equation can

be solved by using the following boundary conditions:

$$\phi_1(x = -d) = \phi_0$$

$$\phi_1(x = 0) = \phi_2(x = 0) \quad (4.27)$$

$$\frac{d\phi_1}{dx} \Big|_{x=0} = \frac{d\phi_2}{dx} \Big|_{x=0} \quad (4.28)$$

$$\phi_2(x \rightarrow \infty) = 0 \quad (4.29)$$

where  $\phi_0$  is the oxygen radical density at the wafer surface. This yields the following solutions:

$$\phi_1(x) = \frac{(\lambda_2 + \lambda_1)\phi_0 e^{\frac{x}{\lambda_1}} + (\lambda_2 - \lambda_1)\phi_0 e^{\frac{x}{\lambda_2}}}{(\lambda_2 + \lambda_1)e^{\frac{d}{\lambda_1}} + (\lambda_2 - \lambda_1)e^{\frac{d}{\lambda_2}}} \quad (4.30)$$

$$\phi_2(x) = \frac{2\lambda_2\phi_0 e^{\frac{x}{\lambda_2}}}{(\lambda_2 + \lambda_1)e^{\frac{d}{\lambda_1}} + (\lambda_2 - \lambda_1)e^{\frac{d}{\lambda_2}}} \quad (4.31)$$

Two extreme cases are examined as follows:

(1) If there is no hardmask ( $d = 0$ ),

$$\phi_2(x) = \phi_0 e^{\frac{-x}{\lambda_2}}. \quad (4.32)$$

(2) If the hardmask has the similar property as the low-k dielectrics ( $\lambda_1 = \lambda_2$ ),

$$\phi_2(x) = \phi_0 e^{\frac{x-d}{\lambda_1}}. \quad (4.33)$$

In addition, by taking the derivative of the hardmask thickness ( $d$ ) on both sides of equation 21, the following relationship can be derived:

$$\frac{\partial \phi_2(x)}{\partial d} = \frac{2\phi_0\lambda_2 e^{\frac{-x}{\lambda_2}} \left[ (\lambda_2 - \lambda_1)e^{\frac{-d}{\lambda_1}} - (\lambda_2 + \lambda_1)e^{\frac{d}{\lambda_1}} \right]}{\lambda_1 \left[ (\lambda_2 + \lambda_1)e^{\frac{d}{\lambda_1}} + (\lambda_2 - \lambda_1)e^{\frac{-d}{\lambda_1}} \right]^2} < 0 \quad (4.34)$$

Equation (4.34) indicates that oxygen radical density inside the low-k region  $\phi_2(x)$  is a monotonic function of hardmask thickness ( $d$ ). By increasing the hardmask thickness, the oxygen radical density impinged on the ULK can be reduced. In Figure 4-20, by assuming  $\lambda_1 = \lambda_2 = 100nm$ , the effect of hardmask thickness was examined. The oxygen radical density in low-k region inside trench ( $\phi_2(x)$ ) was normalized by the oxygen radical density at the wafer surface ( $\phi_0$ ). The results showed that there were more oxygen radicals at the trench top than at the trench bottom. With the hardmask thickness

increasing from 0nm, to 60nm, to 100nm, to 150nm, the oxygen radical density in low-k region inside the trench decreases. Previous studies showed that oxidative plasma induced damage is proportional to the oxygen radical density. Hence, this model predicts that plasma damage at the trench top is more severe than that at the trench bottom. At the same time, the sidewall damage can be reduced by increasing the hardmask thickness. In addition, Liu *et al.* reported that when the hardmask thickness increased from 60nm, to 100nm, to 150nm, the plasma damage to ULK decreased[76]. All of these findings are consistent with the model's predictions.

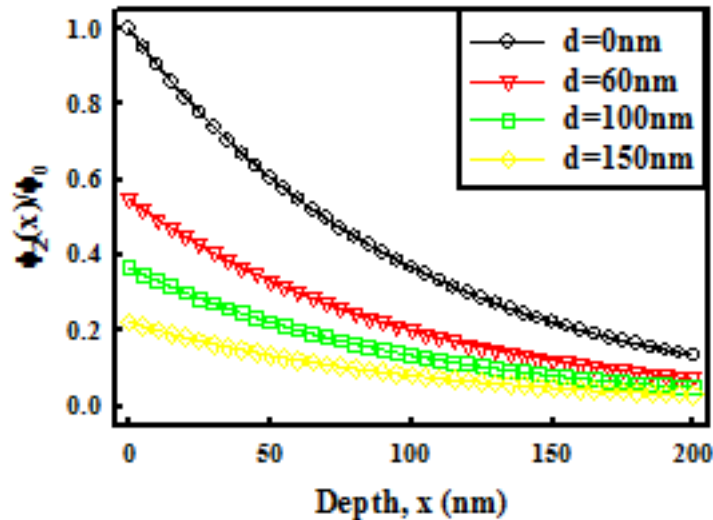


Figure 4-20: Oxygen radical density distribution in low-k region inside the trench of patterned low-k structure.

In Figure 4-21, the oxygen radical density at two positions ( $x=0\text{nm}$  and  $x=100\text{nm}$ ) in the low-k region inside the trench were studied with two hardmask thicknesses (60nm and 150nm). The oxygen radical density in low-k region inside the trench ( $\phi_2(x)$ ) was normalized by the oxygen radical density at the wafer surface ( $\phi_0$ ). The contour plots show that the oxygen radical density impinging on the ULK dielectric decreases with  $\lambda_1$

and  $\lambda_2$ . Hence, plasma damage to ULK dielectric can be reduced by decreasing  $\lambda_1$  and  $\lambda_2$ . This can be achieved by reducing the trench width and the trench length and by increasing the oxygen reaction rate, the recombination rate and the molecular weight.

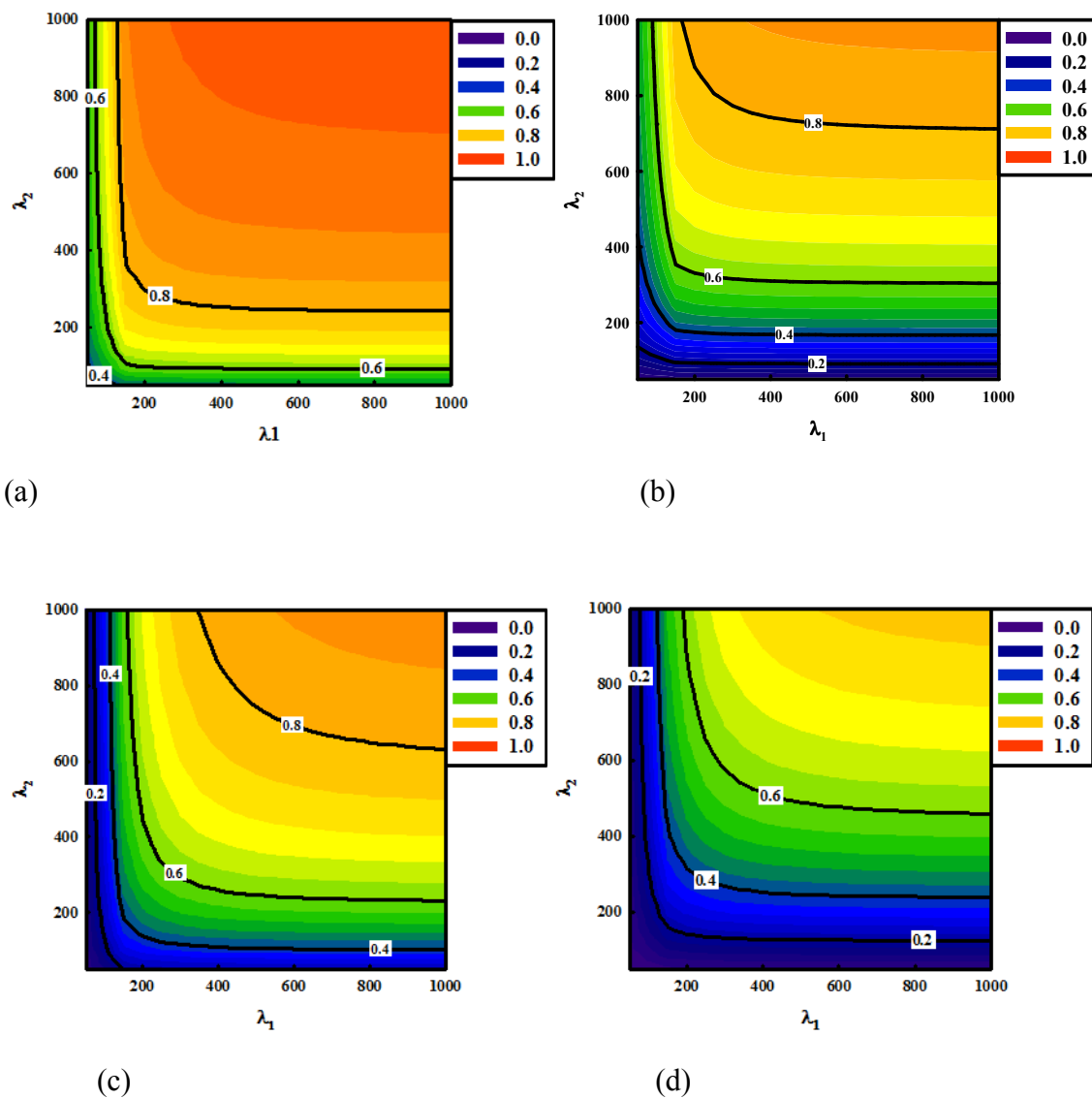


Figure 4-21: The contour plots of oxygen radical density distributions in low-k region inside trench of patterned low-k structure (a)  $x=0\text{nm}$ ,  $d=60\text{nm}$ , (b)  $x=100\text{nm}$ ,  $d=60\text{nm}$ , (c)  $x=0\text{nm}$ ,  $d=150\text{nm}$ , and (d)  $x=100\text{nm}$ ,  $d=150\text{nm}$ .

#### 4.2.4.2. Experiments

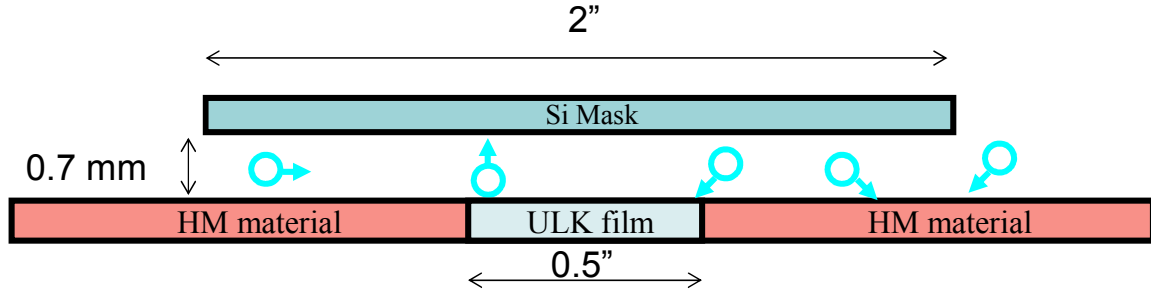


Figure 4-22: The experimental set up of gap structure with a Si mask to simulate the radical kinetics in a patterned structure with a hardmask.

The damage to patterned low-k is very difficult to quantify due to the size limit of the characterization tools. In order to use FTIR and SE methods to study the radical damage of pattern low-k structure, a gap structure was built to simulate the radical kinetics in the trench. The experimental setup is illustrated in Figure 4-22, where a 1” wide and 2” long silicon mask is placed over the low-k with a gap spacing of 0.7mm. The mask is supported and sealed at the long side with Si spacers. Radical species can diffuse into the gap between mask and low-k dielectrics through the two ends of the gap. Different hardmask materials, including SiO<sub>2</sub>, High Carbon doping SiCOH, Low Carbon doping SiCOH, and TiN, are placed at both ends to simulate the hard mask effect.

The type of diffusion is determined by the radical mean free path ( $\lambda$ ) and the size of the gap height ( $h$ ) and width ( $w$ ). For simplicity, the effective radius was defined as

$$\bar{r} = \frac{h+w}{4} \quad (4.35)$$

If  $\lambda > 2\bar{r}$ , the molecules will collide with the wall such as the surfaces of optical mask and low-k dielectrics instead of with one another. Under this situation, the Knudsen diffusion dominates.

When  $\lambda < 2\bar{r}$ , the molecules will collide with each other instead of with the wall. As a result, the molecular diffusion (or Fickian diffusion) dominates. When  $\lambda \approx 2\bar{r}$ , both molecule-molecule and molecule-wall collisions are important. So let us first estimate the radical mean free path. If the atom diameter is 0.2 nm, the collision area will be

$$\sigma = \pi \times (0.2)^2 = 1.26 \times 10^{-15} \text{ cm}^2 \quad (4.36)$$

Assuming the chamber pressure is 5 mtorr and the temperature is 303.15 K, the number density of atoms can be calculated by using the perfect gas law

$$n = \frac{P}{k \cdot T} = \frac{5 \times 0.133}{1.38 \times 10^{-23} \times 303.15} = 1.59 \times 10^{14} \text{ cm}^{-3} \quad (4.37)$$

The radical mean free path will be

$$\lambda = \frac{1}{\sigma \cdot n} = \frac{1}{1.26 \times 10^{-15} \times 1.59 \times 10^{14}} = 5 \text{ cm} \quad (4.38)$$

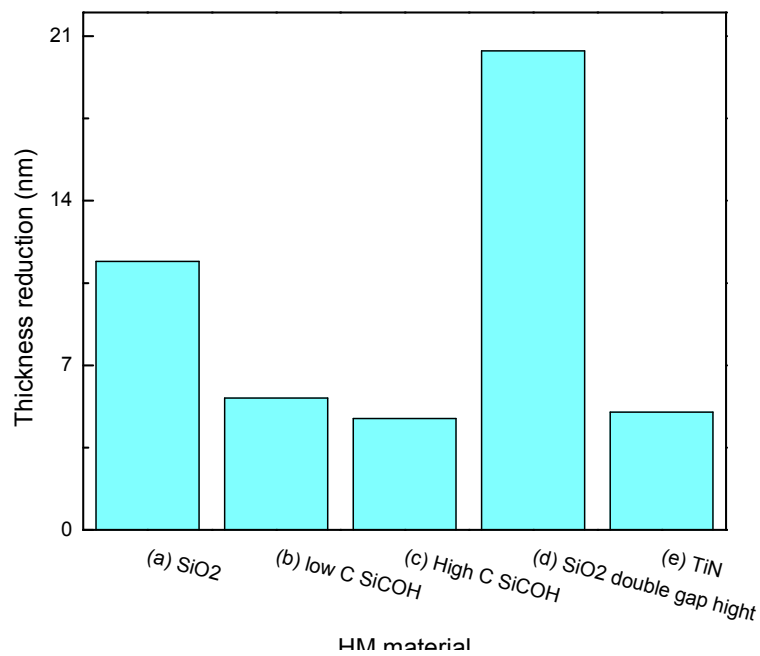
Under the current experimental conditions,

$$h \approx 0.1 \text{ cm}, w \approx 2.5 \text{ cm} \quad (4.39)$$

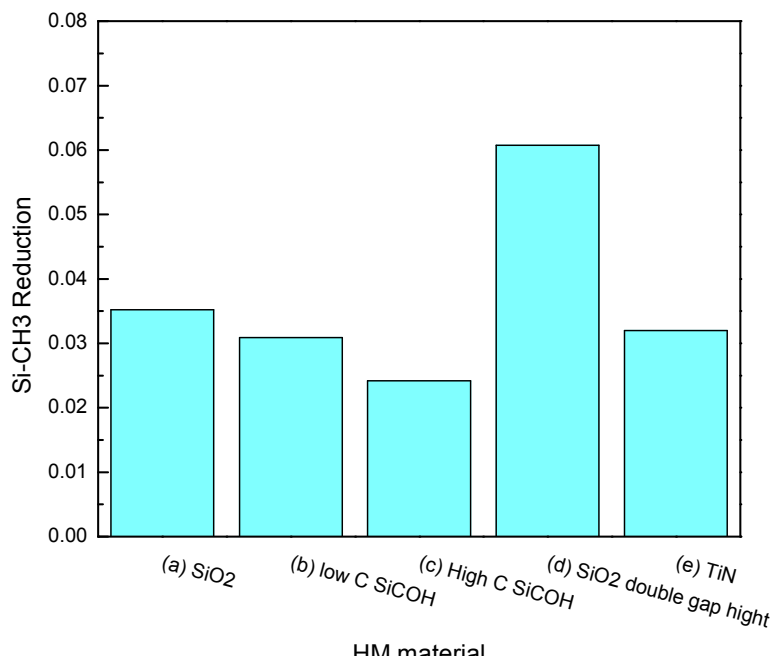
So the effective radius is

$$\bar{r} = \frac{0.1 + 2.5}{4} = 0.65 \text{ cm} \quad (4.40)$$

In this case,  $\lambda > 2\bar{r}$  corresponds to the setup in our experiment where the Knudsen diffusion dominates the radical diffusion inside the gap. Therefore, the analysis described in the previous section (Section 4.2.4.1.) can be applied to the study using this gap structure despite its large geometry.



(a)



(b)

Figure 4-23: Damage formation by O radicals to the ULK with different hardmask materials (a) thickness reduction, (b) methyl depletion

Figure 4-23 shows the thickness reduction and methyl depletion of the low-k film with different hard mask materials after the same oxygen plasma treatment (ICP 200 W, bias 100 W, 5 mtorr, 20 sccm). High carbon doping film (the HM material) has the highest carbon concentration, resulting in the highest reaction rate and the lowest radical diffusion distance (defined by Eq. 4.26). In this case, the material suffers the least damage. The low carbon SiCOH contains less carbon, leading to a lower reaction rate and a higher  $\lambda$ . Thus the material suffers more damage than the one with high carbon film as the hardmask. In general,  $\text{SO}_2$  does not react with oxygen radicals at all, resulting in a higher damage level. When the gap height doubled in sample (d),  $\lambda$  also increased, thereby increasing the radical damage. Overall, these results are in good agreement with the model predictions in the previous section.

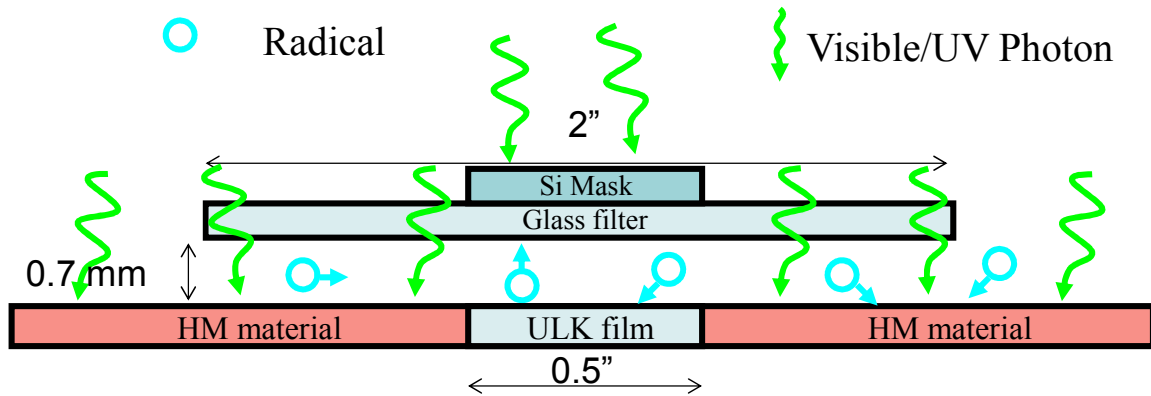


Figure 4-24: The experiment set up of gap structure with Si mask and optical filters to simulate the radical kinetics in a patterned structure with hardmask.

In order to study the effect of UV/VUV photon on the recombination rate, a modified gap structure was built as illustrated in Figure 4-24. The Si mask was replaced by a glass filter of MgF2 or fused silica. A small Si mask was placed on the filter directly above the ULK film. In this way, photons can reach the HM materials but not impinging

on the ULK film. The photon induced effect on a non-carbon-containing material (i.e. SiO<sub>2</sub>) can be investigated.

With VUV photons under the MgF<sub>2</sub> mask, the recombination rate should be higher due to the photon excitation, resulting in a lower radical density and lower damage on the low-k film in the middle. Instead, the result in Figure 4-25 shows the opposite. This is most likely due to the photo-dissociation of oxygen molecules by VUV radiation, which supported the model analysis presented in Section 4.1.3. (See the section on Roles of the photons).

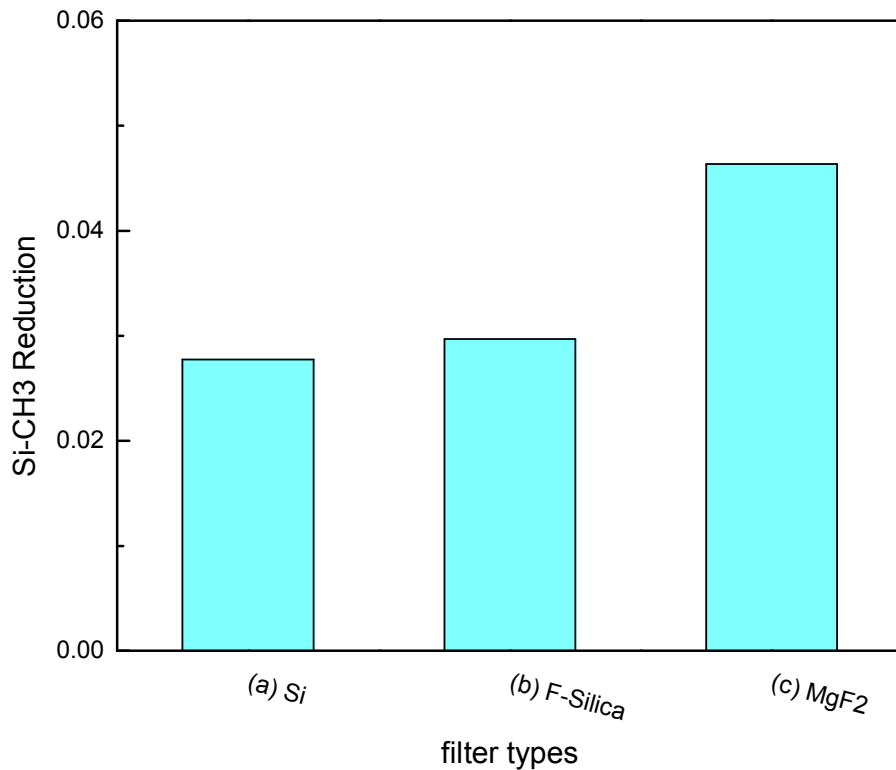


Figure 4-25: Plasma damage produced by O radicals to the ULK with a photo excited SiO<sub>2</sub> hardmask.

### 4.3. SUMMARY

The effects of ions, photons, and radicals were separately investigated using an on-water filter system equipped with four different glass filters and a Si masks. Ion bombardment was found to reduce plasma damage by creating a surface densification layer. Vacuum-ultraviolet (VUV) photon radiation was found to enhance the oxidative plasma induced damage. The energy threshold of this enhancement was narrowed down to around 185nm.

The radical low-k interaction was investigated by examining the kinetic process of damage formation taking into account the oxygen radical diffusion, recombination and reaction. An analytical model based on this kinetic process was formulated and an approximate analytical solution of plasma altered layer was deduced. This analysis provides general guidelines to reduce oxidative plasma damage. The depth of carbon depletion layer can be reduced by decreasing pore radius, plasma treatment time, and oxygen radical concentration and by increasing carbon concentration inside ULK dielectric and the oxygen surface recombination rate.

A Monte Carlo computer simulation computer program was developed based on the plasma altered layer model. The simulation result confirmed the trends predicted by the analytical model. The time evolution of the simulation predicted the slow-down of the rate of carbon depletion, which was confirmed by experimental results.

The altered layer model was extended to examine the radical density distribution in a patterned low-k structure. The model predicted that the sidewall plasma damage can be reduced by optimizing the geometry of the patterned structure including an increase of the hardmask thickness or by increasing the rates of oxygen reaction and recombination. The result of the gap structure experiments were in good agreement with the model predictions.

## Chapter 5: Dielectric Recovery

As the feature size of integrated circuits continues to scale down, the damage of low-k material became more critical. Figure 5-1 demonstrates the contribution of the damaged layer to the total effective capacitance versus half-pitch low-k thickness. Considering the high dielectric constant damaged layer due to moisture absorption, the damaged low-k layer will give up the dielectric advantage over silicon dioxide quickly, as the total low-k thickness reduces. In chapter 4, we try to understand the mechanism of the plasma damage process in order to minimize the depth of the damaged layer. However, damage minimization faces much higher challenges on a smaller scale. For example, even if a low-k film was damaged for 5 nm, it loses the advantage over oxide at 20nm half pitch (thickness).

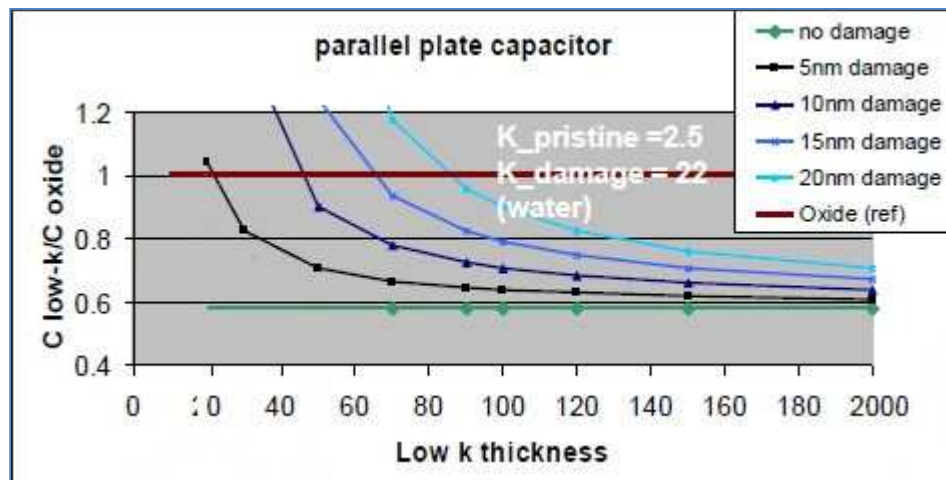


Figure 5-1: The simulated effective dielectric constant with a damaged layer versus half-pitch low-k thickness.[77]

In industry, the problem of the damage layer was usually solved by a subsequent diluted hydrogen fluoride (DHF) dipping process which removes the damage layer and retains the property of the remaining low-k materials. The DHF process can also create a

smooth surface for the following barrier layer deposition and thus improve the electrical properties. This process works well at larger pitch sizes and small low-k damage depths. However, at small pitch sizes and narrow trenches, DHF removal of damage low-k will create undercuts below the edge of the cap layer (Figure 5-2), creating issues like the mechanical collapse of the cap layer, and the uneven distribution of barrier layer and metal fill.

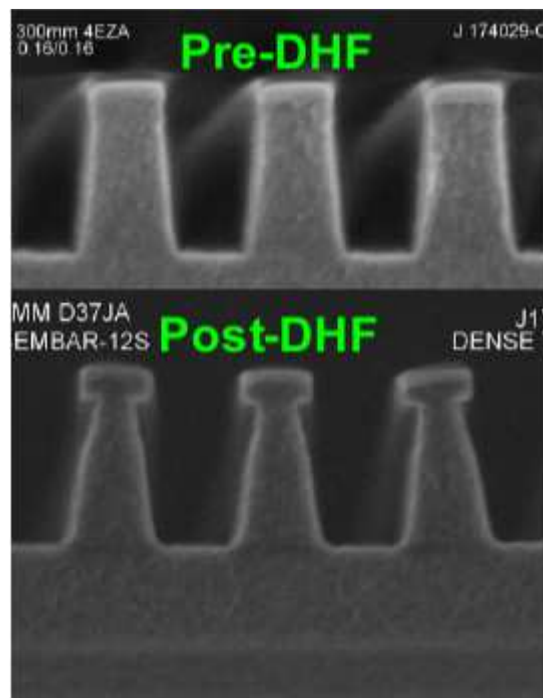


Figure 5-2: SEM images of ULK film undercut below the edge of the cap layer after DHF dipping. Damage-driven undercut with ULK films has made subsequent metal fill very difficult.[78]

Dielectric recovery of the damaged low-k material, as a result, becomes very critical for implementation of porous low-k material at feature size beyond 45nm, despite its costs and intrinsic issues. It has stimulated extensive interests in its process development and mechanism study.

The causes of low-k damage lead to the paths of dielectric recovery. As we discussed in chapter one, the plasma damage in porous low-k dielectrics consists of changes in the bonding characteristic and densification of the low-k material. The main causes of the dielectric degradation lie in the changes in the bonding characteristics, which are observed as a loss of the low dipole moment methyl bonds and an increase of the high dipole moments bonds, such as silanol and the physisorbed water ( $\epsilon=80$ ). Thus the development strategies followed the causes of the dielectric degradation in two basic approaches: one is to restore the methyl groups by plasma beam treatment or by applying silylation agents such as TMCS and DMDCS, and the other is to apply UV irradiation together with thermal treatments to eliminate the -OH bond and the physisorbed water.

In this chapter, the results on dielectric recovery through silylation and UV treatments are discussed. First, the experimental setup for CVD silylation process and UV radiation process in our lab are described. Second, silylation and UV treatments conducted in this setup are discussed separately in section 5.2 and 5.3. Section 5.2 will also discuss the supercritical carbon dioxide silylation process; section 5.3 will include the study on pure thermal treatment and its difference with UV process. This is followed by discussion on results from experiments combining silylation and UV process in section 5.4. Finally, the future trend in the study of dielectric recovery will be described.

### **5.1. EXPERIMENTAL SETUPS**

In this study, an integrated chamber was built to investigate the effect of low-k dielectric recovery via silylation and UV radiation. The setup is shown in the schematic diagram in Figure 5-3, where the main components of this system include a temperature controlled sample stage, a vapor silylation agent supplying system, a UV light source and a vacuum system. The main chamber is based on a stainless steel cylinder of 10 inch in

diameter which was built by MKS instruments. The sample stage, placed in the center of the chamber, was homemade with a titanium sample holder clamped on a Watlow thick film conduction heater. The surface of this stage can be heated up to 500°C. Its temperature was monitored by thermal couples and was controlled by an external PID controller. Vapor phase silylation agents were brought in by carrier gas through a bubbler and heated pipelines. The silylation gas feeding system will be discussed in detail later in section 5.2.2. A board band UV lamp was connected with the sample chamber through a quartz window. The UV lamp (model F600s with a H+ bulb) was supplied by Fusion UV systems Inc. This high power UV lamp was air cooled by a blower and venting system. Finally, the chamber was connected to a vacuum system that can maintain the vacuum level up to  $10^{-6}$  torr. A photograph of this system is shown in Figure 5-4.

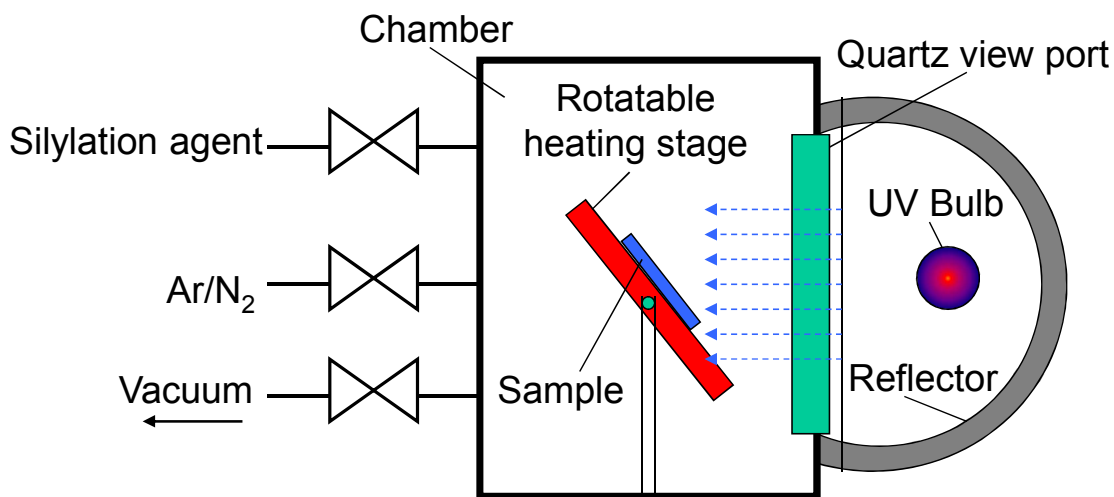


Figure 5-3: The schematic diagram of the silylation and UV treatment chamber.

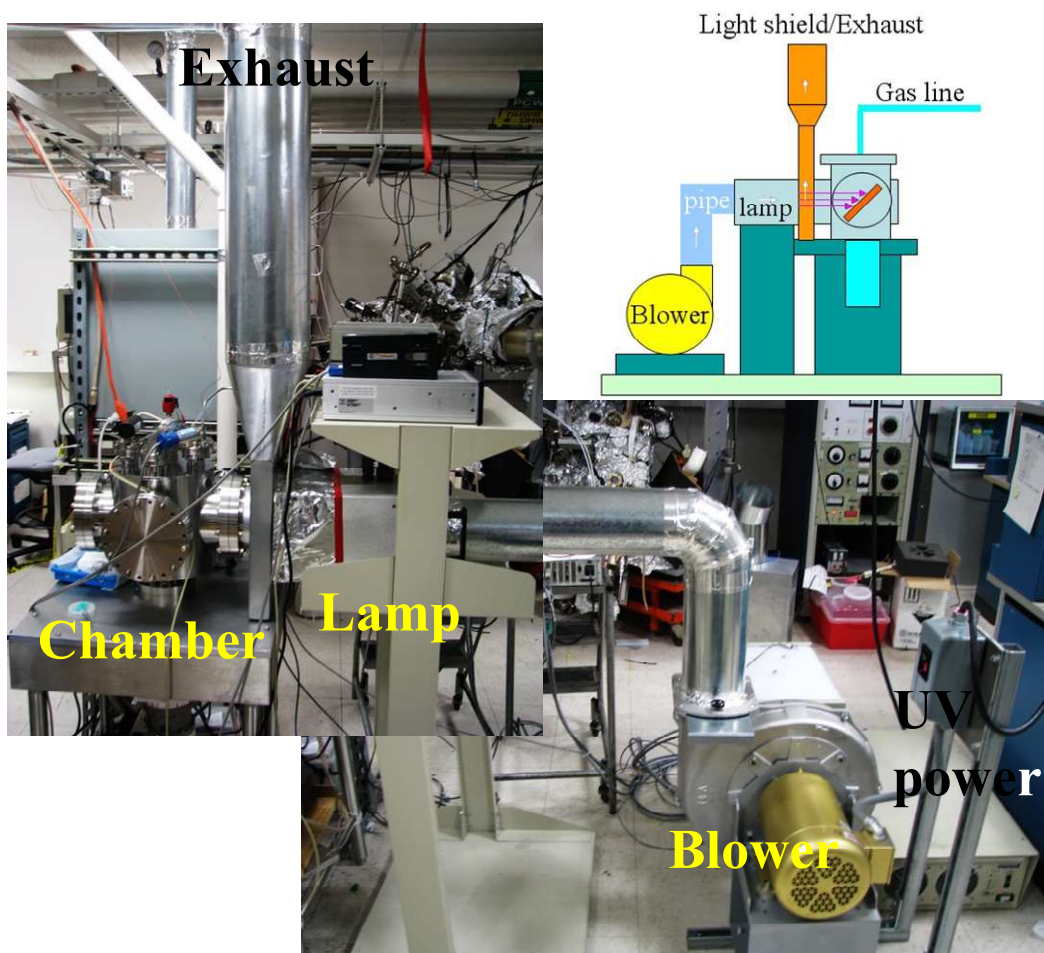


Figure 5-4: The schematic diagram and photograph of the silylation and UV treatment system.

The unique design of this system enables us to study the silylation and UV thermal treatment individually and more importantly makes it possible to study the combined effect of these two processes.

## 5.2. SILYLATION PROCESS ON O<sub>2</sub> PLASMA DAMAGED LOW-K DIELECTRICS

### 5.2.1. Overview and literature survey

Silylation is a promising method for repairing damaged low-k dielectric materials. In a typical silylation process, the chemicals are chosen to reduce or eliminate the silanol

bonds and replace them with the hydrophobic silyl groups. Specifically, for low-k dielectric recovery, a carbon containing silyl group ( $R_3Si-$ ) is introduced to interact with the silanol molecule on the damaged low-k surface to restore the dielectric loss. This reaction is displayed schematically in the following diagram:

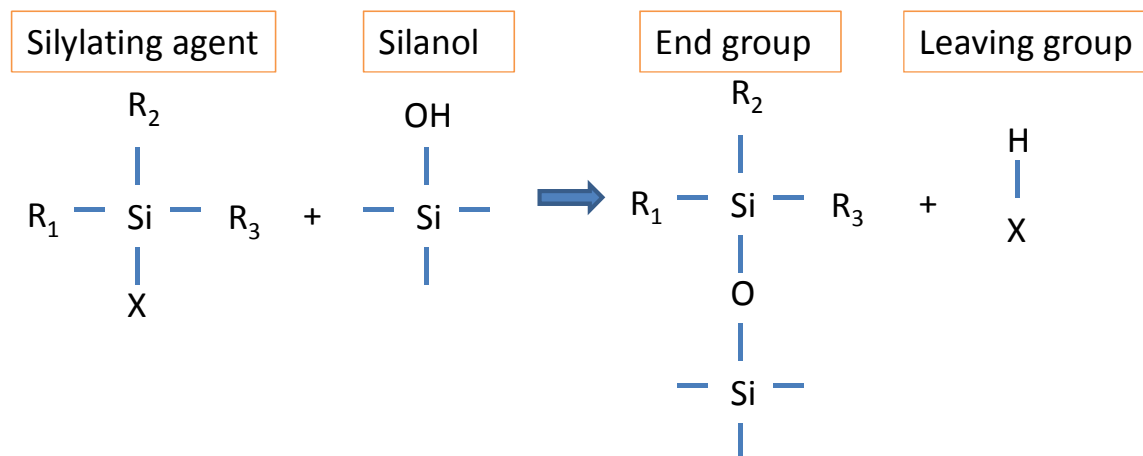


Figure 5-5: The schematic diagram of silylation process on a damaged low-k surface.

As shown in the schematic diagram, the silylating agent is formed by connecting a silicon atom to two distinct groups of moieties: organic moieties denoted by  $R$  and hydrolysable functional moieties denoted by  $X$ . There can be one, two or three functional groups in one silylation agent molecule, and these agents are called monofunctional, bifunctional and trifunctional accordingly. During the recovery process, the hydrolysable functional moieties of the silylating agents react with silanol groups on the damaged low-k surface, forming both end groups and leaving groups. The end groups are bonded to the low-k and contain organic moieties, turning the surface hydrophobic. The leaving groups are formed by functional moieties bonded with the hydrogen atoms, which are carried away from the surface at the end of the process.

Silylation process for low-k recovery has generated extensive interest and some of the recent publications on this subject are summarized in Table 5-1 and Table 5-2. Most of the studies show notable recovery effects. The efficiency of silylation depends on many factors, such as the number of functional moieties, the effectiveness of the leaving group, the pore size of the dielectric, the size of the silylating molecule, the medium in which silylation occurs, and process conditions (temperature, pressure).

The functions of silylation agent is defined by the organic (R in figure 5-4) and hydrolysable (X in figure 5-4) moieties connected to the Si atom. By various combinations of R and X moieties, a large pool of candidate silylation agents can be formed. Considering the chemical stability, hazardness and effectiveness, the popular choices include Trimethylchlorosilane (TMCS), Dichlorodimethylsilane (DMDCS), Hexamethyldisilazane (HMDS), (Bis)dimethylaminodimethylsilane (BDMADMS), (Bis)dimethylaminomethylsilane (BDMAMS), Trimethylbromosilane (TMBS), Trimethyliodosilane (TMIS), Trimethylmethoxysilane (TMMS), Dimethyldimethoxysilane (DMDMS) and Methyltrimethoxysilane (MTMS).

The size, the polarizability of the end group, and the reactivity of the functional group are the major factors controlling the effectiveness of the silylating agent. In general, a small molecular size induces a faster diffusion and less steric hindrance, thus yielding a better recovery. A lower polarizability R moiety corresponds to a lower polarizability of the end group, which directly contributes to a lower dielectric constant of the recovered low-k. A highly reactive X moiety is used to silylate the surface and pore walls of the low k material to increase its reactivity. For example, chlorine based silylation agents are more reactive than the amino based or the silazane based silylation agents in providing a better recovery.

Group	Low-k	Silylation Agent	Process	Characterization	Outcome
Fruehauf 2002[79]	Porous sol-gel derived silica xergel	HMDS TMSDEA OTMSA	Saturated vapor over the liquid	FTIR, Electrical, porosity	Silanol bonds and porosity reduce; leakage current and k value improved; HMDS is the most effective of the three.
Chang 2002[80]; Mor 2002[81]	Organic porous silica (50% porosity)	TMCS	Vapor	FTIR, K, Leakage,	CH3 bond recovered; leakage current and k value improved.
Chang 2002[82]	Hybrid organic siloxane polymer (HOSP)	HMDS	Vapor	FTIR, electrical,	Silanol bonds reduce; leakage current and k value improved
Hu 2003[83]	Porous methyl silsesquioxane (DE-PMSQ)	DMDCS	2% anhydrous solution dipping	FTIR, AES, electrical	Beside others: surface smoothing effect
Gorman 2004[84]	MSQ	Hexane and HMDS	ScCO <sub>2</sub>	FTIR, contact angle, SEM	Enhanced resistance to wet etch processes.
Xie 2004[85]	p-MSQ	HMDS, TMDS, TMCS	ScCO <sub>2</sub>	FTIR, contact angle, Electrical.	Silanol bonds reduce; leakage current and k value improved

Table 5-1: Summary of silylation studies (part I).

Group	Low-k	Silylation Agent	Process	Characterization	Outcome
Xie 2005[86]	p-MSQ	TMCS, TMBS, TMIS	ScCO <sub>2</sub>	FTIR, XPS, contact angle, Electrical.	TMCS < TMBS < TMIS
Smith 2006[87]	MSQ	TMMS, DMDMS, MTMS	ScCO <sub>2</sub>	FTIR, contact angle, AFM	
Rajagopalan 2006[88]	Nano-porous OSG	HMDS	Vapor, ScCO <sub>2</sub>	FTIR	Only modified the surface and ScCO <sub>2</sub> does not help.
Liu 2007[89]	OSG pore size 2.4nm	PTMOS, PDMCS, DPTMDS	Liquid	XPS, FTIR, Electrical	Leakage current and k value improved
Fischer 2011[90]	p-ULK	APRS, HMDS	Liquid, thermal immersion.	FTIR	Silylation shows strong thermal dependency.
Thomas 2011[91]	p-ULK pore size 2nm	HMDS HMCTS DMDMS DMDAS DMADMS	Vapor	FTIR, Electrical, surface free energy.	Reduce RC behavior and leakage current.

Table 5-2: Summary of silylation studies (part II).

To develop an effective silylation process, it is essential to use the appropriate silylating medium and an optimum silylation process. First, for the silylation reaction to be effective, it is necessary to treat the organosilicate film to have an abundance of silanols on the surface, which will ensure that the silylation reaction will occur to a full extent. In most cases, the plasma damaged low-k surface contains sufficient silanols. However, in some cases, a plasma or UV assisted oxidative treatment has to be used before silylation. Second, moisture should be removed before the silylation process since the silylation agents are susceptible to water molecules. In the presence of moisture, the di and tri functional agents tend to oligomerize to form either monolayers or a thin film, which will reduce the reactivity, block the pore, thus prohibit the dielectric recovery and complicate the reaction mechanism. Third, silylation process is normally more efficient at an elevated temperature to thermally activate the silylation agent so that it can diffuse into the low-k films to initiate the chemical reaction between silylation agents and silanol group. Therefore, the silylation process is normally conducted at an elevated temperature high enough to enhance the diffusion and reaction without breaking down the chemical.

The medium used in the silylation process is also an important factor. It can be categorized as liquid, supercritical CO<sub>2</sub> and vapor-phase silylation processes. In liquid process, damaged low-k dielectrics are immersed in the silylation solution or spin-coated with a mono-layer of silylation agent. This is commonly used in the early stage of development due to the easiness of its implementation and the extra benefit of surface planarization. Supercritical CO<sub>2</sub> (scCO<sub>2</sub>) was reported to be an effective medium due to the advantage of low surface tension and high diffusivity in comparison with other vapor and liquid processes. Experimental results show that this process greatly decreases the time necessary to induce hydrophobicity and reduces the concentration of reactive silylation agents needed. However, supercritical CO<sub>2</sub> process presents a tremendous

challenge to process integration due to its requirement of ultra-high pressure. Among these three processes, the vapor process is the most feasible from a process integration point of view, and consequently the focus of our study. Supercritical CO<sub>2</sub> process will be discussed in 5.2.3.

## 5.2.2. Vapor phase silylation

### *The experimental setup*

A CVD silylation process was conducted on Applied Material BD III porous OSG porous ultra low-k with a dielectric constant of 2.2. The schematic experimental setup was shown in Figure 5-6.

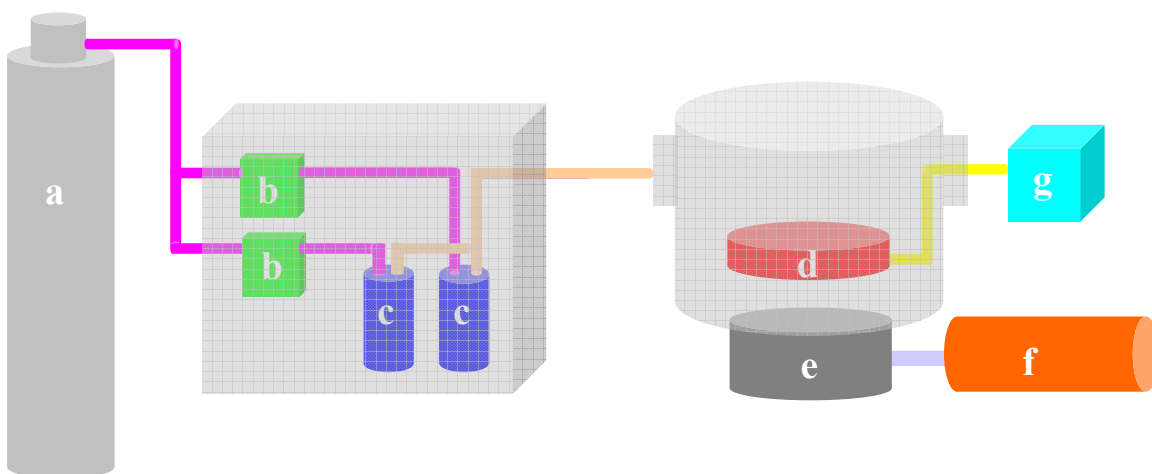


Figure 5-6: The schematic diagram of the experimental setup used in silylation study. (a) Carrier gas bottle, (b)MFC, (c) Bubbler, (d) Heating stage, (e) Turbo pump, (f) Mechanical pump, (g) Temperature controller.

The silylation agents of choice are Trimethylchlorosilane (TMCS), Dichlorodimethylsilane (DMDCS). Their reaction paths are displayed in Figure 5-7.

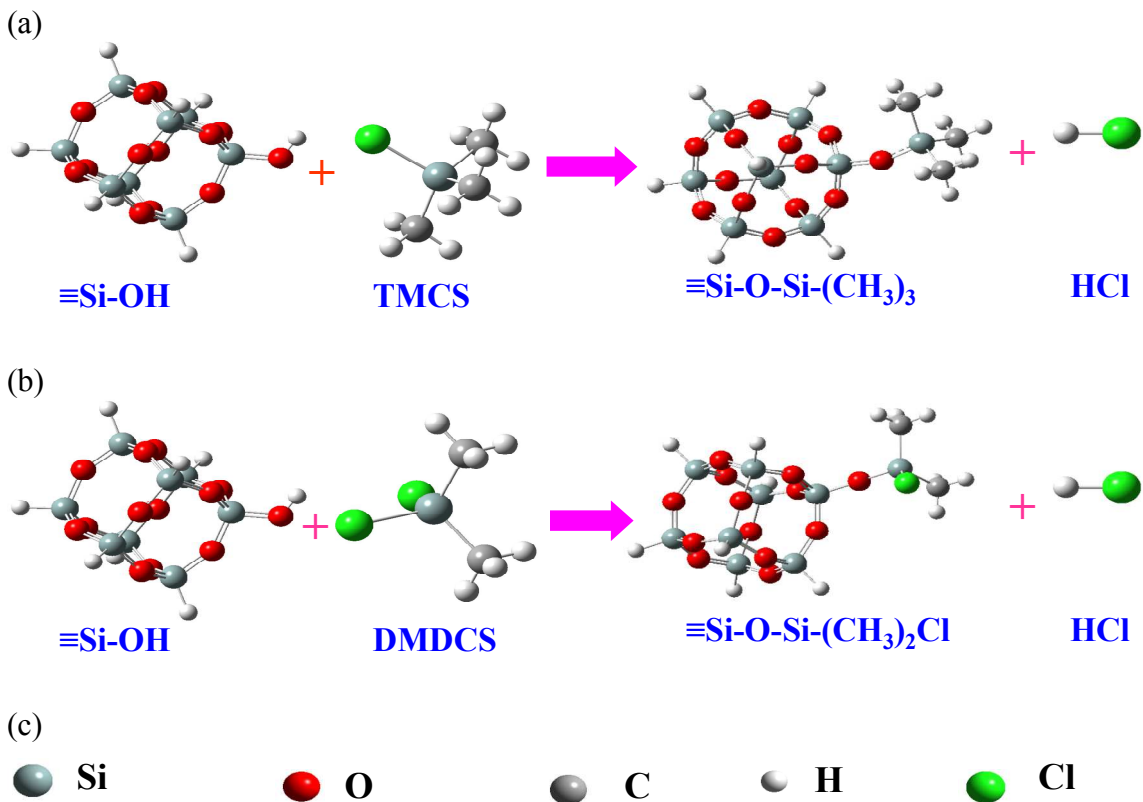


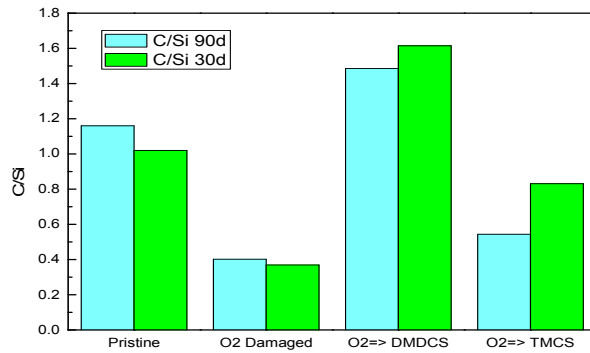
Figure 5-7: The schematic diagram of silylation process. (a) TMCS, (b) DMDCS, (c) legend.

After the TMCS or the DMDCS silylation process, the surface carbon concentrations were measured by XPS at  $90^\circ$  and  $30^\circ$  take-off angles. This together with FTIR was used to measure the chemical bonding changes. Contact angles were measured by a goniometer and the dielectric constant was measured by a MIS method.

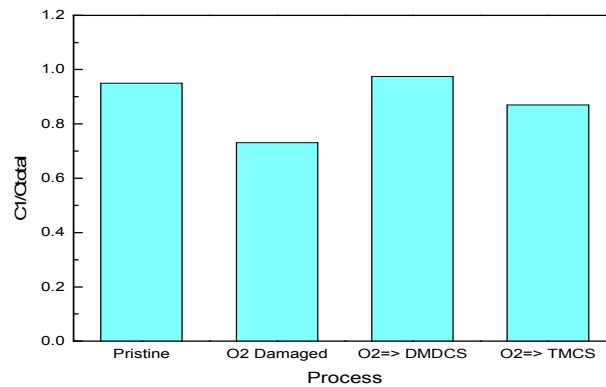
### ***The results and discussion***

The XPS analysis of surface carbon characteristics is shown in Figure 5-8. The surface carbon concentration is completely recovered after the DMDCS treatment of the damaged low-k film, while it is partially recovered after the TMCS treatment. The  $30^\circ$  results show a higher carbon concentration than  $90^\circ$  for both the DMDCS and the TMCS

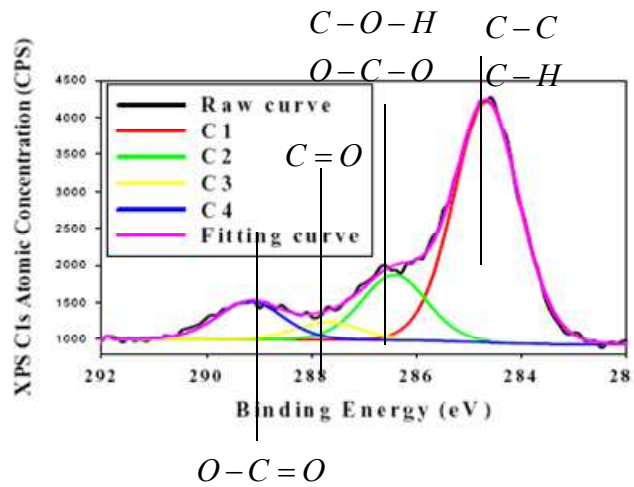
recovery processes. This indicates that the recovering effect is better at surface (<2nm) than the near surface (~5nm) region. The de-convolution of the XPS carbon 1s peak reveals the detailed information of carbon bonding. The Carbon 1s peak can be deconvoluted into four components, denoted by: C1(C-C, C-H), C2(C-O-H, O-C-O), C3 (C=O) and C4 (O-C=O). As shown in Figure 5-8(b), the C1 over C<sub>total</sub> ratio is restored by silylation processes, which can be interpreted as -C-H bonds are recovered from C-O and C=O bonds. In general, DMDCS provided a better recovery result than TMCS as evaluated from the bonding compositions.



(a)



(b)



(c)

Figure 5-8: The XPS spectra analysis of the silylation recovery process. (a) Carbon over silicon ratio, (b) C1 over total C 1s peak area, (c) Carbon decomposition diagram of the C 1s peak.

The surface contact angle is an indicator of surface hydrophobicity (Figure 5-9). After O<sub>2</sub> plasma treatment, the surface became hydrophilic due to formation of the –OH bonds, which resulted in a decrease of the water contact angle. After DMDCS and TMCS silylation treatments, the contact angle increased due to the reformation of the surface methyl bonds, indicating that the surface hydrophobicity was partially recovered. In comparison, the contact angle after DMDCS was higher than that after TMCS recovery.

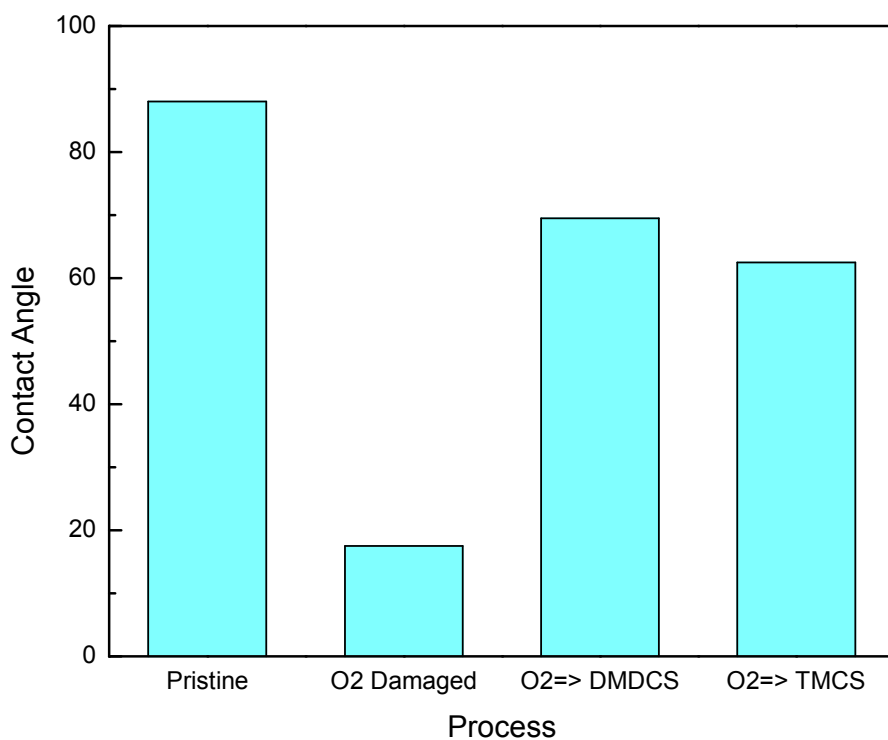
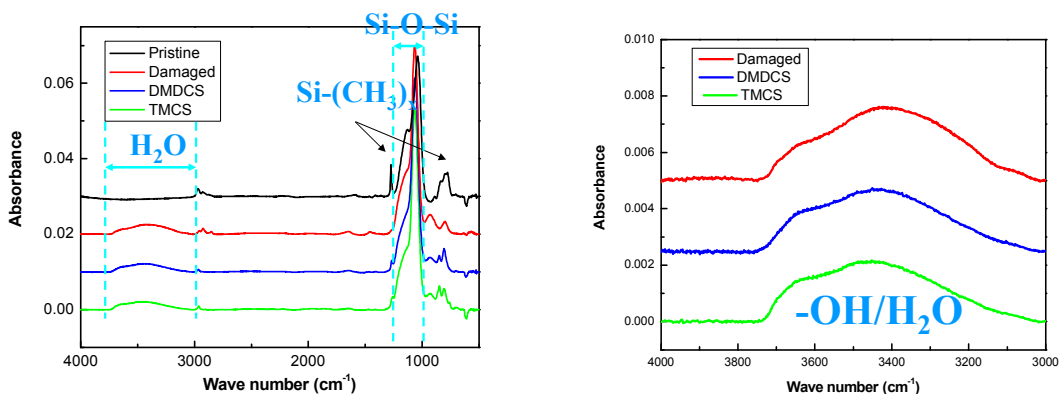


Figure 5-9: Contact angle measurement of after DMDCS and TMCS silylation.

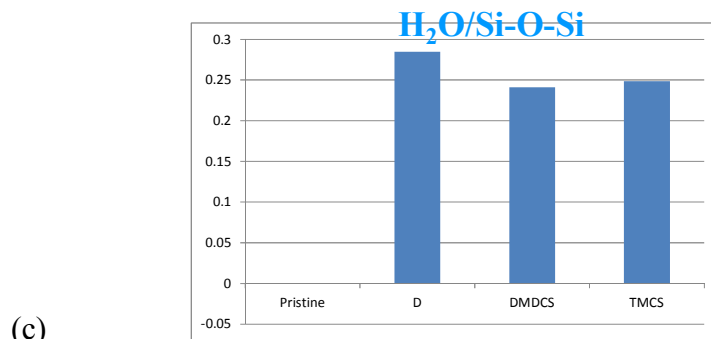
The FTIR spectra analysis of the silylation recovery process is shown in Figure 5-10. Silanol bonds and physisorbed water were only partially removed and the recovery

was less than 20%. The methyl bonds were also partially recovered. Further bonding analysis revealed the recovery of methyl bonds by DMDCS and TMCS corresponding to increases in Si-(CH<sub>3</sub>)<sub>2</sub> and Si-(CH<sub>3</sub>)<sub>3</sub> respectively[92]. This result can be explained by referring to the molecular structure of DMDCS and TMCS, where the formation of Si-(CH<sub>3</sub>)<sub>2</sub> and Si-(CH<sub>3</sub>)<sub>3</sub> may be due to the oligomerization of silylation agents on the surface of the low-k film.

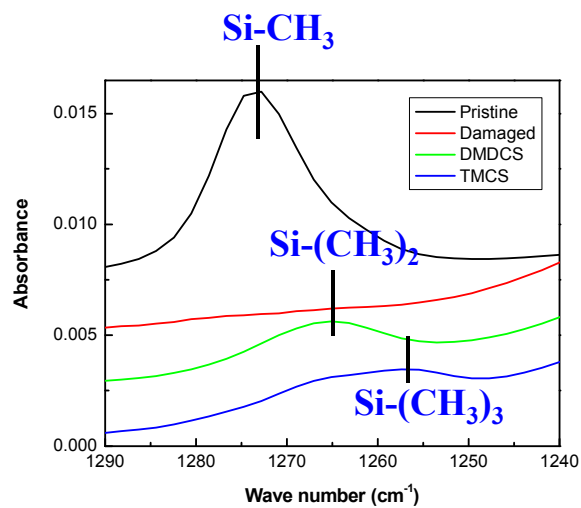


(a)

(b)



(c)



(d)

Figure 5-10: FTIR spectra analysis of silylation recovery process. (a) The whole spectrum, range 522-4000cm<sup>-1</sup>, (b) Enlargement of -OH/ physisorbed water, (c) -OH/H<sub>2</sub>O peak area over Si-O-Si peak area ratio and (d) Si-(CH<sub>3</sub>)<sub>x</sub> bonds.

MIS measurements shown in Figure 5-11 indicate the dielectric constants were reduced after silylation. Again, DMDCS showed a recovery result better than TMCS.

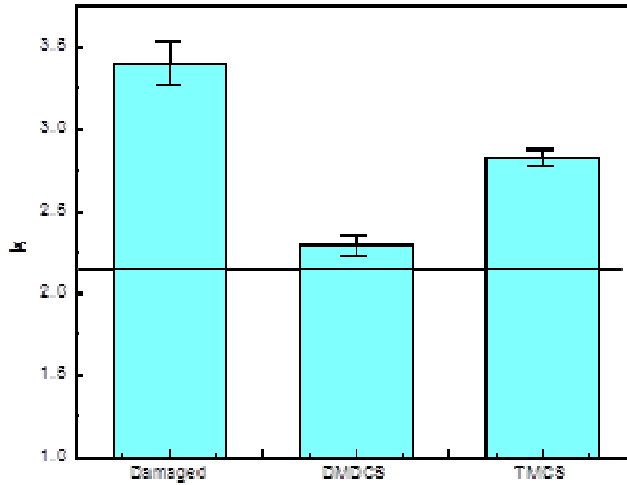


Figure 5-11: MIS measurements of low-k film. Dielectric constant after damage was compared with that after DMDCS and TMCS silylation. The black line indicates the pristine dielectric constant 2.2.

In summary, both CVD DMDCS and TMCS silylation processes show positive recovery effects as shown in the change of the surface carbon concentration and the increase in surface hydrophobicity. This indicates the removal of physisorbed water and silanol bonds together with the recovery of the methyl bonds and dielectric constant. Interestingly, the results from the surface analysis techniques (XPS, contact angle) show more clearly the recovery effect than the bulk analytical techniques (FTIR, MIS). This strongly suggests that the silylation recovery effects occur more at the surface. The major challenge for recovery of porous low k dielectrics, however, is the limited penetration of silylation agents into the pores. The porous ultra low-k materials (AMAT BD III) used in this study, along with other main-stream ULK materials, have nano-pore structures with pore size around 2nm. While oxygen radicals can pass through the small pore structures

to cause plasma damage, the large silylation molecules are difficult to diffuse into the pore structure. In addition, silylation molecules can easily block the diffusion path in the pores by reacting to form a polymer layer on the surface induced by oligomerization reactions. Due to these reasons, it is almost impossible to make the silylation agent penetrate the nano-pore low-k material deeper than 5nm, therefore limiting the dielectric recovery effect.

Another interesting finding is the more effective recovery by DMDCS than TMCS. This finding is in agreement with results reported by other groups[93][94] and previous results in our group[95]. The higher efficiency of DMDCS can be attributed to its smallest molecular size as compared with TMCS, which provides faster diffusion and less steric hindrance effect. On the surface of an OSG low-k film, isolated silanol and di-silanol (also named as germinal silanol) are formed after O<sub>2</sub> plasma damage. The TMCS with a single Cl moiety can easily react with the isolated silanols. However, once reacted, the three CH<sub>3</sub> groups cause steric hindrance, blocking further reactions between other TMCS molecules and the adjacent hydroxyl. In general, Di-functional silylation agent is more effective in eliminating the silanol bonds and recovering more methyl bonds, thus providing the best recovery effect.[93] In the following section, the steric hindrance effect is discussed.

### ***The steric hindrance effect and silylation efficiency***

The number of functional (X) moieties in each silylating molecule is important in controlling the silylation efficiency. There can be one, two or three functional groups in one silylation agent molecule, and these agents are called monofunctional, bifunctional and trifunctional. For example, DMDCS is a bifunctional agent and TMCS is a monofunctional silylation agent.

Difunctional silylation agents are more effective than the monofunctional silylation agents since the latter can react only with a single isolated silanol group on the surface or on the pore wall of the low k material. Once an end group is formed, the subsequent reaction of the adjacent silanols with another monofunctional silylation agent can be blocked due to the steric hindrance effect as illustrated in Figure 5-12(a). In contrast, a di-functional silylation agent can react with two neighboring silanols, as shown in Figure 5-12(b). However, for tri-functional silylation agents, it is unlikely to react simultaneously with three silanols, as this will leave behind an unreacted end group on the low k surface to absorb moisture from the air, leading to additional silanol formation. Also tri-functional silylation agents are more likely to initiate oligomerization and create a mono-layer to block the silylation reaction or cross-link to form contaminants in the system.

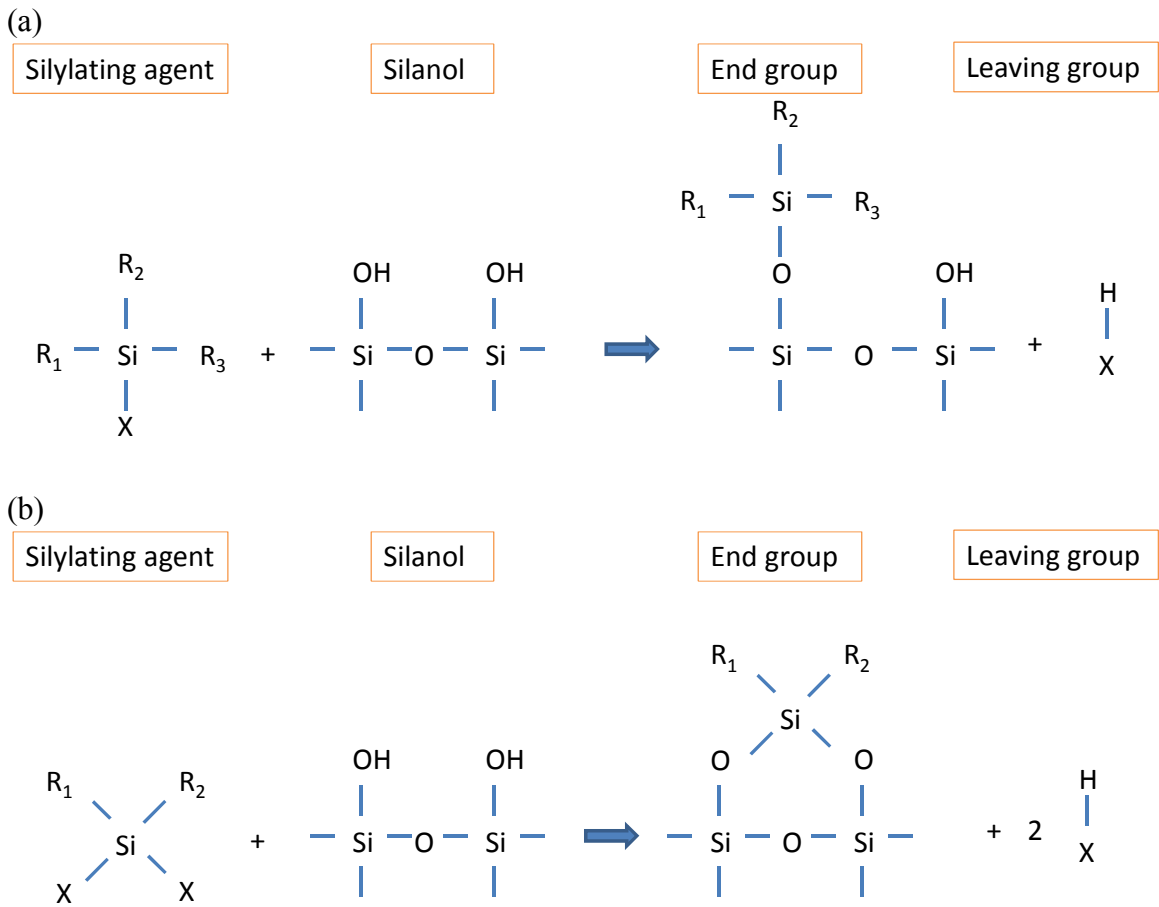


Figure 5-12: Schematic diagram of the silylation process to show the formation of the silanol bond on the damaged low k surface. (a) The steric hindrance effect prevents the simultaneous capture of more than one silanols with a monofunctional silylation agent. (b) Di-functional silylation agents react with two neighboring silanols simultaneously.

### 5.2.3. Supercritical CO<sub>2</sub> silylation process

#### *Overview and the use of supercritical CO<sub>2</sub> silylation*

Supercritical fluids are defined as moieties that exist above their critical temperature and critical pressure. If we move upwards along the gas-liquid coexistence curve, which is indicated as the red line in the phase diagram (Figure 5-13), both temperature and pressure increase. The liquid becomes less dense because of thermal

expansion and the gas becomes denser as the pressure rises. Eventually, the densities of the two phases become identical at a critical point where the coordinates are defined as critical temperature and critical pressure [96]. The range of pressures and temperatures that define the supercritical fluid region of the diagram are also shown in Figure 5-13. Supercritical fluid has been considered as a fourth state of matter where the material is neither a liquid nor a gas but has the beneficial properties of both. In supercritical state the fluid has the diffusivity of a gas, the solvency of a liquid and zero surface tension. Among the supercritical fluids, carbon dioxide (CO<sub>2</sub>) has been the most widely used because of its convenient critical temperature (31°C), relatively low critical pressure (1070 psi), low cost, chemical stability, non-flammability and non-toxicity.

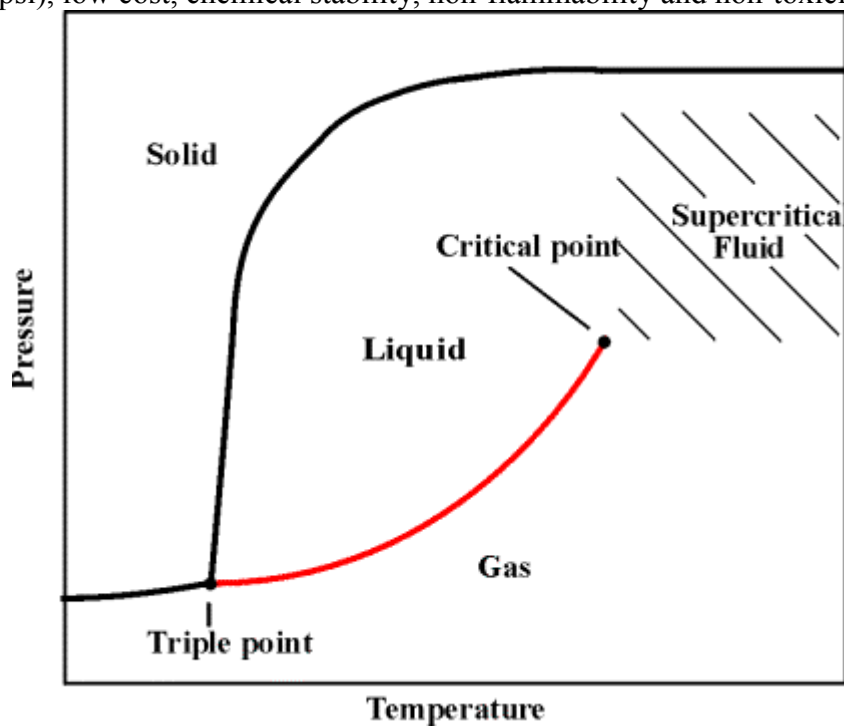


Figure 5-13: The phase diagram of a single substance.[96]

Supercritical fluids are able to spread out along a surface more easily than a true liquid because they have lower surface tensions than liquids. At the same time, a

supercritical fluid maintains a liquid-like ability to dissolve substances that are soluble in the compound, for example photoresists. In late 90s, Los Alamos National Laboratory, IBM and other companies developed a commercialized supercritical CO<sub>2</sub> process (scCO<sub>2</sub>) for resist removal [97] which was used later for ULK/Cu integration [98][99].

With the development of scCO<sub>2</sub> resist removal processes, scCO<sub>2</sub> silylation started to draw a lot of interests because of its potential application for low k integration. Compared to a liquid process, scCO<sub>2</sub> silylation has a low surface tension (almost zero), so that the silylation agents can easily spread and defuse into the small trench figures and even smaller pore structures without obstruction of the capillary pressure. Compared to the gas phase, scCO<sub>2</sub> silylation provides high solubility, high density and high pressure. Due to those unique benefits, scCO<sub>2</sub> silylation is believed to be more effective than the other two.

### Experimental setup and result

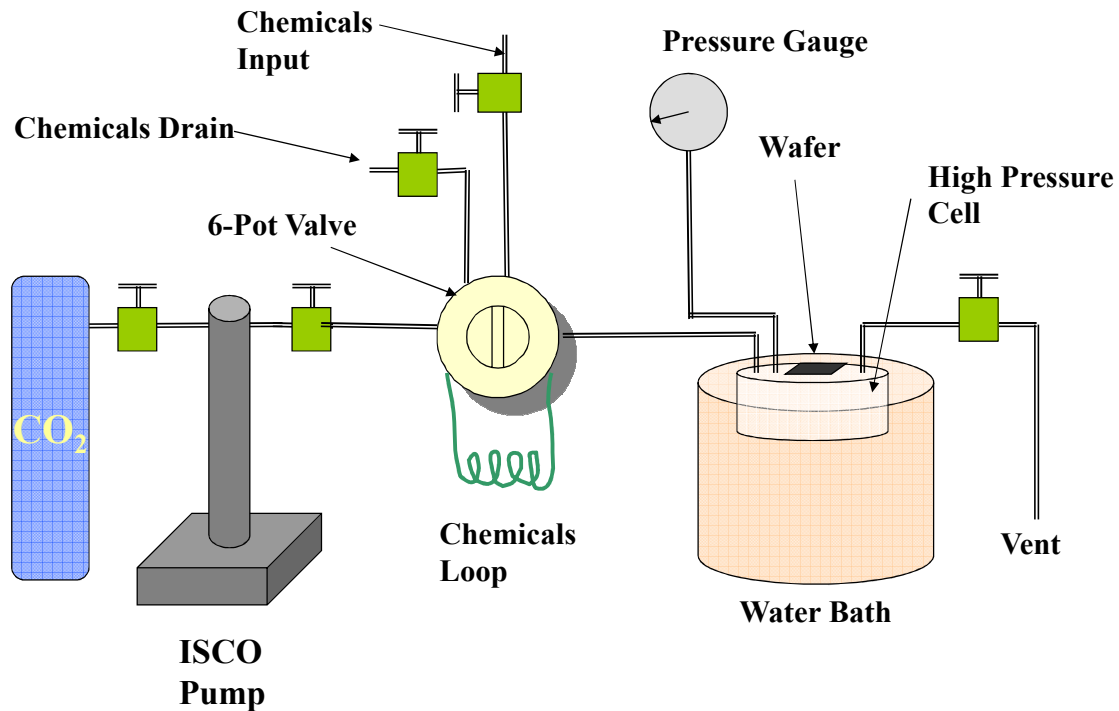


Figure 5-14: scCO<sub>2</sub> Silylation System. (Courtesy of Prof. Kwon Taek Lim and Prof. Keith P. Johnston)

The scCO<sub>2</sub> silylation processes were conducted with the help of Dr. Kwon Taek Lim in Prof. Johnston's lab. The schematic view of the experimental setup is shown in Figure 5-14. The CDO low-k film was damaged by an oxygen RIE process at 150W, 5min and 150 torr. The low-k wafer coupon was then placed in a stainless steel chamber, which was immersed in a water bath (normally kept at 45-65°C). CO<sub>2</sub> from a gas cylinder was brought up to a desired working pressure (1500 psi to 3000 psi) by a ISCO high pressure syringe pump, and mixed with silylation agents(TMCS, DMDCS, HMDS) in a small mix chamber. The mixture then flowed into the process chamber through a stainless steel heat exchanger. The mixture scCO<sub>2</sub> silylation fluid was held in the process

chamber for a desired amount of time and then vented by pure CO<sub>2</sub> at a rate of 10 mL/min. for 1 or 2 minutes at the same temperature and pressure in order to rinse and dry the samples.

The TMCS silylation was performed at 50°C, 2000 psi with 0.5 ml TMCS for 2 min. The FTIR spectra analysis and contact angle measurement results are presented in Figure 5-15 and Table 5-3. Similar to the vapor phase in the silylation process, scCO<sub>2</sub> silylation slightly recovered the methyl bonds and partially removed the silanol bonds and physisorbed water. The water contact angle of the low-k film was also recovered. A subsequent 1 hour long 300°C thermal annealing further removed silanol bond and recovered the surface hydrophobicity.

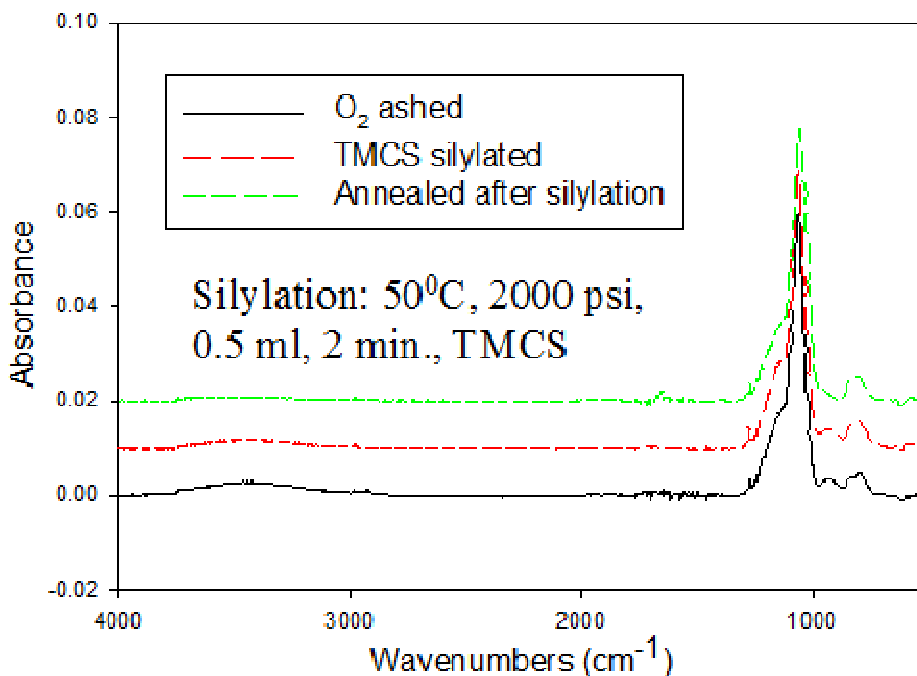


Figure 5-15: FTIR spectra of the sample after plasma O<sub>2</sub> ashing, scCO<sub>2</sub> TMCS silylation and subsequent annealing. (Courtesy of Junjing Bao)

Sample \ Peak Area	Si-OH (3750~3050 cm <sup>-1</sup> )	Si-CH <sub>3</sub> (1290~1260 cm <sup>-1</sup> )	Si-O-Si (1240~980 cm <sup>-1</sup> )	Water Contact Angle(°)
Pristine CDO	0	0.12	5.92	97.8±7.8
O <sub>2</sub> ashed	1.22	0.06	5.61	48.5±0.7
TMCS silylated	0.78	0.07	5.70	86.0±1.0
Annealed after silylation	0.34	0.07	5.83	105.6±0.7

Table 5-3: Areas of major FTIR peaks and results from measurement of water contact angles. (Courtesy of Junjing Bao)

For process optimizations, a series of experiments were carried out by varying the process pressure, time, chemical volume and silylation agents. The base recipe was chosen to be agent TMCS, process pressure 3000psi, process temperature 65°C and process time 10 minutes.

The peak areas of Si-(CH<sub>3</sub>)<sub>3</sub> (1255cm<sup>-1</sup>) was found to increase with process pressure as shown in Figure 5-16(a). Under an isothermal condition, increasing pressure increased the supercritical fluid density, and concomitantly, the mass of reactants at the reaction site. Another possible reason is that the higher pressure may increase the penetration depth of the TMCS, which was found, however, not to be effective for nanopore (~2nm) low-k material. The methyl bond peak area increased also with the treatment time up to 10 minutes (Figure 5-17(a)). The twenty minute treatment showed no significant difference in comparison with the 10 minute treatment, indicating possible reaction saturation. The saturation was also manifested by the fact that little difference was observed when the TMCS volume changed from 0.12ml to 0.22ml. Overall, the recovery of the carbon peak among the three silylation agents showed that DMDCS had the best recovery effect, followed by TMDS and then HMDS (Figure 5-18(a)). These results are in good agreement with the vapor phase silylation results. The difference between TMCS and DMDCS was explained in Section 5.2.2. In comparison, HMDS is a

monofunctional agent with a larger molecule size, therefore a larger steric hindrance effect is expected.

In our study, the trend in Si-OH bond reduction was not clear. This may be due to ambient moisture absorption after silylation which interfered and diminished the effect of moisture removal by scCO<sub>2</sub>.

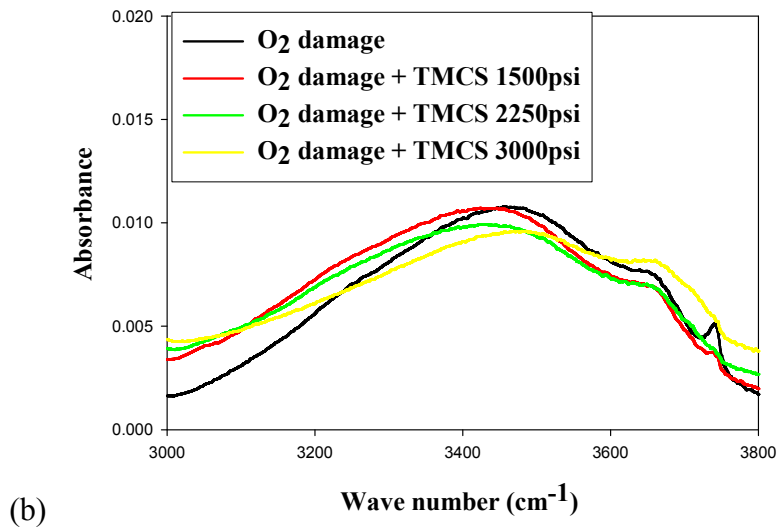
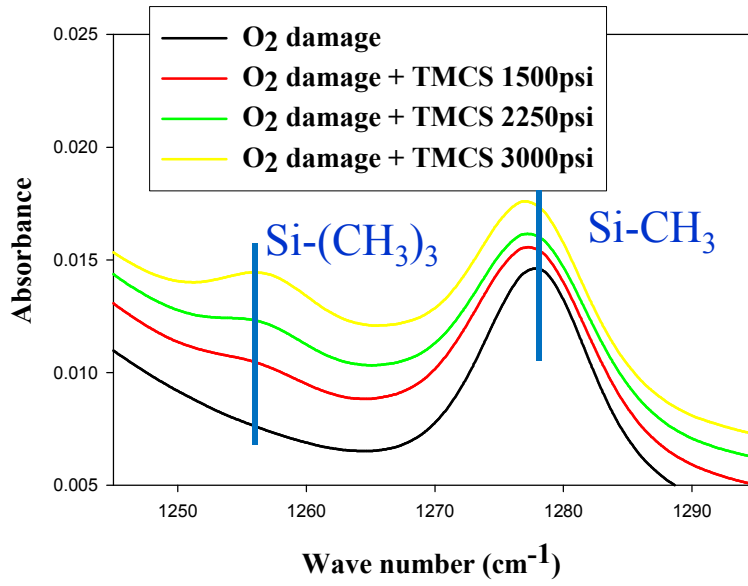
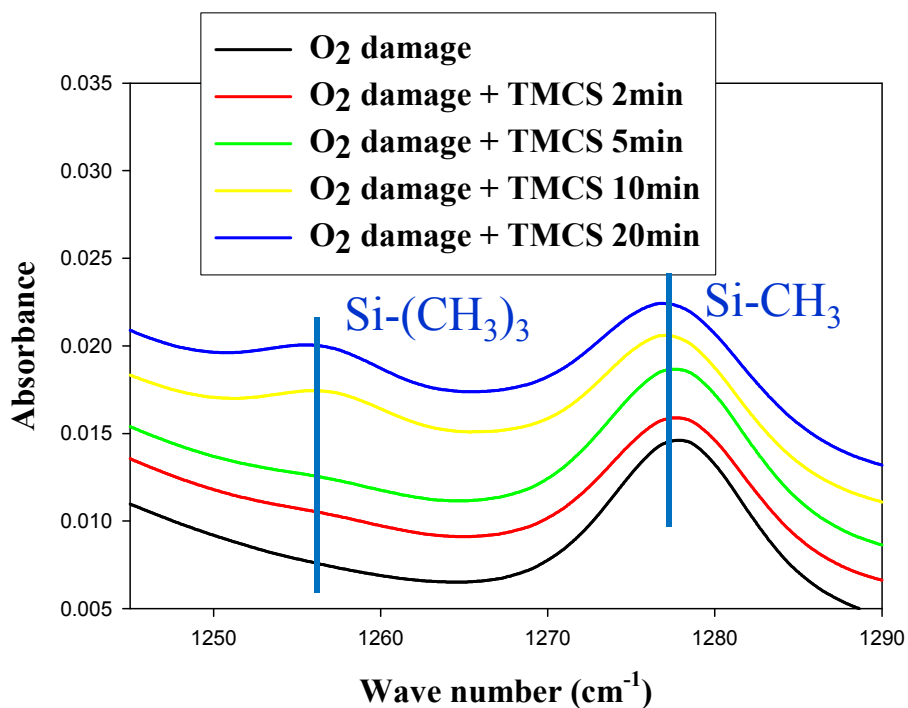
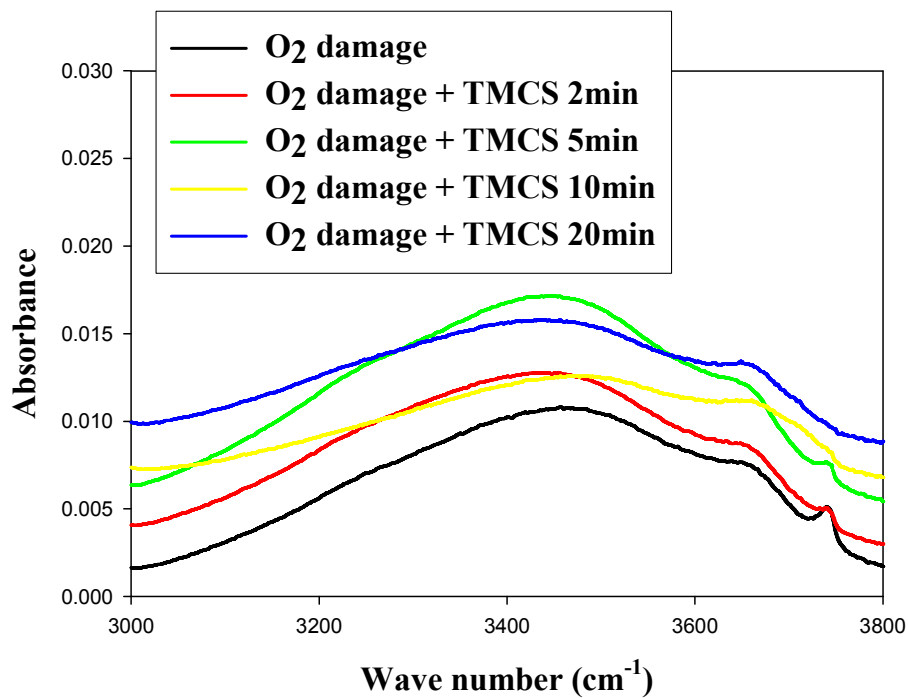


Figure 5-16: FTIR of TMCS scCO<sub>2</sub> process with increasing pressure (a) Methyl peak; (b) -OH peak.

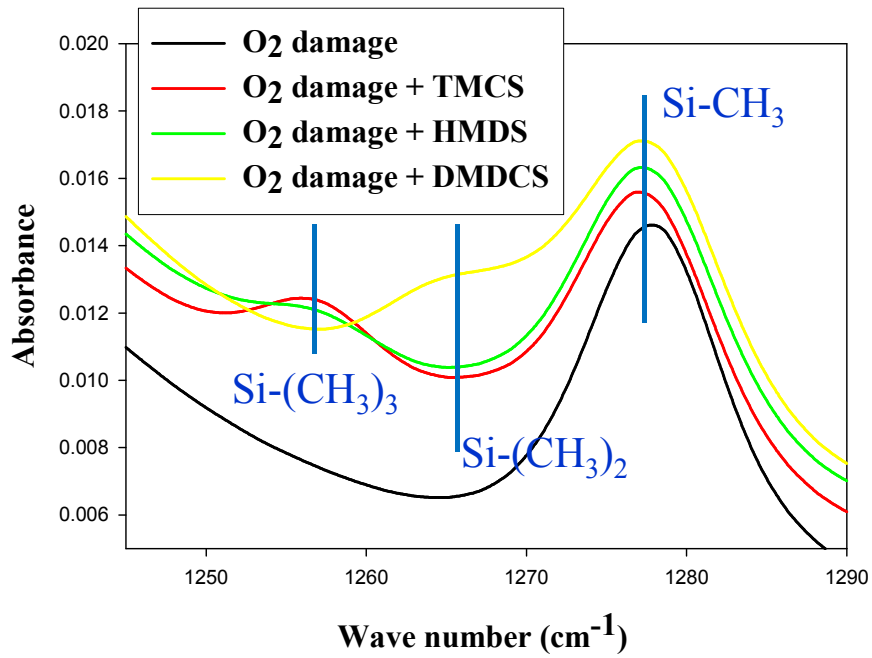


(a)

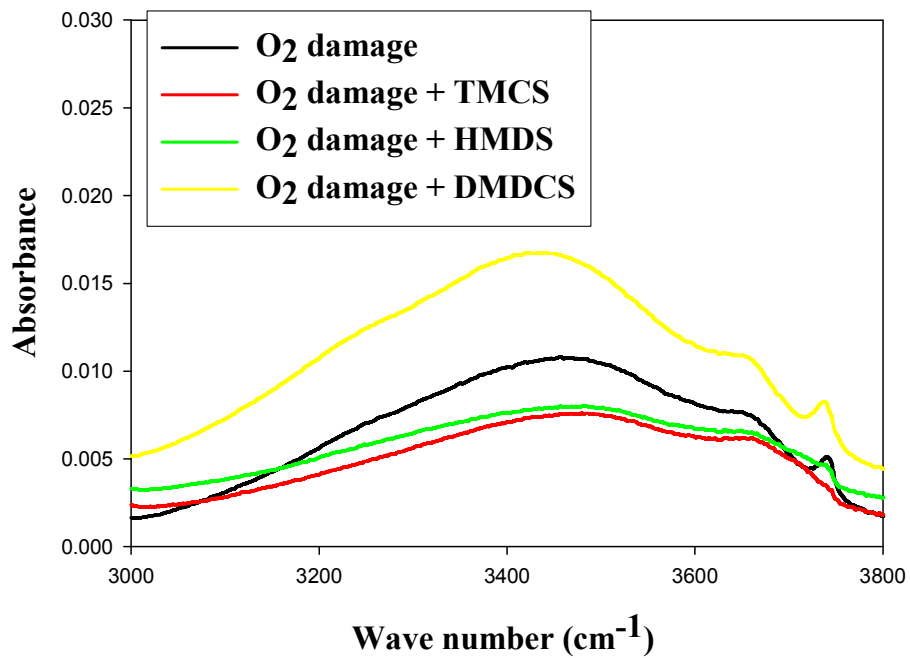


(b)

Figure 5-17: FTIR spectra of TMCS scCO<sub>2</sub> process with increasing process time(a) Methyl peak; (b) -OH peak.



(a)



(b)

Figure 5-18: FTIR spectra comparison of scCO<sub>2</sub> TMCS, HMDS and DMDCS silylation processes (a) Methyl peak; (b) -OH peak.

## ***Discussion***

Results from this study show that scCO<sub>2</sub> silylation is more time efficient than vapor phase silylation; for example, it takes 10 minutes rather than 1 hour to recover the methyl bond to the same extent. However, it has no significant advantage for the total recovery effect. The methyl bond recovery was found to be saturated quickly with the progressive treatment time and the chemical dosage. This can be explained as due to the failure of silylation agents to penetrate deeply into the film. The small pore radius (~2nm) and the initial surface silylation reactions block further diffusion of silylation agents into to the film, thereby preventing the reaction with silanols below the surface layer. The surface limitation of scCO<sub>2</sub> and vapor phase silylation have also been reported by other groups[88].

At this time, ScCO<sub>2</sub> photo resist removal is still not commonly adopted by the industry. Overall, the vapor phase silylation is a better choice from a process integration point of view because the process can be readily integrated using existing vacuum CVD and etching systems.

## **5.3. UV AND THERMAL TREATMENT**

### **5.3.1. Overview**

The UV curing process can be used to increase the hardness, modulus, cohesive strength, adhesion and reliability of low k dielectrics. The process also removes porogens in porogen containing film and decreases water absorption to reduce the dielectric constant and improves dielectric breakdown and chemical stability. Among the applications, thermal assisted UV curing processes are most commonly used and well studied as a post-deposition treatment method[100][101][69]. It is particularly effective in removing the porogen to improve the mechanical properties, such as Young's modulus

and cohesive strength [100] [24]. The improvement of mechanical properties can be attributed to the formation of cross-linking Si-O-Si backbone bonds and the increase in network connections induced by UV radiation. The accompanied thermal treatment increases the bond rearrangement mobility and therefore improves the cross-link efficiency[100]. The bonding modification can be induced by a series of potential reactions listed in the following:

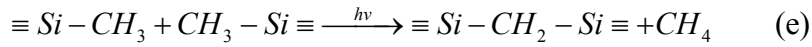
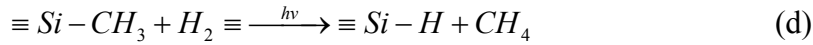
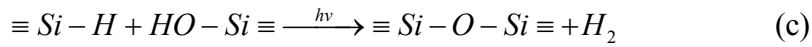
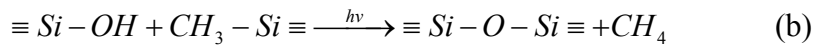
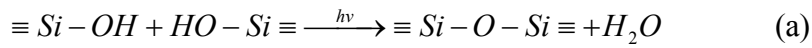


Figure 5-19: Possible structural modifications induced by UV radiation.

The wavelength of the UV radiation is the most important parameter in controlling the effect of UV curing, which will be discussed in Section 5.3.2. In addition to wavelength, other parameters also influence the UV curing performance including the curing temperature, time, radiation intensity and ambient gases.

UV curing has been investigated as a post-deposition method which has provided a base to understand UV low-k interaction. The application of UV curing as a dielectric recovery method has not been systematically reported. Since the low-k films have most likely already subjected to the first round of UV curing before plasma processing, the low k film at the dielectric recovery stage usually does not contain much porogens but contains a lot of Si-OH bonds and physisorbed water. Therefore, the effect of the UV dielectric

recovery process on plasma damaged low-k films is distinctly different from that subjected to UV post-deposition cure.

### **5.3.2. The wave length selection for dielectric recovery.**

Photochemical reactions are processes during which energy required for their activation is provided by electromagnetic radiation. By selecting the photon energy, the photochemical reactions can be filtered and controlled. Therefore, the selection of the wavelength of the UV source is very important for optimizing the UV curing process. For UV curing, different types of broadband UV sources[102][68] and monochromatic excimer lamps[68][67] have been studied and reported in the literature. Berry et al. [102] combined the spectral response of four important properties (k-value, Modules, Porogen removal and porogen crosslinking) into one graph, and found two good region at 200nm – 260nm and 300-400nm for effective UV curing (Figure 5-20). Because the low concentration of porogen in the plasma damaged films, the porogen cross-linking and removal are not major concerns. For damaged film, the silanol bond condensation, physisorbed water removal and photon absorption are important factors. For this purpose, the wavelength needs to be as small as possible. On the other hand, as we learn from the VUV radiation study in Chapter 4, UV with wavelength smaller than 200nm can cause direction session of Si-CH<sub>3</sub> bond and increase the dielectric constant. Therefore, the Fusion UV lamp with H<sup>+</sup> bulb was chosen for this study for its abundant intensity distribution in the wavelength range of 200nm-260nm. Since the UV source was exposed to air and filtered by a quartz view port, VUV radiation was absorbed and blocked by air and the quartz window. Under this condition, the spectrum of the H<sup>+</sup> bulb is displayed in Figure 5-21.

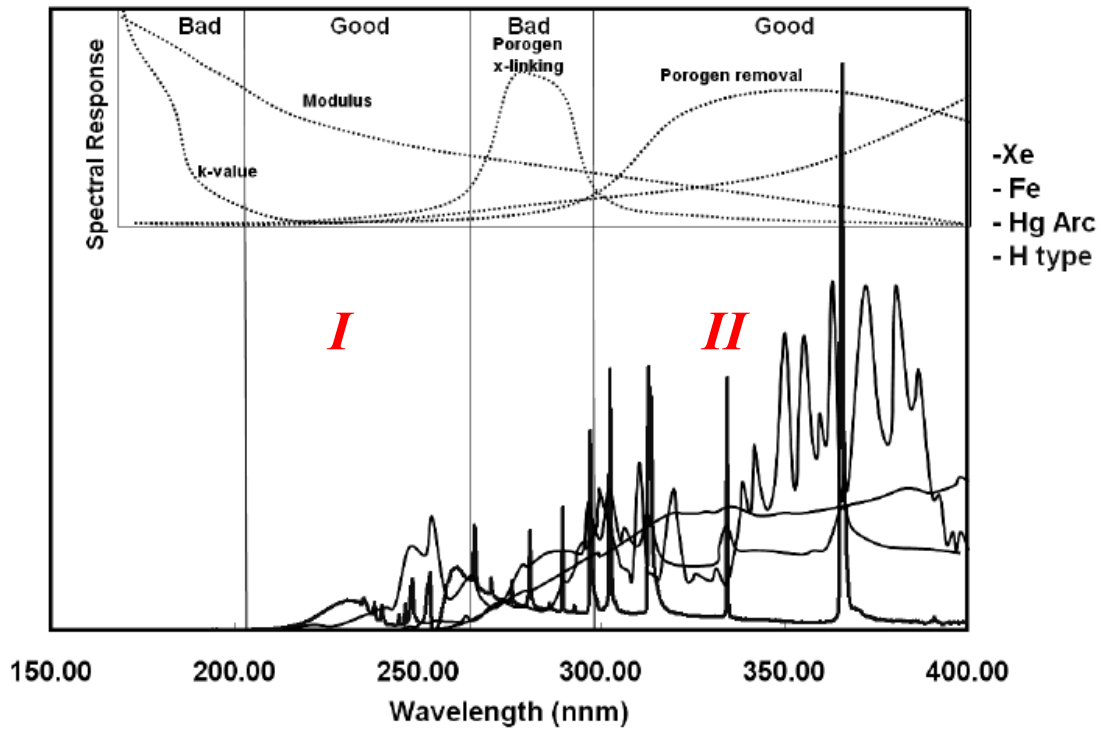


Figure 5-20: Schematic spectral response of four important properties (k-value, Modulus, Porogen Removal and Porogen crosslinking) of a hypothetical low-k material, overlaid on some commercially available UV bulbs (Xe arc, Hg arc, and electrodeless Fe, H, bulbs) UV spectra selection. [102]

### H+ Bulb

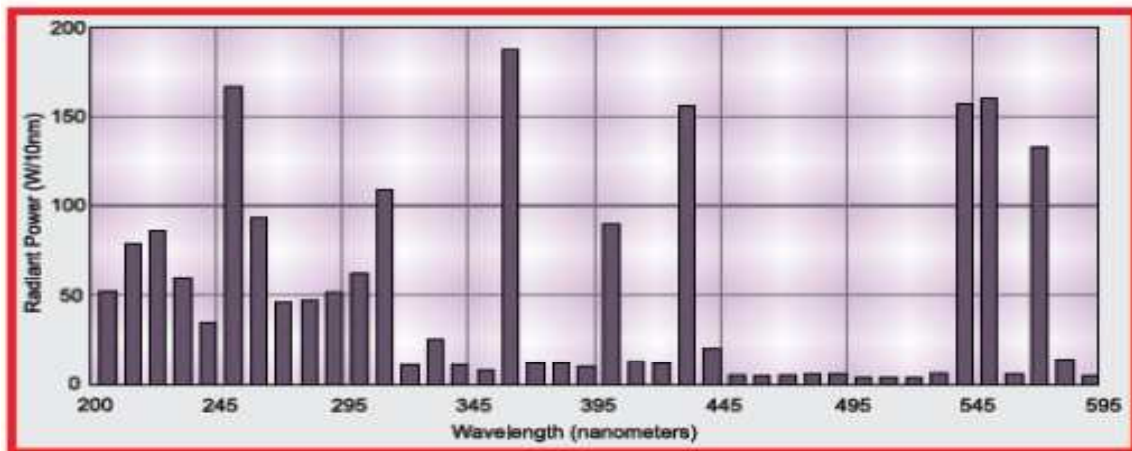
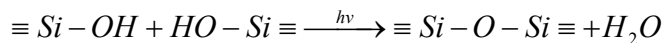


Figure 5-21: UV spectrum of the H+ bulb installed in the fusion F600S UV curing system. <http://www.miltec.com/Catalog/Miltec%20Catalog%202014.pdf>

### 5.3.3. Experimental setup and mechanism of thermal assisted UV curing

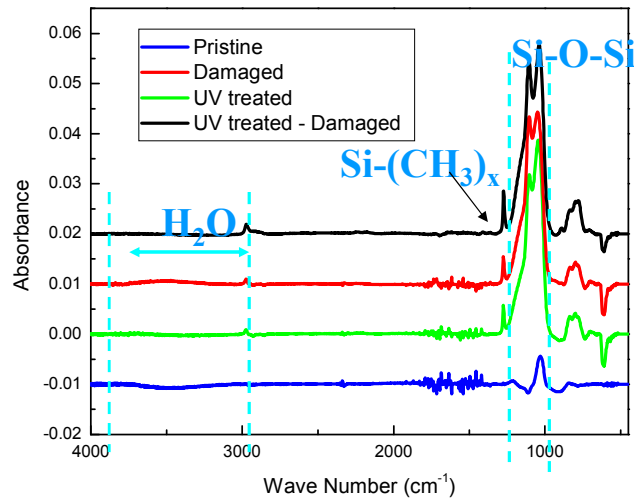
AMAT BD III porous OSG low-k ( $k=2.2$ , thickness~100nm) was first cut into one inch square coupons, then subjected to oxygen plasma in a Trion RIE chamber for 300 seconds (power 150W, pressure 20 Torr, gas flow 20 sccm). The damaged low-k sample was then taken to the UV curing chamber as described in section 5.1, where it was heated to 400°C in a high vacuum environment ( $<10^{-5}$ Torr) and then UV cured by a fusion UV lamp with a H+ bulb for 300 seconds.

The FTIR spectra of pristine, damaged and UV cured low-k films were measured and the results are compared in Figure 5-22. A general chemical bonding information of SiCOH material and its assignment in FTIR spectrum can be found in Chapter 2. From the FTIR absorbance spectra, we observe that the –OH bond and physisorbed H<sub>2</sub>O molecules were significantly removed and restored to the level about the same as the pristine film. Both of these factors contributed to the dielectric recovery. The Si-CH<sub>3</sub> bond around 1275cm<sup>-1</sup> was not changed. In contrast, the Si-O-Si network bonds were found to increase as Si-O-Si cage bonds decreased. These results suggest that the condensation reaction of two silanol groups is the most probable reaction.

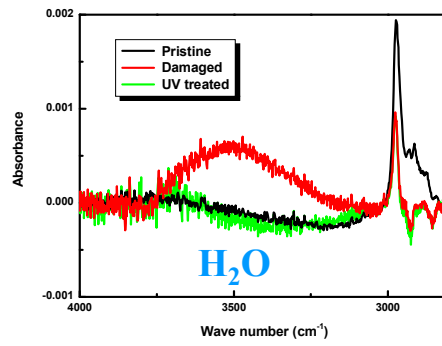


Reaction path (b) in Figure 5-19 is unlikely to happen in the present study as it would lead to considerable loss of methyl groups. Other reactions can be ruled out also due to the same argument.

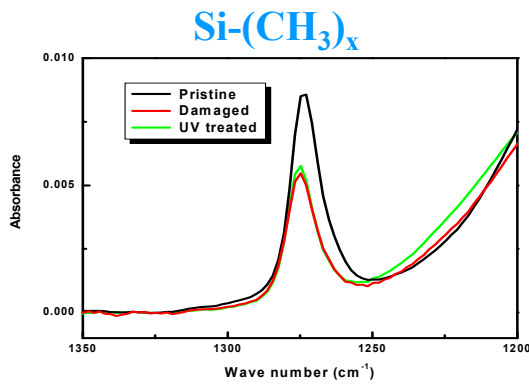
The SE measurement illustrates that the thickness of the film after UV curing is unchanged (within the experimental error range), indicating the condensation of silanol bonds and crosslink did not cause film shrinkage.



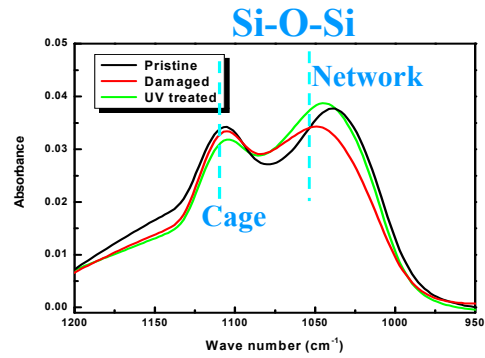
(a)



(b)



(c)



(d)

Figure 5-22: FTIR spectrum of pristine, O<sub>2</sub> damaged and UV cured low-k films. (a) the whole spectrum, (b) the -OH bond and physisorbed water, (c) Si-CH<sub>3</sub> Bond, and (d) Si-O-Si bond.

### 5.3.4. Thermal activation and UV interaction

To investigate the differences between pure thermal treatment and thermal assisted UV treatment, Oxygen plasma damaged low-k films were treated at different temperatures with or without UV radiation.

FTIR spectrums after plasma damage and then after thermal curing are compared in Figure 5-23. After thermal curing at 400°C for one hour, the silanol and physisorbed water was partially removed. This did not change the methyl bond but it did reduce the Si-O-Si cage bonds and increased the network bonds. The bonding changes of pure thermal curing were very similar to that of UV curing, suggesting the same reaction path (i.e. reaction (a) in Figure 5-19).

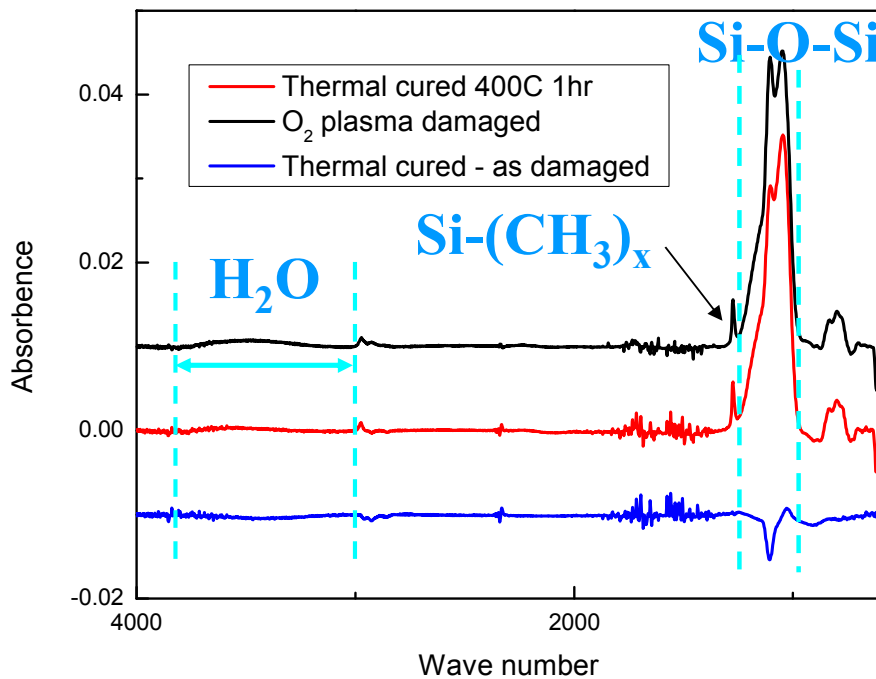


Figure 5-23: FTIR spectrums of low-k film after oxygen plasma damage and then after thermal curing at 400°C for 1 hour.

To differentiate the thermal curing effect and thermal assisted UV curing effect, thermal curing experiments at different temperature were conducted and compared with UV experiments. The FTIR methyl peak areas and –OH bonds areas are shown in Figure 5-24 and contact angle measurements are displayed in Figure 5-25. While the Si-CH<sub>3</sub> bonds remained the same for all treatment, the areas of –OH bonds showed clear differences. After one hour 200°C thermal curing in a high vacuum chamber, the –OH bonds and physisorbed water were only slightly removed. When the thermal curing temperature was increased to 400°C, the –OH and physisorbed water peak area was reduced to half after plasma damage. With a higher temperature, the surface hydrophobicity was recovered to a higher degree. Compared with UV thermal curing in a vacuum chamber, thermal curing alone takes much longer time and removes less silanol bonds and physisorbed water.

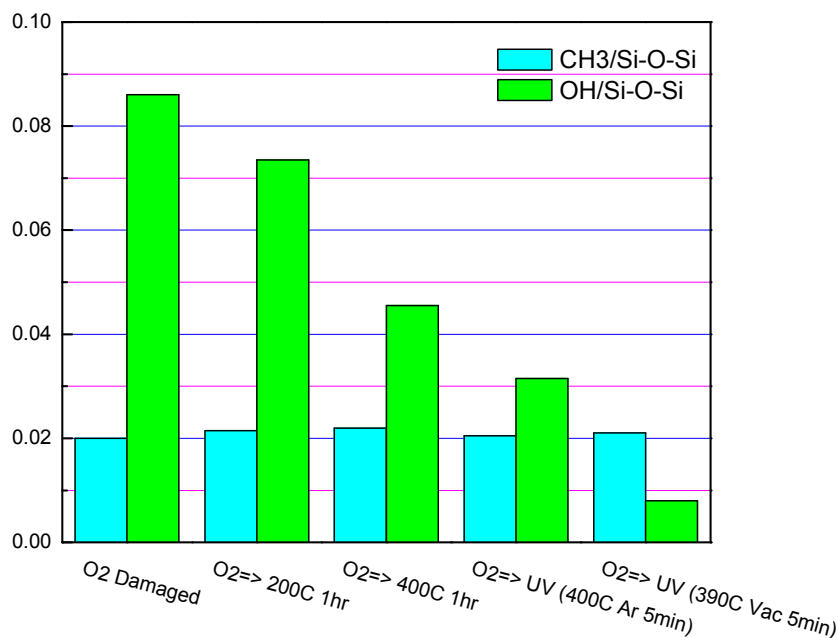


Figure 5-24: FTIR methyl peak and silanol peak of thermal cured and thermal assisted UV cured film

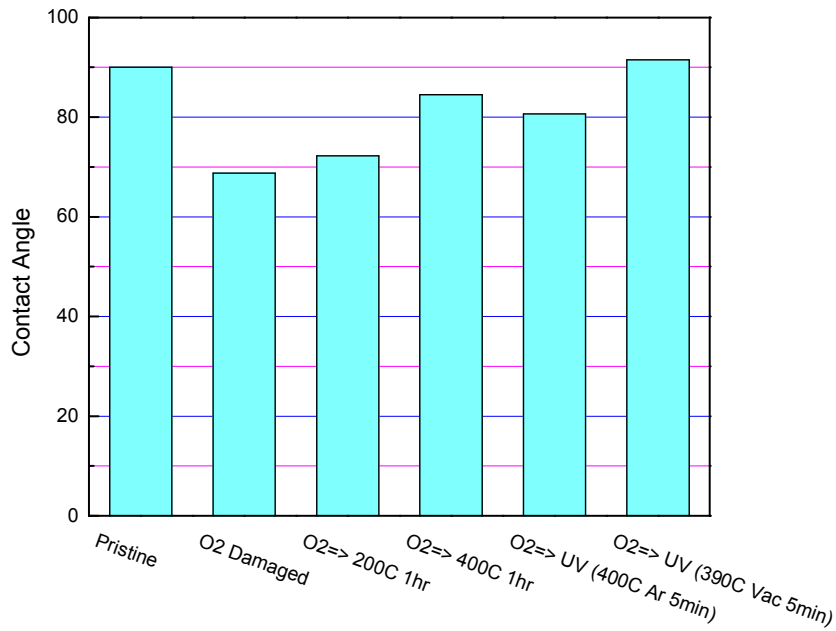


Figure 5-25: Contact angle of thermal cured and thermal assisted UV cured film

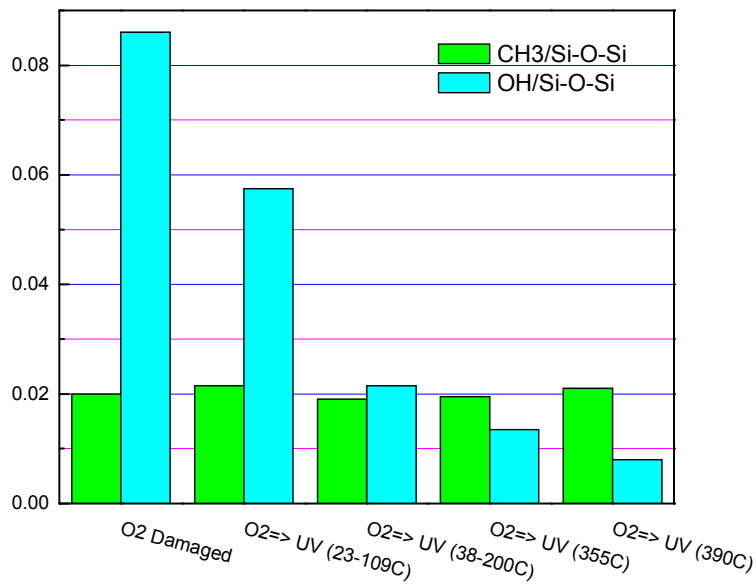


Figure 5-26: FTIR methyl peak and silanol peak of thermal assisted UV cured film at different curing temperatures.

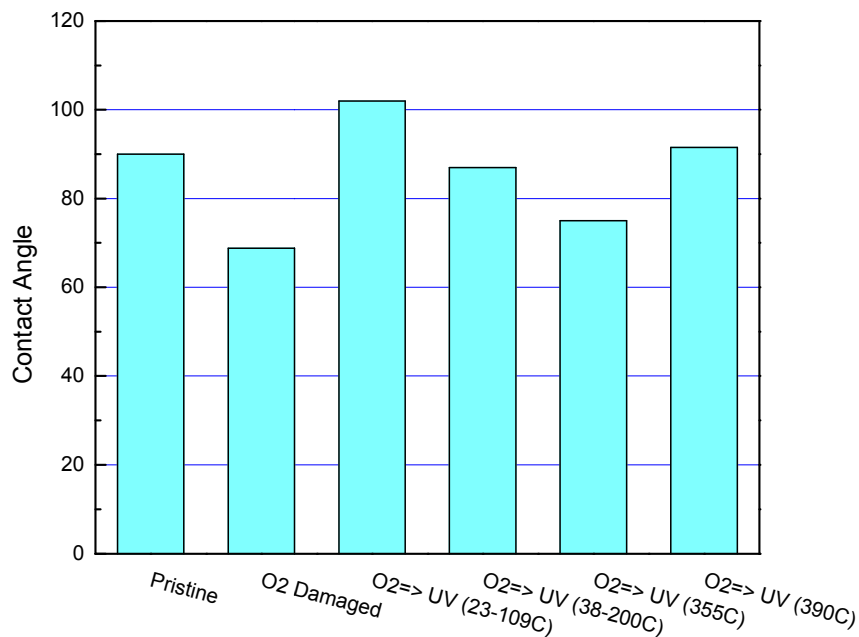


Figure 5-27: Contact angle measurement of thermal assisted UV cured film at different curing temperatures.

The different efficiency of thermal treatment and UV treatment may be related to the water desorption mechanisms in silica based dielectrics. There exist four types of water related chemical groups which are attached to the Si-O-Si skeleton[103][104]. These groups are denoted in the following figure, where  $\alpha$  is the physisorbed water,  $\beta$  is the tightly hydrogen-bonded silanols,  $\gamma_1$  is the hydrogen-bonded silanols, and  $\gamma_2$  is the isolated silanols.

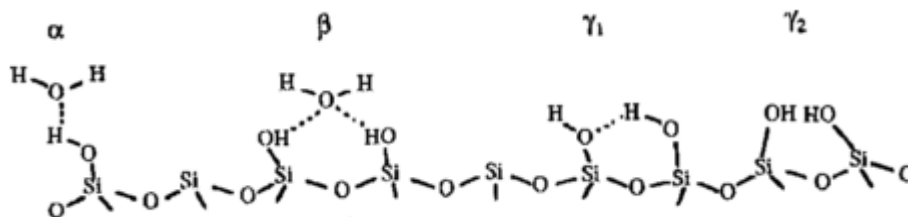
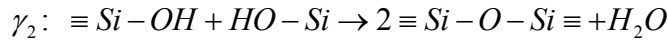
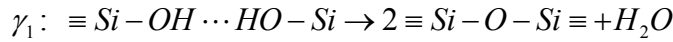


Figure 5-28: Schematic drawing of the various OH species in silica based dielectrics.

The water desorption process of each bonding group can be denoted by the following chemical equations:



In general, the chemical reaction rate is dependent on the temperature and can be described by the Arrhenius equation as

$$k = Ae^{-\frac{E_a}{RT}}$$

where  $k$  is the rate constant for the chemical reaction,  $A$  is the pre-exponential factor,  $E_a$  is the activation energy,  $R$  is the universal gas constant and  $T$  is the temperature. The Arrhenius parameters for those four water desorption processes have been measured by Proost et al.[29][30] using thermal desorption spectroscopy (TDS). Results of the measurements on blanket SOG low-k material are summarized in Table 5-4.

Water component	$A(s^{-1})$	$E_a$ (kJ/mol)	Assignment
$\alpha$	3.7	32	Physisorbed water
$\beta$	$6.0 \times 10^2$	55	Tightly hydrogen-bonded water
$\gamma_1$	$2.5 \times 10^4$	89	Hydrogen-bonded silanols
$\gamma_2$	$1.4 \times 10^{10}$	202	Isolated silanols

Table 5-4: Parameters for water desorption mechanisms[103][104]

Although the results from table 5-4 were measured from SOG materials, it is believed that SiCOH low-k material has very similar behavior[17]. The activation energy

is increasing from reaction  $\alpha$  to  $\gamma_2$ , therefore the temperature required for desorption is also increasing. Li et al. found that the desorption peaks of  $\alpha$  and  $\beta$  groups are at 70°C and 350 °C respectively[17], and the desorption of  $\gamma$  groups are expected at 700 °C. This explains the temperature dependence of water components removal by FTIR measurement in Figure 5-24. The FTIR water and silanol bonding peak monitors all four water groups together. The thermal treatment at 200 °C for one hour mainly removed the  $\alpha$  water group, while the 400 °C thermal treatment for one hour removed both  $\alpha$  and  $\beta$  groups. After 400 °C thermal treatment, there were still significant amount of water groups remaining in the low-k film, which is believed to be the  $\gamma_1$  and  $\gamma_2$  groups. Efficient removal of those groups need annealing temperature of 700 °C or above, which is beyond the chemical stability requirement for low-k materials. However, UV photons can directly supply the activation energy required by  $\gamma$  groups desorption reactions, making it possible to remove those groups at relatively low temperature.

Although UV treatment at 400 °C was the most effective to remove water groups, UV treatment at low temperature in general is less effective as showing in Figure 5-26. The roles of temperature on UV curing can be explained by two possible reasons besides direct removal of water by heat. First and most important, high temperature heating can significantly increase the reaction speed of UV photon induced water desorption reactions. Photon dipole interaction is not temperature dependent; instead it depends on the photon intensity. However, the formation of the new bonds is a typical chemical reaction, therefore it follows the Arrhenius equation and exponentially depends on temperature. Second, a higher temperature increases the mobility of the matrix material, so that  $\gamma_2$  reaction between silanol bonds that are not next to each other could be promoted. Thermal activation of UV curing has already been observed by other groups. For example, Iacopi et al. reported that the 350 °C 300s UV process curing increased the

modulus of OSG low-k by 15%, where modulus improvement was believed to a result from cross-linking by silanol condensation ( $\gamma$  reactions) between Si-O-Si backbone lines[100]. However, at 400 °C, it was improved by 40-45%, indicating the temperature dependence of UV curing is very sensitive.

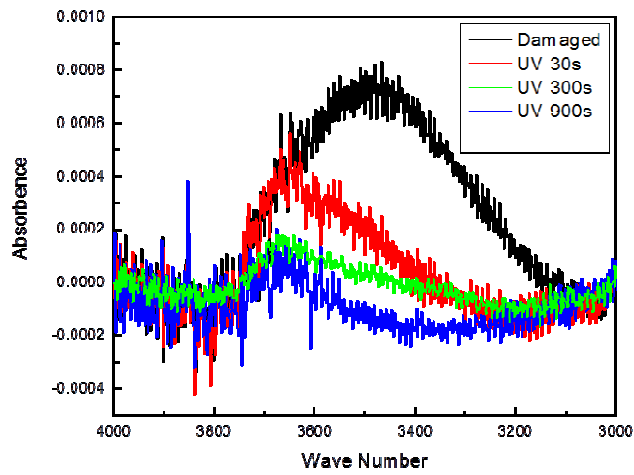
### **5.3.5. Other process optimizations**

To improve the efficiency of the UV curing dielectric recovery process, many adjustable parameters could be optimized, including the wavelength (energy) and intensity of the light source, the thermal curing temperature, the treatment time, the ambient gas type and pressure. The UV wavelength needs to be low enough to enable the water desorption reactions but not too low to damage the methyl bonds, which was discussed in detail in section 5.3.2. The photon density is directly related to the photon absorption probability (Appendix). Higher lamp power and closer sample lamp distance are expected to provide higher photon density, thus to increase the UV curing efficiency. However, it also increases the surface heating, making the process difficult to control. The treatment temperature needs to be as high as possible to provide thermal activation and efficiency, but still within the range of chemical stability and process compatibility. Therefore 400°C is recommended and the experimental details were presented in section 5.3.4. The effects of UV curing time and ambient will be presented in later sections.

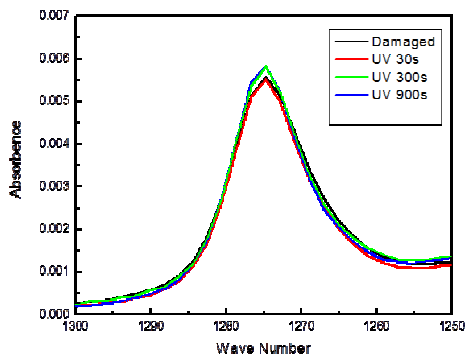
#### ***Recovery Time***

It is expected that more reduction in water and silanol group can be obtained with increasing UV curing time. The experimental result confirmed this expectation. FTIR peak analysis in Figure 5-29, shows that the water and silanol peak area reduced as time increases but the methyl bond peak remained the same. Contact angle measurement results in Figure 5-30 shows the surface hydrophobicity increased even with 30s

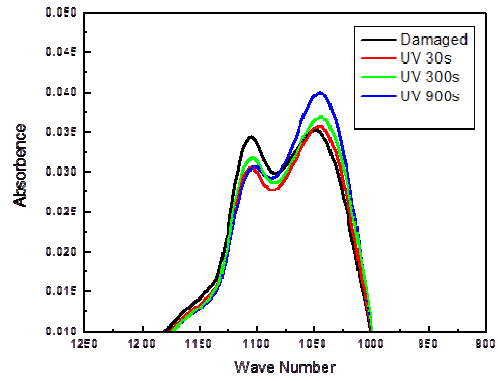
treatment but did not change much with exposure time. Considering the process efficiency and over-heating of the lamp, most of the experiments were conducted with a 300 seconds exposure time.



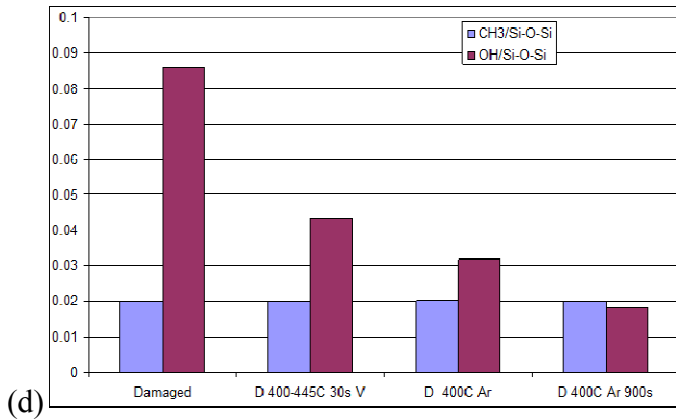
(a)



(b)



(c)



(d)

Figure 5-29: FTIR methyl peak and silanol peak of thermal assisted UV cured film at different curing temperature.

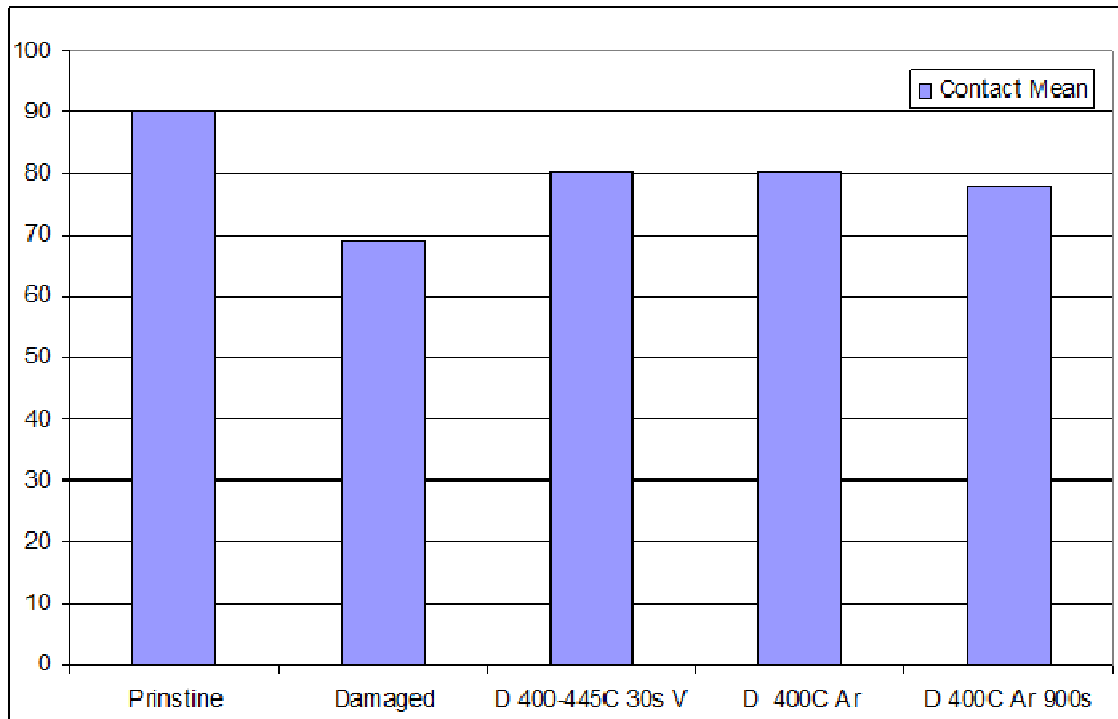


Figure 5-30: Contact angle measurement of thermal assisted UV cured film at different curing time.

***Ambient effect***

The ambient, in which the UV curing process is conducted, is a factor that could potentially affect the result of UV curing. First, the ambient gas may absorb the UV light depending on its absorption characteristics. For example, air absorbs UV light with wavelength lower than about 200nm, which defines the term “Vacuum UV”. On the other hand, pure nitrogen is transparent to wavelengths in the range about 150–200nm. For this study, the UV light went through an air cooling system and a quartz window, where VUV was already removed from the light source. Consequently, absorption of the chamber ambient was not a major concern. Second, the ambient gas species could react with the material in the UV chamber in the presence of UV photons and heat. This included direct

reactions with gas species or with UV induced radicals and metastable gas atoms. The ambient gas species needed to be carefully selected to avoid detrimental reactions. Third, since the UV light generates a significant amount of heat, the ambient gas could also be selected to help with heat transfer to control the film temperature.

The ambient effect was first tested on pristine films with ambient condition: vacuum, 10 Torr argon and 10 Torr carbon dioxide. The surface carbon concentration was unchanged within the error range as displayed in Figure 5-31. The results measured in 30 degree exit angle were smaller than 90 degree, indicating the material close to the surface has slightly smaller carbon concentration. This means the surface may have been damaged by the UV photon, but the damage is restricted to a very small range (<2nm) and the effect is small. The FTIR result in Figure 5-32 shows the water and silanol bonds in the pristine film can be further reduced by UV treatment. This was confirmed by water contact angle measurement (Figure 5-33). Since the change was very small, the effects of various ambient cannot be differentiated.

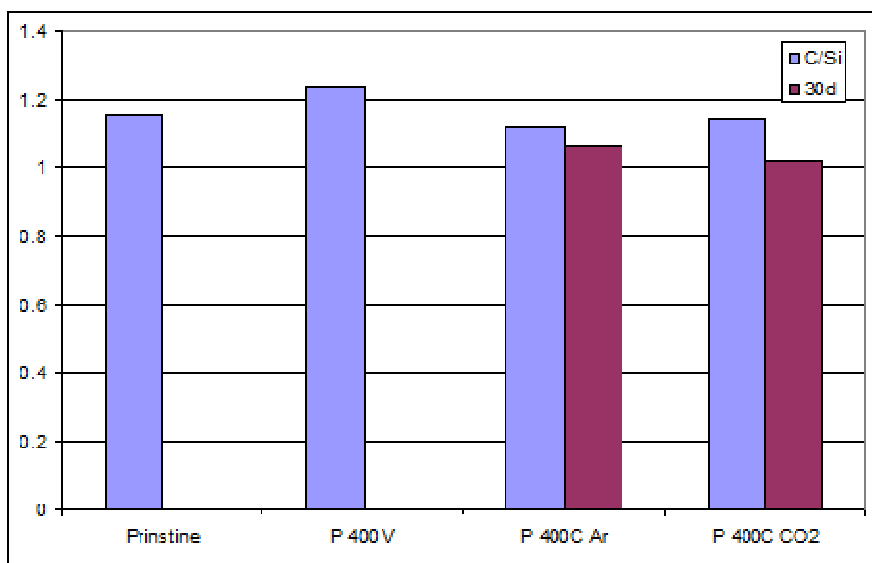


Figure 5-31: XPS surface carbon of UV treated pristine low-k material under different chamber ambient.

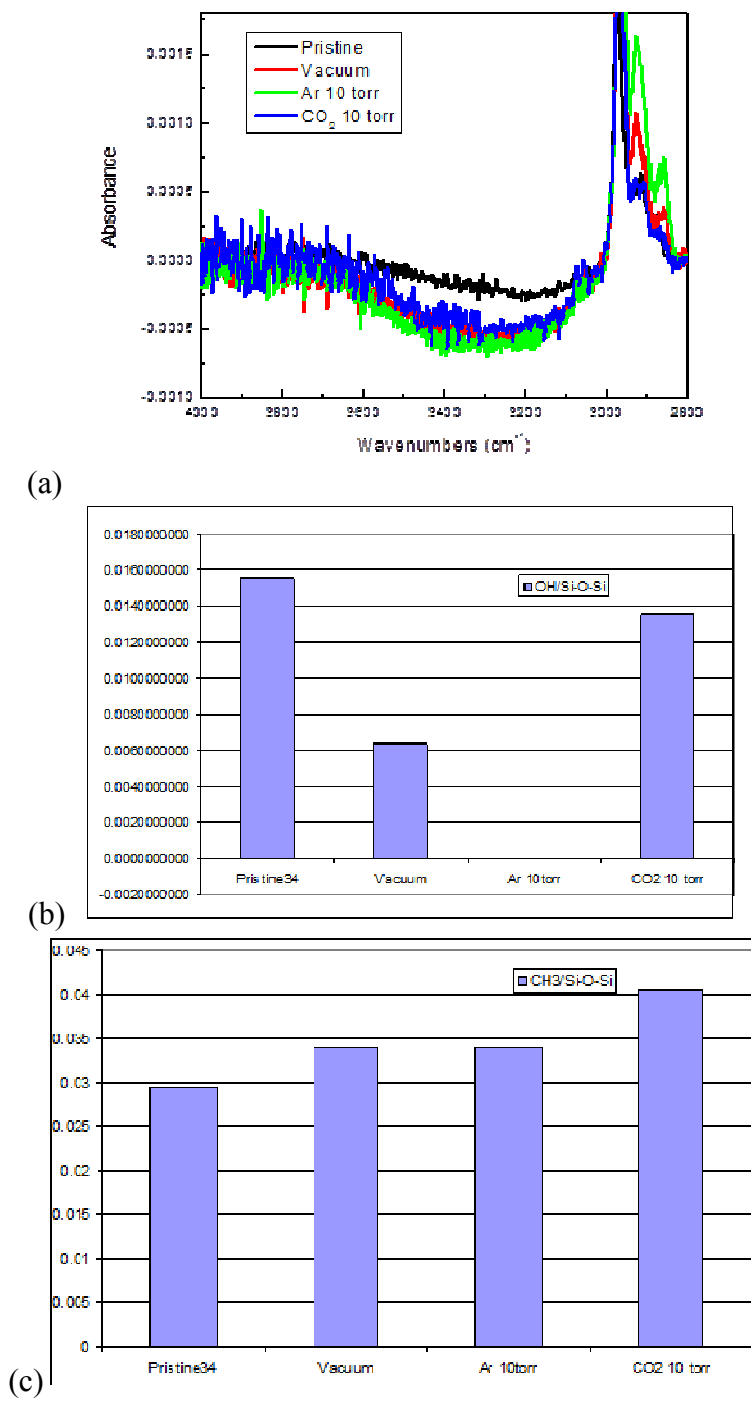


Figure 5-32: FTIR silanol bonds and methyl bonds peak areas of UV treated pristine low-k material under different chamber ambient. (a) FTIR silanol spectrum, (b) FTIR silanol bonding peak ratio, (c) methyl bonds.

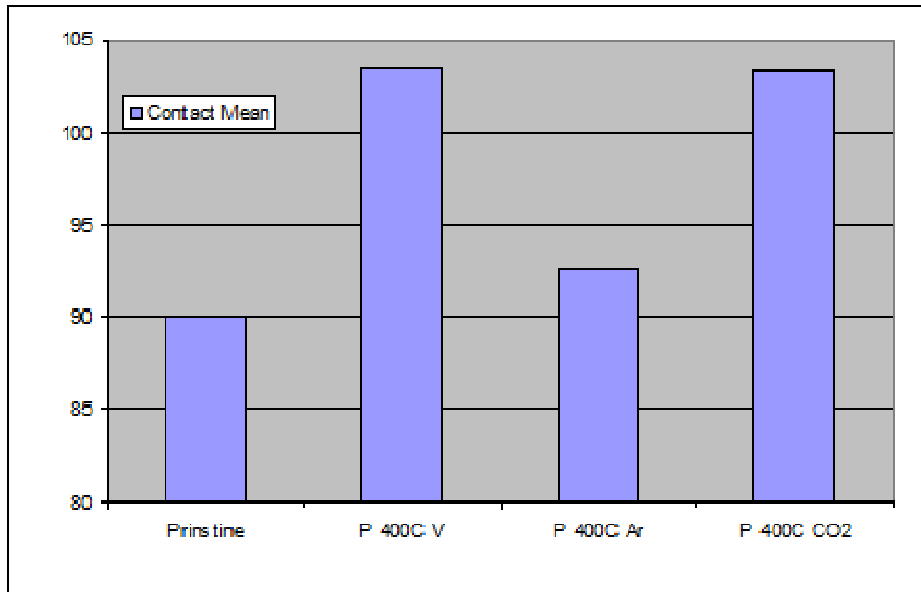


Figure 5-33: Contact angles of UV treated pristine low-k material under different chamber ambient

The ambient effect was then tested on oxygen plasma damaged low-k films. The FTIR and contact angle measurement are shown in Figure 5-34 and Figure 5-35 respectively. Similar to the result of pristine film experiments, the methyl bond peaks are unchanged indicating no significant carbon consuming reactions. Vacuum ambient is the most efficient in water and silanol removal as indicated in FTIR  $-OH$  peak area and surface water contact angle. This may be due to two reasons. One, vacuum is more effective in removing the product of desorption reaction, namely the water vapor. On the other hand, vacuum is the worst in conducting the heat generated by UV radiation, causing the highest effective temperature on the film, which promotes the desorption reaction. The last aspect could become a disadvantage because it could potentially affect temperature control and damage the film with high temperature.

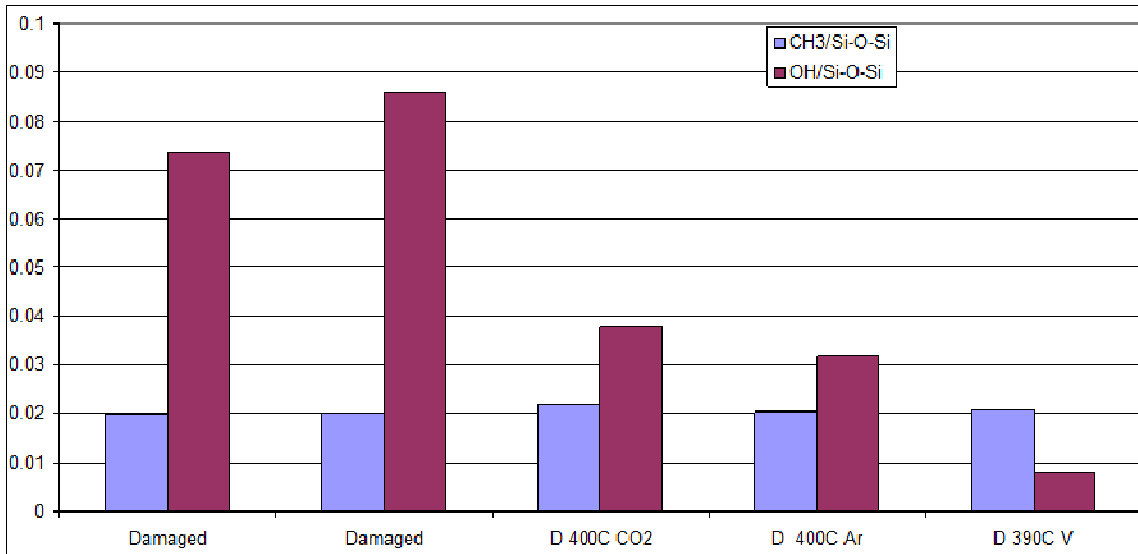


Figure 5-34: FTIR of ambient effect of damaged film, vacuum cure is the best on water removal.

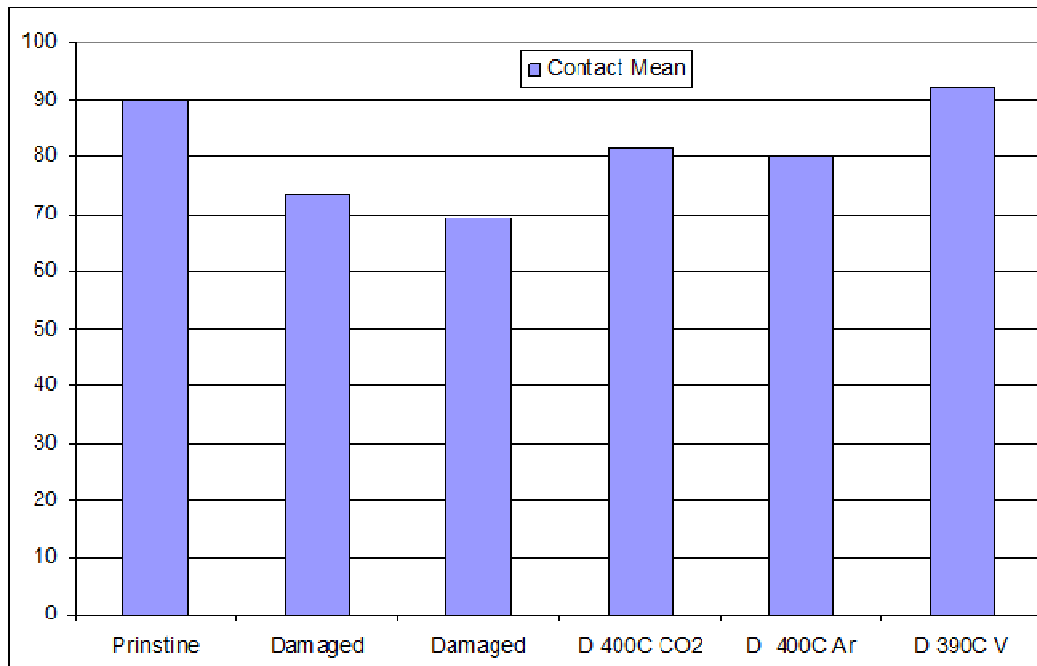


Figure 5-35: Contact angle of the film to show the ambient effect on curing.

## 5.4. UV AND SILYLATION COMBINED

### 5.4.1. Overview:

In sections 5.2 and 5.3, silylation and UV thermal process for dielectric recovery of low-k material were discussed separately in detail. Their advantages and disadvantages were compared in Table 5-5. Silylation excels in recovering the surface hydrophobicity and surface carbon but the recovery was limited to the surface. UV can penetrate deep into the bulk of the low-k materials and can effectively remove the bulk silanol which silylation process failed to accomplish. However, UV thermal process cannot recover the carbon concentration and only partially recovers the surface hydrophobicity. It is expected that by combining these two processes, a better recovering effect can be achieved, which is the objective of this part of the study.

	<b>Silylation</b>	<b>UV</b>
<b>Pro</b>	Surface hydrophobicity and surface carbon were recovered.	Bulk water was almost completely removed.
<b>Con</b>	Bulk water was not removed. Recovery was limited to the surface.	Carbon has no change or slightly reduced, surface hydrophobicity was only partially recovered.
<b>Optimization</b>	Relatively low temperature and long treatment time.	Relatively high temperature and short treatment time.

Table 5-5: Comparison of silylation and UV process.

The question is how to combine these methods to improve dielectric recovery. Silylation process is optimized at relatively low temperatures (130°C) and normally requires long treatment time. UV thermal treatment needs high temperature (around

400°C) for thermal activation. At that temperature the final product of silylation is becoming unstable. This presents a potential challenge for designing an effective combined process for low k integrations.

#### **5.4.2. Experimental results and analysis**

Experiments combining silylation and UV thermal processing were performed in the system described in Section 5.1. The OSG low-k film was first damaged with a standard oxygen plasma recipe (CCP RIE, 300 seconds, power 150W, pressure 20 Torr, gas flow 20 sccm) and treated with a combined recovery methods, including sequential and simultaneous processes.

##### **5.4.2.1. Sequential process**

In the sequential process, the damaged low-k materials were treated in a sequential order using both silylation and UV processes in their individually optimized conditions. The conditions of the silylation process are: temperature 130°C, chamber pressure 20 Torr and treatment time one hour, while conditions of the UV process are: stage temperature 400 °C, chamber ambient Ar at 10 Torr and treatment time 300 seconds. Importantly, our unique setup can conduct the sequential process without exposing the sample to air (moisture).

The surface carbon concentration and hydrophobicity are illustrated in Figure 3-36 with XPS C/Si ratios and contact angle measurements. Results from FTIR measurements indicated changes of the bulk and the  $\text{-OH/Si-O-Si}$  and  $\text{-CH}_3/\text{Si-O-Si}$  peak ratios, which are shown in Figure 5-37. In comparison, sequential treatments achieved better surface dielectric recovery than UV treatment alone. And “UV radiation first, then silylation” sequential treatment achieved a better surface dielectric and bulk methyl recovery and moisture removal than “silylation first, then UV radiation”.

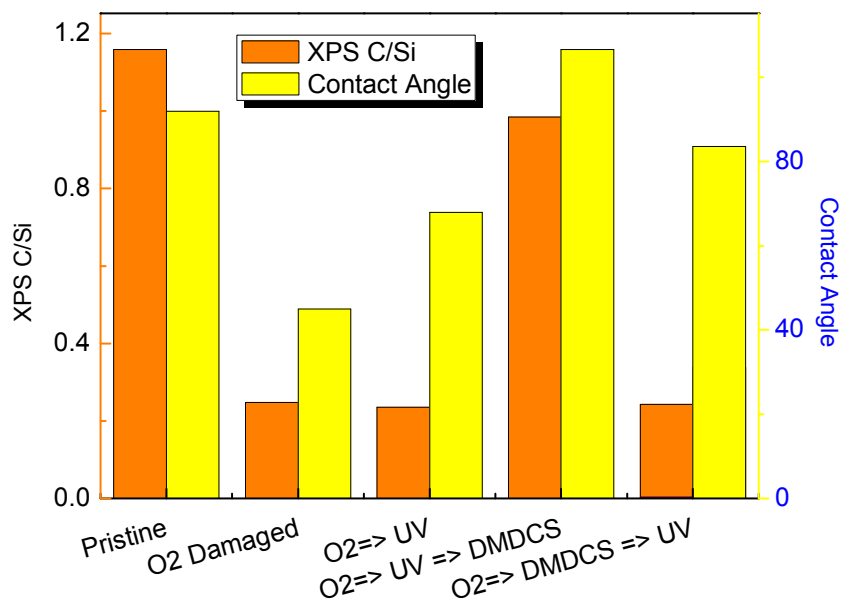


Figure 5-36: XPS and Contact angle measurement results of sequential treatments

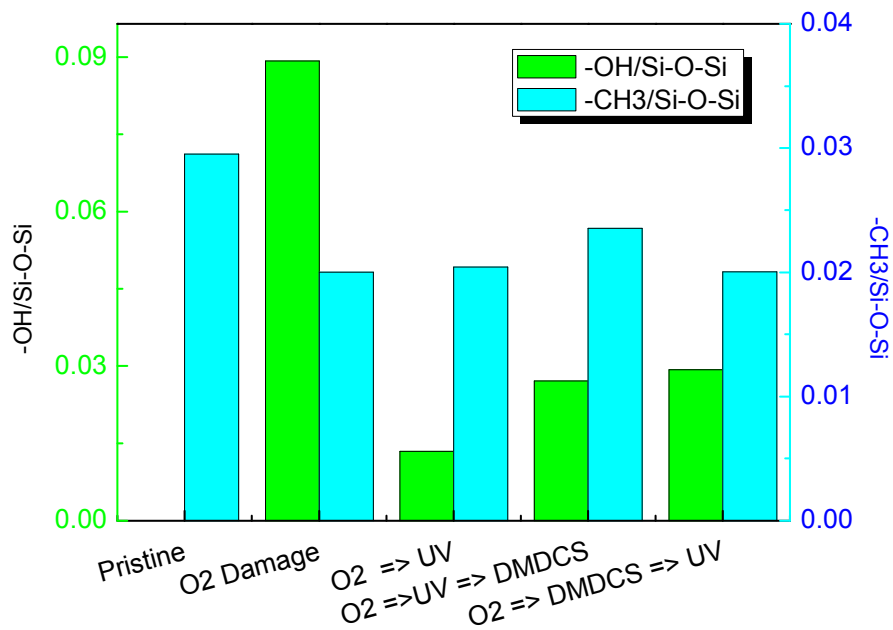


Figure 5-37: FTIR silanol and methyl bond peak area ratio of sequential treatments.

The experiment observation of “UV radiation first, then silylation” seems difficult to explain at first look because the UV radiation removes silanol bonds that are the reactive bonds for the silylation reactions. However, silanol condensation reactions activated by UV radiation required two adjunct silanol bonds, leaving unreacted isolated silanol bonds on the surface of low-k film for the sequential silylation process. More importantly, UV radiation could generate reactive sites on the surface for the following silylation reactions. The surface defects initiated by UV radiation in SiO<sub>2</sub> have been reported in many studies[32][33]. These defects, including the E' centers and silicon dangling bonds, could serve as reaction sites for silylation functional groups. Specifically, Chikaki et al. reported that the UV irradiation (172nm) of Porous-SiO (k=1.9) contributes to improving the following silylation anneal with TMCTS[107]. On the other hand, surface carbon in our study did not increase at all after “silylation first, then UV radiation” treatment. This is probably due to the weak chemical bonding of silylation ending groups, which were burned away by the following UV thermal radiation.

#### **5.4.2.2. Simultaneous process**

The silylation and UV simultaneous treatment was conducted on oxygen plasma damaged OSG low-k films at sample temperatures 400 °C and 130 °C. The process time and pressure are identical at 5 minutes and 20 Torr. The surface carbon concentration by XPS and surface hydrophobicity by contact angle measurement are presented in Figure 5-38. The bulk silanol and methyl bond peak ratios measured by FTIR are illustrated in Figure 5-39. It appears that the surface recovery and moisture removal induced by simultaneous treatments depended on the process temperature. At 130 °C the process favors silylation and therefore better surface recovery is achieved. At 400 °C, the process favors UV treatment and therefore bulk water and silanol bonds removal is more

effective. How to optimize the simultaneous process for both surface and bulk recovery is a challenge.

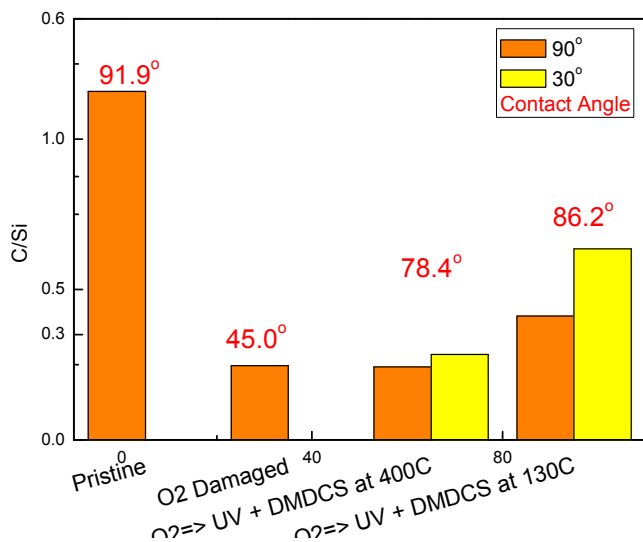


Figure 5-38: XPS and Contact angle measurement results of simultaneous silylation and UV treatments.

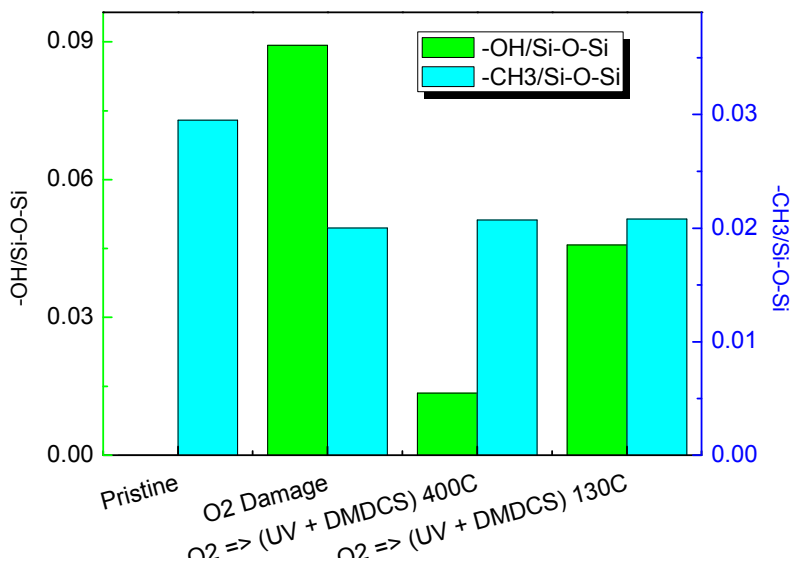


Figure 5-39: FTIR silanol and methyl bond peak area ratios of simultaneous silylation and UV treatments.

To evaluate the synergistic effect of silylation and UV treatment, the simultaneous process was compared to a sequential process at the same condition. This means that both the silylation and the UV treatment in the sequential process were conducted at 130 °C for 5 minutes under the same CO<sub>2</sub> ambient instead of their optimized recipes. The DMDCS silylation process was also conducted with the same treatment time and temperature for comparison.

Results were analyzed in a similar manner as before. The surface carbon concentration measured by XPS and surface hydrophobicity measured by contact angles are presented in Figure 5-40, and the bulk silanol and methyl bond peak ratios measured by FTIR are illustrated in Figure 5-41. These results show that both sequential and simultaneous treatments are better than the silylation process alone for surface dielectric recovery. Simultaneous treatment is more effective than the sequential treatment for surface dielectric recovery and moisture removal. This indicates that the UV and silylation agents act synergistically in low-k dielectric recovery. Two possible mechanisms are proposed. One, as explained earlier in sequential experiments, UV could create active sites for the silylation reactions. And the other one is, similar to the UV induced silanol condensation, that the UV photon energy could lower the reaction barrier and increase the rate of the silylation reactions. The results observed in this study clearly show that the silylation and UV simultaneous treatment can be used to improve the efficiency of the low k dielectric recovery process.

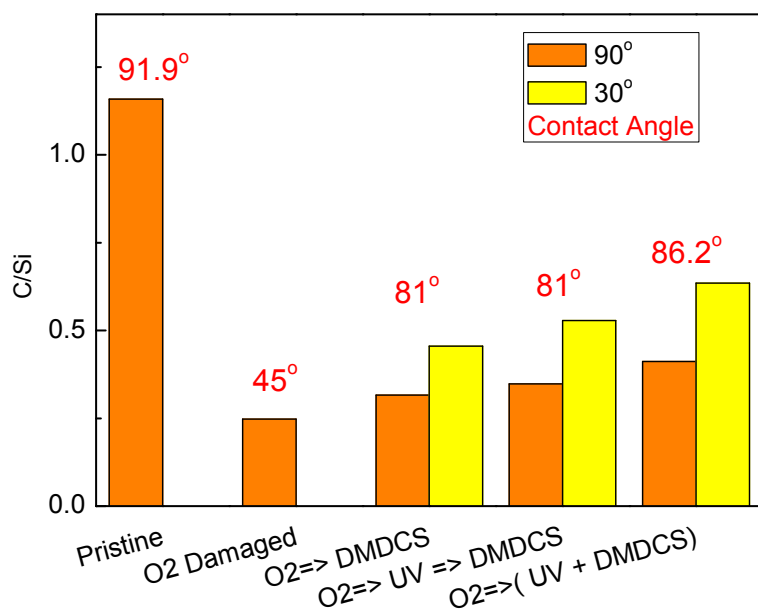


Figure 5-40: Comparison of XPS and Contact angle measurement results of sequential and simultaneous treatments.

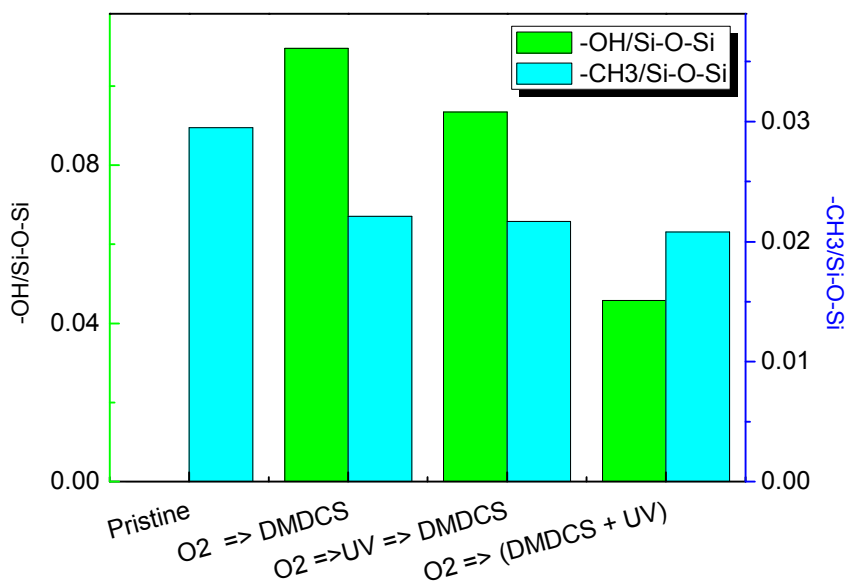


Figure 5-41: Comparison of FTIR silanol and methyl bond peak area ratios of sequential and simultaneous treatments.

## 5.5. SUMMARY

In this chapter, we explored dielectric recovery methods for plasma damaged low-k films, including silylation, UV thermal treatment and their combined processes. After silylation, surface carbon and hydrophobicity were partially recovered. DMDCS was found to be more effective than TMCS, which was attributed to steric hindrance effect. Super critical carbon dioxide silylation was found to be effective in improving the efficiency of the recovery process. However, the carbon restorations were found to be limited to the surface due to the molecular size of the silylation agents. UV treatment with 400°C thermal activation can effectively remove water from the bulk of damaged film. In comparison, thermal treatment alone or UV treatment at low temperature only partially reduced the silanol and water peak as observed by FTIR.

In general, the combination of UV and silylation can achieve better surface recoveries than UV alone. The UV first followed by silylation provided a better recovery in sequential processes. However, under the same conditions, simultaneous treatments achieved better bulk and surface recovery than the sequential process. The best recovery effect is achieved by a UV 400°C 5 minutes treatment followed by a 130°C DMDCS 1 hour silylation.

## Chapter 6: Summary and future work

### 6.1 SUMMARY

Plasma induced damage in etching and stripping processes presents a great challenge for integration of the porous low-k material into the on-chip interconnects. The objective of this dissertation is to study the mechanism of plasma damage to porous low k dielectrics and to develop methods and processes to restore the plasma damage in porous low k materials for process integration. The studies carried out in this dissertation followed two approaches. One approach was to investigate the mechanism of the plasma low-k interaction with the aim to minimize the plasma induced damage. Due to the different functionalities and plasma chemistry of the plasma etching and stripping processes, the etching plasma study was focused on the surface roughness formation and the stripping plasma study was focused on the roles of individual plasma constituents, particularly the kinetics of damage formation induced by the radicals in the plasma. The other approach was to develop processes to recover the low-k properties after the plasma damage processes in order to improve the low k dielectrics for integration into interconnect structures.

Chapter 3 focused on the plasma damage to ULK material from the etching process. The etch-front roughening phenomenon was studied by varying the plasma conditions in a  $\text{CHF}_3$  based RIE plasma. The surface roughness after etching and after DHF dipping was measured by AFM and then correlated with surface polymerization by XPS analysis. Intense surface roughening was found in the low polymerization region. A surface roughening mechanism was proposed as a complicated process which can be traced to the porous nature of the ULK material. Small pits were initiated with the uneven surface polymer distribution caused by ion-shadowing of the porous structure and then intensified by the ion induced surface densification. With  $\text{O}_2$  addition, the surface

roughness and the etch rate were significantly increased due to the radical diffusion process. The ion induced densification layer reduces the radical diffusion, creating a significant etch rate difference between the top and the bottom of the pits, resulting a larger surface roughness. However, all of this roughening process can be suppressed with high surface polymerization. Since the etch rate decreased linearly with the extent of surface polymerization, the roughness vs etch rate ratio can be optimized at the edge of the region, which is defined as the “threshold point”.

In plasma stripping process, oxygen plasma not only effectively removed the photoresist but also caused significant damage to the porous ULK material. Chapter 4 investigated the mechanism of oxygen plasma damage to the porous SiCOH films.

An on-wafer filter system was applied to study the individual and synergistic effect of ions, radicals and photon radiations with different energy ranges. Ions at low energy range were found to reduce the plasma damage. This was explained by the formation of the densification layer due to ion bombardment blocking the radical diffusion. Photon radiations alone did not cause notable damage under the cover of MgF<sub>2</sub> window. However, VUV photons in the wavelength range of 125 nm to 185 nm act synergistically with oxygen radicals and enhance the low-k damage. This mechanism is explained as due to the direct session of the Si-CH<sub>3</sub> bond by interacting with the high-energy photons as well as the photo-dissociation of the oxygen molecules. A special gap-structure experiment confirmed the photo-dissociation effect.

The kinetics of damage formation by radicals was investigated taking into account the diffusion process from the low-k surface to the pore structures, reaction with the low-k carbon groups and recombination on the surface of the pore wall. Considering the carbon consumption in the low-k film, an analytic solution of the carbon depletion depth was derived from a Thiele modulus approach. Based on this approach, a plasma altered

layer model was developed. This model predicted that the damage can be reduced by decreasing the pore size, increasing the carbon concentration or increasing the radical recombination rate without compromising the PR stripping effect. The kinetics of the damage formation process was then simulated by a Monte Carlo method. The simulation result confirms the predictions of the analytic solution. Furthermore, the carbon profile information can be used to study the correlation of the reaction and recombination rates.

The analytical method used in plasma altered layer model was applied to study the radical kinetics in the low-k patterned structure in combination with a hardmask design. The radical density on low-k was predicted and confirmed for increasing hardmask thickness, oxygen reaction and recombination rate. A gap structure with a Si top was used to simulate the trench condition and the result showed that the damage can be reduced by using a high carbon containing hardmask material.

In Chapter 5, a dielectric repair UHV system was developed integrating silylation and UV treatments. The dielectric recovery was studied using silylation and UV broadband thermal treatment, both individually and in combination. After silylation, surface carbon and hydrophobicity were partially recovered. DMDCS was found to be more effective than TMCS. In comparison, UV treatment can effectively remove water from the bulk of damaged film and consolidate the silanol bonds with the help of thermal activation. The combination of UV and silylation treatments can achieve better surface recoveries than UV alone. The “UV first” treatment provided a better recovery in sequential processes. Under the same conditions, simultaneous treatments by silylation and UV irradiation achieved better bulk and surface recovery than the sequential process.

## 6.2. RECOMMENDATIONS FOR THE ULK PLASMA PROCESS INTEGRATION

Combining the results from this dissertation and references in this area, an overall recommendation can be made for the integration of the porous SiCOH into the on-chip interconnects of the future technology nodes.

For etching process, the surface polymerization is critical to the roughness formation. The surface roughening zone should be avoided. Surface roughness vs etch rate can be optimized at the surface polymerization of the “threshold point” as defined in Chapter 3. However, the surface polymerization is also important at the sidewalls of the etch profile, as it prevents radial diffusing into the bulk low-k. Both factors have to be considered for optimization of the plasma process. In the etch process, oxygen radicals greatly increase the etch rate. However, they also significantly damage the low-k on the side wall. As a result, the oxygen addition should be avoided or minimized. High-density plasma (e.g. ICP) increases the radical density and photon intensity, thereby inducing more damage to the low-k material. CCP plasma with low plasma densities should be used in the plasma etching process.

For stripping process, the plasma can be further reduced by applying the downstream plasma. A grid can be placed in the downstream plasma to shade the detrimental photon radiations from the plasma body. Although the grid also blocks the ions, the ions are not required for the stripping or ashing process. Oxygen plasma is the worst enemy of low-k as the oxygen radicals easily remove all hydrocarbons from the low-k. To reduce the low-k damage, CO<sub>2</sub> can be used to replace O<sub>2</sub>[108][109]. However reductive plasma such as hydrogen plasma would be a better choice than the oxidative plasmas[110]. The drawback of hydrogen plasma is the high photon emission. This would not be a problem by using a grid to shade the photons. Therefore, the remote

hydrogen plasma with photon shading grids may be the best choice to minimize the stripping damage.

Finally, the damage to some extent could be restored by silylation or UV treatment. The recovery step becomes increasingly necessary as the feature size continues to shrink. Silylation and UV treatment can be used together to provide a better recovery effect.

### **6.3. FUTURE WORK**

In Chapter 3, the surface polymerization rate was found to be critical for formation of surface roughness. The surface polymerization is controlled by the  $\text{CHF}_3$  ratio in the feeding gas in this study. Ion energy is well known as another key factor for inducing the surface polymerization. It would be interesting to study the ion energy effect on the roughness effect. However, the ion energy is coupled with plasma density in the CCP etcher, thus an ICP-RIE system is needed for this study.

In Chapter 4, a semi-2D Monte Carlo code is used to simulate the profile and provide comparative predictions. This code can be further developed to represent the real material density and geometry. With integration of actual atomic reaction and collisions, the computer simulation can predict the damage process parameters such as carbon depletion depth with real physical units. More accurate simulations can be developed based on an existing (commercial) Monte Carlo code used for material simulation.

The mechanism of UV curing could be better understood by adding a residual gas analyzer (RGA) to the dual process chamber described in Chapter 5. RGA can analyze the reaction products of the UV curing process. Together with precise control of the heating stage, thermal desorption spectra (TDS) can be measured to further understand the temperature effects of the UV thermal curing process.

New silylation agent could be tested. The silylation by-products of TMCS and DMDCS contain corrosive HCl which damages the process chamber and the chips. (Bis)dimethylaminodimethylsilane (BDMADMS), (Bis)dimethylaminomethylsilane (BDMAMS), which use ammonia as functional group, are promising candidate. Silylation agents with smaller molecular size have the potential of increasing recovery depth. Recently, a new attempt to reduce the size of the repair agent was made by Nagano et al. by using methylating chemicals Dimethyl Carbonate (DMC) and Dipivaloyl Methane (DPM)[111].

## References

- [1] G. E. Moore, "Cramming more components onto integrated circuits," *Electronics*, vol. 38, no. 8, 1965.
- [2] R. H. Havemann and J. a. Hutchby, "High-performance interconnects: an integration overview," *Proceedings of the IEEE*, vol. 89, no. 5, pp. 586-601, May 2001.
- [3] M. T. Bohr, "Interconnect scaling - The real limiter to high performance ULSI," *International Electron Devices Meeting, 1995 - Iedm Technical Digest*, p. 241, 1995.
- [4] N. Weste and D. Harris, "CMOS VLSI Design: A Circuits and Systems Perspective," *Addison Wesley*, 2005.
- [5] C. Kittel, *Introduction to solid state physics*. Wiley, 1996.
- [6] M. Morgen, E. T. Ryan, J. H. Zhao, C. Hu, T. H. Cho, and P. S. Ho, "Low dielectric constant materials for ULSI interconnects," *Annual Review of Materials Science*, vol. 30, pp. 645-680, 2000.
- [7] K. Maex, M. R. Baklanov, D. Shamiryan, F. Lacopi, S. H. Brongersma, and Z. S. Yanovitskaya, "Low dielectric constant materials for microelectronics," *Journal of Applied Physics*, vol. 93, no. 11, p. 8793, 2003.
- [8] W. Volksen, R. D. Miller, and G. Dubois, "Low dielectric constant materials.," *Chemical reviews*, vol. 110, no. 1, pp. 56-110, Jan. 2010.
- [9] A. Grill, "Porous pSiCOH Ultralow- k Dielectrics for Chip Interconnects Prepared by PECVD," *Annual Review of Materials Research*, vol. 39, no. 1, pp. 49-69, Aug. 2009.
- [10] P. T. Liu et al., "Enhancing the oxygen plasma resistance of low-k methylsilsequioxane by H-2 plasma treatment," *Japanese Journal of Applied Physics Part I-Regular Papers Short Notes & Review Papers*, vol. 38, no. 6A, pp. 3482-3486, 1999.
- [11] M. Gallitre et al., "Impact of Direct CMP on Porous ULK Properties and Interconnect Propagation Performance on a Wide Frequency Bandwidth," *Advanced Metallization Conference 2008 (Amc 2008)*, 2008.
- [12] hamed chaabouni et al., "Porous SiOCH Ultra Low-k Recovery Treatments After Direct CMP Process," *Advanced Metallization Conference 2008 (AMC2008)*, 2008.
- [13] J. E. Stevens, "Plasma Fundamentals for Materials Processing," in *Handbook of Advanced Plasma Processing Techniques*, 2000, p. 33.

- [14] S. Samukawa, K. Sakamoto, and K. Ichiki, "Generating high-efficiency neutral beams by using negative ions in an inductively coupled plasma source," *Journal of Vacuum Science & Technology A: Vacuum, Surfaces, and Films*, vol. 20, no. 5, p. 1566, 2002.
- [15] B. Jinnai, T. Nozawa, and S. Samukawa, "Damage mechanism in low-dielectric (low-k) films during plasma processes," *Journal of Vacuum Science & Technology B: Microelectronics and Nanometer Structures*, vol. 26, no. 6, p. 1926, 2008.
- [16] J. Bao et al., "Oxygen plasma damage to blanket and patterned ultralow-kappa surfaces," *Journal of Vacuum Science & Technology A*, vol. 28, no. 2, pp. 207-215, 2010.
- [17] Y. L. Li et al., "Influence of absorbed water components on SiOCH low-k reliability," *Journal of Applied Physics*, vol. 104, no. 3, p. -, 2008.
- [18] B. C. Bittel, P. M. Lenahan, and S. W. King, "Ultraviolet radiation effects on paramagnetic defects in low- $\kappa$  dielectrics for ultralarge scale integrated circuit interconnects," *Applied Physics Letters*, vol. 97, no. 6, p. 063506, 2010.
- [19] D. Moore, C. Waldfried, P. Sakthivel, O. Escorcía, A. Technologies, and C. H. Drive, "UV Curing Effects of Low-k Materials under Reactive Conditions," *Materials Research*, vol. 1079, no. 1, 2008.
- [20] A. Grill and D. a. Neumayer, "Structure of low dielectric constant to extreme low dielectric constant SiCOH films: Fourier transform infrared spectroscopy characterization," *Journal of Applied Physics*, vol. 94, no. 10, p. 6697, 2003.
- [21] Y. B. Lin, T. Y. Tsui, and J. J. Vlassak, "Octamethylcyclotetrasiloxane-based, low-permittivity organosilicate coatings - Composition, structure, and polarizability," *Journal of the Electrochemical Society*, vol. 153, no. 7, p. F144-F152, 2006.
- [22] a. Grill and V. Patel, "The Effect of Plasma Chemistry on the Damage Induced to Porous SiCOH Dielectrics," *Journal of The Electrochemical Society*, vol. 153, no. 8, p. F169, 2006.
- [23] P. J. Launer, "Infrared Analysis of Organosilicon Compounds: Spectra-Structure Correlations," in *Silicon Compounds: Register and Review*, 1987, p. 69.
- [24] R. S. Smith, T. Tsui, and P. S. Ho, "Analysis of Ultraviolet Curing Effect on the Dielectric Constant and Molecular Structure of a Porous Dielectric Film," *Journal of Electronic Materials*, vol. 39, no. 10, pp. 2337-2345, Jun. 2010.
- [25] M. P. Marder, "Condensed Matter Physics," *John Wiley & Sons, Inc.*, 2000.
- [26] D. Briggs and M. P. Seah, "Practical Surface Analysis By Auger and X-ray Photoelectron Spectroscopy," *John Wiley & Sons Ltd.*, 1990.

- [27] T. Easwarakhanthan, D. Beyssen, L. Le Brizoual, and J. Bougdira, "Spectroellipsometric analysis of CHF<sub>3</sub> plasma-polymerized fluorocarbon films," *Journal of Vacuum Science & Technology A: Vacuum, Surfaces, and Films*, vol. 24, no. 4, p. 1036, 2006.
- [28] M. a. Worsley et al., "Effect of radical species density and ion bombardment during ashing of extreme ultralow-kappa interlevel dielectric materials," *Journal of Applied Physics*, vol. 101, no. 1, p. 13305, 2007.
- [29] J.-N. Sun, Y. Hu, W. E. Frieze, W. Chen, and D. W. Gidley, "How Pore Size and Surface Roughness Affect Diffusion Barrier Continuity on Porous Low-k Films," *Journal of The Electrochemical Society*, vol. 150, no. 5, p. F97, 2003.
- [30] R. Kumar, T. K. S. Wong, B. R. Murthy, Y. H. Wang, and N. Balasubramanian, "Effects of Plasma Treatments on Ultralow-k Dielectric Film and Ta Barrier Properties in Cu Damascene Processing," *Journal of The Electrochemical Society*, vol. 153, no. 5, p. G420, 2006.
- [31] G. Brunoldi, K. J. Kozaczek, B. Gittleman, and T. Marangon, "Impact of narrow trench geometries on copper film crystallography," *Microelectronic Engineering*, vol. 83, no. 11–12, pp. 2208-2212, Nov. 2006.
- [32] W. Steinhögl, G. Schindler, G. Steinlesberger, M. Traving, and M. Engelhardt, "Impact of line edge roughness on the resistivity of nanometer-scale interconnects," *Microelectronic Engineering*, vol. 76, no. 1–4, pp. 126-130, Oct. 2004.
- [33] M. Stucchi, M. Bamal, and K. Maex, "Impact of line-edge roughness on resistance and capacitance of scaled interconnects," *Microelectronic Engineering*, vol. 84, no. 11, pp. 2733-2737, Nov. 2007.
- [34] L. H. a. Leunissen, W. Zhang, W. Wu, and S. H. Brongersma, "Impact of line edge roughness on copper interconnects," *Journal of Vacuum Science & Technology B: Microelectronics and Nanometer Structures*, vol. 24, no. 4, p. 1859, 2006.
- [35] T. E. F. M. Standaert, "High density fluorocarbon etching of silicon in an inductively coupled plasma: Mechanism of etching through a thick steady state fluorocarbon layer," *Journal of Vacuum Science & Technology A: Vacuum, Surfaces, and Films*, vol. 16, no. 1, p. 239, Jan. 1998.
- [36] T. E. F. M. Standaert, P. J. Matsuo, S. D. Allen, G. S. Oehrlein, and T. J. Dalton, "Patterning of fluorine-, hydrogen-, and carbon-containing SiO<sub>2</sub>-like low dielectric constant materials in high-density fluorocarbon plasmas: Comparison with SiO<sub>2</sub>," *Journal of Vacuum Science & Technology A*, vol. 17, p. 741, 1999.
- [37] M. Schaepekens and G. S. Oehrlein, "A Review of SiO<sub>2</sub> Etching Studies in Inductively Coupled Fluorocarbon Plasmas," *Journal of The Electrochemical Society*, vol. 148, no. 3, p. C211, 2001.

- [38] A. Sankaran and M. J. Kushner, "Fluorocarbon plasma etching and profile evolution of porous low-dielectric-constant silica," *Applied Physics Letters*, vol. 82, no. 12, p. 1824, 2003.
- [39] D. Zhang and M. J. Kushner, "Investigations of surface reactions during C<sub>2</sub>F<sub>6</sub> plasma etching of SiO<sub>2</sub> with equipment and feature scale models," *Journal of Vacuum Science & Technology A: Vacuum, Surfaces, and Films*, vol. 19, no. 2, p. 524, 2001.
- [40] N. R. Rueger et al., "Role of steady state fluorocarbon films in the etching of silicon dioxide using CHF<sub>3</sub> in an inductively coupled plasma reactor," *Journal of Vacuum Science and Technology-Section A-Vacuum Surfaces and Films*, vol. 15, no. 4, pp. 1881-1889, Jul. 1997.
- [41] T. E. F. M. Standaert, C. Hedlund, E. a. Joseph, G. S. Oehrlein, and T. J. Dalton, "Role of fluorocarbon film formation in the etching of silicon, silicon dioxide, silicon nitride, and amorphous hydrogenated silicon carbide," *Journal of Vacuum Science & Technology A: Vacuum, Surfaces, and Films*, vol. 22, no. 1, p. 53, 2004.
- [42] N. Posseme, T. Chevolleau, O. Joubert, L. Vallier, and P. Mangiagalli, "Etching mechanisms of low-k SiOCH and selectivity to SiCH and SiO<sub>2</sub> in fluorocarbon based plasmas," *Journal of Vacuum Science & Technology B: Microelectronics and Nanometer Structures*, vol. 21, no. 6, p. 2432, 2003.
- [43] M. R. Baklanov et al., "Challenges of Clean / Strip Processing for Cu / low-k technology .," in *Proceedings of the IEEE 2004 International Interconnect Technology Conference, 2004.*, 2004, p. 187.
- [44] N. Posseme, T. Chevolleau, O. Joubert, L. Vallier, and N. Rochat, "Etching of porous SiOCH materials in fluorocarbon-based plasmas," *Journal of Vacuum Science & Technology B: Microelectronics and Nanometer Structures*, vol. 22, no. 6, p. 2772, 2004.
- [45] Y. Iba, T. Kirimura, M. Sasaki, Y. Kobayashi, Y. Nakata, and M. Nakaishi, "Effects of Etch Rate on Plasma-Induced Damage to Porous Low- k Films," *Japanese Journal of Applied Physics*, vol. 47, no. 8, pp. 6923-6930, Aug. 2008.
- [46] Y. Yin, S. Rasgon, and H. H. Sawin, "Investigation of surface roughening of low-k films during etching using fluorocarbon plasma beams," *Journal of Vacuum Science & Technology B: Microelectronics and Nanometer Structures*, vol. 24, no. 5, p. 2360, 2006.
- [47] E. T. Ryan et al., "Property modifications of nanoporous pSiCOH dielectrics to enhance resistance to plasma-induced damage," *Journal of Applied Physics*, vol. 104, no. 9, p. 094109, 2008.

- [48] V. Raballand, G. Cartry, and C. Cardinaud, "Porous SiOCH, SiCH and SiO<sub>2</sub> Etching in High Density Fluorocarbon Plasma with a Pulsed Bias," *Plasma Processes and Polymers*, vol. 4, no. 5, pp. 563-573, Jul. 2007.
- [49] F. Bailly et al., "Roughening of porous SiCOH materials in fluorocarbon plasmas," *Journal of Applied Physics*, vol. 108, no. 1, p. 014906, 2010.
- [50] R. a. Gottscho, "Microscopic uniformity in plasma etching," *Journal of Vacuum Science & Technology B: Microelectronics and Nanometer Structures*, vol. 10, no. 5, p. 2133, Sep. 1992.
- [51] O. Joubert, G. Oehrlein, and M. Surendra, "Fluorocarbon high density plasma. VI. Reactive ion etching lag model for contact hole silicon dioxide etching in an electron cyclotron resonance plasma," *Journal of Vacuum Science & Technology A*, vol. 12, no. 3, p. 665, 1994.
- [52] J. Bao et al., "Mechanistic Study of Plasma Damage of Low k Dielectric Surfaces," *AIP Conference Proceedings*, vol. 945, no. 1, pp. 125-141, 2007.
- [53] H. Shi and P. S. Ho, "Mechanistic Study of Plasma Damage to Porous Low-k: Process Development and Dielectric Recovery," vol. Ph. D. The University of Texas at Austin, 2010.
- [54] M. a. M. Goldman, D. B. Graves, G. a. Antonelli, S. P. S. Behera, and J. a. Kelber, "Oxygen radical and plasma damage of low-k organosilicate glass materials: Diffusion-controlled mechanism for carbon depletion," *Journal of Applied Physics*, vol. 106, no. 1, p. 013311, 2009.
- [55] H. Shi, "Mechanistic study of plasma damage to porous low-k: Process development and dielectric recovery," THE UNIVERSITY OF TEXAS AT AUSTIN, 2010.
- [56] P. C. Zalm, "Some useful yield estimates for ion beam sputtering and ion plating at low bombarding energies," *Journal of Vacuum Science & Technology B: Microelectronics and Nanometer Structures*, vol. 2, no. 2. p. 151, 1984.
- [57] C. Steinbruchel, "Universal Energy-Dependence of Physical and Ion-Enhanced Chemical Etch Yields at Low Ion Energy," *Applied Physics Letters*, vol. 55, no. 19, pp. 1960-1962, Jul. 1989.
- [58] H. Huang et al., "O<sub>2</sub> Plasma Damage and Dielectric Recoveries to Patterned CDO Low-k Dielectrics," in *Advanced Metallization Conference 2008 (Amc 2008)*, 2008, p. P. I. 8.
- [59] J.-N. Sun, D. W. Gidley, Y. Hu, W. E. Frieze, and E. T. Ryan, "Depth-profiling plasma-induced densification of porous low-k thin films using positronium annihilation lifetime spectroscopy," *Applied Physics Letters*, vol. 81, no. 8, p. 1447, 2002.

- [60] E. Kunnen et al., "Effect of energetic ions on plasma damage of porous SiCOH low-k materials," *Journal of Vacuum Science & Technology B: Microelectronics and Nanometer Structures*, vol. 28, no. 3, p. 450, 2010.
- [61] H. Shi et al., "Role of ions, photons, and radicals in inducing plasma damage to ultra low-k dielectrics," *Journal of Vacuum Science & Technology B: Microelectronics and Nanometer Structures*, vol. 30, no. 1, p. 011206, Dec. 2012.
- [62] K. Takeda et al., "Mechanism of plasma-induced damage to low-k SiOCH films during plasma ashing of organic resists," *Journal of Applied Physics*, vol. 109, no. 3, p. 033303, 2011.
- [63] D. R. Lide, "Handbook of Chemistry and Physics," *Chemical Rubber Publishing Company*.
- [64] L. Prager et al., "Effect of pressure on efficiency of UV curing of CVD-derived low-k material at different wavelengths," *Microelectronic Engineering*, vol. 85, no. 10, pp. 2094-2097, Oct. 2008.
- [65] J. J. Lin, D. W. Hwang, Y. T. Lee, and X. Yang, "Photodissociation of O<sub>2</sub> at 157 nm: Experimental observation of anisotropy mixing in the O<sub>2</sub>+hv→O(<sup>3</sup>P)+O(<sup>3</sup>P) channel," *The Journal of Chemical Physics*, vol. 109, no. 5, p. 1758, 1998.
- [66] J. Lee and D. B. Graves, "Synergistic damage effects of vacuum ultraviolet photons and O<sub>2</sub> in SiCOH ultra-low- k dielectric films," *Journal of Physics D: Applied Physics*, vol. 43, no. 42, p. 425201, Oct. 2010.
- [67] S. Eslava et al., "Ultraviolet-Assisted Curing of Organosilicate Glass Low-k Dielectric by Excimer Lamps," *Journal of The Electrochemical Society*, vol. 155, no. 11, p. G231, 2008.
- [68] P. Marsik, A. M. Urbanowicz, P. Verdonck, D. De Roest, H. Sprey, and M. R. Baklanov, "Effect of ultraviolet curing wavelength on low-k dielectric material properties and plasma damage resistance," *Thin Solid Films*, vol. 519, no. 11, pp. 3619-3626, Mar. 2011.
- [69] A. M. Urbanowicz et al., "Effect of UV wavelength on the hardening process of porogen-containing and porogen-free ultralow-k plasma-enhanced chemical vapor deposition dielectrics," *Journal of Vacuum Science & Technology B: Microelectronics and Nanometer Structures*, vol. 29, no. 3, p. 032201, 2011.
- [70] J.-francois De Marneffe et al., "Study of Ion and VUV Effects on Self-assembled Organic Low-k Material Exposed to Argon Plasma," in *MRS 2012 Spring*, 2012, p. C2.9.
- [71] J. J. Bao et al., "Mechanistic study of plasma damage of low k dielectric surfaces," *Journal of Vacuum Science & Technology B: Microelectronics and Nanometer Structures*, vol. 26, no. 1, p. 219, 2008.

- [72] M. R. Baklanov, A. M. Urbanowicz, and Y. Travaly, "Plasma-Induced Damage to Porous Low-k Materials," in *MRS Spring Meeting*, 2008, p. N 2.6.
- [73] E. W. Thiele, "Relation between Catalytic Activity and Size of Particle," *Industrial & Engineering Chemistry*, vol. 31, no. 7, p. 916, 1939.
- [74] J. Marschall and J. E. Boulter, "An analytic model for atom diffusion and heterogeneous recombination in a porous medium," *Journal of Physics D: Applied Physics*, vol. 39, no. 17, pp. 3849-3857, Sep. 2006.
- [75] W. Cho et al., "Polymer Penetration and Pore Sealing in Nanoporous Silica by CHF<sub>3</sub> Plasma Exposure," *Journal of The Electrochemical Society*, vol. 152, no. 6, p. F61, 2005.
- [76] H. Liu et al., "Challenges of Ultra Low-k Integration in BEOL Interconnect for 45nm and Beyond," *Proceedings of the IEEE International Interconnect Technology Conference 2009*, 2009.
- [77] M. R. Baklanov, L. Zhao, and B. Vereecke, "Scaling of low-k dielectrics: a bumpy road," 2010.
- [78] E. T. Ryan et al., "Designing Porous Ultra Low-k Dielectrics to Meet Scaling Challenges," in *Advanced Metallization Conference 2011 (Amc 2011)*, 2011, no. October.
- [79] S. Fruehauf et al., "Hydrophobisation Process For Porous Low K Dielectric Silica Layers," in *Conference Proceedings ULSI XVII*, 2002, vol. 287.
- [80] T. C. Chang et al., "Trimethylchlorosilane treatment of ultralow dielectric constant material after photoresist removal processing," *Journal of the Electrochemical Society*, vol. 149, no. 10, p. F145-F148, 2002.
- [81] Y. S. Mor et al., "Effective repair to ultra-low-k dielectric material (k=2.0) by hexamethyldisilazane treatment," *Journal of Vacuum Science & Technology B*, vol. 20, no. 4, pp. 1334-1338, 2002.
- [82] T. C. Chang et al., "Recovering Dielectric Loss of Low Dielectric Constant Organic Siloxane during the Photoresist Removal Process," *Journal of The Electrochemical Society*, vol. 149, no. 8, p. F81, 2002.
- [83] J. C. Hu et al., "Self-Organized Nanomolecular Films on Low-Dielectric Constant Porous Methyl Silsesquioxane at Room Temperature," *Journal of The Electrochemical Society*, vol. 150, no. 4, p. F61, 2003.
- [84] B. P. Gorman, R. a. Orozco-Teran, Z. Zhang, P. D. Matz, D. W. Mueller, and R. F. Reidy, "Rapid repair of plasma ash damage in low-k dielectrics using supercritical CO<sub>2</sub>," *Journal of Vacuum Science & Technology B: Microelectronics and Nanometer Structures*, vol. 22, no. 3, p. 1210, 2004.

- [85] B. Xie and A. J. Muscat, "Silylation of porous methylsilsesquioxane films in supercritical carbon dioxide," *Microelectronic Engineering*, vol. 76, no. 1–4, pp. 52-59, Oct. 2004.
- [86] B. Xie and A. Muscat, "The restoration of porous methylsilsesquioxane (p-MSQ) films using trimethylhalosilanes dissolved in supercritical carbon dioxide," *Microelectronic Engineering*, vol. 82, no. 3–4, pp. 434-440, Dec. 2005.
- [87] C. Smith, D. Mueller, and P. Matz, "Topographical and Chemical Surface Modification of Porous MSQ Using Silylating Agents With Different Numbers of Methoxy Groups," in *MATERIALS RESEARCH SOCIETY SYMPOSIUM PROCEEDINGS*, 2006, vol. 914, pp. 0914-F04-04.
- [88] T. Rajagopalan et al., "Investigation on hexamethyldisilazane vapor treatment of plasma-damaged nanoporous organosilicate films," *Applied Surface Science*, vol. 252, no. 18, pp. 6323-6331, Jul. 2006.
- [89] J. Liu, W. Kim, J. Bao, H. Shi, W. Baek, and P. S. Ho, "Restoration and pore sealing of plasma damaged porous organosilicate low k dielectrics with phenyl containing agents," *Journal of Vacuum Science & Technology B: Microelectronics and Nanometer Structures*, vol. 25, no. 3, p. 906, 2007.
- [90] T. Fischer, N. Ahner, S. Zimmermann, M. Schaller, and S. E. Schulz, "Influence of thermal cycles on the silylation process for recovering k-value and chemical structure of plasma damaged ultra-low-k materials," *Microelectronic Engineering*, pp. 1-6, May 2011.
- [91] O. Thomas et al., "Electrical property improvements of ultra low-k ILD using a silylation process feasible for process integration.," in *2011 IEEE International Interconnect Technology Conference*, 2011.
- [92] A. D. Ross and K. K. Gleason, "Effects of condensation reactions on the structural, mechanical, and electrical properties of plasma-deposited organosilicon thin films from octamethylcyclotetrasiloxane," *Journal of Applied Physics*, vol. 97, no. 11, p. 113707, 2005.
- [93] S. V. Nitta et al., "Use of difunctional silylation agents for enhanced repair of post plasma damaged porous low k dielectrics," *the Advanced Metallization Conference 2005 Proceedings*, 2005.
- [94] V. Gun'ko, M. Vedamuthu, G. Henderson, and J. Blitz, "Mechanism and Kinetics of Hexamethyldisilazane Reaction with a Fumed Silica Surface.," *Journal of colloid and interface science*, vol. 228, no. 1, pp. 157-170, Aug. 2000.
- [95] H. Shi et al., "Dielectric Recovery of Plasma Damaged Organosilicate Low-k Films," in *MATERIALS RESEARCH SOCIETY SYMPOSIUM PROCEEDINGS*, 2008, pp. 1079-N02-10.

- [96] T. Clifford, *Foudamentals of Supercritical Fluids*. Oxford University Press, 1999, p. 2.
- [97] K. A. Reinhard and W. Kern, Eds., *Handbook of Silcon Wafer Cleaning Technology*, Second. 2008.
- [98] A. Danel et al., "Supercritical CO<sub>2</sub> for ULK/Cu integration," in *Proceedings of the IEEE 2003 International Interconnect Technology Conference*, 2003, vol. 33, no. 0, p. 248.
- [99] P. D. Matz and R. F. Reidy, "Supercritical CO<sub>2</sub> Applications in BEOL Cleaning," *Solid State Phenomena*, vol. 103–104, p. 315, Mar. 2005.
- [100] F. Iacopi et al., "Short-ranged structural rearrangement and enhancement of mechanical properties of organosilicate glasses induced by ultraviolet radiation," *Journal of Applied Physics*, vol. 99, no. 5, p. 053511, 2006.
- [101] a. M. Urbanowicz, K. Vanstreels, P. Verdonck, D. Shamiryan, S. De Gendt, and M. R. Baklanov, "Improving mechanical robustness of ultralow-k SiOCH plasma enhanced chemical vapor deposition glasses by controlled porogen decomposition prior to UV-hardening," *Journal of Applied Physics*, vol. 107, no. 10, p. 104122, 2010.
- [102] I. Berry, C. Waldfried, K. Durr, and I. L. Berry III, "Requirements and Constraints on Optimizing UV Processing of Low-k Dielectrics," *Mater. Res. Soc. Symp. Proc.*, vol. 990, p. 15, 2007.
- [103] J. Proost, E. Kondoh, G. Vereecke, M. Heyns, and K. Maex, "Critical role of degassing for hot aluminum filling," no. October 1997, pp. 2091-2098, 1998.
- [104] J. Proost, M. Baklanov, K. Maex, and L. Delaey, "Compensation effect during water desorption from siloxane-based spin-on dielectric thin films," *Journal of Vacuum Science & Technology B: Microelectronics and Nanometer Structures*, vol. 18, no. 1, p. 303, 2000.
- [105] T. Yunogami, T. Mizutani, K. Tsujimoto, K. Suzuki, and S. Nishimatsu, "Radiation Damage in SiO<sub>2</sub>/Si Induced by VUV Photons," *Japanese Journal of Applied Physics*, vol. 28, no. 10, pp. 2172-2176, Oct. 1989.
- [106] H. Hosono, Y. Ikuta, T. Kinoshita, K. Kajihara, and M. Hirano, "Physical Disorder and Optical Properties in the Vacuum Ultraviolet Region of Amorphous SiO<sub>2</sub>," *Physical Review Letters*, vol. 87, no. 17, pp. 2-5, Oct. 2001.
- [107] S. Chikaki et al., "Ultralow-k/Cu Damascene Multilevel Interconnects Using High Porosity and High Modulus Self-Assembled Porous Silica," *Journal of The Electrochemical Society*, vol. 157, no. 5, p. H519, 2010.
- [108] H. Shi et al., "CO<sub>2</sub> and O<sub>2</sub> Plasma Induced Damage to Porous OSG Low-k Dielectrics," in *the Advanced Metallization Conference 2008 Proceedings*, 2008, p. P. VI. 6.

- [109] H. Shi et al., "Impact of CO<sub>2</sub> Plasma on Porous Organosilicate (OSG) Low-k Dielectrics," *Future Fab International*, no. 27, p. 88, 2008.
- [110] X. Hua et al., "Damage of ultralow k materials during photoresist mask stripping process," *Journal of Vacuum Science & Technology B: Microelectronics and Nanometer Structures*, vol. 24, no. 3, p. 1238, 2006.
- [111] S. Nagano, K. Sakoda, S. Hasaka, and K. Kobayashi, "Effectiveness of Dimethyl Carbonate and Dipivaloyl Methane Chemicals for Internal Repair of Plasma-Damaged Low- k Films," *Japanese Journal of Applied Physics*, vol. 50, no. 5, p. 05EB08, May 2011.